

UNIVERSITÉ DE  
CERGY-PONTOISE

LABORATOIRE DE PHYSIQUE  
THÉORIQUE ET MODÉLISATION



# THÈSE

Présentée pour obtenir le grade de

DOCTEUR DE L'UNIVERSITÉ PARIS SEINE

Spécialité Physique Théorique

**Mobile spins on lattice as model for liquid crystals and  
topological excitations and skyrmions**

par Aurélien BAILLY-REYRE

Soutenue le 15 octobre 2018 devant la commission d'examen composée de :

Président :	Dr. Alphonse Finel	Directeur de Recherche à l'ONERA Laboratoire d'Étude des Microstructures
Rapporteurs :	Prof. Jean-Claude Levy	Laboratoire Matériaux et Phénomènes Quantiques Université Paris-Diderot
	Prof. Jorge Linares	Groupe d'Étude de la Matière Condensée Université de Versailles-Saint-Quentin
Examineurs :	Prof. Damien Foster	Centre for Flow Measurement and Fluid Mechanics Coventry University
	Prof. Miron Kaufmann	Department of Physics Cleveland State University
Directeur de thèse :	Prof. Hung T. Diep	Laboratoire de Physique Théorique et Modélisation Université de Cergy-Pontoise



À mon grand-père et ma mère,



# Remerciements



Voici enfin achevée la rédaction de ce manuscrit. À ce propos, j'entends déjà les exclamations de soulagement de ma mère mais aussi de Silvia, sans oublier ceux du directeur du laboratoire, Jean : "Enfin!", "Ouf!", "Il était temps!"... J'entends aussi les railleries de mes amis me disant que je n'ai plus aucune excuse valable pour rester cloîtrer chez moi et refuser de sortir, les moqueries de mon parrain me demandant si je suis bien sûr d'en avoir fini avec les études... C'est beau d'être soutenu. Le point positif, hormis la satisfaction personnelle d'être allé jusqu'au bout, est que je n'entendrai plus jamais la fatidique et pesante question (n'est-ce pas Alice) "Et ta thèse?", m'évitant ainsi de répondre par un espèce de grognement.

Il est vrai que j'ai pris mon temps pour terminer cette thèse, mais à ma décharge il est difficile de poursuivre une activité de recherche et rédaction en parallèle d'un travail à temps plein. Poussé par certains de mes collègues (promis, je révélerai le nom des responsables), j'ai en effet passé un concours avant la fin de mon contrat de thèse, pour finalement obtenir un poste d'ingénieur en calcul scientifique (moi qui m'étais juré à la sortie de ma première année de licence de ne plus jamais toucher à une ligne de code) dans deux laboratoires de Jussieu. Je dois dire que je ne le regrette absolument pas étant donné mon épanouissement dans mon nouveau métier et l'ambiance de travail qui y règne grâce à mes *nouveaux* (tout est relatif) collègues. D'ailleurs cette prise de poste m'oblige (dans un sens positif) à allonger ma liste de personnes à remercier. Pour clore cette longue parenthèse, je tiens à préciser qu'il ne faut pas voir cette *reconversion* comme un choix par défaut et/ou un dégoût de la physique liée à la thèse. Mais bien au contraire, c'est cette dernière qui m'a conduit à mon poste actuel en me permettant de développer des compétences dans le calcul numérique et de découvrir une nouvelle profession notamment en interagissant fortement avec le responsable du centre de calcul de l'université de Cergy, Yann. De plus, étant entouré de physiciens, je reste en contact avec le monde de la physique et je sais que je continuerai de discuter avec mon comparse de thèse Valentin, entre autres choses, de physique. Je rajouterai que ces années passées en thèse ont été les plus belles de toutes mes études et que je souhaite à tout thésard de vivre ce que j'ai vécu (excepté ce long retard pour soutenir) : une ambiance chaleureuse presque familiale, des amitiés sincères et un sujet

intéressant.

Trêve de sérieux ! Il est grand temps de remercier sincèrement toutes les personnes qui m'ont aidé, soutenu de près ou de loin pendant ma thèse. N'en déplaise à Valentin, qui, bien que contraire à ses habitudes, se moque et bafoue les usages (cf. ses remerciements de thèse), je commencerai par remercier mon directeur de thèse et terminerai par ma famille.

En qualité de vingtième et avant-dernier (je n'aurai pas le privilège d'être le *der des ders* ; pourtant ce n'est pas faute d'avoir essayé) d'une longue lignée de thésards formés par celui que l'on pourrait surnommer le *sensei* (maître en japonais) du Monte Carlo, le *shishō* (celui qui détient la compétence, le savoir en japonais) de la physique statistique et de la matière condensée, j'ai été à très bonne école. De mon directeur de thèse j'ai appris, parmi tant de choses, qu'il n'y avait jamais de problèmes mais que des solutions. D'ailleurs si une devise ou plutôt une sorte de cri de guerre devait lui être attribuée ce serait la phrase connue de tous au LPTM : "Y a pas problème !". Une autre caractéristique de Hung, dont tout le monde convient, est sa puissance de travail. Je devrais même parler de puissance de frappe. Être capable de rédiger un livre de plus de quatre cents pages en moins de deux mois avec en parallèle des rédactions d'articles, cela force le respect. La forêt amazonienne n'a qu'à bien se tenir ; *le Diep des bouquins* (*sic* un de mes anciens professeurs, Joseph Scola, qui m'avait demandé qui était mon directeur de thèse) est maintenant à la retraite. Libéré de toutes contraintes administratives, je gage que le nombre de publications va s'envoler (je parie un *bo bu nem*, sur onze papiers par an ; qui en est ?). Je dois ajouter que je suis heureux d'avoir été ton thésard et que cela a été un plaisir de travailler ensemble. À ce titre, j'espère toujours pouvoir entretenir une collaboration, ne serait-ce que mineure. Merci Hung !

Une page et demie, seulement une seule personne de remerciée. Et si je me laissais aller, je pourrais aisément remplir un nombre de pages blanches égalant celui de cette thèse tant j'ai d'anecdotes, d'histoires et de bêtises à raconter. Quelle poisse de travailler dans une si bonne ambiance. Par où poursuivre...

Si j'en suis Sylvie, je peux me contenter de la remercier et de m'arrêter là. Oui Sylvie, j'ose révéler publiquement notre dernière conversation téléphonique et montrer ton vrai visage, toi qui as oublié mon précédent anniversaire. La pauvre, je ne suis pas très reconnaissant ; mais elle m'avait trop bien habitué. Chaque année, au mois de novembre, j'avais droit à un gâteau de sa part (je me souviens de presque tous...). Mais plus objectivement, *la maman du labo* bichonne (je ne parle pas de toi Fabien) et dorlote chaque membre du laboratoire toujours avec le sourire et c'est sur ses épaules que tout repose. Pour la remercier d'un tel dévouement, Valentin et moi l'avons gratifiée de notre plus belle trouvaille : un magnifique nain de jardin (dont l'esthétisme n'a pas su être apprécié à sa juste valeur par son mari Bernard). Les ingrats !! Heureusement qu'elle peut compter sur sa fidèle alliée Claire dont

le bureau est presque devenu mien à force de venir l'embêter et discuter. D'ailleurs, tu me dois toujours une explication de la DMRG et une collaboration scientifique (hélas pour toi, ma mémoire sélective n'a rien oublié de tout ça). Mais en réalité, c'est moi qui lui suis redevable (par égard pour Claire je ne révélerai pas ses surnoms) notamment pour son soutien et son aide dans la préparation de mes auditions de concours. Son dévouement est sincère et entier, et nos étudiants de CUPGE ne le savent que trop bien. Et puis il y a la force tranquille, le bon samaritain du laboratoire, *Guyyy*. Malgré sa phrase fétiche "Je suis large!", Guy a refusé de parier une caisse de *romanée-conti* qu'il soutiendrait son HDR avant ma thèse. Et pourtant, Dieu sait à quel point il était *large*. Nul n'aurait été besoin de tricher en changeant les termes du contrat et jouant sur l'ambiguïté de la définition de la fin de thèse (fin de contrat ou soutenance?) comme l'a fait Sylvie en mauvaise perdante pour un pari similaire...

Viennent ensuite Cédric et Fabien, les deux compères sarcastiques et moqueurs toujours plein d'humour. C'est d'ailleurs certainement pour cette raison que l'on s'est vite si bien entendu. Mais avis aux nouveaux doctorants, méfiez-vous de Cédric si vous souhaitez garder un secret. Il a un don inné pour vous faire parler. Sa méthode... il vous cuisine jusqu'à que vous craquiez. C'est un expert pour cela. Et à propos de cuisine, il se défend comme un chef et je dois avouer que c'est un véritable plaisir de s'inviter à manger chez lui. D'ailleurs Cédric, qu'est-ce-qu'on mange ce soir? Quant à Fabien, il a lui aussi un talent caché. Et pas des moindres! Il peut imiter le cri du *predator*. Cela peut faire peur. Mais, malgré son apparence de mauvais garçon à la mine "patibulaire mais presque" comme disait Coluche, vêtu d'une veste de cuir et chevauchant une mobylette faisant *mmmmhhMMMMHHH*, il n'aboie pas plus fort qu'un petit bichon maltais, surnom qui lui a été donné par l'ineffable Valentin. *Mais tout ça, c'est des conneries!* N'est-ce pas bichon? N'est-ce pas poussin?

Parler de Valentin et de ses *valentinades* (nom donné à ses actions ayant des conséquences relevant du burlesque) s'avère être un exercice plus compliqué qu'il ne m'y paraissait. En effet, je ne sais par où commencer.

Lors de ma première rencontre avec Valentin, je n'aurais jamais parié qu'il deviendrait un si bon ami (et je crois que cela est réciproque). Premièrement parce que les cliquetis (plusieurs centaines par minute) de sa souris lorsqu'il jouait au solitaire sur son ordinateur avaient le don de m'agacer. Et deuxièmement parce que ce provincial de normand refusait ma compagnie (peut-être trop versaillaise à son goût) et préférerait rentrer manger tout seul chez lui. Soit-disant que Monsieur n'était pas encore payé et ne pouvait pas se permettre de prendre un bon repas au CROUS. Puis les jours passèrent et au détour d'une longue conversation, nous nous rendîmes compte que nous avions plus d'affinités qu'on pouvait le croire et qu'elles ne se limitaient pas seulement au film les *Visiteurs* et à la série *Kaamelot* qui ont occupés plus d'une de nos soirées durant notre thèse autour de repas très équilibrés. "C'est pas faux!", me répondra-t-il sûrement. Nos soirées ne se sont d'ailleurs pas seulement

limitées à cela. Nous avons eu de nombreuses promenades nocturnes à pieds ou à *caddie* en chantant à tue tête dans la campagne neuvilloise, de nombreuses et longues discussions de politique, d'histoire, d'héraldique et de bien d'autres choses. En bref, durant cette thèse je me suis fait un ami véritable de plus au laboratoire et c'est avec toute la sympathie et l'estime que je te porte, que je te donne ce conseil, toi le docteur à l'écu de sinople aux glands d'or : ne prends pas le plus gros citron !

Et puis il y a *Monsieur bonnet* ou *Bibou*, Sahbi de son vrai nom, avec ses conversations téléphoniques passionnées et ses bavardages incessants. Et maintenant à ta place, il y a Claudia à qui je souhaite une bonne continuation et fin de thèse et de trouver un bon *vietnamique*. Il y aussi Pierre que je félicite d'avoir obtenu sa thèse deux jours avant moi (petit effronté) et à qui je dis *in bocca al lupo per il tuo postdoc!*

Ayant utilisé abondamment le *cluster* de calcul pour mes simulations numériques, il serait profondément injuste d'oublier l'amoureux du béton et de la ville de Cergy, à savoir Yann qui gère à merveille sa machine et qui m'a apporté conseils et soutiens dans l'optimisation de mes codes. Je tiens aussi à remercier chaleureusement les deux Thierry et Sylvain pour les conversations que nous avons eues et qui m'ont aidées dans la rédaction de ce manuscrit. Mention spéciale pour Thierry H. et son excellent *cacleute*.

J'ai aussi une pensée particulière pour Tuong, alias *Mister T* (à qui la fonction cube, bien qu'elle ne soit pas spéciale, sied parfaitement) qui m'a encouragé et poussé à passer les concours (voici enfin révélé, le nom du fautif de mon retard de soutenance).

La rédaction de ce manuscrit n'aurait pas abouti sans la compréhension de mes *nouveaux* collègues, qui m'ont soutenu et encouragé dans cette *épreuve* en acceptant que je prenne de mon temps de travail pour me consacrer à la rédaction (en contre partie je subis les blagues navrantes de mon chef de service François à longueur de journée).

Elle n'aurait pas abouti non plus sans l'aide d'Hervé et de Florence (alias Floflo) qui ont gentiment accepté que je travaille dans les locaux de leur école, le CDE à Versailles (pour ne pas faire de publicité), afin d'avoir un cadre studieux (ou presque; ces deux-là rigolant beaucoup).

Il y a aussi des remerciements sincères bien que sonnante comme une vieille promesse faite à une *argentinienne*, qui parle, paraît-il, très bien le français et qui s'enquiert régulièrement de savoir où en est ma thèse et comment je me porte. *Muchas gracias*, Vicki.

Et puis il y a aussi tous mes autres amis qui m'en voudront si je ne les cite pas. Louis, Richard, Charles, Fred, Caroline et Mumu avec qui j'ai fait une partie de mes études à

l'université, mais qui n'ont pas eu la foi ou la folie nécessaire pour me suivre en thèse. Il y a aussi mes amis du karaté Benoît, Pierre, Mélanie, Thierry mon professeur, Alice, Claire, Romain, Fée et Aurore bien que parfois un peu *lourdingue* en ce qui concerne ma thèse, répondent toujours présents en toute circonstance.

Je n'oublie évidemment pas Silvia dont la patience légendaire a été mise à rude épreuve ces derniers mois, mais qui malgré cela a été d'un soutien moral qui me fait dire que je suis un homme plus que chanceux. Elle a été aussi la petite voix qui me disait d'arrêter de perfectionner encore et encore la mise en page du manuscrit. *Grazie mille Miss Ciao*, je te suis sincèrement reconnaissant.

J'ai aussi une forte pensée pour Michel qui m'a permis d'ouïr correctement lorsque j'étais petit, me donnant ainsi la possibilité d'étudier.

Enfin, cette thèse n'aurait pu être écrite sans l'aide de ma mère, qui a dépensé une énergie folle pour me faire travailler plus jeune à l'école et "[m']emmener jusqu'au bac" comme elle savait si bien me le dire. Merci infiniment Maman ! Et puis, il y a mon grand-père Christian qui m'a donné le goût des mathématiques, de la physique, qui m'a toujours soutenu et qui, je le sais, aurait été très heureux et fier d'assister à ma soutenance. Un seul regret, et pas des moindres, subsiste. Celui d'avoir trop tardé à achever l'écriture de ce manuscrit et de ne pas avoir pu permettre, que cela se réalise.

Aurélien



# Abstract / Résumé

## English version



In this thesis, we are initially interested in the phase transitions that take place in liquid crystals (LC), from a theoretical and numerical point of view. Indeed, the results presented here are derived from Monte Carlo (MC) simulations and analytical developments based on statistical physics and condensed matter models.

A strong analogy exists between spin systems and LC. For example, the latter have phases where the molecules are all aligned in the same direction (orientational order) comparable to spins in ferromagnetic materials. Other phases, called cholesteric, are characterized by a molecular arrangement very similar to the helimagnetic structures. But liquid crystals being an intermediate state of matter, between the solid and the liquid phase, it is necessary to take into account the motions of the molecules in the models and to adapt accordingly the MC algorithm.

After a short and general introduction on LC and their applications in the first chapter, the second chapter is devoted to MC methods and the adaptation of the Metropolis-Hastings algorithm in order to introduce the mobility of molecules in our systems.

Chapter III is a test case to simulate LC. We consider a set of molecules (which we will call spins for convenience in analogy with condensed matter) on a lattice. The number of molecules is smaller than the number of the lattice sites to allow for a molecule mobility between sites. The interaction between nearest neighbouring spins is supposed to be a Potts model. The lowest energy state corresponds to the case where all the spins are packed at the bottom of the *tank*. This solid ground state becomes a liquid at high temperatures. This system is first treated with a mean-field (grand-canonical) analysis whose results are confirmed by the MC simulations. It appears that the surface layers undergo a melting and that the core of the remaining solid undergoes a first-order phase transition. The influence of the size effects, the concentration of the number of spins and the shape of the tank was studied.

The following chapter is devoted to particularly topological structures which are *skyrmions* and *stripe structures*. These structures are often observed in LC. We use a Dzyaloshinski-Moria (DM) interaction of strength  $D$  in addition to an exchange interaction  $J$  to study properties of thin films. In a first part of the chapter, we study the spin-wave excitations, also termed *magnons*, that are the result of a collective excitation of spins. Using the Green's function, we calculate the spin-wave spectrum which is used next to determine properties at  $T = 0$  (quantum fluctuations) and at finite temperatures. In the second part of the chapter, we apply a magnetic field  $H$  orthogonal to the thin film making appear a crystal of skyrmions. Using MC simulations, we show that skyrmions arranged on a super-structure of a triangular geometry. Depending on the value of  $D/H$ , these simulations also show a labyrinth-like structure very close to the filament-shaped structures found in certain LC. We show the stability of the crystal of skyrmions at finite temperatures and a stretched exponential relaxation law.

The next chapter is devoted to the study of the dynamics leading to the formation of the nematic and smectic phases using a mobile Potts model. We observe here how the nematic and smectic liquid crystals are dynamically formed upon cooling from the isotropic phase. The choice of the interactions is crucial to model these two phases. Various physical quantities have been calculated, confirming thus the transition from the isotropic phase to a LC structure.

In the chapter VI, we deal with the dipolar interaction in nanodots using the Heisenberg spin model. The first part of the chapter is devoted to the determination of the ground state exhibiting a vortex around the center of the dot. The spins lie in the  $xy$  plane at the border of the dot but go out of the  $xy$  plane at the dot center to give rise to a non-zero  $z$  component. We then study the effect of the temperature and the melting of the dot. The melting temperature of the dot do not depend on the size of the system. This is very different with the case of localised spins where the transition temperature increases with increasing the film thickness. This chapter is not directly related to liquid crystals. It was the first step towards a more complicated model describing the mechanism leading to cholesteric LC phases.

## Version française



ans cette thèse, nous nous sommes intéressés initialement aux transitions de phase qui ont lieu dans les cristaux liquides (CL), d'un point de vue théorique et numérique. En effet, les résultats présentés ici découlent de simulations numériques Monte Carlo (MC) et de développements analytiques basés sur modèles de physique statistique et de matière condensée. Une forte analogie existe entre les systèmes de spins et les CL. Par exemples, ces derniers présentent des phases où les molécules sont toutes alignées dans le même sens (ordre *orientationnel*) comparables aux spins dans les matériaux ferromagnétiques. D'autres phases, dites *cholestériques*, sont caractérisées par un arrangement moléculaire ressemblant beaucoup aux structures *héli-magnétiques*. Mais les cristaux liquides étant un état de la matière intermédiaire, situé entre le solide et le liquide, il est nécessaire de tenir compte des mouvements des molécules dans les modèles et d'adapter en conséquence l'algorithme de Monte Carlo utilisé.

Après une courte introduction sur les CL et leurs applications dans le premier chapitre, le second chapitre est longuement dédié aux méthodes MC et à l'adaptation de l'algorithme de Metropolis-Hastings afin d'introduire la mobilité des molécules dans nos systèmes.

Le chapitre III est en quelque sorte un cas test pour simuler les CL. On considère un ensemble de molécules (que l'on appellera spins par commodité et analogie avec la matière condensée) sur réseau et dont le nombre est inférieur au nombre de sites du réseau. L'interaction entre spins de plus proches voisins est de type Potts. L'état de plus basse énergie correspond au cas où tous les spins sont tassés au fond de la *cuve*. Ce système est d'abord traité par une étude de champ moyen (grand-canonique) dont les résultats sont confirmés par les simulations. Il apparaît que les couches de surface subissent une fusion et que le coeur du solide restant subit une transition du premier ordre. L'influence des effets de taille, de la concentration du nombre de spins ainsi que de la forme de la cuve a été étudiée.

Le quatrième chapitre est consacré à des structures topologiques particulières qui sont des *skyrmions* et des *structures en bandes* que l'on peut trouver dans les CL. A l'aide d'interactions Dzyalozhinski-Moria (DM)  $D$  en présence d'une interaction d'échange  $J$  dans des films minces, nous étudions dans un premier temps les excitations des ondes de spin, également appelées *magnons*, qui sont le résultat d'une excitation collective de spins. En utilisant les fonctions de Green, nous calculons le spectre d'ondes de spin permettant ainsi de déterminer les propriétés à  $T = 0$  (fluctuations quantiques) et à température finie. Dans un deuxième temps, nous appliquons un champ magnétique  $H$  orthogonal au film mince faisant apparaître un cristal de skyrmions. En utilisant des simulations MC, nous montrons des vortex pour lesquels chaque centre peut être considéré comme le noeud d'une super-structure. Nous parlons alors de cristal de skyrmions. Selon les valeurs de  $D/H$  les simulations peuvent montrer également une structure semblable à un labyrinthe très proche des structures

en forme de filaments que l'on trouve dans certains CL.

Le chapitre suivant est consacré à l'étude de la dynamique conduisant à la formation des phases nématiques et smectiques à l'aide d'un modèle mobile de Potts. Nous observons ici les mécanismes qui se produisent pour former un cristal liquide nématique ou smectique lors du refroidissement à partir d'une phase isotrope. Le choix des interactions est crucial pour modéliser ces deux phases. Différentes grandeurs physiques ont été calculées confirmant ainsi le passage d'une phase isotrope à une structure CL.

Dans le chapitre [VI](#), nous traitons de l'interaction dipolaire dans les *nanodots* avec un modèle de spin d'Heisenberg. La première partie du chapitre est consacrée à l'état fondamental présentant un vortex autour du centre du *dot*. Les spins sont coplanaires au plan du *dot* sauf à proximité du centre du *dot* où ils ont une composante  $z$  non nulle. Nous étudions ensuite l'effet de la température et la fusion du *dot*. La température de fusion du *dot* ne dépend pas de la taille du système, ce qui est très différent de ce qui se passe dans le cas des spins localisés, où la température de transition augmente avec l'épaisseur du film. Ce chapitre n'est pas directement lié aux cristaux liquides. Il était le premier pas dans la construction d'un modèle plus complet pour décrire le mécanisme conduisant aux phases cholestériques.

# Table of Contents

<b>Acknowledgement</b>	<b>i</b>
<b>Abstract</b>	<b>vii</b>
<b>List of Figures</b>	<b>xv</b>
<b>Acronyms</b>	<b>xxix</b>
<b>I Introduction</b>	<b>1</b>
<b>II Monte Carlo method for mobile spin systems</b>	<b>13</b>
II.1 Monte Carlo methods . . . . .	14
II.1.1 Theoretical framework: the statistical physics . . . . .	15
II.1.2 Sampling techniques . . . . .	16
II.1.3 Metropolis algorithm . . . . .	19
II.2 Adaptation to the mobile spin . . . . .	29
II.2.1 Non micro-reversible moves . . . . .	29
II.2.2 Mobile spin algorithm . . . . .	29
II.3 Sources of errors in Monte Carlo . . . . .	31
II.3.1 Systematic and statistical errors . . . . .	31
II.3.2 Random numbers generator . . . . .	34
<b>III A toy model for the study of liquid crystals: the Mobile Potts model</b>	<b>37</b>
III.1 Introduction . . . . .	38
III.2 Mobile Potts Model . . . . .	39
III.3 Mean-Field Theory . . . . .	40
III.3.1 Hamiltonian . . . . .	40
III.3.2 Mean-Field Theory . . . . .	41
III.4 Monte Carlo results . . . . .	48
III.4.1 Transition . . . . .	48
III.4.2 Effect of concentration . . . . .	53

III.4.3	Surface sublimation . . . . .	53
III.5	Conclusion . . . . .	56
<b>IV</b>	<b>Spin systems with Dzyaloshinskii-Moriya interaction</b>	<b>59</b>
IV.1	Introduction . . . . .	60
IV.2	Magnons in thin films . . . . .	61
IV.2.1	Introduction . . . . .	61
IV.2.2	Magnons with Dzyaloshinskii-Moriya interaction . . . . .	62
IV.3	Skyrmion Crystal . . . . .	71
IV.3.1	Model and Ground State . . . . .	71
IV.3.2	Stability at finite temperatures . . . . .	75
IV.4	Conclusion . . . . .	80
<b>V</b>	<b>Potts model to study the dynamics of nematic and smectic liquid crystals</b>	<b>83</b>
V.1	Introduction . . . . .	84
V.2	Method of simulation . . . . .	84
V.3	The smectic phase . . . . .	85
V.3.1	Model . . . . .	85
V.3.2	Results . . . . .	86
V.4	The nematic phase . . . . .	88
V.4.1	Model . . . . .	88
V.4.2	Results . . . . .	89
V.5	Conclusion . . . . .	91
<b>VI</b>	<b>Nanodots: dipolar interaction</b>	<b>93</b>
VI.1	Introduction . . . . .	94
VI.2	Ground state . . . . .	95
VI.2.1	Model and method of ground-state determination . . . . .	95
VI.3	Melting: Mobile Spin Model . . . . .	97
VI.3.1	Model and method . . . . .	97
VI.3.2	Comparison with a localized-spin system . . . . .	99
VI.3.3	Effect on the number of layers that can melt . . . . .	100
VI.4	Conclusion . . . . .	102
<b>VII</b>	<b>Conclusion</b>	<b>105</b>
<b>A</b>	<b>Markov chains</b>	<b>109</b>
A.1	Introduction . . . . .	110
A.2	Discrete-time Markov Chains . . . . .	110
A.2.1	Definitions . . . . .	110
A.2.2	Chapman-Kolmogorov equation . . . . .	112
A.2.3	Irreducibility (ergodicity) . . . . .	114

A.2.4	Stationary distribution and reversibility . . . . .	116
A.2.5	Asymptotic theorem . . . . .	118
A.2.6	Generalisation to continuous space state . . . . .	120
A.3	Continuous-time Markov chain . . . . .	120
<b>B</b>	<b>Monte Carlo error analysis</b>	<b>121</b>
B.1	Statistical error and correlation time . . . . .	122
B.2	Numerical error analysis methods . . . . .	124
<b>C</b>	<b>Metropolis criterion: a non normalised transition probability matrix?</b>	<b>125</b>
C.1	A brief reminder of the theoretical framework . . . . .	126
C.2	Metropolis criterion and transition matrix . . . . .	126
<b>D</b>	<b>Green's functions</b>	<b>129</b>
D.1	Classical Green's functions . . . . .	130
D.2	Quantum Green's functions . . . . .	131
D.2.1	Schrödinger equation and propagators . . . . .	131
D.2.2	Single-particle quantum Green's function . . . . .	132
D.3	Some calculations . . . . .	133
D.3.1	Equation of motion . . . . .	134
D.3.2	Layer magnetisation . . . . .	136
	<b>List of publications</b>	<b>139</b>
	<b>Bibliography</b>	<b>141</b>



# List of Figures

I.1	Schematic representation of the microscopic arrangement of the matter in two phases. <i>Left:</i> Crystalline phase. Atoms or groups of atoms are periodically arranged. There is a long-range order. The red cube represents a <i>primitive cell</i> (cf. crystallography's concepts [49]) allowing to determine the position of atoms in the crystal from the position of one atom. <i>Right:</i> Liquid phase. There is no order and constituents are weakly bound to each other, allowing thus to the liquid to change form. . . . .	3
I.2	Schematic representations of the different rode-like molecules arrangement that can be found in liquid crystals. <i>Left:</i> Nematic mesophase. Molecule have no position order but aligned according to a common direction, having thus a long-range direction order. <i>Middle and right:</i> The last schemas represent two smectic mesophases : smectic A (left) and smectic C (right). Molecules are organised in layers, giving thus a long-range positional order in one direction. There is no ordered arrangement within layers and molecules are still characterised by a directional order. For the smectic A structure, molecules are aligned along the normal to the layers, while for smectic C, they are tilted. . . . .	4

I.3	<p>Pictures of liquid crystals (LC) viewed under a polarising microscope (composed of two cross linear polarisers). The sample, illuminated by a linear polarised light, is observed through a linear polariser. The color of the LC is due to their birefringent properties. <i>Left:</i> Nematic mesophase. The black lines, called <i>disclinations</i> lines, are the regions where the global orientation of the molecules change abruptly, due to topological defects occurring, for instance, under electric or magnetic field or simply because of the mechanical constraints applied by the recipient on the sample. It corresponds to extinction zones of light passing through cross polariser. <i>Right:</i> Smectic A mesophase. Molecules have the same global orientation and structured in layers. . . . .</p>	5
I.4	<p>Schematic representations of the cholesteric also termed chiral nematic mesophase. Molecules have no long-range position order but are stacked in very thin layers and have a preferred orientation which varies from a layer to another with a certain periodicity. . . . .</p>	6
I.5	<p>Columnar mesophase made of disk-like molecules that are stacked making a columnar structure. Molecules have a two-dimensional positional order within the plane and no order along the third dimension. This mesophase is also termed <i>columnar liquid</i>. . . . .</p>	6
I.6	<p>Schematic representation of a liquid crystal display (LCD). The incident light is polarised linearly by the first polariser. The electric field of the polarised light is orthogonal to the polarisation axis of the analyser such as there is extinction in output. Thus, The polarisation surface of the light must be rotated, thanks to the orientation of the molecules, in order to pass through the analyser. <i>Left:</i> The molecules have an helix configuration. This is a chiral nematic mesophase. The light is transmitted. Its polarisation follows the helix structure. <i>Right:</i> By applying a voltage, the molecules change their orientation. If molecules are parallel or orthogonal (like on the figure) the polarisation of the light is not changed and there is extinction. . . . .</p>	7

I.7 Schema showing the physical principle to determine the temperature of a surface using *cholesteric* liquid crystals (LC). The system is based on simple optical laws. A beam of white light is sent on an interface containing liquid crystals with an angle of incidence  $\theta_i$  to the normal  $\mathbf{n}_0$ . It is then refracted and dispersed in several beams that are reflected on the **cholesteric layers** undergoing a diffraction similar to the Bragg's diffraction [23] giving birth to a wave packet crossing again the surface with a certain wave length  $\lambda$  and consequently with a certain color.  $\lambda$  depends on  $\theta_i$ , on  $\theta_r$  and on the orientation of the molecules in the **layers** which is a function of the temperature. With these three quantities, it is then possible to know the temperature of the surface on which is placed the device. . . . . 8

II.1 Representation, inspired by [132], of the balance conditions for probability flow in Markov chain process. Each *cell* represent an accessible state or configuration. The arrows denote a transition from a configuration to another and the circular ones indicate a *self*-transition (from a state to itself). The total probability transition flow is conserved for every single *cell*. To be consistent with the text, the **blue** letters denote the *initial* states called *i* and obviously, the **red** letter the *final* state *f*. *Left*: Global balance criterion. The sum of every moves from outside a *cell* to inside is equal to the sum of all the outflows. *Right*: Detailed balance criterion. The states are reversible. The inflow  $i \rightarrow f$  is automatically compensated by the reverse outflow  $f \rightarrow i$ . 21

II.2 Representation of the circulation of money between different economic players (*W* for workers, *R* for retired persons, *F* for firms, *S* for State and *B* as bank) to illustrate an unsustainable economy of a society modelled by a system with five different possible states with a *non-ergodic strategy*. In terms of physics, starting from a state, certain states will never be visited over the time and each arrow represents a possible transition with its probability transition  $W_{i \rightarrow j}$ . *Left*: Only the *self*-transitions are authorized ( $W_{i \rightarrow i} = 1$ ). It corresponds to the situation where every entity saves up its money. There is then no *money-flow*. *Right*: The money will never transit over all the protagonist. It flows essentially from the firm to the bank as repayment of loans or to its workers as salaries or to the State as taxes. Eventually, only the retired persons, receiving their pension from the State, participate to the commercial activity of the firm by buying what it produces. At the end, the situation is critical for the global economy of the society, because money is bad distributed. . . . . 23

II.3 Representation of an ergodic system with five states. Each arrow represents a possible transaction between different economic players:  $W$  for workers,  $R$  for retired persons,  $F$  for firms,  $S$  for State and  $B$  for banks. The system is ergodic because the money can circulate from an entity or a person to another one and never *gets stuck* in a place like a bank for instance. Every transaction coming out of the bank are loans and those coming in are either repayment loans (with interest rates) or simply bank charges. The State has a central role. It receives money from taxes or loans from the bank and reverses money as social benefits (except to the banks) to help people or firms. Workers are paid by their firms and buy what they produce and takes out sometimes a loan (dashed arrow). They also can borrow money for the retired persons. The latter receive their pension from the State and participate to the benefits of the firm. . . . . 24

II.4 Snapshots of an Ising system on a 2D  $500 \times 500$ -square lattice with nearest neighbours interactions at different Monte Carlo sweeps (MCS). Each column corresponds to a special initial configuration at a given temperature  $T$  (expressed in  $k_b/J$ , with  $J$  the interaction exchange constant) and each row to the configuration at a certain numbers of MCS. The spins up  $\uparrow$  are in **blue** and the spins down  $\downarrow$  in **red**. *Left* : Evolution of an anti-ferromagnetic configuration at  $T = 0.1$ . The different snapshots show the system evolves progressively to a ferromagnetic system. *Middle* : The initial configuration is randomly generated. At the critical temperature  $T = T_c = 2.269$ , some clusters of spins **up** and spins **down** appear. The system is stuck in this kind of configuration. The Metropolis algorithm is not adapted for the study of the system at  $T_c$  contrary to a cluster flip algorithm. *Right* : At  $T = 3.0$ , the system moves rapidly from a ferromagnetic phase to a disordered one. It appears there are almost no differences between the three last configurations. 28

II.5 Diagram showing the different steps of the Monte Carlo algorithm for mobile spin systems. These steps must be repeated until all the lattice sites have been visited before calculating the physical quantities of the system (energy, magnetisation...) . . . . . 30

II.6	Plot of magnetisation $M$ versus temperature $T$ (in unit $J/k_B$ ) obtained by Monte Carlo simulation of an Ising model without external magnetic field on a square lattice of size $L$ with periodic boundary conditions. The figure shows a finite size scaling effect; indeed the evolution of the order parameter $M$ depends clearly on $L$ . For instance, when $L = 5$ , the magnetisation decreases slightly. But when $L$ becomes larger and larger, the behaviour of $M$ tends towards the behaviour described by the analytical solution [148], <i>i.e.</i> a brutal drop to zero of the order parameter at the critical temperature $T_c \simeq 2.27 J/k_B$ . . . . .	33
II.7	Parking lot test performed over $3 \times 10^4$ cars with two different generators: RANDU and Mersenne Twister (MT). A 3-dimensional distribution has been used to generate the coordinates $(r_n, r_{n+1}, r_{n+2})$ to build the graphs. Only the non-overlapping cars, modelled by one unit length side squares, are plotted. <i>Left</i> : Result obtained for the RANDU random generator. It appears clearly a correlation between numbers because of the presence of fifteen two-dimensional stripes. The generated numbers are not random at all. <i>Right</i> : Results obtained with the MT algorithm. There is no sign of correlations between generated numbers because of the absence of striped patterns on the plot. . . . .	36
III.1	Ground state (GS) of the system with $N_x = N_y < N_z$ , where the interaction between nearest neighbours spins is ruled by a ferromagnetic Hamiltonian (6-Potts model here). A GS configuration is then reached when all the spins are stacked in the bottom of the recipient and have all the same state (in <b>blue</b> on the figure). . . . .	40
III.2	Average number of particles per site $n$ (curve 1, <b>red</b> , left scale) and order parameter $Q = qm$ (curve 2, <b>blue</b> , right scale) versus temperature $T$ for different chemical potential $\mu$ : (a) $\mu = -0.3$ , (b) $\mu = -0.4$ , (c) $\mu = -0.51$ . For small $\mu$ , the order parameter show a discontinuity (first-order phase transition) that is reduced when $\mu$ is increased, while decreasing $\mu$ destroys totally the order. Indeed for $\mu = 0.51$ the order parameter is constant and equal to zero. . . . .	44
III.3	Phase diagram in the plane $(T, \mu)$ . The solid <b>red</b> line is a first-order transition line. Above this line, <i>i.e.</i> low temperature $T$ and high chemical potential $\mu$ , the system is in an ordered phase (solid), while under the red line, it corresponds to a disordered phase (gas). . . . .	45

III.4	Phase diagram in the plane $(T, p)$ . The <b>red</b> line brands the separation between the solid phase (above the line; low temperature and high temperature) and the gas phase (below the line; high temperature). . . . .	45
III.5	Isotherms $(p, n)$ are shown by thick curves for $T = 0.25$ (curve 1, <b>violet</b> ), 0.23 (curve 2, <b>green</b> ), 0.2 (curve 3, <b>blue</b> ) and 0.18 (curve 4, <b>red</b> ). Thin broken lines indicate discontinuities of $n$ . The system exhibits a first-order phase transition for $T < 0.25$ . The higher $n$ branch corresponds to a solid phase while the lower branch to a gas. . . . .	46
III.6	Phase diagram in the plane $(T, n)$ . The <b>red</b> squares and <b>blue</b> circles lines represent the densities of the solid and of the gas, respectively. The region between the <b>red</b> line and the <b>blue</b> line correspond to a solid phase. Below the <b>blue</b> line, <i>i.e.</i> at high temperature, the system is in gaseous phase. The coalescence point occurs at $T = 0.25$ and corresponds to the infinite chemical potential limit, <i>i.e.</i> no vacancies. . . . .	46
III.7	Entropy ( <i>left</i> ) and energy ( <i>right</i> ) as functions of temperature and chemical potential. Note that the entropy is a concave function, which is in accord with the second law of thermodynamics. Indeed, the equilibrium of a system is reached when the entropy is maximal. . . . .	47
III.8	Surface in the space <i>temperature</i> $T$ , <i>pressure</i> $P$ and <i>chemical potential</i> $\mu$ . The discontinuity in slope of $\mu$ is sign of first-order transition. . . . .	47
III.9	Magnetization $M$ versus temperature $T$ (in unit of $J/k_B$ ) for a lattice of $15 \times 15 \times 30$ sites with a spin concentration $c = 50\%$ . The system is completely ordered at $T = 0$ , then surface spins are little by little evaporated with increasing $T$ . The phase transition of spin orientations of the solid core occurs at $T_c \simeq 1.234$ . . . . .	49
III.10	Energy histogram $P(U)$ recorded at $T_c = 1.234$ for a lattice $15 \times 15 \times 30$ with concentration $c = 50\%$ . It represents the probability $P$ of observing a state of energy $U$ . The presence of the two peaks, <i>i.e.</i> two co-existing phases, indicates that the transition is of first-order. . . . .	49

III.11 Comparison of the evolution of (a) the magnetisation $M$ , (b) the energy per spin $U$ , (c) the specific heat $C_V$ and (d) the magnetic susceptibility $\chi$ versus the temperature of a half-filled lattice $N_x \times N_y \times N_z$ for several sizes $N_x = N_y = N_z/2 = 10$ ( <b>red</b> void circles), 15 ( <b>blue</b> filled circles), 20 ( <b>green</b> void diamonds), 25 ( <b>black</b> stars), 30 ( <b>magenta</b> crosses) and 35 ( <b>sky-blue</b> void squares). For the small box, <i>i.e.</i> for $N_x = 10$ , the transition looks like to a second-order phase transition because of the finite-size effect, while for the other sizes of box the discontinuities suggest first-order transitions. . . .	50
III.12 Transition temperature versus lattice size $N_x \times N_y \times N_z$ at concentration $c = 50\%$ where $N_x = N_y = N_z/2$ , with $N_z = 30, 40, 50, 60, 70$ and $80$ . . . .	51
III.13 Simulation for a half filled lattice size $35 \times 35 \times 70$ (concentration $c = 50\%$ ): (a) Snapshot of the system at $T = 1.3128$ close to the transition. Each color corresponds to a spin state. <i>i.e.</i> to a specific orientation. (b) $R$ vs $Z$ , $R$ being the percentage of lattice sites having $Z$ nearest neighbours, at $T = 1.3128$ . Note that the solid phase is well indicated by the number of sites with 6 neighbours. . . . .	52
III.14 Effect of concentration: (a) Magnetization versus temperature for a lattice $15 \times 15 \times N_z$ where $N_z = 20$ ( <b>red</b> void circles) , 30 ( <b>blue</b> filled circles) , 40 ( <b>green</b> diamonds), 50 ( <b>black</b> stars) , 60 ( <b>magenta</b> crosses). For each case, only the fifteen first layers are filled, corresponding to concentrations $15/N_z$ . (b) Transition temperature versus the recipient height $N_z$ . . . . .	53
III.15 (a) Total magnetisation $M$ and (b) energy per spin $U$ versus $T$ . <b>Red</b> void circles indicate results of localized spins and <b>blue</b> filled circles indicate those of the completely mobile model. Between these two limits, <b>green</b> void diamonds, <b>black</b> stars and <b>magenta</b> crosses correspond respectively to the cases where one, two and four surface layers are allowed to be mobile. . . .	54
III.16 Diffusion coefficient $D$ versus $T$ . <b>Red</b> void circles (lowest curve) indicate results of localized spins and <b>blue</b> filled circles (topmost curve) indicate those of the completely mobile model. Between these two limits, from below <b>green</b> void diamonds, <b>black</b> stars and <b>magenta</b> crosses correspond respectively to the cases where one, two and four surface layers are allowed to be mobile. .	54

III.17 (a) Magnetic susceptibility $\chi$ and (b) heat capacity $C_V$ versus $T$ . <b>Red</b> void circles indicate results of localized spins and <b>blue</b> filled circles indicate those of the completely mobile model. Between these two limits, <b>green</b> void diamonds, <b>black</b> stars and <b>magenta</b> crosses correspond respectively to the cases where one, two and four surface layers are allowed to be mobile. . . .	55
III.18 Layer magnetisations for the first four layers: <b>red</b> void circles, <b>blue</b> filled circles, <b>green</b> diamonds and <b>black</b> stars are the magnetisations of the first, second, third and fourth layers, respectively. The solid <i>retains</i> the fourth layer, <i>i.e.</i> the closest to the solid, up to the bulk transition that occurs at $T_c = 1.330$ . The three other layers on the top evaporate at temperature well below $T_c$ . They are not retained by the first layer. . . . .	55
III.19 (a) Magnetization, (b) energy and (c) diffusion coefficient for two system shapes $20 \times 20 \times 40$ ( <b>red</b> void circles) and $40 \times 20 \times 20$ ( <b>blue</b> filled circles) at concentration $c = 50\%$ . It appears clearly, there is no phase transition for the <i>lying box</i> $40 \times 20 \times 20$ , because this kind of shape offers a larger free surface. . . . .	56
IV.1 Example of a geometry to define $D_{ij}$ : large gray circle is the non-magnetic ion, red small circles are spins, vectors $\mathbf{r}_i$ and $\mathbf{r}_j$ are defined as indicated. See text for comments. . . . .	63
IV.2 Local coordinates in the $xz$ -plane. The spin quantization of $\mathbf{S}_i$ and $\mathbf{S}_j$ are $\hat{\zeta}_i$ and $\hat{\zeta}_j$ , respectively. . . . .	64
IV.3 (a) The ground state is a planar configuration on the $xz$ plane. The figure shows the case where $\theta = \pi/6$ ( $D = -0.577$ ), $J_{\parallel} = J_{\perp} = J = 1$ ; (b) a zoom is shown around a spin with its nearest neighbors. . . . .	65
IV.4 Value $d_c$ above which the SW energy $E(\mathbf{k} = \mathbf{0})$ is real as a function of $\theta$ (in radian), for a 4-layer film. Note that no spin-wave excitations are possible near the perpendicular configuration $\theta = \pi/2$ . See text for comments. . . .	69
IV.5 Spin-wave spectrum $E(k)$ versus $k \equiv k_x = k_z$ for a thin film of 8 layers: (a) $\theta = \pi/6$ (in radian) (b) $\theta = \pi/3$ , using $d = d_c$ for each case ( $d_c = 0.012$ and $0.021$ , respectively). Positive and negative branches correspond to right and left precessions. Note the linear- $k$ behaviour at low $k$ for the large $\theta$ case. . .	69

IV.6 Spin length $S_0$ at $T = 0$ of the first 4 layers as a function of $\theta$ , for $N = 8$ , $d = 0.1$ . <b>Red</b> circles, <b>blue</b> void circles, <b>green</b> void triangles and <b>magenta</b> squares correspond respectively to the first, second, third and fourth layer. . . . .	70
IV.7 Surface effect: (a) spin-wave spectrum $E(k)$ versus $k = k_x = k_z$ for a thin film of 8 layers: $\theta = \pi/6$ , $d = 0.2$ , $J_{\parallel}^s = 0.5$ , $J_{\perp}^s = 0.5$ , the gap at $k = 0$ is due to $d$ . The surface-mode branches are detached from the bulk spectrum. (b) Layer magnetisations versus $T$ for the first, second, third and fourth layer ( <b>red</b> circles, <b>green</b> void circles, <b>blue</b> void circles and <b>magenta</b> filled squares, respectively). . . . .	70
IV.8 Critical temperature $T_c$ versus the film thickness $N$ calculated with $\theta = \pi/6$ and $d = 0.1$ . For the infinite thickness (namely 3D), $T_c \simeq 2.8$ which is displayed by the horizontal blue line. . . . .	71
IV.9 Ground state for $D/J = 1$ and $H/J = 0.5$ (in unit of $J = 1$ ). We can observe a crystal of skyrmions. (a): Skyrmion crystal viewed in the $xy$ plane. (b) <i>top</i> : a 3D view. (b) <i>bottom</i> : Zoom of the structure of a single vortex. The value of $S_z$ is indicated on the color scale. . . . .	73
IV.10 (a): Ground state for $D/J = 1$ and $H/J = 0$ (in unit of $J = 1$ ), a mixing of domains of long and round islands. (b): Ground state for $D/J = 1$ and $H/J = 0.25$ (in unit of $J = 1$ ), a mixing of domains of long islands and vortices. The latters are due to the increase of $H$ . These structure can be termed <i>labyrinth phase</i> . (c): Experimental observation (with a transmission electronic microscope) of a cholesteric liquid crystal (LC). The <i>fingerprints</i> structure is similar to the figure above. The dark and bright lines correspond to the region where molecules of LC are parallel and perpendicular, respectively, to the image plane (cf. article of Mitov <i>and al.</i> [134]). . . . .	74
IV.11 Phase diagram in the $(D, H)$ plane for a lattice size $100 \times 100$ . The region above the <b>blue</b> line corresponds to the field-induced ferromagnetic phase, while below the <b>red</b> line it corresponds to <i>labyrinth phase</i> , <i>i.e.</i> a phase with rectangular domains and skyrmions. The narrow <b>grey</b> band is the region of the skyrmion crystal phase. . . . .	75

IV.12	<p><b>Red</b> circles: order parameter defined in equation (IV.44) versus <math>T</math>, for <math>H = 0.5</math> and <math>N = 1800</math>, averaged during <math>t_f = 10^5</math> MC steps per spin after an equilibrating time <math>t_0 = 10^5</math> MC steps. <b>Blue</b> crosses: the projection of the <math>S_z</math> on <math>S_z^0</math> of the ground state as defined in equation (IV.44) but for the <math>z</math> components only. The magnetisation <math>M</math> does not vanish totally because of the applied field. . . . .</p>	76
IV.13	<p>Order parameters defined in Eqs. (IV.45)-(IV.46) versus <math>T</math>, for <math>H = 0.5</math> and <math>N = 800</math>, <math>t_0 = 10^5</math>, <math>t_f = 10^6</math>. <b>Red</b> circles: total positive <math>z</math> component (<math>Q_+(T)</math>). <b>Green</b> circles: total negative <math>z</math> component <math>Q_-(T)</math>. <b>Blue</b> circles: total <math>z</math> component. After the transition, all spin have positive <math>z</math> component. . . . .</p>	77
IV.14	<p>The order parameter <math>M</math> defined by equation (IV.44) versus MC time <math>t</math> in unit of 1000 MC steps per spin, for <math>H = 0.5</math> and <math>N = 800</math> (a) <math>T = 0.01</math>, values of fitting parameters <math>\alpha = 0.6</math>, <math>A = 0.008 \pm 0.00001</math>, <math>\tau = (364 \pm 19) \times 10^3</math>, <math>c = 0.984505 \pm 0.00012</math>; (b) <math>T = 0.094</math>, <math>\alpha = 0.6</math>, <math>A = (0.0653 \pm 0.0013)</math>, <math>\tau = (277 \pm 36) \times 10^3</math>, <math>c = (0.822 \pm 0.018)</math>; (c) <math>T = 0.17</math>, <math>\alpha = 0.8</math>, <math>A = 0.31 \pm 0.01</math>, <math>\tau = (891 \pm 100) \times 10^3</math>, <math>c = 0.43 \pm 0.017</math>. . . . .</p>	78
IV.15	<p>The order parameter <math>M(T)</math> versus <math>T</math> for several waiting times <math>t</math>, for <math>H = 0.5</math> and <math>N = 800</math>: from above <math>t = 10^5, 2 \times 10^5, 10^6, \infty</math> (by fitting with equation (IV.47)). . . . .</p>	79
V.1	<p>Snapshot of the system at two different temperatures. Spins are contained in a <i>box</i> with periodic boundary conditions. There is <math>N_L = 15 \times 15 \times 30 = 6750</math> sites and 2025 spins, <i>i.e.</i> a spin concentration equal to <math>c = 30\%</math>. Each colored point corresponds to a spin state. <i>Left</i>: Initial configuration of the system at a high temperature <math>T = 5</math>. The system is completely disordered. <i>Right</i>: Final configuration at low temperature <math>T = 0.1</math>. The system was cooled down from the disordered phase. Spins are staged in independent layers and within a layer all the spins have the same orientation (color). It corresponds to a smectic phase. . . . .</p>	86
V.2	<p>Evolution of energy and diffusion coefficient as functions of temperature. The spin concentration <math>c</math> is <math>c = N_s/N_L = 30\%</math>, with <math>N_L = 15 \times 15 \times 30</math>. The exchange interactions are <math>J_{\parallel} = 3.0</math>, <math>J_{\perp} = -1.0</math>. . . . .</p>	87
V.3	<p>Histogram showing the percentage <math>R</math> of sites having <math>\mathcal{Z}</math> nearest neighbors at <math>T = 0.1</math>, <i>i.e.</i> corresponding to the snapshot at the bottom in the Figure V.1. Spins are distributed such as they have only 4 neighbors, meaning they are staged in layers. . . . .</p>	87

V.4	Evolution of magnetisation and susceptibility as functions of temperature. The spin concentration $c$ is $c = N_s/N_L = 30\%$ , with $N_L = 15 \times 15 \times 30$ . The exchange interactions are $J_{\parallel} = 3.0$ , $J_{\perp} = -1.0$ . . . . .	88
V.5	Snapshot of the system at two different temperature. Spins are contained in a <i>box</i> . There is $N_L = 15 \times 15 \times 30 = 6750$ sites and 2025 spins, <i>i.e.</i> a spin concentration equal to $c = 30\%$ . Each colored point corresponds to a spin state. <i>Left:</i> Initial configuration of the system at high temperature $T = 3$ . The system is completely disordered. <i>Right:</i> Final configuration at low temperature $T = 0.1$ obtained by a slow cooling. Note that that there is no positional order like for liquids. It corresponds to a nematic phase. A video showing the cooling of the system is available <a href="#">here</a> . . . . .	89
V.6	Evolution of energy $U$ and diffusion coefficient $D$ versus $T$ . The spin concentration $c$ is $c = N_s/N_L = 30\%$ , with $N_L = 15 \times 15 \times 30$ . The exchange interactions are $J_1 = -1.0$ , $J_2 = 2.0$ and the anisotropy is equal to $A_z = 0.5$ . . . . .	90
V.7	Evolution of the orientational order parameter and its susceptibility as functions of $T$ . The spin concentration $c$ is $c = N_s/N_L = 30\%$ , with $N_L = 15 \times 15 \times 30$ . The exchange interactions are $J_1 = -1.0$ , $J_2 = 2.0$ and the anisotropy is equal to $A_z = 0.5$ . . . . .	90
V.8	Histogram showing the percentage $R$ of sites having $\mathcal{Z}$ nearest neighbors at $T = 0.1$ , <i>i.e.</i> corresponding to the snapshot on the right in the Figure V.5. Spins have distributed such as they have no neighbors. . . . .	91
VI.1	Ground state (GS) of the nanodot. The lattice size is $15 \times 15 \times 12$ with a spin concentration equal to $c = 30\%$ and with a dipolar interaction $D = 0.7$ . The GS exhibits a vortex around the center of the dot. The spins lie in the $xy$ plane at the border except around the vicinity of the center where they have a non-zero $z$ component. . . . .	96
VI.2	Effect of the concentration. The lattice size of the system is: $15 \times 15 \times 12$ with an interaction exchange in-plane and between layers equal to $J_{\parallel} = 4$ and $J_{\perp} = 1$ , respectively. The <b>blue curve</b> corresponds to a spin concentration equal to $c = 50\%$ with a magnetic dipole-dipole interaction equal to $D = 0.3$ . The <b>green curve</b> corresponds to $c = 0.3\%$ and $D = 0.7$ . The <b>red curve</b> corresponds to $c = 25\%$ and $D = 1$ . . . . .	98

VI.3 Effect of the concentration. The lattice size of the system is:  $15 \times 15 \times 12$  with an interaction exchange in-plane and between layers equal to  $J_{\parallel} = 4$  and  $J_{\perp} = 1$ , respectively. The **blue curve** corresponds to a spin concentration equal to  $c = 50\%$  with a magnetic dipole-dipole interaction equal to  $D = 0.3$ . The **green curve** corresponds to  $c = 0.3\%$  and  $D = 0.7$ . The **red curve** corresponds to  $c = 25\%$  and  $D = 1$ . . . . . 99

VI.4 No mobile spin. The lattice size of the system is:  $15 \times 15 \times 12$  with an interaction exchange in-plane and between layers equal to  $J_{\parallel} = 4$  and  $J_{\perp} = 1$ , respectively. The **blue curve** corresponds to a spin concentration equal to  $c = 50\%$ , *i.e.* 6 layers, with a magnetic dipole-dipole interaction equal to  $D = 0.3$ . The **green curve** corresponds to  $c = 30\%$  (4 layers) and  $D = 0.7$ . The **red curve** corresponds to  $c = 25\%$  (3 layers) and  $D = 1$ . . . . . 99

VI.5 No mobile spin. The lattice size of the system is:  $15 \times 15 \times 12$  with an interaction exchange in-plane and between layers equal to  $J_{\parallel} = 4$  and  $J_{\perp} = 1$ , respectively. The **blue curve** corresponds to a spin concentration equal to  $c = 50\%$ , *i.e.* 6 layers, with a magnetic dipole-dipole interaction equal to  $D = 0.3$ . The **green curve** corresponds to  $c = 0.3\%$  (4 layers) and  $D = 0.7$ . The **red curve** corresponds to  $c = 25\%$  (3 layers) and  $D = 1$ . . . . . 100

VI.6 Effect of the number of layers that can melt. The lattice size of the system is:  $15 \times 15 \times 12$  with an interaction exchange in-plane and between layers equal to  $J_{\parallel} = 4$  and  $J_{\perp} = 1$ , respectively and  $D = 0.7$ . The concentration is fixed to  $c = 30\%$ , *i.e.* 4 filled layers. The **red curve** corresponds to a localized-spin system. The **green curve** corresponds to the two first layers (starting from the top) can melt; the **blue curve** to three mobile layers and the **cyan curve** to four mobile layers. . . . . 101

VI.7 Effect of the number of layers that can melt. The lattice size of the system is:  $15 \times 15 \times 12$  with an interaction exchange in-plane and between layers equal to  $J_{\parallel} = 4$  and  $J_{\perp} = 1$ , respectively and  $D = 0.7$ . The concentration is fixed to  $c = 30\%$ , *i.e.* 4 filled layers. The **red curve** corresponds to a freezed system. The **green curve** corresponds to the two first layers (starting from the top) can melt; the **blue curve** to three mobile layers and the **cyan curve** to four mobile layers. . . . . 101

VI.8 Occupation rate per layer  $c_{\ell}$  versus temperature. The lattice size of the system is:  $15 \times 15 \times 12$  with an interaction exchange in-plane and between layers equal to  $J_{\parallel} = 4$  and  $J_{\perp} = 1$ , respectively and  $D = 0.7$ . The concentration is fixed to  $c = 30\%$ , *i.e.* 4 filled layers. . . . . 102

A.1	Example of directed graph of a transition matrix $P$ , where the nodes are elements belonging to $\mathcal{S}$ and each directed arc is labelled by a probability transition. . . . .	111
A.2	Directed graphs of two Markov chains. <i>Left</i> : All the states communicate; the Markov chain is then irreducible. <i>Right</i> : The states $x_2$ and $x_3$ are not accessible from $x_0$ and $x_1$ . Moreover $x_3$ is inaccessible from $x_2$ . The chain is then not irreducible. . . . .	115
A.3	Ehrenfest model with three balls. Let $\mathcal{S} = \{0, 1, 2, 3\}$ be the state space of system. Each state of $\mathcal{S}$ correspond to zero, one, two or three balls contained in the red urn, respectively. <i>Top</i> : Representation of the Ehrenfest's urns for each state. <i>Down</i> : The oriented graph of the Markov chain associated to the model. The <b>red</b> arrows correspond to a move from the <b>blue</b> urn to the <b>red</b> one. The <b>blue</b> arrows are for the opposite moves. . . . .	116



# Acronyms

DM	Dzyaloshinskii-Moriya
EA	Edwards Anderson
FT	Fourier Transform
GF	Green's Functions
GS	Ground State
LC	Liquid Crystals
LCD	Liquid Crystal Display
LCG	Linear Congruential Generator
MC	Monte Carlo
MCMC	Markov Chain Monte Carlo

MCS Monte Carlo Sweep

MT Mersenne Twister

NN Nearest Neighbours

NNN Next Nearest Neighbours

PBC Periodic Boundary Condition

PRNG Pseudo Random Numbers Generator

SRG Shift Register Generator

SW Spin-Wave

TEM Transmission Electronic Microscopy

TN Twisted Nematic





# Chapter I

## Introduction

### Contents

---

General context . . . . .	2
Liquid crystals: a mesophase . . . . .	2
Technical applications . . . . .	7
State of the art and purpose . . . . .	9

---

We give first the historical context in which liquid crystals have been discovered before to define and introduce them. This chapter is also dedicated to their extraordinary physical properties and their numerous applications. In the light of these generalities about liquid crystals, we will set the context and the purpose of this thesis.

## General context



he present work takes place in the soft matter physics, which is actually part of a larger domain : the condensed matter. The latter deals with systems having very high density of particles and with numerous and strong interactions. It concerns the physical properties of the matter present on earth and that can be studied in a laboratory (like for instance glasses, magnets, liquids, etc.), while other systems like neutron stars (one of the most dense *objects* of the universe) fall within the astrophysics field. Soft matter is more specifically about materials that can be deformed under the action of a stress due to, e.g., an electric or magnetic field or thermal fluctuations. It includes liquids, polymers, colloids and naturally the *liquid crystals* (LC).

While in the nineteenth century only three states of matter were known (solid, liquid and gas), the chemist and botanist Freidrich Reinitzer discovered in 1888, by working on the melting of the *cholesteryl benzoate*, a new state of matter termed *liquid crystals* by Otto Lehmann one year later [110], enabling thus to complete this classification. Reinitzer noticed this substance has two melting points, one at 418 K giving an opaque liquid that becomes transparent at 451 K and related his observations in a letter addressed to Lehmann [98] :

"If you let cool it [the cholesteryl benzoate substance] down, at first a violet and blue appearance of color is appearing, whereon the mass stays milky cloudy and liquid. With further cooling down once again the violet and blue color appearance is appearing and right afterwards the substance is congealing to a white crystalline mass [...] In the former case, the clouding is not caused because of crystals but because of certain liquidity, which forms in the melted mass oily stripes..."

Lehmann confirmed this discovery of this intermediate phase (between crystal and liquid) and found an optical anisotropy properties of the clouding phase. Despite of this, the enthusiasm for liquid crystals faded away for fifty years until a renewed interest in the seventies. During the second part of the twentieth century, they have been intensively studied allowing thus to find various technical applications, particularly for the digital display and the determination of surface temperatures as we will see after.

## Liquid crystals: a mesophase

It is quite disconcerting to think that a material has a structure halfway between crystal and liquid. Crystals are materials where atoms, or more generally its constituents, are periodically arranged on a lattice. There is a long-range order correlation and position of atoms in a crystal can be *guessed* thanks to *primitive pattern* [49] that is persistently repeated by translational symmetry. While the components of a liquid do not *respect* a specific medium- or long-range order and are weakly bound to each other (see Figure I.1), making impossible

to determine the position of a particle from another one. This is the consequence of the existence of an isotropic length scale  $\xi$ , termed "correlation length", over which correlations disappear. Thus a crystalline solid is characterised both by its form and volume whereas a liquid has a definite volume but no definite shape. Liquid crystals are systems having no order at least in one dimension like liquids and having in the same time a position or/and an directional order in another direction like in crystals. It is therefore more appropriate to define liquid crystals as a *mesomorphic*<sup>(1)</sup> phase [41] or simply a *mesophase*.

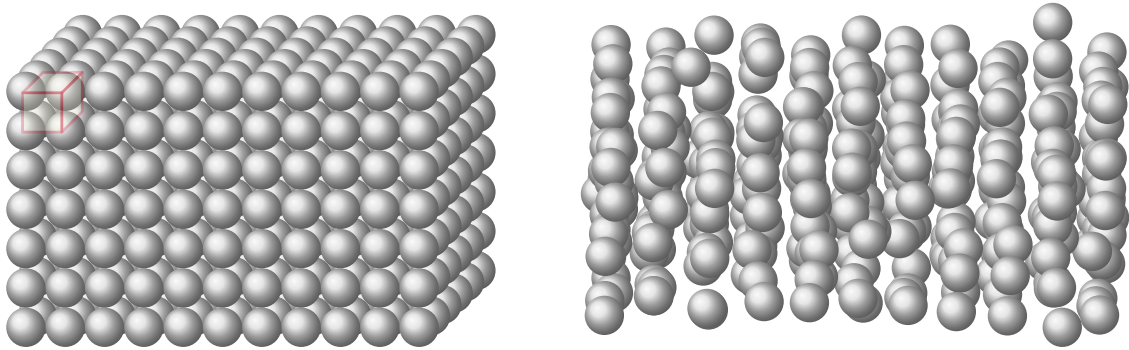


**Figure 1.1** – Schematic representation of the microscopic arrangement of the matter in two phases. *Left*: Crystalline phase. Atoms or groups of atoms are periodically arranged. There is a long-range order. The red cube represents a *primitive cell* (cf. crystallography's concepts [49]) allowing to determine the position of atoms in the crystal from the position of one atom. *Right*: Liquid phase. There is no order and constituents are weakly bound to each other, allowing thus to the liquid to change form.

Liquid crystals are often made of elongated organic molecules, called *calamitic*<sup>(2)</sup> or reed-shaped molecules, or of *discotic*, *i.e.* disk-like, molecules. Thus LC are generated by strong structural anisotropy objects [30]. The way how these constituents are arranged to form LC depends usually on the temperature. We speak then of *thermotropic* liquid crystals. For some mesomorphic phases, it can also be function of the concentration of the molecules in a solvent; these are *lyotropic* liquid crystals.

The physicist Georges Friedel is the first to have proposed in 1922 a classification of the mesophases [65] based on microscopic observations allowing thus to characterise the degrees of symmetry and the physical properties of LC according to their molecular arrangement. According to this classification<sup>(3)</sup>, the mesophase counts four kinds of structure, namely :

---

<sup>(1)</sup> From the ancient Greek *mésos* (μέσος) meaning middle or intermediate and *morphé* (μορφή), shape.

<sup>(2)</sup> From the Latin word *calamus*, reed.

<sup>(3)</sup> For G. Friedel, there were initially two mesophases, that he termed himself *nematic* and *smectic*. Moreover, the *cholesteric* mesophase, presented here, belongs for him (and also for J. Prost, P.G de Gennes [41] and S. Chandrasekhar [30]) to the nematic mesophase. But in the literature, it is frequent that authors consider the cholesteric mesophase as a full one as we do here.

- **Nematic** : This mesophase is characterised by the fact that molecules<sup>(4)</sup> have no long-range position order but they have a long-range directional order as showed by Figure I.2. In other words, molecules are randomly arranged and have globally the same orientation represented by a vector  $\mathbf{n}$ , called the *director*, indicating the *preferred* (in average) orientation. This is the nearest mesophase of an isotropic liquid and is termed *nematic* (from the Greek *néma* ( $\nu\eta\mu\alpha$ ), thread) because of the thread-like topological defects, called *disclinations* lines, which are regions where the direction of the director changes abruptly of direction (see Figure I.3).

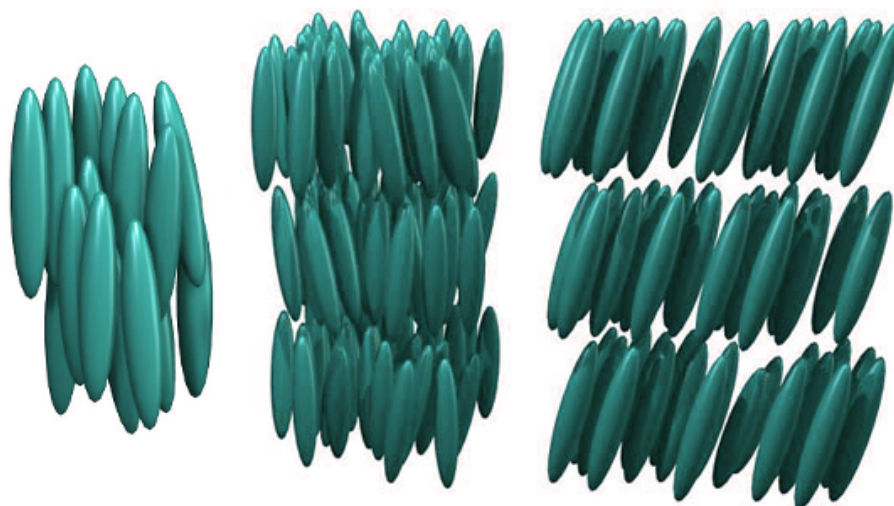


**Figure I.2** – Schematic representations of the different rod-like molecules arrangement that can be found in liquid crystals. *Left*: Nematic mesophase. Molecules have no position order but aligned according to a common direction, having thus a long-range directional order. *Middle and right*: The last schemas represent two smectic mesophases : smectic A (left) and smectic C (right). Molecules are organised in layers, giving thus a long-range positional order in one direction. There is no ordered arrangement within layers and molecules are still characterised by a directional order. For the smectic A structure, molecules are aligned along the normal to the layers, while for smectic C, they are tilted.

- **Smectic** : Mesophase in which molecules have also a common orientation but are organised in equidistant layers (positional order following one direction). However there is no specific positional order within the plane of each layer, that can be considered as a two-dimensional liquid. The name of *smectic*, deriving from the Greek word *smegma* ( $\sigma\mu\tilde{\eta}\gamma\mu\alpha$ ) for soap, is due to the fact layers can slide over one another, similar to the mechanical properties of soaps. This mesophase is then more ordered than the nematic one and is the closest to a crystalline solid. The domain's temperature in which this mesophase appears is usually below that of the nematic phase.

Note that the smectic mesophase can be subdivided into different *classes*<sup>(5)</sup> (distinguishing

<sup>(4)</sup>Whether they have a rod-like or a disk-like shape.

<sup>(5)</sup>This sub-classification was not established by G. Friedel.

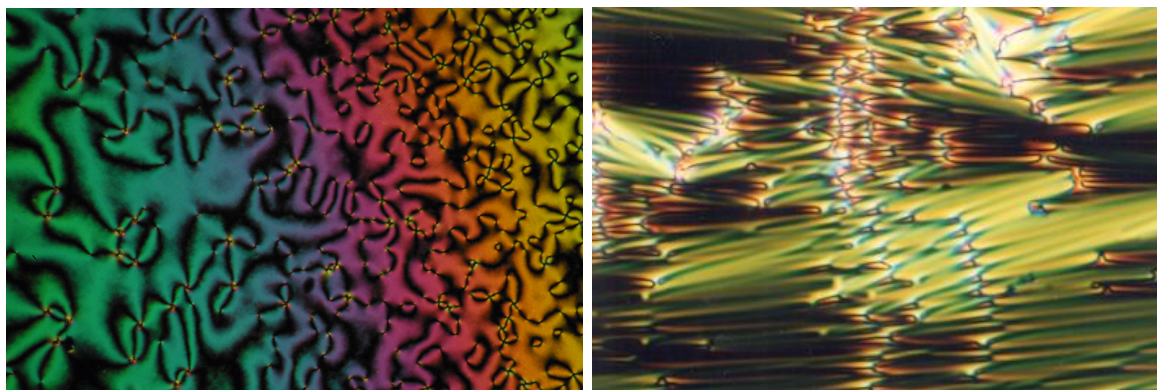


**Figure I.3** – Pictures of liquid crystals (LC) viewed under a polarising microscope (composed of two cross linear polarisers). The sample, illuminated by a linear polarised light, is observed through a linear polariser. The color of the LC is due to their birefringent properties. *Left:* Nematic mesophase. The black lines, called *disclinations* lines, are the regions where the global orientation of the molecules change abruptly, due to topological defects occurring, for instance, under electric or magnetic field or simply because of the mechanical constraints applied by the recipient on the sample. It corresponds to extinction zones of light passing through cross polariser. *Right:* Smectic A mesophase. Molecules have the same global orientation and structured in layers.

guished by a letter), like for instance smectic A and C [41, 30] (being the most known). In the smectic A phase, molecules are oriented along the normal to the surface (cf. Figure I.3), while for a smectic C its direction makes a non-zero angle to the normal (cf. Figure I.2).

- **Cholesteric** : This mesophase has been observed for the first time in cholesterol esters which are chiral<sup>(6)</sup> molecules. For this reason, this mesophase is historically called *cholesteric* although it also appears in other chiral chemical species that do not derive from cholesterol. We also speak then of *chiral nematic*. It presents similitude locally with the nematic mesophase in the sense that molecules have non long-range position order and still have a preferred orientation labelled by the director  $\mathbf{n}$  discussed above, within a plane. However, contrary to the *pure* nematic mesophase, molecules are stacked in very thin layers<sup>(7)</sup> and the direction of  $\mathbf{n}$  is not constant in space, changing from a plane to another, making appear thus a periodic helical structure, as we can see on the Figure I.4. The spatial period is equal to one-half of the pitch  $p$ , which is the distance over which the director has completed a  $2\pi$ -rotation along the helix axis. Thanks to the chirality of the molecules, this mesophase has interesting optical properties. In effect, it is optically active, *i.e.* it is able to make rotate the polarisation plane of linearly polarised light. For optically inactive molecules<sup>(8)</sup>, the pitch is infinite corresponding then to the nematic phase.

<sup>(6)</sup> An object is said chiral if it cannot be superposed to its mirror image.

<sup>(7)</sup> That can be viewed as two-dimensional nematic-like layers and must not be confused with the planar arrangement found in smectic mesophases.

<sup>(8)</sup> A material is optically inactive if it is made of achiral molecules or composed of a *racemic mixture*, *i.e.*

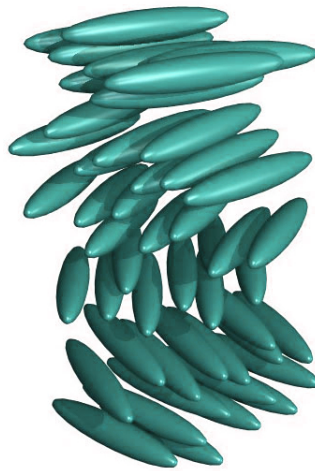


**Figure I.4** – Schematic representations of the cholesteric also termed chiral nematic mesophase. Molecules have no long-range position order but are stacked in very thin layers and have a preferred orientation which varies from a layer to another with a certain periodicity.

Let us make the remark<sup>(9)</sup> that molecules of the smectic C\* mesophase present also a periodic twisted arrangement due to their chirality. They have the same kind of order as in smectic C liquid crystals except that their orientation is different in each layer. The director  $\mathbf{n}$  has a non-zero  $z$ -component (unlike in the chiral nematic mesophase) and precesses then around the helical axis.

- **Columnar** : This mesophase appears often with discotic molecules (but this is not necessary as a prerequisite [41]) and is such that molecules are *packed* to form columns showing thus a directional order (see Figure I.5). Molecules have a two-dimensional

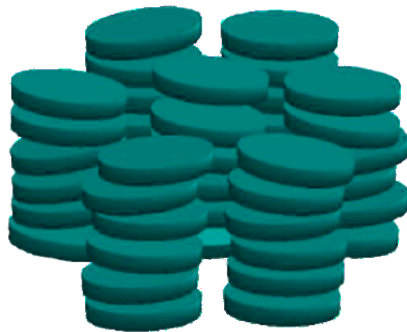


**Figure I.5** – Columnar mesophase made of disk-like molecules that are stacked making a columnar structure. Molecules have a two-dimensional positional order within the plane and no order along the third dimension. This mesophase is also termed *columnar liquid*.

position order and a liquid-like order, because of short correlation length  $\xi$  along

---

there is exactly the same amount of left- and right-handed enantiomers of a chiral molecule.

<sup>(9)</sup>The smectic C\* mesophase belongs, as its name suggests, to the family of the smectic liquid crystals. But because of the property and the structure of such LC, it is preferable here, for our study, to include this specific mesophase into the *cholesteric* one, in order to cover all LC with periodic molecular arrangement under a single designation.

the columnar axis (the third dimension). We speak then of *columnar liquid*. Like for the smectics, the columnar liquid crystals present also different *sub-phases* (hexagonal, rectangular or oblique phases), but we will not enter in details on them.

## Technical applications

Because of their amazing optical properties, liquid crystals have been intensively studied and used for technical applications for decades, like, *i.e.*, for the liquid crystals display (LCD) or for the measure of surface temperature. In order to highlight the physical properties of LC, we briefly discuss here how these applications work.

One of the most notable features of certain liquid crystals (often nematic), observed the first time by Lehmann, is the birefringence, *i.e.* the propriety of a material in which the refractive index depends on the polarisation and the direction of propagation of the light and making then the light spread anisotropically. LC can thus be used to polarise light or to manipulate the polarised light beams. Thanks to that, a natural application of LC is then the display monitors.

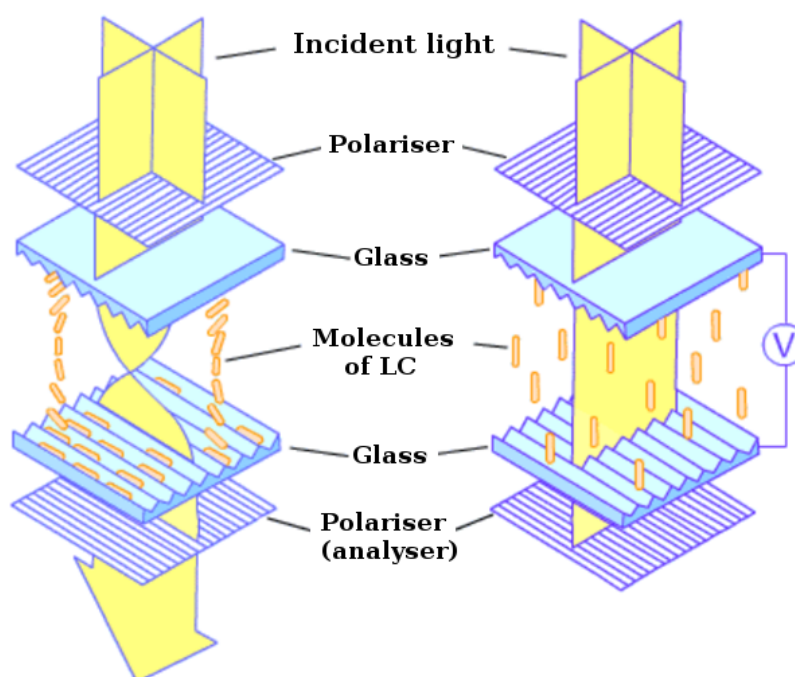


**Figure I.6** – Schematic representation of a liquid crystal display (LCD). The incident light is polarised linearly by the first polariser. The electric field of the polarised light is orthogonal to the polarisation axis of the analyser such as there is extinction in output. Thus, The polarisation surface of the light must be rotated, thanks to the orientation of the molecules, in order to pass through the analyser. *Left*: The molecules have an helix configuration. This is a chiral nematic mesophase. The light is transmitted. Its polarisation follows the helix structure. *Right*: By applying a voltage, the molecules change their orientation. If molecules are parallel or orthogonal (like on the figure) the polarisation of the light is not changed and there is extinction.

The principle underlying the operation of liquid crystal display is quite simple. It relies on the control of the molecules orientation in order to let polarised light propagate or not. A LCD, is made up with two crossed polarisers, liquid crystals and electrodes. The light crosses the first polariser is linear polarised such as the direction of the electric field is orthogonal to the axis of polarisation of the second one, termed *analyser*, *i.e.* there is extinction in output. The electrodes are used here to apply a voltage on the LC, in order to change the orientation of their molecules<sup>(10)</sup> and then to rotate the *polarisation surface* of the electromagnetic wave. If the molecules are orthogonal or parallel to electric field there is extinction. But if they are arranged such as they form a helix, the polarisation of the light is modified progressively, like shown by the Figure I.6 on the previous page. LCD requires then chiral nematic liquid crystals. One of the technologies the most used in LCD is moreover called TN for *twisted nematic*. Note that by controlling the pitch of the helix, it is possible to control the contrast in output.

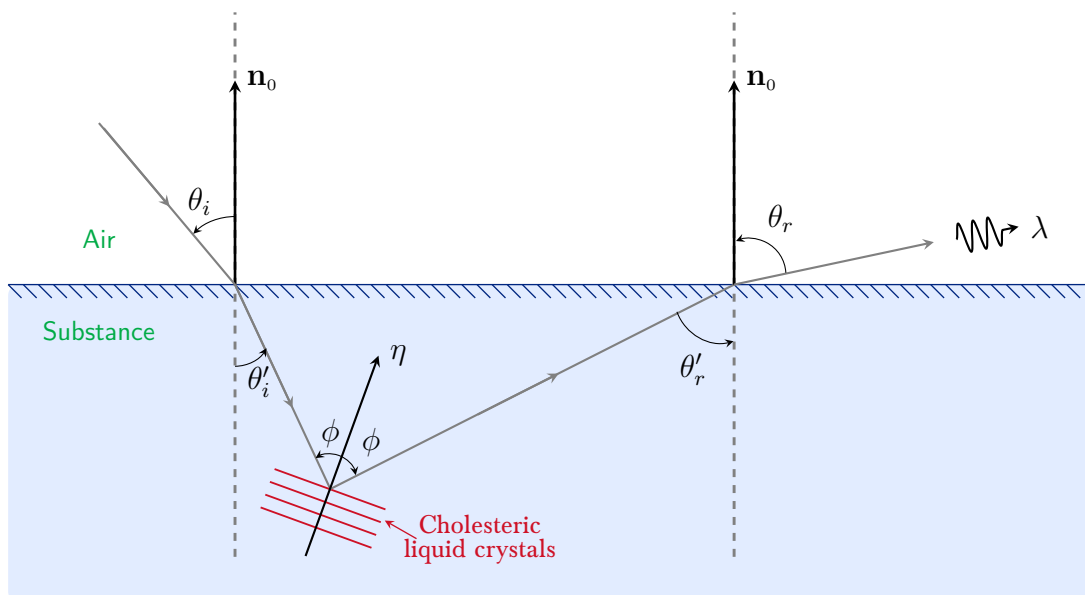


**Figure I.7** - Schema showing the physical principle to determine the temperature of a surface using *cholesteric* liquid crystals (LC). The system is based on simple optical laws. A beam of white light is sent on an interface containing liquid crystals with an angle of incidence  $\theta_i$  to the normal  $\mathbf{n}_0$ . It is then refracted and dispersed in several beams that are reflected on the **cholesteric layers** undergoing a diffraction similar to the Bragg's diffraction [23] giving birth to a wave packet crossing again the surface with a certain wave length  $\lambda$  and consequently with a certain color.  $\lambda$  depends on  $\theta_i$ , on  $\theta_r$  and on the orientation of the molecules in the **layers** which is a function of the temperature. With these three quantities, it is then possible to know the temperature of the surface on which is placed the device.

Another useful application of the liquid crystal is the determination of surface temperature. The physical principle is quite simple. It is based on selective wave lengths of reflected white light beams thanks to nematic chiral liquid crystals. The orientation of the LC, contained

<sup>(10)</sup>Due to the fact chiral mesophases present ferroelectric properties.

in the device landed on a surface, depends on the temperature. More exactly, it is the pitch  $p$  of the helical structure which varies, making thus the wave length  $\lambda$  of the reflected light depend on the temperature [60]. Thus, knowing  $\lambda$  and thanks to a simple theoretical model [42] we are able to determine the temperature. More details are given in Figure I.7.

We have seen here the most important and most famous applications of liquid crystals in the industry. Our work takes place far from the applied physics and is dedicated to a theoretical study in order to understand better the phase transition taking place in the LC thanks to models of statistical physics and magnetism as shown in the next section.

## State of the art and purpose

Pierre-Gilles de Gennes considered liquid crystals beautiful and mysterious, perhaps because of their astonishing physical and more especially optical properties and probably also because of their complexity. Indeed, different aspects of LC can be investigated, mixing thus different research fields, as briefly exposed hereafter.

Naturally, one of the first research domain that comes to mind about liquid crystals is chemistry [43, 41]. Indeed, the explanation of the different mesophases involves the chemical properties of the complex molecules constituting the LC.

Liquid crystals can also be investigated under a mechanical point of view in a large sense, fluid mechanics and elasticity to be more specific. Indeed, their hydro-statics and hydro-dynamics properties have been extensively studied [41, 29, 39, 116], in the same manner it has been done for the superfluid Helium [155] (numerous analogies can be found between certain mesophase and superfluids or superconductors [92, 40]). The study of the elasticity has given rise to numerous publications and considerable debates for several decades, as for the distortion free energy density<sup>(II)</sup> [64, 149] of the nematic mesophase, given by

$$\mathcal{F}_d = \frac{1}{2} \left\{ K_1 (\nabla \cdot \mathbf{n})^2 + K_2 [\mathbf{n} \cdot (\nabla \times \mathbf{n})]^2 + K_3 [\mathbf{n} \times (\nabla \times \mathbf{n})]^2 \right\}, \quad (\text{I.1})$$

where  $\mathbf{n}$  is the normalised director and the  $K_i$  ( $i = 1, 2, 3$ ) are positive elastic constants associated to a type of deformations. The first term with  $K_1$  corresponds to a *splay*-constraint, the second with  $K_2$  to a twist and the last one to a *bend*-distortion. The fundamental equation (I.1) of the elastic theory for nematics, as said above, is just an example of the kind of mathematical developments which have been generalised [29, 41].

Another very interesting approach is the statistical physics [30] that appears as a natural choice in the study of LC. Indeed, the different mesophases exhibit phase transitions, like for instance the transition from a nematic phase to an isotropic phase characterised by

---

<sup>(II)</sup> Commonly termed the Frank free energy and has the dimension of an energy per unit of volume.

the discontinuity of the following order parameter for rode-like molecules<sup>(12)</sup> [198]

$$S = \frac{1}{2} \langle 3 \cos^2 \theta - 1 \rangle, \quad (\text{I.2})$$

where  $\theta$  is the angle between the normal to the layer and the director  $\mathbf{n}$  and  $\langle \cdot \rangle$  denotes a statistical average over all the molecules. This order parameter, that has been confirmed experimentally [36], totally looks like the type of order parameter used to describe phase transitions of spin models. Moreover de Gennes, who initially comes from the condensed matter's community, has made analogies between phase transitions occurring in superconductors and liquid crystals [38] and generalized the Ginzburg-Landau phase transition theory [50] by making the free energy, known as the Landau-de Gennes free energy, be a *functional* of a second-order tensor [164, 27, 121, 30]. However, despite of the huge contribution of de Gennes, there is no model with a Hamiltonian to describe microscopic interactions between molecules in liquid crystals as it exists for in magnetism with spin models.

It is in this context, *i.e.* the one of the statistical physics, condensed matter and the physics of spin systems, that our study of LC leads us also to the study of topological structures. Indeed, as mentioned at the beginning of the chapter, some mesophases like the nematics for instance present disclinations (see Figure I.3), that are regions of topological defects as mentioned above. These regions look like *threads* or *filaments*. In certain nematic and chiral LC, other specific topological structures, termed *skyrmions* [22, 111] can also be observed.

Skyrmions were first predicted and described as *quasi*-particles by T. H. R. Skyrme [170, 171] in the particle physics field in the 60's and their study has been then intensively extended to the condensed matter field [1, 139] giving birth to *magnetic skyrmions*. They are promising *physical objects* for the magnetic data storage and more generally in the spintronic's domain. We can give a global definition of skyrmions as being regions where the orientation of spins follows a non-trivial topological structures. But they can be seen as structures giving raise to circular arrangements of spins (or molecules in the case of LC), *i.e.* vortices.

Because the results presented in this thesis are based mostly on Monte Carlo (MC) simulations, the next chapter is dedicated to the MC methods in general and its adaptation for the simulation of systems of mobile spins.

The third chapter can be considered as a toy model. It is about a system of mobile spins for which the concentration is fixed and the interaction between spins is ruled by the Potts model. Spins can freely move on vacant sites. The ground state corresponds to the case where all spins are stacked at the bottom of the tank. At high temperature  $T$ , this solid

---

<sup>(12)</sup>Generalised by Alfred Saupe for molecules with arbitrary shapes [166], the order parameter being thus a 2-order tensor.

phases becomes liquid (isotropic phase). We will show by MC simulations that when  $T$  arises, the surface layers melt and the bulk undergoes a first-order phase transition. This has been confirmed by a mean-field analysis. We study in details the effect the influence of the size and the shape of the system.

The fourth chapter deals with *skyrmions* and *stripes structure* that are topological structures that can appear in liquid crystals. They are modeled here with Dzyaloshinskii-Moriya interaction in addition to Heisenberg exchange interaction. In a first time, we calculate the spin-wave excitations (termed *magnons* that are collective excitations of spins) in thin films. Thanks to the Green's function, we are able to determine the spin-wave spectrum used to calculate physical properties of the thin film at  $T = 0$  (quantum fluctuations) and at finite temperatures. Then, we apply a magnetic field orthogonal to the film making appear a crystal of skyrmions. MC simulations show that skyrmions arranged on a super-structure of a triangular geometry. These simulations show also stripes structure or labyrinth-like structures similar to the filament-shaped structure that can be found in some LC. The stability of the skyrmions at high temperatures is shown and the relaxation is found to follow a stretched exponential law.

The next chapter (the fifth) is devoted to the study of the dynamics leading to the formation of a nematic and smectic LC. We use here a mobile Potts model and cool the system from a liquid phase. The choice of the interactions is really important to get to model this both mesophases. Various physical quantities have been calculated, confirming thus the transition from the isotropic phase to a LC structure.

The chapter VI is about dipolar interaction in nanodots with Heisenberg spin model. The first part of the chapter is devoted to the determination of the ground state. We show that it is a vortex around the center of the dot. The spins lie in the  $xy$  plane at the border of the dot but have a non-zero  $z$  component around the center of the dot. We next study the effect of the temperature and the melting of the dot and we show that the melting temperature does not depend on the thickness of the system, which is totally different with the case of localised spins. This chapter can be seen as preparative work to model cholesteric mesophase.

The last chapter is a general conclusion about the results and this thesis in general.



# Chapter II

## Monte Carlo method for mobile spin systems

### Contents

---

II.1	Monte Carlo methods . . . . .	14
II.1.1	Theoretical framework: the statistical physics . . . . .	15
II.1.2	Sampling techniques . . . . .	16
II.1.3	Metropolis algorithm . . . . .	19
II.2	Adaptation to the mobile spin . . . . .	29
II.2.1	Non micro-reversible moves . . . . .	29
II.2.2	Mobile spin algorithm . . . . .	29
II.3	Sources of errors in Monte Carlo . . . . .	31
II.3.1	Systematic and statistical errors . . . . .	31
II.3.2	Random numbers generator . . . . .	34

---

In this chapter, we introduce the numerical methods used for the computer simulations presented in the next chapters. Indeed we have adapted the classical Monte Carlo Metropolis algorithm to investigate in details the phase transitions that occur in our mobile spin systems.

## II.1 Monte Carlo methods



For twenty years, numerical simulations play a very important part in physics (and also in other fields like biology, economics, financial markets...). It allows to investigate systems with high degrees of freedom that theoretical physicist could not study analytically (or with extreme difficulties), like for example the three-dimensional Ising model. It also allows to test the validity of certain model by confronting numerical results to experimental data [35, 19]. Indeed, among a significant number of parameters (e.g. the temperature, the volume, the number of particles...), only a few governs a real system. That is why computational physics turns out to be sometimes the best and maybe the only way to identify the relevant parameters. Thus simulations can be considered as *numerical experiments* preceding *traditional* experiments in order to better target the experimental research [158].

The large family of Monte Carlo (MC) methods falls perfectly within this context of described just above. These stochastic methods are first of all used to solve multiple integrals<sup>(1)</sup> by generating random numbers. For example, a basic way (rudely expressed here) to evaluate a simple integral is to draw randomly points and to look if they are *under the curve* or not. It is like playing with a slot machine in casino; we understand then the name of those methods. In statistical physics, the high-dimensional integrals we are interested in, is the *partition function* as we will see in the next subsection. It is the highest difficulty that can be encountered in this field.

One can also mention the molecular dynamics (MD) method. But because the systems presented in this thesis are all based on equilibrium statistical physics and because we are less interested in the dynamic of a system than in the study of phase transition, this method is less adapted for our purpose.

For all these reasons, our study of the transitions of phase in liquid crystals requires a numerical approach based on MC. We present in the following parts, how to generate *samples* (of possible configurations) during a Monte Carlo simulation and the Metropolis algorithm. Then we will introduce our adaptation of the Metropolis algorithm for the study of mobile spin system. And to finish, we will discuss about the statistical error in MC and also about the link between the reliability of such simulations and the generation of random numbers.

---

<sup>(1)</sup>The strength of Monte Carlo methods for integral's calculations lies in the fact they work whatever the space dimension considered.

### II.1.1 Theoretical framework: the statistical physics

Before to go into the details of Monte Carlo methods, we need to set the physical and mathematical context in which we have performed the simulations. As mentioned just above, this context is the statical physics and the calculation of its partition function.

The essence of the statistical physics is to be able to explain the macroscopic behaviour and the evolution of a large system of particles only by knowing the features of the constituents (namely the classical spin in this thesis). It relies on the notion of *microstates* abusively called hereafter *configurations*  $\mathcal{C}$ , and on the fact these configurations do not have the same importance. This importance is evaluated by a probability  $P$  for a system to be in a configuration  $\mathcal{C}$ . In the *canonical description* [50], for a physical system ruled by an Hamiltonian  $\mathcal{H}$  at a given equilibrium temperature  $T$ , this probability is given by

$$P[\mathcal{C}] = \frac{1}{Z} e^{-\beta \mathcal{H}[\mathcal{C}]}, \quad (\text{II.1})$$

where  $\mathcal{H}[\mathcal{C}]$  denotes the energy of a configuration  $\mathcal{C}$ ,  $Z$  the partition function and  $\beta = 1/k_B T$ . Note that the choice of the canonical description is not fortuitous. Indeed, the systems studied in the next chapters correspond to systems in thermal equilibrium with a heat bath at fixed  $T$  with no particles exchange with the environment.

The unique challenge in this statistical description lies in the capacity to determine  $Z$  from which all the thermodynamic quantities derived. If we know the partition function, we can get a large amount of informations about the system and calculate the statistical averages of observables  $\mathcal{O}$  such as

$$\left\{ \begin{array}{l} \langle \mathcal{O} \rangle = \sum_{\mathcal{C}} \mathcal{O}[\mathcal{C}] P[\mathcal{C}] = \frac{1}{Z} \sum_{\mathcal{C}} \mathcal{O}[\mathcal{C}] e^{-\beta \mathcal{H}[\mathcal{C}]}, \\ Z = \sum_{\mathcal{C}} e^{-\beta \mathcal{H}[\mathcal{C}]}. \end{array} \right. \quad (\text{II.2})$$

The sums are performed over all the accessible states that may be infinite. It is then convenient and habitual in statistical physics to *transform* the discrete sum over  $\mathcal{C}$  into an integral when the thermodynamic limit is reached. It allows us also, in the same time, to relate later this part to the historical purpose of the Monte Carlo methods (cf. the next section) namely the calculation of multiple integrals. Thus equation (II.2) becomes

$$\langle \mathcal{O} \rangle = \int_{\mathcal{D}} \mathcal{O}(\mathbf{x}) \frac{e^{-\beta \mathcal{H}(\mathbf{x})}}{Z} d\mathbf{x}, \quad (\text{II.3})$$

where the states of the system are characterised by a  $n$ -tuple  $\mathbf{x}^{(2)}$  defined on a domain  $\mathcal{D}$ . From this equation, it comes then that the probability to find the system in a state  $\mathbf{x}$

---

<sup>(2)</sup>For example,  $\mathbf{x}$  can represent the positions of the  $n$  particles of a system:  $\mathbf{x} = (\mathbf{r}_1, \mathbf{r}_2, \dots, \mathbf{r}_n)$  with  $\mathbf{r}_i \in \mathbb{R}^3$ . Therefore,  $\mathbf{x}$  is a  $3n$ -tuple.

included in the *hypervolume* (noted abusively here)  $[\mathbf{x}, \mathbf{x} + d\mathbf{x}]$  is

$$dP = \frac{e^{-\beta \mathcal{H}(\mathbf{x})}}{Z} d\mathbf{x}, \quad (\text{II.4})$$

with the partition function  $Z$  defined by a multiple integral such as

$$Z = \int_{\mathcal{D}} e^{-\beta \mathcal{H}(\mathbf{x})} d\mathbf{x}. \quad (\text{II.5})$$

In most cases, these equations cannot be exactly solved express for only several simple models. We can cite for examples the well known two-dimensional Ising model [148], the 8-vertex model [9] or the 16-vertex free-fermion model [9, 66]. Different methods have been developed to get around the problem of the calculation of the partition function like the series expansion, the field theory [29] and obviously the computer simulations. We will dwell exclusively on the Monte Carlo methods.

## II.1.2 Sampling techniques

In the light of the previous section, we are looking for a Monte Carlo method allowing to browse intelligently the configurations of a system. Indeed, we want that this method respects the statistical distribution of the configurations, namely here the Boltzmann's distribution. It means that the method must *visit* with a higher *priority* the most probable configurations  $\mathcal{C}$ .

We present in this section two different methods. With the first one, which is *naive*, the configurations are chosen with the same probability. While the second one is more *smarter* and is such that the choice of the configurations follows the statistical distribution desired.

### a) Simple sampling

One of the methods to estimate the average value of the observable  $\mathcal{O}$  (eq. (II.2)) consists in generating a set  $\mathcal{E}$  of  $\mathcal{N}$  accessible configurations  $\mathcal{C}_i$  among all those possible, such as

$$\mathcal{E} = \{\mathcal{C}_i\}_{i \in \llbracket 1, \mathcal{N} \rrbracket}. \quad (\text{II.6})$$

$\langle \mathcal{O} \rangle$  can be estimated with

$$\langle \mathcal{O} \rangle_{\mathcal{E}} = \frac{1}{Z_{\mathcal{E}}} \sum_{\mathcal{C} \in \mathcal{E}} \mathcal{O}[\mathcal{C}] e^{-\beta \mathcal{H}[\mathcal{C}]}, \quad (\text{II.7})$$

where  $\langle \mathcal{O} \rangle_{\mathcal{E}}$  denotes the thermal average value of the observable over the selected configurations (*i.e.*  $\forall \mathcal{C} \in \mathcal{E}$ ) and  $Z_{\mathcal{E}}$  the corresponding partition function defined as

$$Z_{\mathcal{E}} = \sum_{\mathcal{C} \in \mathcal{E}} e^{-\beta \mathcal{H}[\mathcal{C}]}. \quad (\text{II.8})$$

Obviously, the estimate's quality of  $\langle \mathcal{O} \rangle$  depends on  $\mathcal{N}$ : when  $\mathcal{N} \rightarrow +\infty$  the result becomes more accurate<sup>(3)</sup>. But the simple sampling method suffers from a serious problem.

There are two manners to choose the configurations  $\mathcal{C}_i$  in simple sampling method. The first one is to draw randomly (with an uniform probability) the configurations. The other choice is to discretise uniformly and to browse the very high-dimensional phase space. In any case all the configurations must be weighted by a Boltzmann factor (as we can see with the equation (II.7)). But none of these methods is satisfactory, because the generated configurations  $\mathcal{C}_i$  have all the same statistical weight and do not then correspond most of the time to the equilibrium states for a given temperature [108]. In other terms, they do not contribute significantly in the expression of the partition function, distorting thus the calculation of the mean value of the observable:  $\langle \mathcal{O} \rangle_\varepsilon$  is then a rough approximation of  $\langle \mathcal{O} \rangle$ .

A more sophisticated scheme, allowing to get a better accuracy on the calculation of  $\langle \mathcal{O} \rangle$  by browsing the configurations in the respect of the Boltzmann's distribution, is presented next.

### b) Importance sampling

The importance sampling is a technical used to reduce the variance of the estimates in Monte Carlo methods. Unlike the simple sampling, the idea of this method is to replace, during the simulations, a uniform density probability by a *biased* one  $\wp$  [103]. In other words, one chooses the most relevant microscopic states, *i.e.* those which are dominant in the partition function, allowing thus to decrease the time of the simulations and to have reliable results in the same time.

For a better understanding, let us consider, as an example, the integral  $\mathcal{I}$  on a domain  $\mathcal{D}$  of the function  $\psi : \mathbb{R} \mapsto \mathbb{R}$ <sup>(4)</sup> such as

$$\mathcal{I} = \int_{\mathcal{D}} \psi(x) dx. \quad (\text{II.9})$$

Let  $\wp$  be a probability density function such as  $\wp(x) > 0$  for all  $x \in \mathcal{D}$  and  $\int_{\mathcal{D}} \wp(x) dx = 1$ . We can rewrite (II.9) thus

$$\mathcal{I} = \int_{\mathcal{D}} \frac{\psi(x)}{\wp(x)} \wp(x) dx, \quad (\text{II.10})$$

---

<sup>(3)</sup>For really small system, we could imagine to generate all the microstates and to calculate their probabilities. We would get then an exact calculation of the average of the observable such as  $\langle \mathcal{O} \rangle = \langle \mathcal{O} \rangle_\varepsilon$ . But the kind of systems we are interested in do not allow us to do that. For instance, even for a small 2D-Ising system of  $10 \times 10 = 100$  spins there are  $2^{100} \approx 10^{30}$  possible configurations. It is clearly impossible to generate them all.

<sup>(4)</sup>It can be generalised for a  $n$ -dimensional space, but here for more convenience  $n = 1$ .

which is totally equivalent to

$$\mathcal{I} = \mathbb{E} \left[ \frac{\psi(X)}{\wp(X)} \right] = \mathbb{E}[Y], \quad (\text{II.11})$$

$X$  denoting a continuous random variable distributed following  $\wp$ . It represents the expected value (stochastic average) of the random variable  $Y = \psi(X)/\wp(X)$ . If we perform  $\mathcal{N}$  draws of  $X_i$  following the probability law  $\wp(x) dx$  and approximating (II.11) with an arithmetic series, we define a new random variable

$$S = \frac{1}{\mathcal{N}} \sum_{i=1}^{\mathcal{N}} \frac{\psi(X_i)}{\wp(X_i)} = \frac{1}{\mathcal{N}} \sum_{i=1}^{\mathcal{N}} Y_i, \quad (\text{II.12})$$

or in terms of realisations  $x_i$ , the *experimental mean*

$$\tilde{\mathcal{I}} = \frac{1}{\mathcal{N}} \sum_{i=1}^{\mathcal{N}} \frac{\psi(x_i)}{\wp(x_i)} = \frac{1}{\mathcal{N}} \sum_{i=1}^{\mathcal{N}} y_i, \quad (\text{II.13})$$

with  $y_i = \psi(x_i)/\wp(x_i)$ . According to the strong law of large numbers,  $\tilde{\mathcal{I}}$  converges *almost surely* on  $\mathcal{I}$  when  $\mathcal{N}$  goes to infinity [5], *i.e.*

$$\tilde{\mathcal{I}} \xrightarrow[\mathcal{N} \rightarrow +\infty]{\text{a.s.}} \mathcal{I}. \quad (\text{II.14})$$

The purpose of the importance sampling is to find the density probability  $\wp$  that makes the quantity

$$\begin{aligned} \text{Var}[Y] &= \mathbb{E}[Y^2] - \mathbb{E}[Y]^2, \\ &= \int_{\mathcal{D}} \left[ \frac{\psi(x)}{\wp(x)} \right]^2 \wp(x)^2 dx - \mathcal{I}^2, \end{aligned} \quad (\text{II.15})$$

called the variance of the estimate, the smallest possible.  $\text{Var}[Y]$  is minimal, *i.e.* equal to zero, for

$$\wp(x) = \frac{\psi(x)}{\int_{\mathcal{D}} \psi(x) dx}. \quad (\text{II.16})$$

That is why, in the context of the calculation of the integral (II.3), we want to generate configurations, noted  $\mathbf{x}$  in the subsection (II.1.1), with a density probability

$$\wp_0(\mathbf{x}) = \frac{e^{-\beta \mathcal{H}(\mathbf{x})}}{\int_{\mathcal{D}} e^{-\beta \mathcal{H}(\mathbf{x})} d\mathbf{x}} = \frac{e^{-\beta \mathcal{H}(\mathbf{x})}}{Z}. \quad (\text{II.17})$$

Indeed, if we are able to draw configurations satisfying  $\wp_0(\mathbf{x})$ , then according to the theorem A.3 on page 119, the experimental mean of  $\mathcal{O}(\mathbf{x})$ , *i.e.*  $\langle \mathcal{O} \rangle_{\varepsilon}$ , is equivalent to the expected value of the random variable  $\mathcal{O}(X)$ <sup>(5)</sup> such as

$$\langle \mathcal{O} \rangle_{\varepsilon} \xrightarrow[\mathcal{N} \rightarrow +\infty]{\text{a.s.}} \mathbb{E}[\mathcal{O}(X)] = \langle \mathcal{O} \rangle, \quad (\text{II.18})$$

<sup>(5)</sup>Which is actually the definition of  $\langle \mathcal{O} \rangle$  given by the equation (II.2).

and from (II.13) and (II.14), it comes that the estimator  $\langle \mathcal{O} \rangle_\varepsilon$  of  $\langle \mathcal{O} \rangle$  is defined by

$$\langle \mathcal{O} \rangle_\varepsilon = \frac{1}{\mathcal{N}} \sum_{i=1}^{\mathcal{N}} \mathcal{O}[\mathbf{x}_i]. \quad (\text{II.19})$$

Consequently, if the density distribution to draw the configurations is well chosen, the Monte Carlo algorithm is then improved compared to the simple sampling method. Indeed, we see from the equation (II.19) that there is no use for the terms  $\mathcal{O}[\mathbf{x}_i]$  to be weighted by Boltzmann's factor like in the equation (II.7).

But all these results are based on a condition we have omitted. To generate configurations with a such probability density, we need to know the denominator of  $\wp_0$  (or of  $\wp$  in general) but this is precisely what we are looking for. It leads to the following questions: are we able and how to generate such random variables? Indeed we do not know how to evaluate the partition function  $Z$ , but Metropolis and al. proposed in 1953 a method [130] to overcome this difficulty and to draw a set of configurations obeying to (II.17).

### II.1.3 Metropolis algorithm

#### a) Markov chain and detailed balance

The idea of the Metropolis algorithm relies on a Markov chain<sup>(6)</sup> between two successive configurations to engender the appropriate distribution. It is one of the numerous methods belonging to the *class* of the *Markov Chain Monte Carlo* (MCMC) algorithms<sup>(7)</sup>. The particularity of those methods is that the knowledge of the recent past influences the future, but there is no memory of the *ancient time*.

A configuration  $\mathcal{C}_f$  at time  $t + dt$  is chosen from a configuration  $\mathcal{C}_i$  at  $t$  according to the transition probability (per unit of time)  $W_{i \rightarrow f}$  [184]. The matrix  $W$ <sup>(8)</sup> is crucial, because it *decides of the strategy* of the evolution of the Markov chain. And because, one does not change of strategy during a simulation run, all the entries of  $W$  are independent of the time. The dynamic of the system can be modelled by a *flow* equation. Indeed, the probability  $P_f(t + dt)$  of occurrence of state  $f$  at time  $t + dt$  is equal to this probability at  $t$  increased by the probability to pass from a state  $i$  to  $f$  weighted<sup>(9)</sup> by  $P_i(t)$  minus the probability to *leave* the state  $f$  weighted by  $P_f(t)$ . The evolution of the chain is thus governed by the *master*

---

<sup>(6)</sup>The reader is invited to refer to the appendix A for further information on the topic.

<sup>(7)</sup>One can cite different examples of MCMC algorithms: the *simulated annealing*, importance sampling, Gibbs sampling, slice sampling, on the contrary of the simple or rejection sampling (academic case to calculate the value of  $\pi$ ). Note that in the following, when we will mention Monte Carlo methods, it will imply only MCMC algorithms.

<sup>(8)</sup> $W$  is the transition probability matrix also termed stochastic matrix or even Markov matrix. Note that  $W_{i \rightarrow f}$  is a conditional probability to move from  $i$  to  $f$ .

<sup>(9)</sup>It is equivalent to tell the probability transition is regulated by the population  $N_\ell$  ( $\ell = i, f$ ) of a state. Indeed  $p_\ell$  is the ratio between  $N_\ell$  and the whole population  $N$ . That is why, sometimes  $p_\ell$  is named *population*.

equation [108, 103]

$$P_f(t + dt) = P_f(t) + \sum_{i \neq f} \left[ W_{i \rightarrow f} P_i(t) - W_{f \rightarrow i} P_f(t) \right] dt, \quad (\text{II.20})$$

that can be derived in<sup>(10)</sup>

$$\frac{dP_f}{dt}(t) = \sum_{i \neq f} \left[ W_{i \rightarrow f} P_i(t) - W_{f \rightarrow i} P_f(t) \right], \quad (\text{II.21})$$

with the constraints (by definition of the stochastic matrix) [162]

$$\sum_f W_{i \rightarrow f} = 1 \text{ and } W_{i \rightarrow f} \geq 0, \forall (i, f). \quad (\text{II.22})$$

In the same spirit, we have obviously

$$\sum_i P_i(t) = 1 \text{ and } P_i(t) \geq 0, \forall i. \quad (\text{II.23})$$

The principle of the Monte Carlo is to reach an equilibrium configuration starting from a configuration out of equilibrium. The question remaining is how to choose the transition matrix  $W$  to make the Markov chain converge on the equilibrium distribution  $P_f^{eq}$ , *i.e.* to ensure that configurations are distributed according to (II.17) in our case? We then look for  $W$  such as when  $t \sim +\infty$  we have  $P_f(t) = P_f^{eq}$ , which leads to

$$\frac{dP_f}{dt}(t) = 0, \quad (\text{II.24})$$

leading to the trivial solution

$$\sum_i W_{i \rightarrow f} P_i^{eq} - \sum_i W_{f \rightarrow i} P_f^{eq} = 0, \quad (\text{II.25})$$

known as the *global balance* equation, which is, with respect to the transition matrix rules (II.22), totally equivalent to

$$\sum_i W_{i \rightarrow f} P_i^{eq} = P_f^{eq}. \quad (\text{II.26})$$

There is a large choice of transition matrix satisfying the equation (II.25), but much less verifying the particular solution of (II.24) :

$$W_{i \rightarrow f} P_i^{eq} = W_{f \rightarrow i} P_f^{eq}. \quad (\text{II.27})$$

---

<sup>(10)</sup>In this thesis, we focus mainly on classical spins system on a lattice and Monte Carlo simulations. But this formula is general and rules for other physical systems. For instance, this master equation can be an approach for the study of electronic transport in quantum dots [58]. In this case, the probability of transition (under the effect of a perturbing Hamiltonian  $\mathcal{H}$ ) from an eigenstate  $|i\rangle$  to another one  $|f\rangle$  is given by the Fermi's golden rule:

$$W_{i \rightarrow f} = \frac{2\pi}{\hbar} |\langle f | \mathcal{H} | i \rangle|^2 \rho,$$

where  $\rho$  is the density of final states  $|f\rangle$ .

The passage from a state to another is now reversible<sup>(11)</sup> [184, 162], adding (at least) a supplementary constraint on  $W$ . It can be rephrased as the move from  $i$  to  $f$  implies a move from  $f$  to  $i$  with a non-zero probability. Moreover, the condition (II.27), named *detailed balance*, guarantees the invariance<sup>(12)</sup> of the probability law by satisfying the equation (II.26). We get thus a regime in which the probabilities  $P_\ell^{eq}$  ( $\ell = i, f$ ) are compatible with the given transition coefficients  $W_{i \rightarrow f}$  such as they correspond to their conditional probabilities (cf. Bayes'theorem [4]). Once the equilibrium is reached it cannot be defeated.

To summarize, the detailed balance criterion is more constrained than the global balance. The probability flow to move from a state  $i$  to a state  $f$  is compensated by the reverse probability flow to pass from  $f$  to  $i$ , whereas with the global balance condition, it is the total probability flow that must be conserved (see Figure II.1), *i.e.*, the total flow out of a given state has to be equal to the total flow into this given state.

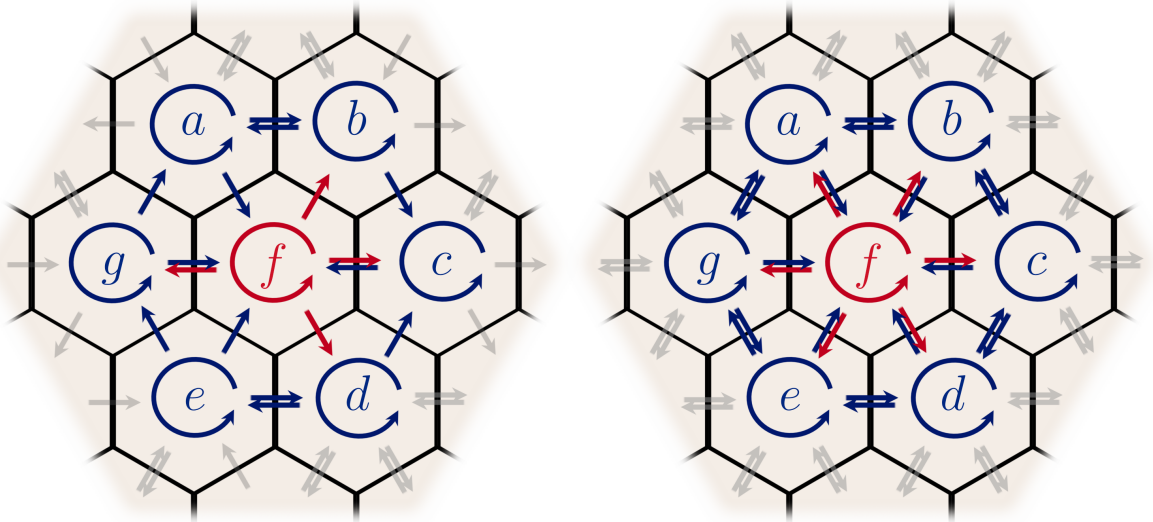


**Figure II.1** - Representation, inspired by [132], of the balance conditions for probability flow in Markov chain process. Each *cell* represent an accessible state or configuration. The arrows denote a transition from a configuration to another and the circular ones indicate a *self*-transition (from a state to itself). The total probability transition flow is conserved for every single *cell*. To be consistent with the text, the **blue** letters denote the *initial* states called *i* and obviously, the **red** letter the *final* state *f*. *Left*: Global balance criterion. The sum of every moves from outside a *cell* to inside is equal to the sum of all the outflows. *Right*: Detailed balance criterion. The states are reversible. The inflow  $i \rightarrow f$  is automatically compensated by the reverse outflow  $f \rightarrow i$ .

Note that only the global balance is required to reach the equilibrium. But during a simulation, it is hard<sup>(13)</sup> to ensure that this condition is satisfied while with the detailed balance,

<sup>(11)</sup> One speaks then of reversible Markov chain.

<sup>(12)</sup> The equation (II.27) implies (II.26). See the annexe A.

<sup>(13)</sup> By drawing a analogy with the geometry, the global balance condition has a *topology* more complex than the *topology* characterising the detailed balance, making thus the global balance condition more difficult to

the ratio of the transition rates is directly given by the rapport of the equilibrium probabilities. A natural choice is the ratio of the Boltzmann weights<sup>(14)</sup>, according to equation (II.17), leading to

$$\frac{W_{i \rightarrow f}}{W_{f \rightarrow i}} = \frac{P_f^{eq}}{P_i^{eq}} \stackrel{\text{canonical distribution}}{=} e^{-\beta(E_f - E_i)}, \quad (\text{II.28})$$

where  $E_f$  and  $E_i$  denote the energy of the final and initial configuration<sup>(15)</sup>, respectively. The evaluation of the partition function is then unnecessary<sup>(16)</sup> because of the linearity of (II.25) and the compatibility with the equilibrium is furthermore totally ensured. These are the interests of the Markov chain Monte Carlo algorithms.

## b) Ergodicity

As said in the introduction of the subsection, MCMC algorithms are methods producing Markov chains, as the name suggests, but with the particularity they are *ergodic*. We therefore think it is important to spend a bit of time on this notion on which the Monte Carlo is based on.

A system is said ergodic, if starting from any configuration it can access to the whole configurations in a certain time. It depends then on the transition matrix. The choice of the *strategy*, namely the  $W_{i \rightarrow f}$ , to decide the move from a state to another one is crucial to converge toward a stationary distribution. An intuitive way, for a better understanding, is to draw a parallel with the circulation of the money between different protagonists and the economy of a country, by considering the probabilities  $P_i(t)$  in the master equation (II.21) represent a quantity of money and the  $W_{i \rightarrow f}$  a transaction rate. Note that, in the examples show in the following, there is no *creation of new money*, because the matrix  $W$  just distributes the total amount of money, which is fixed by (II.23).

For instance, let us consider a *society* organised in different entities: a State<sup>(17)</sup>, banks, companies, workers, retired persons and etc... Roughly speaking, the economy of this society depends on how the wealth circulates between all these *entities*. The case they all save up their money is the worse case for the economy of the society. It corresponds to the very specific (senseless) situation where only the *self*-transitions, *i.e.*  $W_{i \rightarrow i} = 1$ , are allowed (see the graph on the left of the figure II.2), making money be useless.

---

use in an simulation.

<sup>(14)</sup> Instead of Boltzmann distribution, which is the most known, other choices can be considered, like for example in the multi-histogram methods [62].

<sup>(15)</sup> With the respect to the notations of the subsection II.1.1, we have  $E_\ell = \mathcal{H}[C_\ell]$  ( $\ell = i, f$ ).

<sup>(16)</sup> Actually, this is firstly true for the global balance condition, whose the detailed balance criterion being only a restriction.

<sup>(17)</sup> State is written in a French way, *i.e.* with a capital letter, to prevent possible confusions with the states of a physical system.

Another foolish situation is the following, with an entity, like a firm for instance having only expenses and almost no income. In the end, it will have no money left and money will be bad distributed (see Figure II.2). In a realistic context, it corresponds to a firm produces something that nobody buys, except maybe the pensioners, because people prefer once again to *keep safe* their personal savings. It is really damageable for its treasury. Indeed, it spends lots of money (salaries, taxes...) but without ever making profits. It is then impossible for the firm, and by consequence for the persons working in it, to reach a durable and profitable equilibrium state, making it to decline.

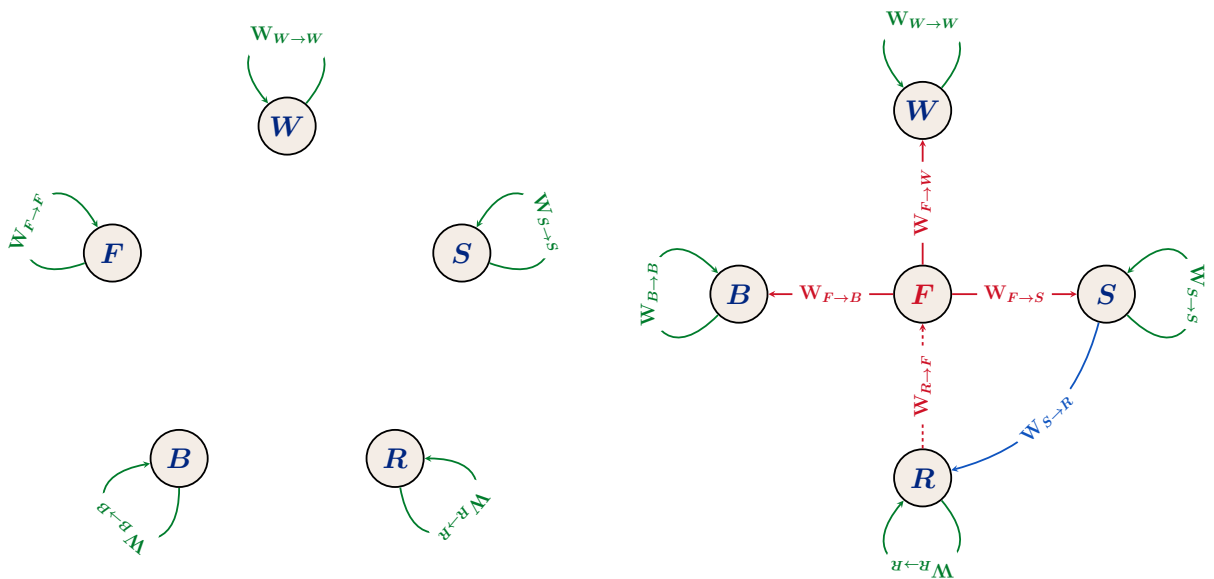


**Figure II.2** - Representation of the circulation of money between different economic players ( $W$  for workers,  $R$  for retired persons,  $F$  for firms,  $S$  for State and  $B$  as bank) to illustrate an unsustainable economy of a society modelled by a system with five different possible states with a *non-ergodic strategy*. In terms of physics, starting from a state, certain states will never be visited over the time and each arrow represents a possible transition with its probability transition  $W_{i \rightarrow j}$ . *Left*: Only the *self*-transitions are authorized ( $W_{i \rightarrow i} = 1$ ). It corresponds to the situation where every entity saves up its money. There is then no *money-flow*. *Right*: The money will never transit over all the protagonist. It flows essentially from the firm to the bank as repayment of loans or to its workers as salaries or to the State as taxes. Eventually, only the retired persons, receiving their pension from the State, participate to the commercial activity of the firm by buying what it produces. At the end, the situation is critical for the global economy of the society, because money is bad distributed.

A good strategy to adopt for the general interest of the society is to be sure that the money *flows* between all the economic players of the society (see Figure II.3) and is at the end *intelligently* distributed. That is why, the State encourages people to consume more by taxing or by decreasing the interest rates of their savings. Thus firms can sell what they produce allowing them to donate a part of the benefits to their employees as salaries and to the Sates as taxes. A *steady state* for a society is reached when the money circulates between

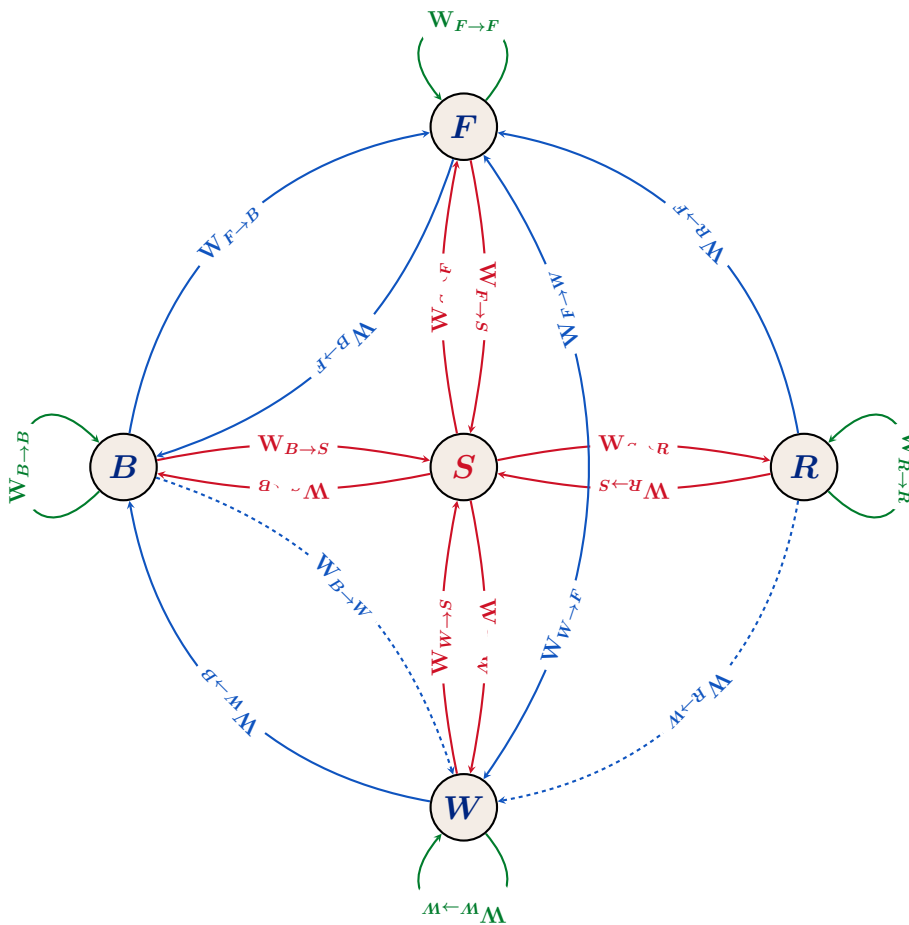


**Figure II.3** – Representation of an ergodic system with five states. Each arrow represents a possible transaction between different economic players:  $W$  for workers,  $R$  for retired persons,  $F$  for firms,  $S$  for State and  $B$  for banks. The system is ergodic because the money can circulate from an entity or a person to another one and never *gets stuck* in a place like a bank for instance. Every transaction coming out of the bank are loans and those coming in are either repayment loans (with interest rates) or simply bank charges. The State has a central role. It receives money from taxes or loans from the bank and reverses money as social benefits (except to the banks) to help people or firms. Workers are paid by their firms and buy what they produce and takes out sometimes a loan (dashed arrow). They also can borrow money for the retired persons. The latter receive their pension from the State and participate to the benefits of the firm.

all the entities: from hand to hand (freely or not) between people, from the companies to their employees and vice-versa and passing obviously by the State as taxes that can be partially redistributed as social benefits for example. In other words, it is when all the exchanges, made in different proportions and that are represented by the  $W_{i→j}$ , verify the global balance. In the case where the detailed balance is verified, a transaction between two protagonists becomes reversible and then can be cancelled.

Let us going back to a more classical and physical view of the ergodicity. We have now

understood the ergodicity is the *ability* for a system to access to all the possible states existing. Thus, we are able to have enough informations about the system over the time<sup>(18)</sup> to have the equivalence between time average and the ensemble average<sup>(19)</sup> of a quantity. About the above example, we can easily imagine that if we follow every transaction over the time we will converge to a good approximation of the global economy. To calculate the theoretical average, we would need to know the repartition of the money between all the economic players, *i.e* the  $P_i^{eq}$  of the equation (II.27). It is has to be agreed that it is much easier than to *follow the money* step by step (in an ideal world).

In the light of the foregoing about the theoretical context in which the Monte Carlo is taking place, we can now discuss in details about the Metropolis algorithm and its use on the Ising spin system.

### c) The Metropolis algorithm: single spin flip algorithm

The transition probabilities must be well-designed to satisfy the detailed balance equation (II.28). Metropolis and al. [130] proposed a solution<sup>(20)</sup>, known as the *Metropolis acceptance rate* or also *Metropolis criterion*, such as

$$W_{i \rightarrow f} = \min \left( 1, \frac{P_f^{eq}}{P_i^{eq}} \right) \stackrel{\text{canonical distribution}}{=} \min \left( 1, e^{-\beta(E_f - E_i)} \right). \quad (\text{II.29})$$

It appears clearly<sup>(21)</sup> the acceptance rate is valid for any kind of distribution  $P^{eq}$ . In the canonical description, the Metropolis criterion depends only on the difference of energy between two configurations. Basically, it means that if the energy of the final configuration  $C_f$  is lower than the one of the initial configuration  $C_i$ , *i.e.* if  $E_f \leq E_i$ , then the transition from  $C_i$  to  $C_f$  is fully accepted ( $W_{i \rightarrow f} = 100\%$ ). But if it is *expensive* (in terms of energy) for the system to move from a configuration to another one, *i.e.* if  $E_i < E_f$ , the configuration is accepted with a probability  $W_{i \rightarrow f} = e^{-\beta(E_f - E_i)}$ .

The Metropolis algorithm works as follows:

1. pick randomly a spin in the lattice (we will refer later to this operation as the *a priori choice* [102] or *proposed update*);
2. flip the spin (attempt a move from a state  $i \rightarrow f$ )
3. draw a random number  $r$  uniformly distributed on  $[0, 1]$ ; two situations :

---

<sup>(18)</sup> If the time is large enough to be sure all the states have been visited several times.

<sup>(19)</sup> The time average can be seen as an experimental average and the ensemble average as the theoretical one.

<sup>(20)</sup> One could have choose the Glauber's dynamic [108], with  $W_{i \rightarrow f} = \frac{\tau}{2} [1 - \text{th}(\beta \frac{E_i}{2})] = \frac{\tau}{1 + e^{\beta E_i}}$ , that also satisfies the detailed balance condition.

<sup>(21)</sup> By replacing equation (II.29) into equation (II.27).

- if  $r \leq W_{i \rightarrow f}$ , the configuration is accepted, *i.e.*,  $\mathcal{C}_f$  is the next configuration of the Markov chain;
- if  $r > W_{i \rightarrow f}$ , the attempted move is rejected and the system remains in the same configuration  $\mathcal{C}_i$ ; the next configuration of the Markov chain is then the same as the current one.

The set of these three operations is called a Monte Carlo *step*; it only concerns one spin. When  $N$  spins on a lattice containing  $N$  spins have been updated, we speak then of a Monte Carlo *sweep* (MCS) <sup>(22)</sup>. At the end of a cycle of  $N_s$  MCS, a data set  $\{\mathcal{O}_i\}_{i \in [1, N_s]}$  of a physical quantity, e.g. the energy or the magnetisation, is generated. The thermodynamic average of  $\mathcal{O}$  can be readily computed as an arithmetic mean of the  $N_s$  values  $\mathcal{O}_i$  (see eq. (II.19)). To be pertinent, the calculation of the averages needs a number of cycle sufficient, corresponding to the generation of a Markov chain long enough.

#### d) Application to the Ising model

Let us now apply the Monte Carlo procedure to a simple model. The first step of the program is to define the crystalline structure; here we choose a two-dimensional square lattice. The following step is to decide of the interactions between the spins, described, for instance by the well known Ising model under a zero magnetic field ( $h = 0$ ) ruled by the Hamiltonian

$$\mathcal{H}_i = -J \sum_{\langle i, j \rangle} S_i S_j - h \sum_i S_i, \quad (\text{II.30})$$

where  $J$  is the interaction exchange constant between the spins and the first sum is performed over the nearest neighbours (NN), with periodic boundaries conditions. The spin  $S_i$  of a site  $i$  can take two values 1 or  $-1$  corresponding to a spin up or a spin down, respectively. If  $J > 0$ , the ground state is reached when all the spins are aligned (up or down): one speaks then of a ferromagnetic configuration. The configuration of highest energy is the *anti-ferromagnetic* configuration, *i.e.* the spins are alternatively in the opposite state. If  $J$  is negative, it is the contrary.

The next stage is to choose an initial configuration and then to launch the Monte Carlo procedure on the system to have some measurements (e.g. the energy, the magnetisation, specific heat...). This configuration being not necessarily at the thermal equilibrium, the first measurements are often wrong. We have to discard them and to ensure our system would have *thermalized*, which means the Markov chain has reached the equilibrium distribution  $P^{eq}$ . The energy is calculated for each spin by summing the interactions with other spins, *i.e.* here only the NN ones and the spin is flipped according to the Metropolis criterion (cf. eq. (II.29)). We do that for every spin on the lattice until the equilibrium is reached, *i.e.* after

<sup>(22)</sup>One MCS is equal to  $N$  Monte Carlo steps.

several Monte Carlo sweeps<sup>(23)</sup>. Then, we can proceed to the calculation of the averages of the physical quantities we are interested in. The purpose in this part is not to detail the behaviour of the Ising system, but to see how it evolves in different situations.

On the Figure II.4 on the next page are represented some snapshots of the two dimensional Ising model on a square lattice of size  $L = 500$ . The spins up are in blue and the down in red. To each column corresponds an initial configuration and a temperature and to each row the *time* (*i.e.* the number of MCS performed).

The first situation (first column of Figure II.4) concerns an anti-ferromagnetic configuration at low temperature. The system being in the highest energy level, it tends progressively towards the ferromagnetic state. Indeed, it is more favourable for the system to have all the spins in the same orientation: an *update* aligning the spins (according to the orientation of its neighbours) is necessarily accepted because  $E_f < E_i$ ; a proposal of spin in opposite state with its NN is rejected at low temperature because  $W_{i \rightarrow j} \xrightarrow{T \rightarrow 0} 0$ <sup>(24)</sup>. If we had performed the simulation on a longer *time* we would have got a perfect blue square, meaning the equilibrium corresponds to a ferromagnetic configuration (at low temperature).

The column in the middle (cf. Figure II.4) concerns the evolution of the system, in a random configuration, at the *critical temperature* or the *Curie temperature*  $T_c$ . The system (when it is in the equilibrium configuration) is characterised by a zero (global) magnetisation and the quantities like the specific heat or the susceptibility magnetic diverges in the thermodynamic limit for an infinite size due to *long range correlations*<sup>(25)</sup> between the spins. It means, their states fluctuate a lot but not independently of the others. They are strongly correlated to each other (even with those located at very long distances) giving *birth* to *clusters* or *domains* of parallel spins persisting along the time, increasing deeply the *relaxation time*  $\tau$  [85]: this phenomenon is named *critical slowing-down* [49]. The Metropolis algorithm, updating the system spin after spin, is not adapted for the study of the system at  $T_c$ . A wiser choice would be to perform the simulations with a *cluster flip* algorithm such as proposed by Swendsen and Wang [176] or by Wolff [186, 187], improving the relaxation time  $\tau$ <sup>(26)</sup>.

---

<sup>(23)</sup> cf. the previous sub-subsection II.1.3.c.

<sup>(24)</sup> This is why, if all the spins were initially aligned, the system would have stayed in the same configuration, *i.e.* ferromagnetic. One could have seen appear, during the simulation, some spins in opposite state because we are not at zero temperature.

<sup>(25)</sup> Near the critical temperature, the *correlation length*  $\xi$ , *i.e.* the distance below which the fluctuation between two spins are correlated, increases.  $\xi$  diverges at  $T_c$ . For a finite size  $L$  system with periodic boundaries, a phase transition occurs when  $\xi \sim L$ . At  $T_c$ ,  $\xi$  diverges [49] (for a second order phase transition).

<sup>(26)</sup> The relaxation time is actually proportional to the correlation length  $\xi$ , such as  $\tau \propto \xi^z \sim L^z$ , where  $z$  is the *dynamic exponent* [49]. Near  $T_c$ ,  $z \sim 2$  [145] with the standard Metropolis algorithm and with a cluster flip algorithm  $z \sim 0.5$  [177]. The efficiency of this kind of algorithm near  $T_c$  is obvious.

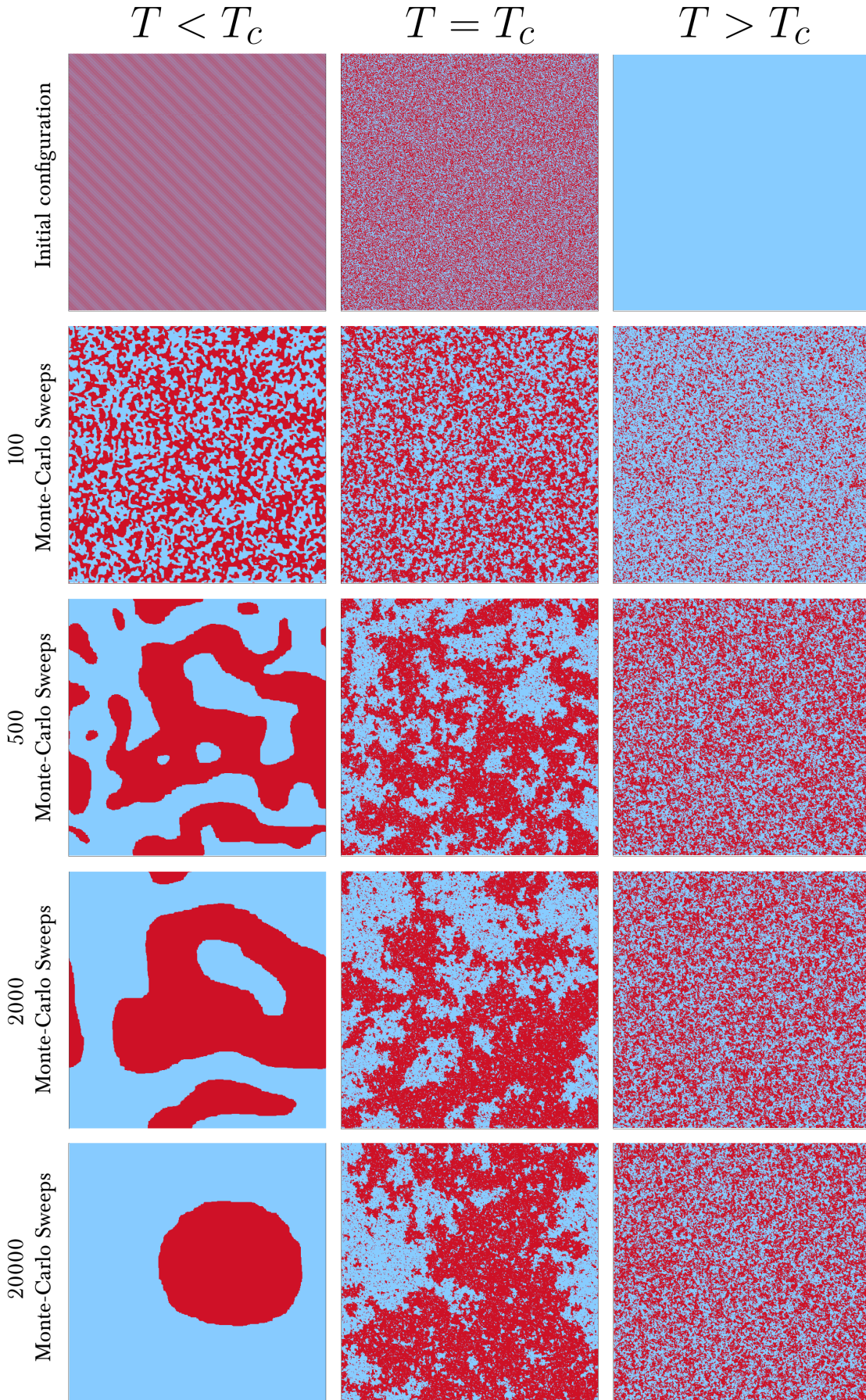


**Figure II.4** – Snapshots of an Ising system on a  $2D\ 500 \times 500$ -square lattice with nearest neighbours interactions at different Monte Carlo sweeps (MCS). Each column corresponds to a special initial configuration at a given temperature  $T$  (expressed in  $k_b/J$ , with  $J$  the interaction exchange constant) and each row to the configuration at a certain numbers of MCS. The spins up  $\uparrow$  are in **blue** and the spins down  $\downarrow$  in **red**. *Left* : Evolution of an anti-ferromagnetic configuration at  $T = 0.1$ . The different snapshots show the system evolves progressively to a ferromagnetic system. *Middle* : The initial configuration is randomly generated. At the critical temperature  $T = T_c = 2.269$ , some clusters of spins **up** and spins **down** appear. The system is stuck in this kind of configuration. The Metropolis algorithm is not adapted for the study of the system at  $T_c$  contrary to a cluster flip algorithm. *Right* : At  $T = 3.0$ , the system moves rapidly from a ferromagnetic phase to a disordered one. It appears there are almost no differences between the three last configurations.

At high temperature (cf. snapshots of the the last columns of the Figure II.4), the system evolves readily from a ferromagnetic to a disordered phase termed paramagnetic. Following the same arguments, a spin flip is almost always accepted since  $W_{i \rightarrow j} \xrightarrow{T \rightarrow +\infty} 1$ . In these conditions, all the configurations are accessible. Theoretically, it should be possible for the system to reach an anti-ferromagnetic phase. But the degeneracy [148] of the disordered state being too high (compared to the one of the ordered phases), the probability<sup>(27)</sup> it happens is very low.

## II.2 Adaptation to the mobile spin

We present in this section the algorithm we developed for our mobile spin systems.

### II.2.1 Non micro-reversible moves

The micro-states of a system are not always reversible, *i.e.* the proposed update (cf. the part II.1.3.c) from  $i$  to  $f$  is not symmetric to the reverse move from  $f$  to  $i$ . We need then to adapt the detailed balance (see equation (II.27)) for this purpose. The probability transition can expressed [102] as the product of two probabilities such as

$$W_{i \rightarrow f} = \mathcal{S}_{i \rightarrow f} \mathcal{A}_{i \rightarrow f}, \quad (\text{II.31})$$

where

- $\mathcal{S}_{i \rightarrow f}$  denotes the selection rate of a specific state among the set of all the accessible states, *i.e.* the proposed update (or *a priori* choice) probability,
- and  $\mathcal{A}_{i \rightarrow f}$  the acceptance probability of the *a priori* choice.

In the same manner we can show the equation (II.29) satisfies the detailed balance, we can prove that

$$W_{i \rightarrow f} = \mathcal{S}_{i \rightarrow f} \min \left( 1, \frac{P_f^{eq} \mathcal{S}_{f \rightarrow i}}{P_i^{eq} \mathcal{S}_{i \rightarrow f}} \right) \quad (\text{II.32})$$

is also a valid transition rate satisfying the detailed balance equation (II.27). This is known as the Metropolis-Hastings criterion [76].

### II.2.2 Mobile spin algorithm

Until now, we implicitly only mentioned the spin orientation as degrees of freedom. But for modelling our mobile spin systems (cf. chapter III), we need to add some others to take into accounts the displacement of the spins on the lattice.

---

<sup>(27)</sup> cf. the canonical probability of degenerated states [50].

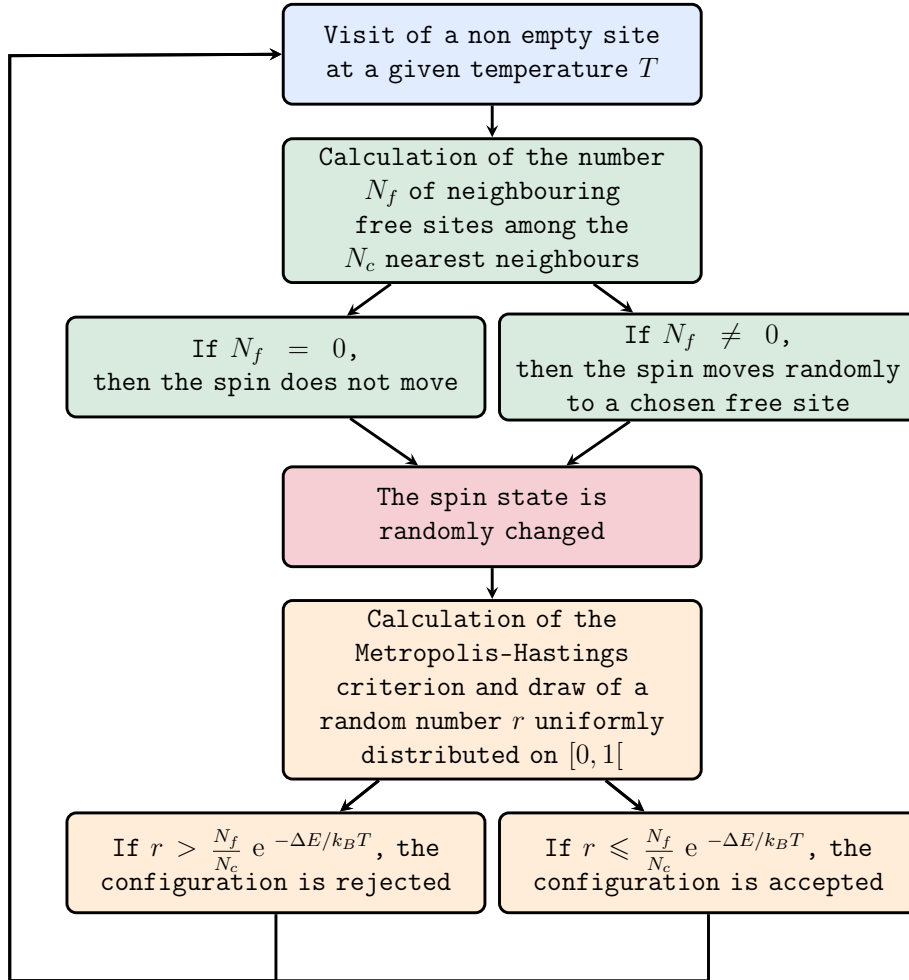


**Figure II.5** - Diagram showing the different steps of the Monte Carlo algorithm for mobile spin systems. These steps must be repeated until all the lattice sites have been visited before calculating the physical quantities of the system (energy, magnetisation...)

We have performed the simulations of a partially filled lattice. The concentration  $c$  of spins is fixed (canonical situation). It is defined by  $c = N/N_T$ , where  $N$  is the number of spins and  $N_T = N_x \times N_y \times N_z$  the total number of lattice sites where  $N_i (i = x, y, z)$  is the number of site in the  $i$  direction<sup>(28)</sup>. The spin has then here three supplementary degrees of freedom (one by direction of possible displacement).

Now the framework of this algorithm is defined, let us explain how a step is performed. At a given  $T$ , we visit a non empty lattice site: the algorithm counts the number  $N_f$  of empty neighbouring sites. If this number is different from zero, the spin moves to a randomly chosen (with a certain probability) free site with a randomly chosen spin state. If  $N_f$  is equal to zero, only the state is changed. The energy of the spin is calculated and the new configuration is accepted or not according to the Metropolis-Hastings criterion. We go to another site and update its position and its spin state until all sites are visited. The

<sup>(28)</sup>This method can be applied on a three-dimensional system as well on a two-dimensional one.

algorithm is summarised thanks to the Figure II.5. Once a Monte Carlo sweep has been realized, the physical quantities, such as the energy and the magnetisation for instance, can be calculated.

## II.3 Sources of errors in Monte Carlo

As said in the introduction of the chapter, Monte Carlo simulations allow to study physical systems that can not be solved analytically. But the use of computers to perform calculations implies necessarily numerical and statistical errors. It is then important to have a good knowledge about the possible causes of these errors in order to minimize them and to get the most accurate results. Therefore, we deal in this section with the statistical and systematic errors in Monte Carlo [61], like the simulation time, the finite-size effects. And because Monte Carlo methods rely on stochastic processes, we also treat the generation of random numbers.

### II.3.1 Systematic and statistical errors

#### a) Time effect

**Autocorrelation function and relaxation times** We have seen with the equation (II.19) that the average value of a given observable  $\mathcal{O}$  is calculated thanks to a simple arithmetic mean, *i.e.* by summing the  $\mathcal{N}$  recorded values<sup>(29)</sup>  $\mathcal{O}_n$  of the observable. It is then obvious that to get a *good* statistic, the  $\mathcal{O}_n$  must be decorrelated as far as possible. But a Markov chain does not engender statistically independent configurations. Therefore, it can be appropriate to evaluate the amount of correlation between configurations by calculating the normalised time-displaced autocorrelation function<sup>(30)</sup>

$$R_{\mathcal{O}\mathcal{O}}(t) \equiv \frac{\langle \mathcal{O}_n \mathcal{O}_{n+t} \rangle - \langle \mathcal{O}_n \rangle^2}{\langle \mathcal{O}_n^2 \rangle - \langle \mathcal{O}_n \rangle^2}, \quad (\text{II.33})$$

$$= \frac{1}{\sigma_{\mathcal{O}_n}^2} \left[ \frac{1}{\mathcal{N} - t} \sum_{n=1}^{\mathcal{N}-t} \mathcal{O}_n \mathcal{O}_{n+t} - \frac{1}{(\mathcal{N} - t)^2} \sum_{n=1}^{\mathcal{N}-t} \mathcal{O}_n \sum_{n'=1}^{\mathcal{N}-t} \mathcal{O}_{n'} \right], \quad (\text{II.34})$$

where  $\langle \cdot \rangle$  denotes the average taken over the time-index  $n$  (estimated here by an arithmetic sum) and the normalisation factor (the denominator) is simply the variance of the observable. This function tells us how two measurements of  $\mathcal{O}$ , separated by  $t$  MCS, are correlated. By definition, we have  $R_{\mathcal{O}\mathcal{O}}(0) = 1$  and  $\lim_{t \rightarrow +\infty} R_{\mathcal{O}\mathcal{O}}(t) = 0$ . Actually for systems at the equilibrium, the autocorrelation function has an exponentially decaying behaviour

<sup>(29)</sup> Throughout a Monte Carlo run, with  $\mathcal{O}_n$  the  $n$ -th stored value and where  $n \in [1, \mathcal{N}]$ .

<sup>(30)</sup> Known in statistic as the (normalised) *autocovariance function*. In signal processing, this function is often not normalised and reduced to the first term of the equation (II.34): it is a convolution product.

for large  $t$  [28, 172] such as<sup>(31)</sup>

$$R_{\mathcal{O}\mathcal{O}}(t) \xrightarrow{t \rightarrow +\infty} e^{-t/\tau}, \quad (\text{II.35})$$

where  $\tau$  is the *relaxation time*<sup>(32)</sup> (diverging around the critical temperature  $T_c$  for second order phase transition) and is a good indicator of the average time-scale between two independent measurements. Note that the relaxation time depends on the state of the system and also on the observable  $\mathcal{O}$  considered (energy, magnetisation...) and therefore  $\tau$  represents the largest one. There are two ways to obtain it; either from the equation (II.35) leading to the *exponential* relaxation time  $\tau_e$  or from the integration of the autocorrelation function leading to the *integrated* relaxation time, such as

$$\tau_i \simeq \frac{1}{2} + \sum_{t=1}^{+\infty} R_{\mathcal{O}\mathcal{O}}(t). \quad (\text{II.36})$$

The integrated and exponential relaxation time do usually not totally coincide [91]. Actually they do not play the same role giving thus different informations [172].  $\tau_e$  tells about the number of MCS to discard before considering the Markov chain has reached an invariant probability distribution, *i.e.* before the system has thermalised. Once the equilibrium is attained, any subsequent Monte Carlo moves from a state to another one leave the system in the equilibrium and thus any time of the simulation can be considered as the *time zero*  $t_0$  for the calculation of the averages. Thus  $t_0 \gg \tau_e$  is a sufficient condition for a system to be well thermalised. On the other hand,  $\tau_i$  takes place in the statistical errors of the estimation of  $\langle \mathcal{O} \rangle$  due to the fluctuation of the stored values  $\mathcal{O}_n$ . The mean squared error  $\varepsilon_{\mathcal{O}}^2$ <sup>(33)</sup> on the estimated mean  $\langle \mathcal{O} \rangle$  is given by

$$\varepsilon_{\mathcal{O}}^2 = \frac{2\tau_i}{\mathcal{N}} \left[ \langle \mathcal{O}_n^2 \rangle - \langle \mathcal{O}_n \rangle^2 \right] = \frac{\langle \mathcal{O}_n^2 \rangle - \langle \mathcal{O}_n \rangle^2}{\mathcal{N}_{eff}}, \quad (\text{II.37})$$

where  $\mathcal{N}$  is still the number of recorded measurements and  $\mathcal{N}_{eff}$  the number of independent measurements  $\mathcal{O}_n$  that are approximatively uncorrelated after  $2\tau_i$  iterations.

## b) Size effect

In order to get data quickly, it might be sometimes tempting to perform simulations on small systems leading to a high risk to have wrong results. Indeed, the size or volume  $V = L^d$ ,  $d$  being the dimension of the lattice, of a sample is a source of errors, since the simulations are made on finite systems. To get around this, one can use *periodic boundary conditions*<sup>(34)</sup> (PBC) to simulate an infinite system. But this *trick* is not infallible and works

<sup>(31)</sup>This behaviour can be demonstrated with a spectral analysis of the Markov transition matrix [173] and the time-scale  $\tau$  is related to the eigenvalues of this matrix. For certain systems, like spin glass [70], the autocorrelation function scales with a stretched exponential function [2], *i.e.* with  $e^{(-t/\tau)^b}$  where  $0 < b \leq 1$ .

<sup>(32)</sup>Also termed *autocorrelation time*.

<sup>(33)</sup>For more details see the appendix B.

<sup>(34)</sup>The way how to treat boundaries of a lattice is a crucial problem in numerical simulations. Different kinds of boundary conditions and their effects are exposed in Landau and Binder's book [108].

for high enough  $L$ . For instance, a Monte Carlo simulation of an Ising model on a square lattice of size  $L = 10$  with PBC is far from the analytical Onsager's solution [148]. This is shown with a finite size scaling study (see Figure II.6). We give now a short explanation about the importance the size of the system in phase transition and about the errors it occurs.

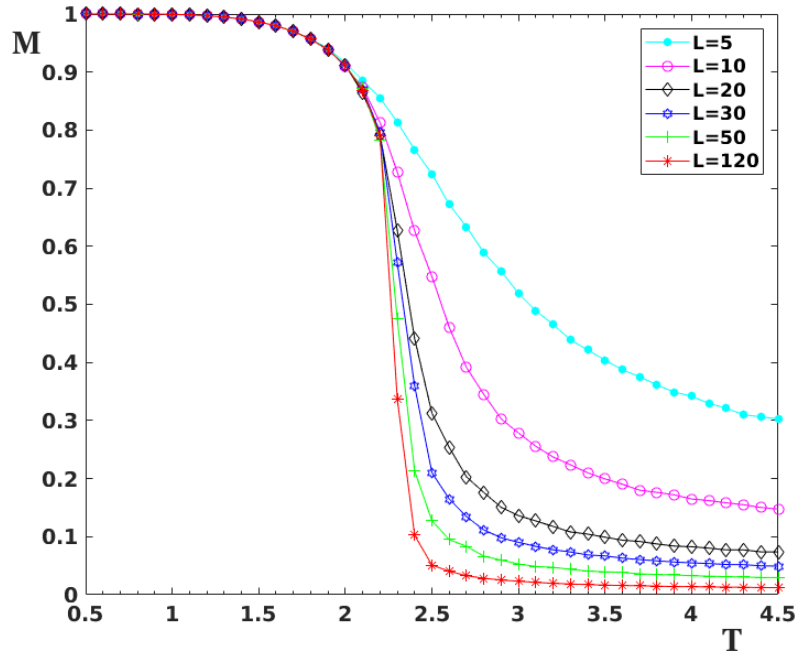


**Figure II.6** – Plot of magnetisation  $M$  versus temperature  $T$  (in unit  $J/k_B$ ) obtained by Monte Carlo simulation of an Ising model without external magnetic field on a square lattice of size  $L$  with periodic boundary conditions. The figure shows a finite size scaling effect; indeed the evolution of the order parameter  $M$  depends clearly on  $L$ . For instance, when  $L = 5$ , the magnetisation decreases slightly. But when  $L$  becomes larger and larger, the behaviour of  $M$  tends towards the behaviour described by the analytical solution [148], *i.e.* a brutal drop to zero of the order parameter at the critical temperature  $T_c \simeq 2.27 J/k_B$ .

When a second order phase transition *truly*<sup>(35)</sup> occurs, the correlation length  $\xi$ , *i.e.* the distance between spins below which they are correlated, diverges<sup>(36)</sup> just as the relaxation time  $\tau$ , since they are linked through the relation [85]

$$\tau \propto \xi^z \propto \left( \frac{T_c}{T - T_c} \right)^{z\nu}, \quad (\text{II.38})$$

where  $T_c$  denotes the critical temperature,  $\nu$  is a critical exponent and  $z$  the *dynamic* exponent depending on the algorithm. But because of the finiteness of the system, the transition takes place when  $\xi$  is the order of  $L$ <sup>(37)</sup>, *i.e.*  $\xi \sim L$ . We understand then that if  $L$  is *too*

<sup>(35)</sup> Meaning for infinite system.

<sup>(36)</sup> This is known as the *critical slowing down* phenomenon.

<sup>(37)</sup> To be more accurate, with PBC, we have  $\xi \sim L/2$  [108].

small, the study of a phase transition may be biased, like for instance: a bad estimation of the transition temperature  $T_c$ , a first order phase transition looking like a second order one<sup>(38)</sup> (namely with continuous order parameters and characterised by scaling laws), etc... Moreover, it appears clearly the relaxation time depends on the size of the system [135, 15, 108] through

$$\tau(L) \propto L^z \quad (\text{II.39})$$

or for a first order transition through

$$\tau(L) \propto L^z e^{2\sigma L^{d-1}}, \quad (\text{II.40})$$

where  $\sigma$  denotes the interface free energy between two phases and  $2L^{d-1}$  the surface of the interfaces with PBC; the argument of the exponential function being then the height of the free energy barrier [152, 50]. By replacing these two last equations in the equation (II.37), we see the errors depends now on the ratio of the size  $L$  of the system to the observation time  $t_{obs}$ .

### II.3.2 Random numbers generator

In general terms, the generation of random numbers is a crucial point for the stochastic algorithms and can constitute a source of errors in Monte Carlo simulations [124]. Indeed, the reliability of the results in Monte Carlo simulation and the quality of the random numbers generators are strongly correlated. The production of random numbers is still subject to an intensive research<sup>(39)</sup> and an entire thesis could be written on it, which is not the purpose here. We provide hereafter only informations about the generators used for our simulations.

It exists different kinds of generators. The most efficient are the ones based on a physical methods such as, for example, the diode noise, the radioactivity or photonic devices [79, 179]. But the method we used for the simulations relies on software [99] for generating *pseudo* random numbers (PRNG), *i.e.* producing a deterministic sequence of numbers. A PRNG must meet the following requirements to be considered as reliable :

- the distribution of random numbers has to be as close as possible to the desired distribution (uniform in our case),
- the correlation between successive numbers must be the lowest possible,
- the period of a cycle must be preferably larger than the total amount of generated numbers<sup>(40)</sup>,

---

<sup>(38)</sup> Fortunately, methods exist (besides a finite size scaling study), like the *Binder cumulant* [14] and the *histogram method* ( see chapter III and [62]) to distinguish the order of a phase transition, to locate precisely a critical point and to calculate the critical exponents.

<sup>(39)</sup> Particularly in the domain of the cryptography [151] and parallel computing [109].

<sup>(40)</sup> Typically equal to the number of sites times the number of Monte Carlo sweeps for a *classical* spin system (*i.e.* with no spin moving on the lattice).

- and the algorithm must be efficient in view of the colossal amount of random numbers that requires a Monte Carlo simulation.

The PRNGs can be classified in different families all based on a recurrence relation, *i.e.* each generated number  $r_n$  is function of the previous ones, such as  $r_n = f(r_0, r_1, \dots, r_{n-1})$ . *Linear congruential* generators (LCG) are probably the simplest generators. They rely on the sequence  $r_n = (a \times r_{n-1} + c) \bmod m$ , where  $a$ ,  $c$  and  $m$  have to be set carefully in order to get the longest period  $m$ . LCG were popular but show noticeable correlation between consecutive random numbers, as for instance the (really bad) RANDU<sup>(41)</sup> generator used in the sixties. Their quality have been improved by mixing two (in the simplest case) distinct congruential generators. A first LCG generates a list of random numbers that is *shuffled* with another generator [120]. The random numbers are then drawn from the shuffled list reducing the correlation between numbers and increasing the period. Later appears a new class of generators based on shift of *bit* registers using only bitwise exclusive-or (XOR) operations. These generators, known as *shift register* generators (SRG) are reputed to be faster than LCGs [97, 114]. The SRG is a special type of generators of a more general family: the *lagged Fibonacci* generator [126]. The XOR operation can be replaced by multiplications, additions or other operations increasing the periodicity ( $2^{144} \propto 10^{43}$  for the RANMAR generator). Further informations about PRNG can be found in the James' article [90].

For the simulations, we used the *Mersenne Twister* algorithm [127] (MT) that meets the requirement listed above. This PRNG, based on a twisted generalized shift register algorithm, is probably one of the most used, among all the uniform generators, in numerous domains<sup>(42)</sup>, like in Monte Carlo simulations, because of its very wide period equal to the Mersenne prime<sup>(43)</sup>  $M_{19937} = 2^{19937} - 1$ , *i.e.* of the order of  $10^{6000}$ . It is also reputed for its rapidity since only 32-bits logical bit operation are performed. Moreover, the MT algorithm assures a high  $k$ -dimensional distribution, with  $k = 623$ . The  $k$ -tuples (for which components are made up with consecutive numbers) are equidistributed over a whole period in an unit hypercube (of dimension  $k \leq 623$ ), passing thus the  $k$ -distribution test. It also passed some of the empirical *diehard* tests proposed by Marsaglia [125, 89]. We performed one them: the *parking lot test* [88, 108] which is easy to implement. The initial version is such as a square with a side length of 100 units is filled by squares of one unit side length (representing cars). 12000 points (centers of the cars) of coordinates  $(r_n, r_{n+k})$  are randomly drawn<sup>(44)</sup>. We count and plot then the numbers of cars *parked* in the square, *i.e.* the numbers of non-overlapping squares. The purpose of this test is to highlight potential

---

<sup>(41)</sup> LCG for which  $r_n = (65539 \times r_{n-1}) \bmod 2^{31}$ .

<sup>(42)</sup> Except in cryptography. A sequence of random numbers can be predicted from a subsequence (long enough) of previous generated numbers. This weakness comes from the fact these sequences are generated by a linear recursion.

<sup>(43)</sup> They are prime numbers of the Mersenne sequence  $M_n = 2^n - 1$ , ( $n \geq 1$ ). A necessary but not sufficient condition for  $M_n$  to be a prime number is that  $n$  is prime too.

<sup>(44)</sup> Several tests can be performed with different values of  $k$ .

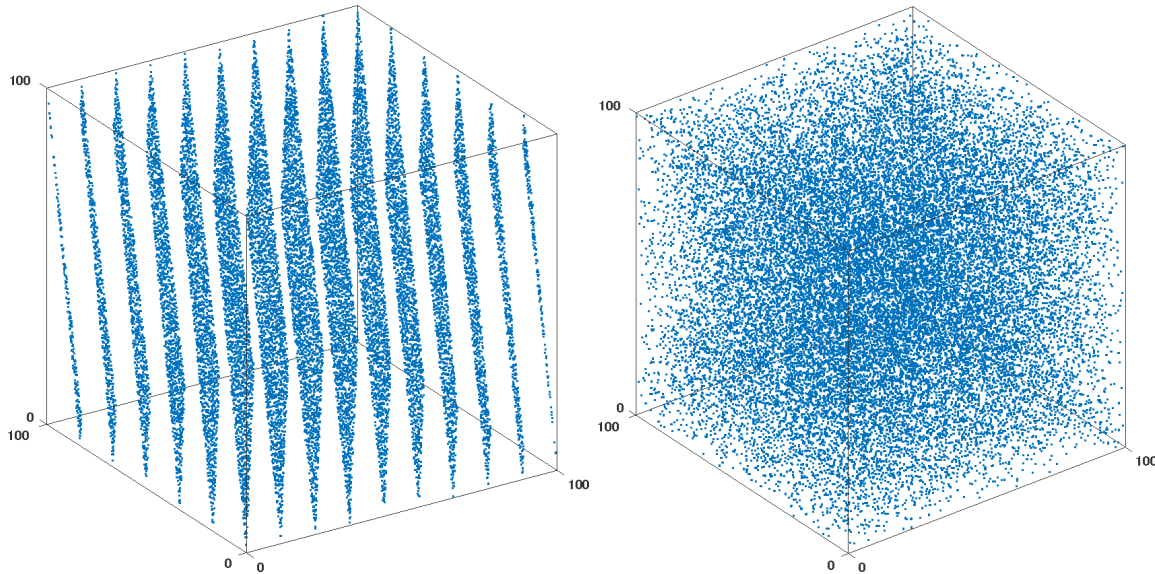


**Figure II.7** – Parking lot test performed over  $3 \times 10^4$  cars with two different generators: RANDU and Mersenne Twister (MT). A 3-dimensional distribution has been used to generate the coordinates  $(r_n, r_{n+1}, r_{n+2})$  to build the graphs. Only the non-overlapping cars, modelled by one unit length side squares, are plotted. *Left*: Result obtained for the RANDU random generator. It appears clearly a correlation between numbers because of the presence of fifteen two-dimensional stripes. The generated numbers are not random at all. *Right*: Results obtained with the MT algorithm. There is no sign of correlations between generated numbers because of the absence of striped patterns on the plot.

correlations between numbers [108]. In this case some striped patterns would appear. To illustrate this phenomenon, we plotted (Figure II.7) the results obtained after a parking lot test performed in three dimension with two different PRNG: the RANDU and the Mersenne Twister, both mentioned above.

As a conclusion illustrating the importance to perform Monte Carlo simulations with a *good* (*i.e.* in accordance with the criteria mentioned above) random numbers generator, one can read the Coddington’s analyses [33, 34] and the article of Parisi and Rapuano [150].

# Chapter III

## A toy model for the study of liquid crystals: the Mobile Potts model

### Contents

---

III.1	Introduction	38
III.2	Mobile Potts Model	39
III.3	Mean-Field Theory	40
III.3.1	Hamiltonian	40
III.3.2	Mean-Field Theory	41
III.4	Monte Carlo results	48
III.4.1	Transition	48
III.4.2	Effect of concentration	53
III.4.3	Surface sublimation	53
III.5	Conclusion	56

---

We introduce in this chapter an adaptation the well known Potts model. Indeed, the interaction between neighbouring spins is still ruled by the Potts Hamiltonian, but in our model the spins can move on free neighbouring site. We show here the results obtained after a mean-field analysis and also after Monte Carlo simulations.

### III.1 Introduction



Phase transition is a fascinating subject that has attracted an enormous number of investigations in various areas during the last fifty years. Much of progress has been achieved in the seventies in the understanding of mechanisms which characterize a phase transition: the renormalization group shows that the nature of a phase transition depends on a few parameters such as the space dimension, the symmetry of the order parameter and the nature of the interaction between particles [185, 3, 197].

There has been recently a growing interest in using spin systems to describe properties of dimers and liquid crystals [80]. Spin systems are used in statistical physics to describe various systems where a mapping to a spin language is possible. In two dimensions (2D) Ising-Potts models were studied extensively [188, 144, 94]. Interesting results such as hybrid transitions on defect lines were predicted with renormalization group and confirmed with Monte Carlo (MC) simulations [53]. Unfortunately, as for other systems of interacting particles, exact solutions can be obtained only for systems up to 2D with short-range interactions [9, 47]. We will focus in this chapter on the  $q$ -state Potts model in three dimensions (3D) where Bazavova *et al.* have recently shown precise results for various values of  $q$  for the localized Potts models [10]. High-temperature series expansions for random Potts models have been studied by Hellmund and co-workers [178]. Other investigations have been carried out on critical properties in the 3D site-diluted Potts model [140] and Potts spin glasses [87, 6, 73, 74, 68].

We are interested here in the problem of moving particles such as atoms or molecules in a crystal. To simplify, we consider the case of mobile  $q$ -state Potts spins moving from one lattice site to a nearby one. The  $q$  states express the number of internal degrees of freedom of each particle, such as molecular local orientations. We simulate the mobile 6-state Potts model on a cubic lattice. It is known that the pure Potts model in three dimensions undergoes a continuous transition for  $q = 2$  and a first-order transition for  $q=3, 4, \dots$ . We use here MC simulation and a theoretical analysis to elucidate properties of such a system. The mobility depends on the temperature. At low temperatures, all spins gather in a solid, compact phase. As the temperature increases, spins at the surface are detached from the solid to go to the empty space forming a gaseous phase. We show that the phase transformation goes through several steps and depends on the concentration of the Potts spins in the crystal.

The mobile Potts model presented here is expected to be equivalent to the dilute Potts model in as far as the bulk thermodynamics is concerned. The kinematics at the interface between the solid and the gas phases may be affected by the constraint that atoms move only to empty neighbouring cells in the mobile model as opposed to the case where atoms move to any other vacant cell in the diluted model.

At a sufficiently high concentration, spins are not entirely evaporated and the remaining solid core undergoes a transition to the orientationally disordered phase. We anticipate here that there is only one phase transition in the model, a first-order transition from higher-density (solid) phase with non-zero Potts order parameter to a lower-density phase with vanishing Potts order parameter. The sublimation observed below is analogous to surface melting, which in the melting of a solid can begin well below the bulk melting temperature. Details are shown and discussed in terms of surface sublimation and melting. We note in passing that direct studies of melting using continuous atomic motions are efficient for bulk melting [71, 72, 20] but they have often many difficulties to provide clear results for complicated situations such as surface melting (see references cited in Ref. [21]). Using discrete spin displacements as in the present model we show that bulk melting and surface sublimation can be clearly observed. We believe that these results bear essential features of real systems.

Section III.2 is devoted to the description of our mobile Potts model. The mobile Potts model is related to a diluted Potts model. The latter model is analysed within the mean-field approximation for bulk properties in section III.3 below. The two models are not identical. While in the mobile Potts model a spin can move to a void location nearby, in the diluted model there is no constraint on the proximity of the locations of the spin and the vacancy. The thermodynamics of two models may be identical in the long run, even though the kinematics may be different. Section III.4 is devoted to the presentation of MC simulation results. Concluding remarks are given in section III.5.

## III.2 Mobile Potts Model

We consider a lattice of  $N_L$  sites. A site  $i$  can be vacant or occupied at most by a Potts spin  $\sigma_i$  of  $q$  states:  $\sigma_i = 1, 2, \dots, q$ . Potts spins can move from one site to a neighbouring vacant site under effects of mutual spin-spin interaction and/or of temperature  $T$ . In order to allow for spin mobility, the number  $N_s$  of Potts spins should be smaller than  $N_L$ . Let us define the spin concentration  $c$  by  $c = N_s/N_L$ . The Hamiltonian is given by the Potts model:

$$\mathcal{H} = -J \sum_{\langle i,j \rangle} \delta_{\sigma_i, \sigma_j} \quad (\text{III.1})$$

where  $J$  is the interaction constant between nearest neighbours (NN), denotes the Kronecker delta and the sum is taken over NN spin pairs. To this simple Hamiltonian, we can add a chemical potential term when we deal with the system in the grand-canonical description [50] and an interaction term between neighbouring vacancies (see below).

The ground state (GS) of the system described by equation (III.1) is the one with the minimum of interaction energy: each spin maximizes the number of NN of the same values. As a consequence, all spins have the same value and form a compact solid. If the lattice is a

recipient of dimension  $N_x \times N_y \times N_z$ , then the GS is a solid with a minimum of surface spins (surface spins have higher energies than interior spins due to a smaller number of NN). In a recipient with  $N_x = N_y < N_z$  with periodic boundary conditions in the  $xy$  plane and close limits on the  $z$  direction for example, the free surface is the  $xy$  surface. We show in Figure III.1 such an example.

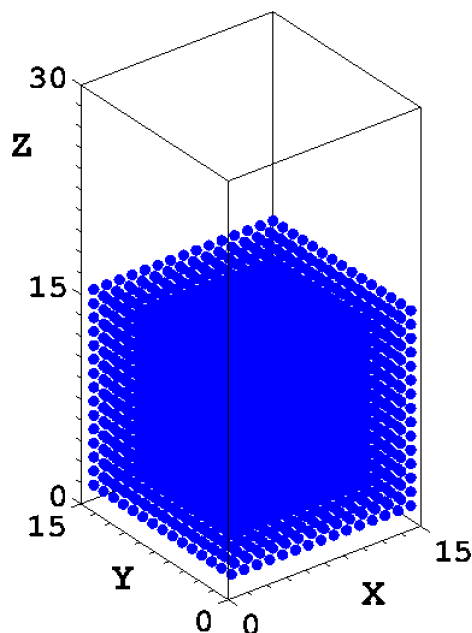


**Figure III.1** - Ground state (GS) of the system with  $N_x = N_y < N_z$ , where the interaction between nearest neighbours spins is ruled by a ferromagnetic Hamiltonian (6-Potts model here). A GS configuration is then reached when all the spins are stacked in the bottom of the recipient and have all the same state (in blue on the figure).

When  $T$  is increased, surface spins are detached from the solid to go to the empty space. At high  $T$ , the solid becomes a gas. The path to go to the final gaseous phase will be shown in this chapter. We start with the bulk case and examine the surface behaviour in what follows.

### III.3 Mean-Field Theory

In this section, we present the mean-field theory for the mobile Potts model. It is more convenient to work in the grand-canonical description. The results do not depend on the approaches for large systems [50]. To that end we consider a vacancy as a spin with value zero. The model becomes  $(q + 1)$ -state model. In addition, we add a chemical term in the Hamiltonian and rewrite it in a more general manner in the following.

#### III.3.1 Hamiltonian

We divide the space into  $M$  cells, of equal volume  $v$ , centred each on a site of a cubic lattice. Any cell is either vacant or occupied by a single particle characterized by a  $q$ -value spin.

neighbouring particles that have the same spin value get a lower interaction energy  $-J$  than if they have different spin values. Zero energy is assigned to neighbouring cells that have at least a vacancy. We assign an energy  $-K$  to neighbouring cells that are occupied irrespective of their spin values. In the grand canonical ensemble we allow for fluctuating number of particles and include in the Hamiltonian a single site (cell) term proportional to the chemical potential  $H$  if there is a particle at the cell. This model can be described by assigning at each site a  $(q + 1)$ -Potts spin  $\sigma = 0, 1, \dots, q$ . The zero value corresponds to vacancy while the values  $1, 2, \dots, q$  correspond to a particle having a spin. The Hamiltonian is

$$\begin{aligned}
 -\frac{\mathcal{H}}{k_B T} = & J \sum_{\langle i,j \rangle} \delta_{\sigma_i, \sigma_j} \left[ 1 - \delta_{\sigma_i, 0} \right] \left[ 1 - \delta_{\sigma_j, 0} \right] \\
 & + K \sum_{\langle i,j \rangle} \left[ 1 - \delta_{\sigma_i, 0} \right] \left[ 1 - \delta_{\sigma_j, 0} \right] \\
 & + H \sum_i \left[ 1 - \delta_{\sigma_i, 0} \right], \tag{III.2}
 \end{aligned}$$

where the two first sums are performed over all the NN and the third one over each site. This corresponds to the grand canonical ensemble: fixed temperature  $T$ , chemical potential  $H = \mu/k_B T$  and volume  $V$ .

### III.3.2 Mean-Field Theory

The mean-field theory of the diluted Potts model [95] is exact for the equivalent-neighbour lattice. The thermodynamic grand potential  $\Phi$  divided by  $N_c$  is proportional to the pressure:

$$-pv = \frac{\Phi}{N_c} = -k_B T \frac{\ln \mathcal{Z}}{N_c} = k_B T \min(\Psi) \tag{III.3}$$

where

$$\Psi = \frac{J}{2} \left( \sum_{\sigma=1}^q m_\sigma^2 \right) - \ln \left( 1 + \sum_{\sigma=1}^q e^{Jm_\sigma + H} \right). \tag{III.4}$$

Obviously,  $\min(\Psi)$  represents the free energy of the system. The two main tricks to determine  $\Psi$  [95] are to write the grand partition function  $\mathcal{Z}$  as a Gaussian integral (Hubbard-Stratonovich transformation) and to apply the saddle point method. Note also that the above equations are for  $K = 0$  and that the minimum of  $\Psi = \ln \mathcal{Z}/N_c$  is taken because we are at the equilibrium. The optimization equations are

$$m_\sigma = \frac{e^{Jm_\sigma + H}}{1 + \sum_{\ell=1}^q e^{Jm_\ell + H}}, \tag{III.5}$$

for  $\sigma = 1, \dots, q$ . The  $m_\sigma$  gives the average number of particles of spin  $\sigma$  normalized by the total number of sites (cells)  $N_c$ . The number of particles normalized by  $N_c$  is

$$n = \sum_{\sigma=1}^q m_\sigma = \sum_{\sigma=1}^q \frac{e^{(Jm_\sigma+H)}}{1 + e^{(Jm_1+H)} + e^{(Jm_2+H)} + \dots + e^{(Jm_q+H)}}. \quad (\text{III.6})$$

Assuming the ordering of the Potts spin to occur in state 1, we parameterize<sup>(1)</sup> the  $m_\sigma$ 's as follows

$$m_1 = \frac{n}{q} + (q-1)m \quad \text{and} \quad m_2 = m_3 = \dots = m_q = \frac{n}{q} - m, \quad (\text{III.7})$$

where  $m$  is the local dimensionless magnetisation. The optimization equation (III.6) is now

$$\begin{aligned} n &= \frac{e^{J(\frac{n}{q}+(q-1)m)+H} + (q-1)e^{J(\frac{n}{q}-m)+H}}{e^{J(\frac{n}{q}+(q-1)m)+H} + (q-1)e^{J(\frac{n}{q}-m)+H} + 1}, \\ &= \frac{e^{J(\frac{n}{q}-m)+H}(e^{Jqm} + q - 1)}{e^{J(\frac{n}{q}-m)+H}(e^{Jqm} + q - 1) + 1} \end{aligned} \quad (\text{III.8})$$

and starting from (for instance)

$$m_q = \frac{n}{q} - m, \quad (\text{III.9})$$

the optimization equation (III.5), by inserting equation (III.7) in it, becomes now

$$\begin{aligned} \frac{mq}{n} &= 1 - \frac{qm_q}{n}, \\ &= 1 - \left[ \frac{e^{J(\frac{n}{q}-m)+H}(e^{Jqm} + q - 1)}{e^{J(\frac{n}{q}-m)+H}(e^{Jqm} + q - 1) + 1} \right]^{-1} \frac{q e^{J(\frac{n}{q}-m)+H}}{e^{J(\frac{n}{q}-m)+H}(e^{Jqm} + q - 1) + 1} S, \\ &= \frac{e^{Jqm} - 1}{e^{Jqm} + q - 1}. \end{aligned} \quad (\text{III.10})$$

In the following we denote  $X = qm/n$ . The energy  $u$  scaled by  $N_c$ , number of cells, is

$$\begin{aligned} u &= -\frac{1}{2} \sum_{\sigma=1}^q m_\sigma^2, \\ &= -\frac{1}{2} \frac{e^{2J(\frac{n}{q}-m)+2H}(e^{2Jqm} + q - 1)}{\left(1 + \sum_{\ell=1}^q e^{Jm_\ell+H}\right)^2}, \\ &= -\frac{1}{2} \frac{e^{2Jqm} + q - 1}{(e^{Jqm} + q - 1)^2} n^2. \end{aligned} \quad (\text{III.11})$$

<sup>(1)</sup>Such as the  $m_\sigma$  satisfy the condition:  $\sum_{\sigma=1}^q m_\sigma = 1$ .

In order to express the energy in function of  $X$ , we look for a second-order polynomial such as

$$\alpha X^2 + \beta X + \gamma = \frac{e^{2Jqm} + q - 1}{(e^{Jqm} + q - 1)^2}, \quad (\text{III.12})$$

where  $X$  is given by equation (III.10). By identification, we determine the coefficients  $\alpha, \beta$  and  $\gamma$  giving thus

$$\alpha = 1 - \frac{1}{q}, \beta = 0 \text{ and } \gamma = \frac{1}{q}, \quad (\text{III.13})$$

and it comes finally that

$$u = -\frac{1}{2} \frac{n^2}{q} [(q-1)X^2 + 1]. \quad (\text{III.14})$$

The specific heat at fixed number of particles  $n$  is

$$C_v = \frac{\partial u}{\partial T} = -n^2 \frac{q-1}{2q} \frac{\partial X^2}{\partial T}. \quad (\text{III.15})$$

The second optimization equation, equation (III.8), provides a formula for the chemical potential, since  $H = \mu/T$ . Thus, by taking the natural logarithm of  $n$ , we get

$$H = \ln \left( n \left[ e^{J(\frac{n}{q}-m)+H} (e^{Jqm} + q - 1) + 1 \right] \right) - \ln (e^{Jm} + q - 1) - J \frac{n}{q} \left( 1 - \frac{qm}{n} \right) \quad (\text{III.16})$$

and by noticing that

$$\frac{1}{1-n} = e^{J(\frac{n}{q}-m)+H} (e^{Jqm} + q - 1) + 1 \quad \text{and} \quad \frac{1-X}{q} = \frac{1}{2} e^{Jqm} + q - 1, \quad (\text{III.17})$$

it comes

$$\mu = T \ln \left( \frac{n}{1-n} \right) + T \ln \left( \frac{1-X}{q} \right) - \frac{n(1-X)}{q}, \quad (\text{III.18})$$

by setting  $J = 1/T$ . The pressure  $p$  is obtained from equation (III.3). Thanks to the expression of the energy  $u$  and the equation (III.17), we reach

$$pv = -\frac{n^2}{2q} [1 + (q-1)X^2] - T \ln(1-n). \quad (\text{III.19})$$

Note in the disordered (gas) phase  $X = 0$  and  $n \ll 1$ . The equation of state reduces to the ideal gas equation  $pv = nT$ . The entropy  $S$  normalized by  $M$  is obtained from the thermodynamic Euler equation

$$S = \frac{u + pv - \mu n}{T}, \quad (\text{III.20})$$

$$= -n \ln(n) - (1-n) \ln(1-n) - n \ln \left( \frac{1-X}{q} \right) - \frac{n^2}{qT} [(q-1)X^2 + X]. \quad (\text{III.21})$$

The model exhibits a first-order phase transition tied to the Potts  $q$ -state transition. In Figure III.2 we show  $n$  by curve 1 (red) and the order parameter  $Q = qm$  (see equation III.10) by curve 2 (blue) as functions of  $T$  for fixed chemical potential  $\mu = -0.4$  (Figure III.2b). Increasing the chemical potential reduces the discontinuity in  $n$  as seen for  $\mu = -0.3$  (Figure III.2a). While, decreasing the chemical potential below  $\mu = -0.5$  destroys order at all temperatures as seen for  $\mu = -0.51$  (Figure III.2c).

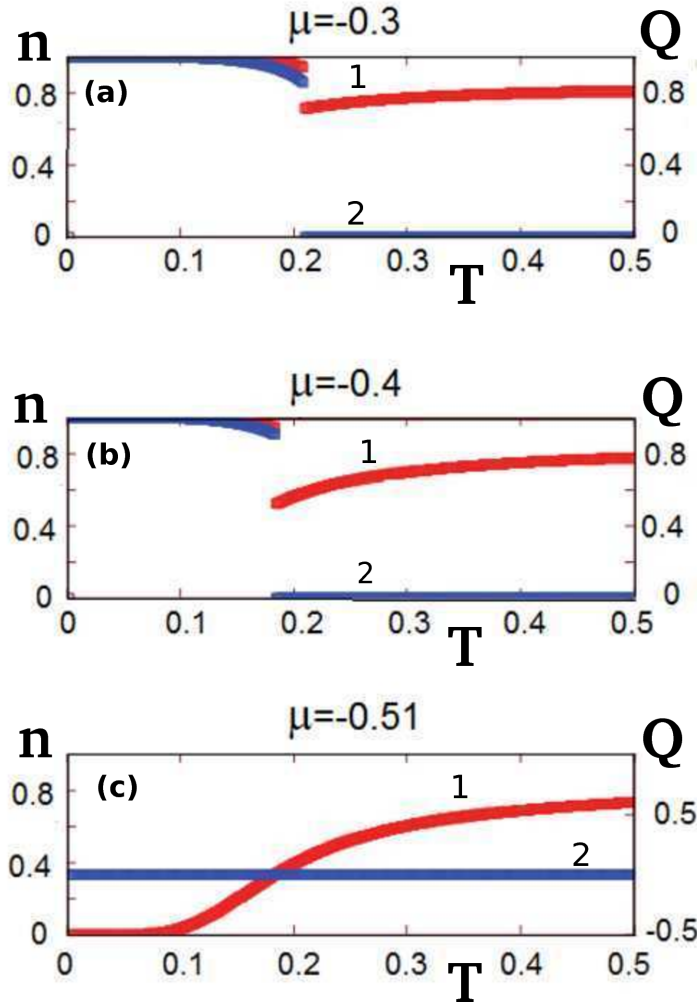


**Figure III.2** - Average number of particles per site  $n$  (curve 1, red, left scale) and order parameter  $Q = qm$  (curve 2, blue, right scale) versus temperature  $T$  for different chemical potential  $\mu$ : (a)  $\mu = -0.3$ , (b)  $\mu = -0.4$ , (c)  $\mu = -0.51$ . For small  $\mu$ , the order parameter show a discontinuity (first-order phase transition) that is reduced when  $\mu$  is increased, while decreasing  $\mu$  destroys totally the order. Indeed for  $\mu = 0.51$  the order parameter is constant and equal to zero.

This is understood by comparing the energy of any pair  $(i, j)$  in the ordered (solid) phase  $E_{i,j} = J + 2H$  to the energy in the disordered (gaseous) phase  $E_{i,j} = 0$ . The two energies cross when  $H = -0.5J$ , or when  $\mu = -0.5$ .

The phase diagram in the  $(T, \mu)$  plane shown in Figure III.3 includes an ordered (solid)

phase (low  $T$  and high  $\mu$ ) and a disordered (gas) phase. The two phases are separated by a line of first-order transitions. In the limit of large chemical potential the number of

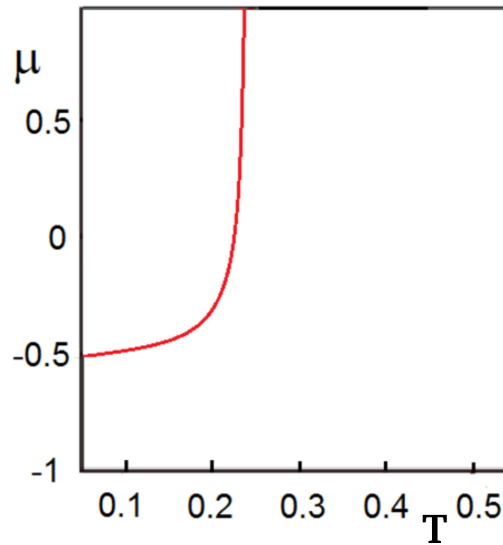


**Figure III.3** - Phase diagram in the plane  $(T, \mu)$ . The solid red line is a first-order transition line. Above this line, *i.e.* low temperature  $T$  and high chemical potential  $\mu$ , the system is in an ordered phase (solid), while under the red line, it corresponds to a disordered phase (gas).

vacancies becomes negligible and thus the model reduces to the  $q$ -state Potts model. As a result the transition line approaches  $T = 0.25$ .

The phase diagram in the temperature-pressure plane is shown in Figure III.4. The zone above the red line corresponds to the region in which the system is in a solid phase. While below this line, the system is in a gaseous phase (high temperature region).

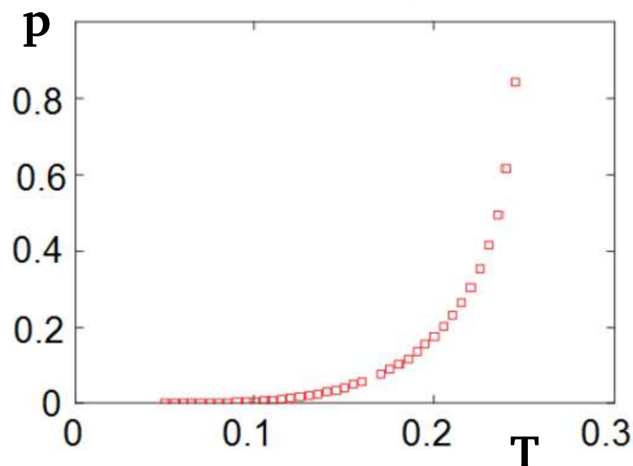


**Figure III.4** - Phase diagram in the plane  $(T, p)$ . The red line brands the separation between the solid phase (above the line; low temperature and high temperature) and the gas phase (below the line; high temperature).

Isotherms pressure  $p$  versus  $n$  are shown in Figure III.5. For  $T = 0.25$  there is no phase

transition while for  $T = 0.23, 0.2, 0.18$  the first-order transitions line is crossed. As a result, we see the gap in the density  $n$ . The higher  $n$  branch corresponds to the ordered solid. Note that the solid exists only for  $n$  large enough ( $n > 0.95$ ). In other words the presence of 5% vacancies destroys the solid. This is summarized in the phase diagram in the  $(T, n)$

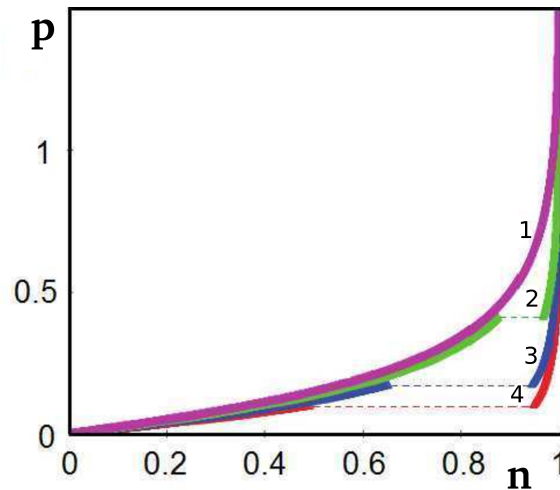


**Figure III.5** - Isotherms  $(p, n)$  are shown by thick curves for  $T = 0.25$  (curve 1, **violet**),  $0.23$  (curve 2, **green**),  $0.2$  (curve 3, **blue**) and  $0.18$  (curve 4, **red**). Thin broken lines indicate discontinuities of  $n$ . The system exhibits a first-order phase transition for  $T < 0.25$ . The higher  $n$  branch corresponds to a solid phase while the lower branch to a gas.

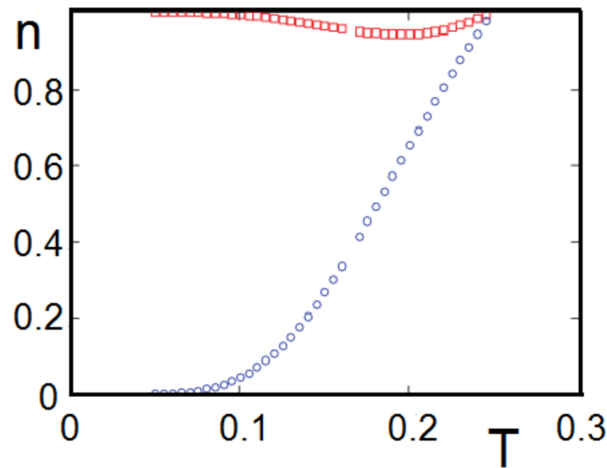


**Figure III.6** - Phase diagram in the plane  $(T, n)$ . The **red** squares and **blue** circles lines represent the densities of the solid and of the gas, respectively. The region between the **red** line and the **blue** line correspond to a solid phase. Below the **blue** line, *i.e.* at high temperature, the system is in gaseous phase. The coalescence point occurs at  $T = 0.25$  and corresponds to the infinite chemical potential limit, *i.e.* no vacancies.

plane shown in Figure III.6. The two lines represent the densities of the solid (**red** squares) and of the gas (**blue** circles). The two branches coalesce at a temperature of  $0.25$ . Note that this is not a critical point but the end of the thermodynamic space as it occurs in the limit of infinite chemical potential (*i.e.* no vacancies).

### III.3. Mean-Field Theory

Entropy and energy versus temperature and chemical potential are shown in Figure III.7. The fundamental equation, chemical potential as a function of temperature and pressure, is concave as required by the second law of thermodynamics (thermodynamic stability). It is a continuous function and the first-order transitions manifest as discontinuities in slope of the chemical potential when graphed against temperature and pressure (Figure III.8).

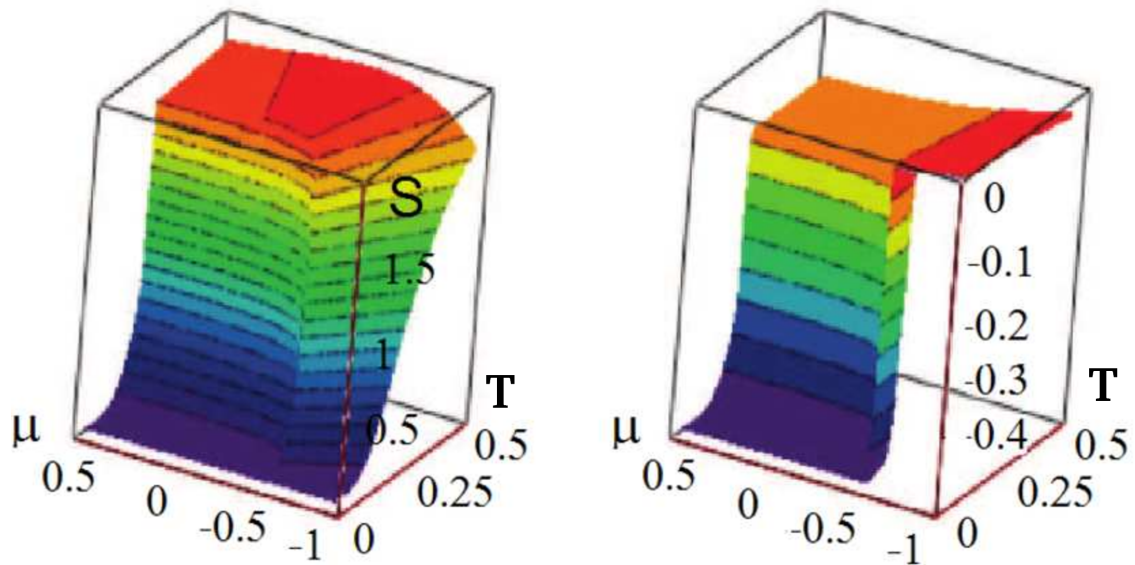


**Figure III.7** - Entropy (*left*) and energy (*right*) as functions of temperature and chemical potential. Note that the entropy is a concave function, which is in accord with the second law of thermodynamics. Indeed, the equilibrium of a system is reached when the entropy is maximal.

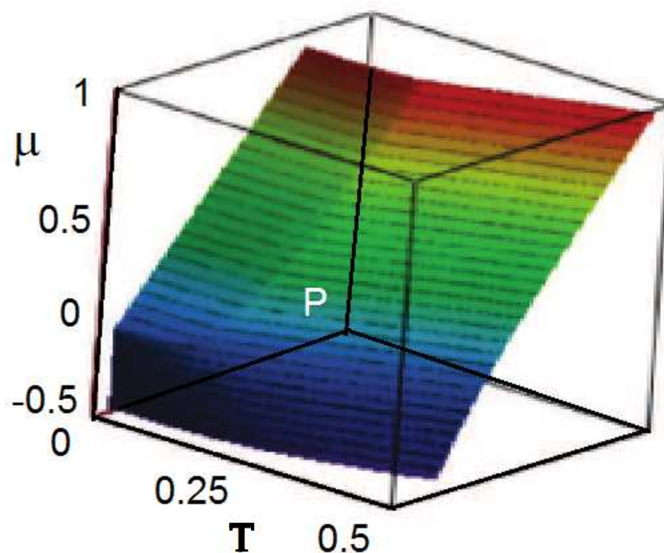


**Figure III.8** - Surface in the space *temperature*  $T$ , *pressure*  $P$  and *chemical potential*  $\mu$ . The discontinuity in slope of  $\mu$  is sign of first-order transition.

## III.4 Monte Carlo results

In this section, we present our results from MC simulations. The method has been largely described in the chapter II. Note that in our simulations, we used  $10^5$  MCS/spin to equilibrate the system before averaging physical quantities over the following  $10^6$  MCS/spin. We have verified that longer MC run times do not change the results. We used various system sizes and shapes to examine finite-size and shape effects on the results.

### III.4.1 Transition

We study here the melting behaviour of a solid contained in a recipient described in section III.2. The recipient has the dimension  $N_x = N_y < N_z$  and is filled with molecules (Potts spins) in the lower part of the recipient. The number of filled layers is smaller than  $N_z$  (Figure III.1). Molecules under thermal effect can be evaporated from the upper surface to the empty space. To study the behaviour of such a system, we choose to heat the system from low to high  $T$ . Cooling the system from a random initial configuration, namely molecules in a gas state with positions distributed over all space, will result in a compact solid phase at low temperature but the surface of this solid is not so flat so that the system energy is about 5% higher than the GS energy shown in Figure III.1. However, the system behaviour at higher  $T$  as well as the phase transition are the same as obtained by heating. We will show this later.

Let us show now results for a lattice of  $15 \times 15 \times 30$  sites where only the fifteen first layers in the  $z$  direction are filled ( $c = 50\%$ ) in the GS configuration shown in Figure III.1. As said above, this configuration corresponds to the one with a minimal free surface when the system is in the solid state.

Our simulation in real time shows that when  $T$  increases atoms on the surface are progressively evaporated. The solid core of the system remains in a Potts spin order, though its volume is little by little reduced with increasing  $T$ . At a high enough value of  $T$ , say  $T_c$ , the Potts orientational order of the solid core is broken. However, the spins still stay in the solid state up to a very high  $T$  when the whole system melts to a gas (or liquid) phase. We will show later evidence of such a change of the system at several  $T$  with snapshots and corresponding distributions of the NN number.

The magnetisation  $M$  versus  $T$  is displayed in Figure III.9 and is defined as follow [49]

$$M = \frac{1}{q-1} \left[ \frac{q}{N_s} \max_{j \in [1,q]} \left( \sum_{i=1}^{N_s} \delta_{j,\sigma_i} \right) - 1 \right]. \quad (\text{III.22})$$

For an ordered system, *i.e.* containing only one kind of spin  $\sigma$ ,  $M = 1$  while for a disordered system  $q$  kinds of spins are present in the same proportion  $1/q$ , then  $M = 0$ .

$M$  in Figure III.9 indicates a perfect order at low  $T$ . When  $T$  is increased  $M$  decreases linearly with  $T$ : a careful examination of the system dynamics reveals that this regime corresponds to the evaporation of surface spins. This regime ends with a discontinuity of  $M$  at a transition temperature  $T_c \simeq 1.234$ .

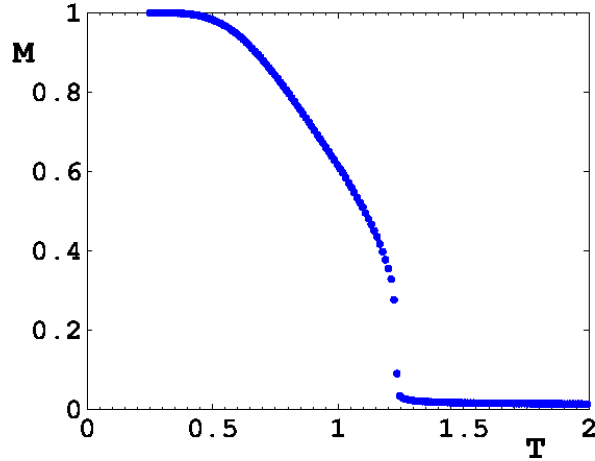


**Figure III.9** - Magnetization  $M$  versus temperature  $T$  (in unit of  $J/k_B$ ) for a lattice of  $15 \times 15 \times 30$  sites with a spin concentration  $c = 50\%$ . The system is completely ordered at  $T = 0$ , then surface spins are little by little evaporated with increasing  $T$ . The phase transition of spin orientations of the solid core occurs at  $T_c \simeq 1.234$ .

The discontinuity at  $T_c$  indicates a first-order phase transition. We have verified this by recording the energy histogram  $P(U)$  at the transition temperature  $T_c = 1.234$ . The double-peak structure shown in Figure III.10 confirms the first-order character of the transition. Note that disordered evaporated atoms, namely atoms outside the system solid core, do not participate in the transition.

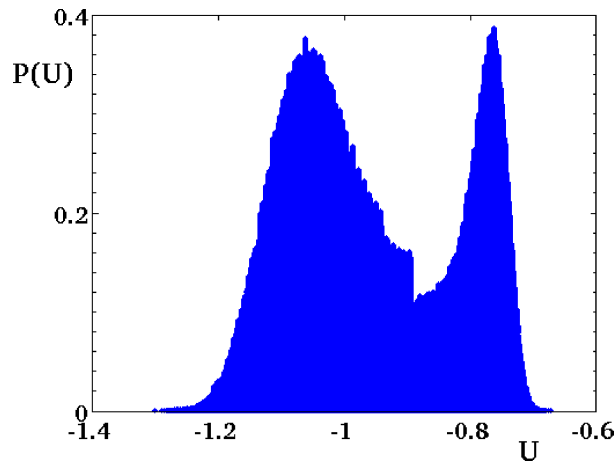


**Figure III.10** - Energy histogram  $P(U)$  recorded at  $T_c = 1.234$  for a lattice  $15 \times 15 \times 30$  with concentration  $c = 50\%$ . It represents the probability  $P$  of observing a state of energy  $U$ . The presence of the two peaks, *i.e.* two co-existing phases, indicates that the transition is of first-order.

We have studied the finite-size effect on the transition at  $c = 50\%$ . Since the shape of the recipient has a strong effect on the phase transition as seen below, we have kept the same recipient shape to investigate the finite-size effect: to compare results at the same concentration with those of the lattice  $15 \times 15 \times 30$  sites, we have used lattices of  $10 \times 10 \times 20$ ,  $20 \times 20 \times 40$ ,  $25 \times 25 \times 50$ ,  $30 \times 30 \times 60$  and  $35 \times 35 \times 70$  sites in which half of the recipient is filled with spins, namely  $c = 50\%$ . In Figure III.11 the magnetisation, the energy, the specific heat and the magnetic susceptibility versus  $T$  for several sizes is shown.

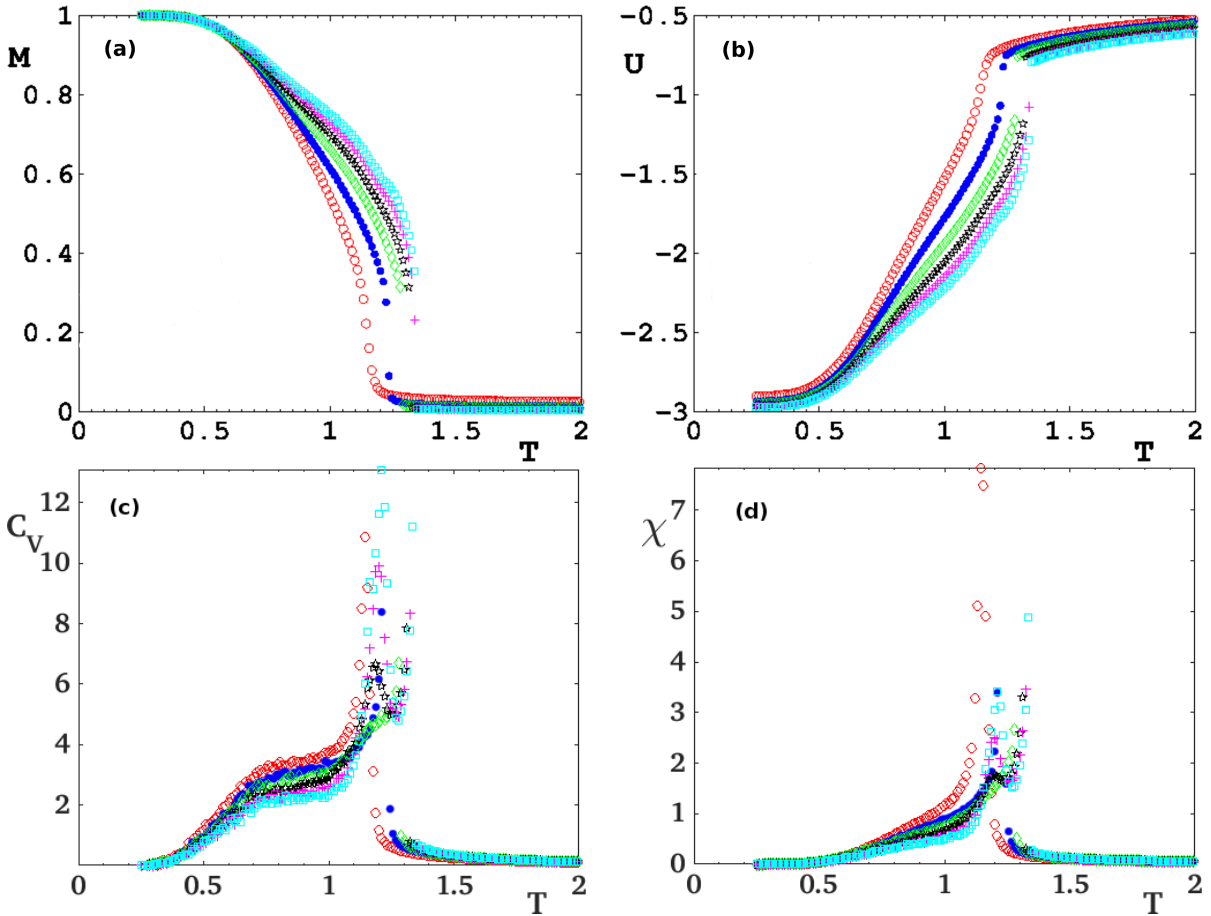


**Figure III.11** – Comparison of the evolution of (a) the magnetisation  $M$ , (b) the energy per spin  $U$ , (c) the specific heat  $C_V$  and (d) the magnetic susceptibility  $\chi$  versus the temperature of a half-filled lattice  $N_x \times N_y \times N_z$  for several sizes  $N_x = N_y = N_z/2 = 10$  (red void circles), 15 (blue filled circles), 20 (green void diamonds), 25 (black stars), 30 (magenta crosses) and 35 (sky-blue void squares). For the small box, *i.e.* for  $N_x = 10$ , the transition looks like to a second-order phase transition because of the finite-size effect, while for the other sizes of box the discontinuities suggest first-order transitions.

Figure III.11 shows that the transition looks like a second-order transition when the size of the box is small. This is a well-known finite-size effect: when the linear size of a system is smaller than the correlation length at the transition, the system behaves as a second-order transition. We have to use therefore a finite-size scaling to ensure that the transition is of first-order. To do this, let us show the transition temperatures for systems at various sizes

in Figure III.12. By fitting simulation results with the finite-scaling formula

$$T_c(L) = T_c(\infty) + \frac{A}{L^\alpha}, \quad (\text{III.23})$$

we find the following best non-linear least mean square fit with the relative change of the last (8th) iteration less than  $-1.30954 \times 10^{-10}$ , such as

$$T_c(\infty) = 1.35256 \pm 0.004089 \quad (0.3023\%), \quad \alpha = 2.9, \quad (\text{III.24})$$

$$A = -2335.24 \pm 170.9(7.316\%). \quad (\text{III.25})$$

This is shown by the continued line in Figure III.12.

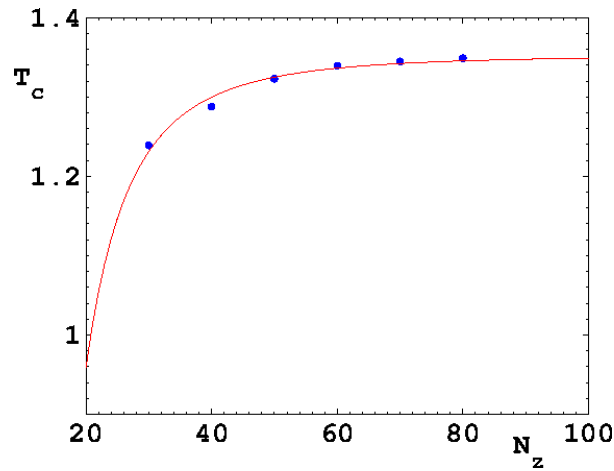


**Figure III.12** - Transition temperature versus lattice size  $N_x \times N_y \times N_z$  at concentration  $c = 50\%$  where  $N_x = N_y = N_z/2$ , with  $N_z = 30, 40, 50, 60, 70$  and  $80$ .

Several remarks can be made concerning these results:

- The value of  $\alpha$  indicates that, within statistical errors,  $T_c(L)$  does scale with the system volume  $L^3$  as it should for a first-order transition [7, 10],
- Our value of  $T_c(\infty)$  is in excellent agreement with that found for the localized model

$$T_c = 1.35242 \pm 0.00001, \quad (\text{III.26})$$

obtained with the state-of-the-art multi-canonical method [10] with periodic boundary conditions in three directions (note that in the original paper the authors have used a factor 2 in the Hamiltonian),

- The fact that our system follows the same finite-size scaling as the localized model confirms that the transition observed in our mobile model is triggered by the orientational disordering of Potts spins in the remaining solid core at the transition temperature.

Following the last argument, it is then obvious that if the quantity of matter remaining in the solid phase is so small due to the evaporation, then there is no transition. This should be seen if we lower the concentration.

Before showing the effect of concentration, let us show a snapshot in the case of  $c = 50\%$  in Figure III.13. The transition scenario discussed above is seen in these snapshots: the observed transition is that of Potts orientational order in the solid core. Note that unlike the

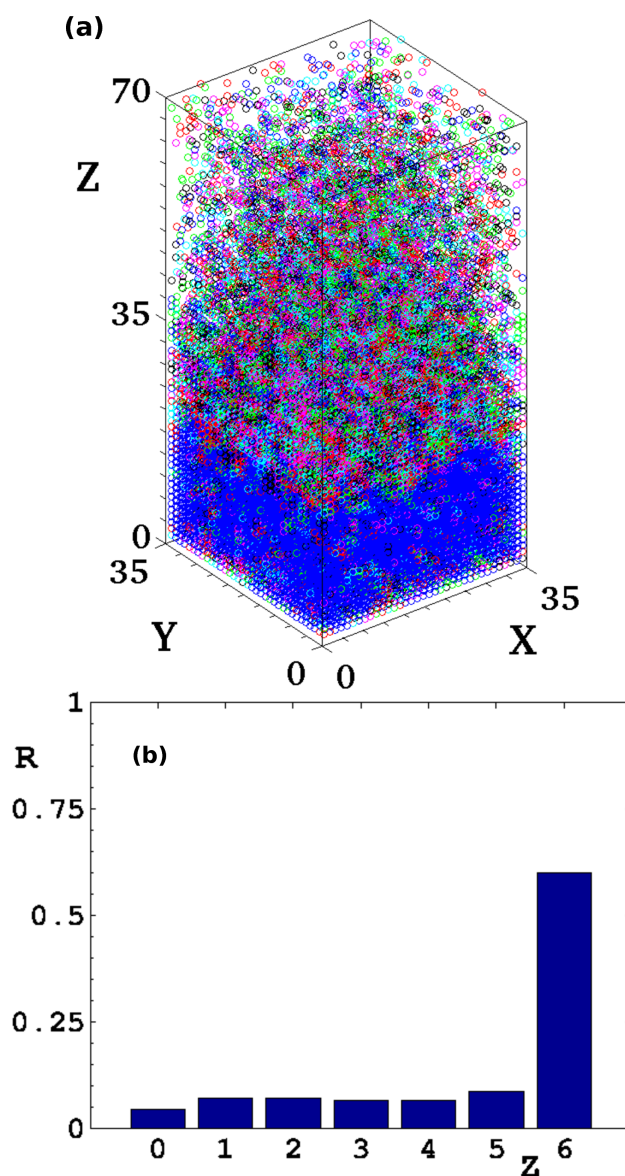


**Figure III.13** - Simulation for a half filled lattice size  $35 \times 35 \times 70$  (concentration  $c = 50\%$ ): (a) Snapshot of the system at  $T = 1.3128$  close to the transition. Each color corresponds to a spin state. *i.e.* to a specific orientation. (b)  $R$  vs  $Z$ ,  $R$  being the percentage of lattice sites having  $Z$  nearest neighbours, at  $T = 1.3128$ . Note that the solid phase is well indicated by the number of sites with 6 neighbours.

crystal melting where atoms suddenly quit their low- $T$  equilibrium positions to be in a liquid state, our model shows that the passage to the gaseous phase takes place progressively

with slow evaporation, atom by atom, with increasing  $T$ .

Before showing the concentration effect let us compare results of heating and cooling. As said above, cooling the system from an initial configuration where molecules are distributed at random over the whole space results in a compact solid phase at low  $T$  shown in Figure III.1. However, this is realized only if we do a slow cooling: the final configuration at a temperature is used as initial configuration for a little bit lower temperature and so on. A rapid cooling will result in a solid with an irregular form having flat surfaces of various sizes.

### III.4.2 Effect of concentration

Let us examine now results of simulations with smaller concentrations. The absence of the phase transition is seen when we decrease the concentration down to  $c = 20\%$ . As we can see in Figure III.14, at low temperatures, in all cases the system is in a condensed state. As  $T$  increases, the magnetisation decreases faster at lower concentrations. All atoms are evaporated for small concentrations below the Potts transition temperature. Note, however,

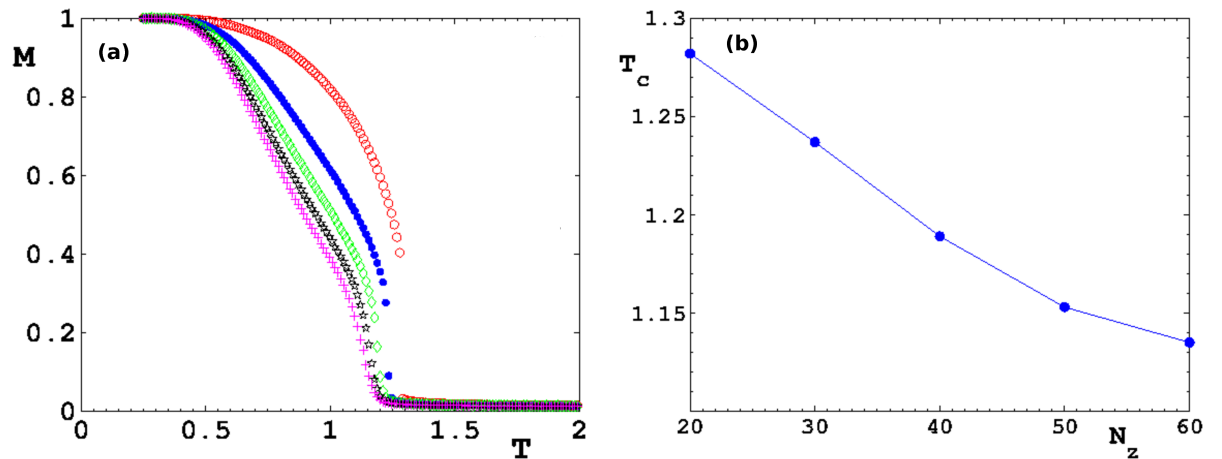


**Figure III.14** – Effect of concentration: (a) Magnetization versus temperature for a lattice  $15 \times 15 \times N_z$  where  $N_z = 20$  (red void circles), 30 (blue filled circles), 40 (green diamonds), 50 (black stars), 60 (magenta crosses). For each case, only the fifteen first layers are filled, corresponding to concentrations  $15/N_z$ . (b) Transition temperature versus the recipient height  $N_z$ .

that for low concentrations, there is no transition but the magnetisation disappears only when the very small solid core disappears, namely at  $T \simeq 1.1$ .

### III.4.3 Surface sublimation

Let us show the results using the system size  $20 \times 20 \times 40$  with 50%. To appreciate the surface sublimation, we show also the results of the localized model where spins stay each on its site. Figure III.15 shows the total magnetisation and the energy per spin.

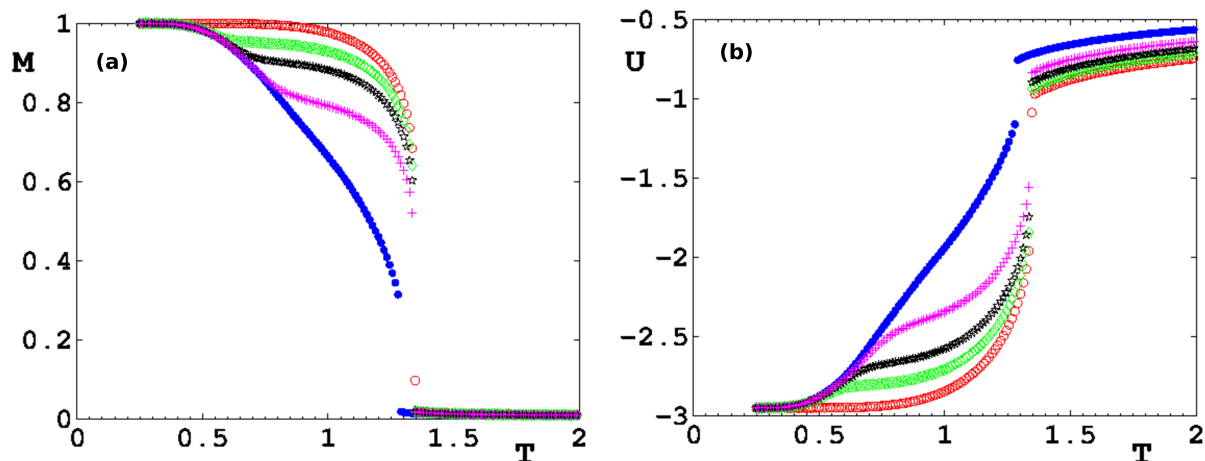


**Figure III.15** - (a) Total magnetisation  $M$  and (b) energy per spin  $U$  versus  $T$ . **Red** void circles indicate results of localized spins and **blue** filled circles indicate those of the completely mobile model. Between these two limits, **green** void diamonds, **black** stars and **magenta** crosses correspond respectively to the cases where one, two and four surface layers are allowed to be mobile.

We show in Figure III.16 the diffusion coefficient  $D$  for the cases where one, two and four layers are allowed to be mobile.  $D$  is defined as the cumulative sum of the displacement's distance between the new and the old position (at each MC step) of a spin. The sum is performed over all the spin. As seen, the evaporation is signalled by the change of curvature of  $D$ . Only when all layers are allowed to be mobile that the transition becomes really of first-order with a discontinuity.

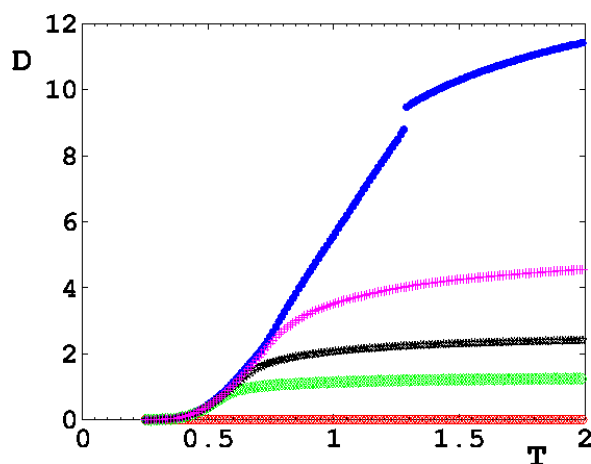


**Figure III.16** - Diffusion coefficient  $D$  versus  $T$ . **Red** void circles (lowest curve) indicate results of localized spins and **blue** filled circles (topmost curve) indicate those of the completely mobile model. Between these two limits, from below **green** void diamonds, **black** stars and **magenta** crosses correspond respectively to the cases where one, two and four surface layers are allowed to be mobile.

The magnetic susceptibility and the heat capacity are shown in Figure III.17 where the same observation is made: only when all layers are allowed to be mobile that the sublima-

tion is a first-order transition. Note that the small peaks at low  $T$  correspond to the surface evaporation.

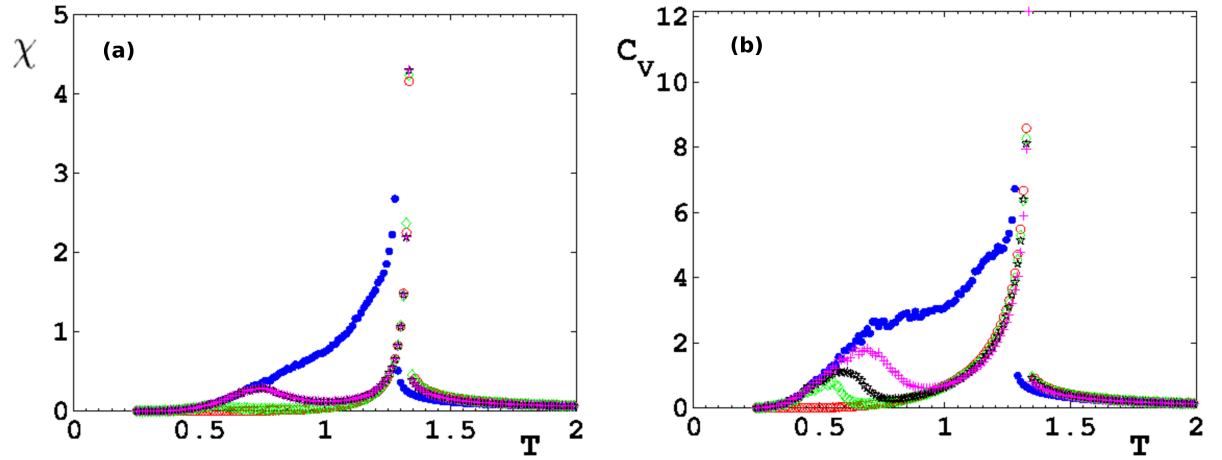


**Figure III.17** – (a) Magnetic susceptibility  $\chi$  and (b) heat capacity  $C_V$  versus  $T$ . **Red** void circles indicate results of localized spins and **blue** filled circles indicate those of the completely mobile model. Between these two limits, **green** void diamonds, **black** stars and **magenta** crosses correspond respectively to the cases where one, two and four surface layers are allowed to be mobile.

We show in Figure III.18 the layer magnetisation for the first four layers in the cases where four surface layers are mobile. As seen, the layer next to the solid substrate is *retained* by the latter up to the bulk transition occurring at  $T_c \simeq 1.330$ . Other layers are evaporated starting from the first layer, at temperatures well below  $T_c$ .

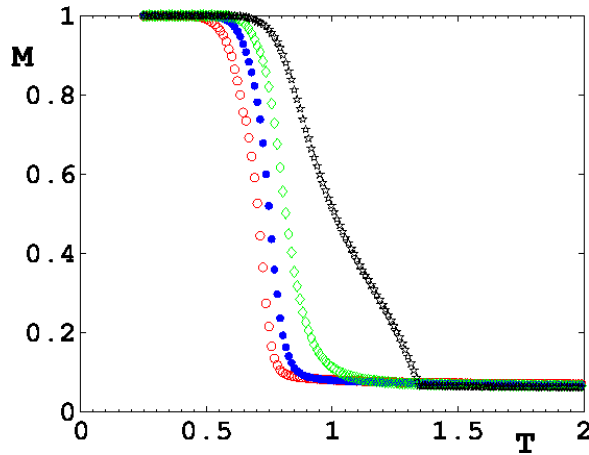


**Figure III.18** – Layer magnetisations for the first four layers: **red** void circles, **blue** filled circles, **green** diamonds and **black** stars are the magnetisations of the first, second, third and fourth layers, respectively. The solid *retains* the fourth layer, *i.e.* the closest to the solid, up to the bulk transition that occurs at  $T_c = 1.330$ . The three other layers on the top evaporate at temperature well below  $T_c$ . They are not retained by the first layer.

To close this section let us compare the results obtained for two system shapes  $20 \times 20 \times 40$  and  $40 \times 20 \times 20$  with concentration  $c = 50\%$ . It is obvious, when we look at the Figure

III.19, that the second shape has a larger free surface which facilitates the evaporation. As a consequence, there is no first-order transition because the solid core disappears at a temperature lower than the Potts transition temperature  $T_c \simeq 1.330$  at the size  $20 \times 20 \times 40$ .

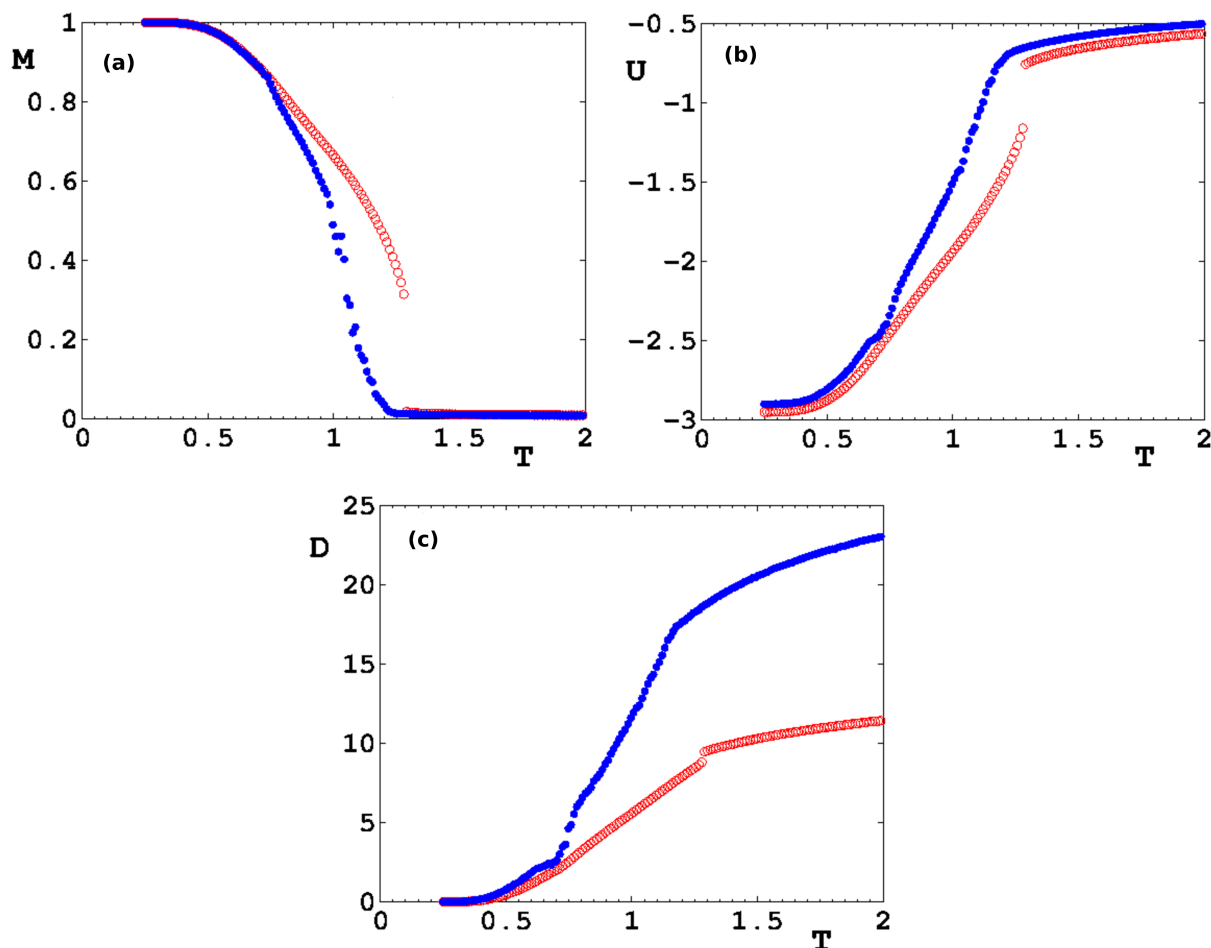


**Figure III.19** - (a) Magnetization, (b) energy and (c) diffusion coefficient for two system shapes  $20 \times 20 \times 40$  (red void circles) and  $40 \times 20 \times 20$  (blue filled circles) at concentration  $c = 50\%$ . It appears clearly, there is no phase transition for the *lying box*  $40 \times 20 \times 20$ , because this kind of shape offers a larger free surface.

## III.5 Conclusion

In this chapter, we studied the properties of the mobile Potts model by the use of a mean-field theory and Monte Carlo simulations. The two methods confirm the first-order character of the phase transition in the bulk with  $q = 6$ . As discussed in the Introduction, the mean-field approach does not consider the real-time dynamics of the particles on the lattice sites. Rather, it considers the average numbers of particles per site. In other words, it is equivalent to taking the spatial average first before considering the interaction between the particles uniformly distributed on lattice sites. Such a mean-field average is often used while

dealing with disordered systems (dilution, bond-disorder, ...). In MC simulations, the local environment of each particle is first taken into account before calculating its average over all particles. During the MC averaging, all local situations are expected to be taken into account in the final results. Hence the mean-field approximation takes the spatial average before the ensemble average, while in MC simulations the calculation is first done for each spatial particle configuration and the statistical average is next made over configurations. Furthermore the mean field approximation is applied to the diluted Potts model which is somewhat different than the mobile Potts model. In the MC simulations of the mobile Potts model a particle can be moved to a nearby vacant site while in the diluted Potts model a particle could be moved to a vacant site anywhere on the lattice. This difference is expected to be important for the kinetics but not for the thermodynamics of the two models.

From a finite-size scaling we showed that the transition of an evaporating solid belongs to the  $q = 6$  localized Potts model. The reason is that a portion of the low- $T$  solid phase of the mobile Potts model still remains solid at the transition temperature of the localized Potts model so that the orientational disordering of Potts spins occurs in this solid portion before the complete melting. Mean-field results for various parameters in the phase space are shown and discussed. In particular, we showed that there exists a threshold value of the chemical potential above which there is a solid-gas transition. Monte Carlo simulations have been carried out to study the surface evaporation behaviour: we found that atoms are evaporated little by little from the surface at temperatures much lower than the bulk transition. We believe that the model presented in this chapter, though simple, possesses the essential evaporation properties.

In the next chapter, we are interested in the generation of specific topological phases whose vortices. This study is completed successfully with a model based on Dzyaloshinskii-Moriya interaction and classical MC simulations (*i.e.* spin are fixed on the lattice).



# Chapter IV

## Spin systems with Dzyaloshinskii-Moriya interaction: magnons and skyrmions

### Contents

---

IV.1	Introduction . . . . .	60
IV.2	Magnons in thin films . . . . .	61
IV.2.1	Introduction . . . . .	61
IV.2.2	Magnons with Dzyaloshinskii-Moriya interaction . . . . .	62
IV.3	Skyrmion Crystal . . . . .	71
IV.3.1	Model and Ground State . . . . .	71
IV.3.2	Stability at finite temperatures . . . . .	75
IV.4	Conclusion . . . . .	80

---

In this chapter, we are interested in specific structures present in liquid crystals, like *skyrmions* and the disclinations lines (specific to the nematic mesophase). We model these structure thanks to Dzyaloshinskii-Moriya interaction. In a first time, we look at spin-waves excitations in thin films by using the Green functions method. Then, we apply a magnetic field orthogonal to the film, leading to the apparition of crystal of skyrmions and *stripes* structures. They are exhibited thanks to classical (no particle moving) Monte Carlo Metropolis simulations.

## IV.1 Introduction



skymions have been extensively investigated in condensed matter physics [63] since its theoretical formulation by T. H. R. Skyrme [170, 171] in the context of nuclear matter. There are several mechanisms and interactions leading to the appearance of skyrmions in various kinds of matter. The most popular one is certainly the Dzyaloshinskii-Moriya (DM) interaction which was initially proposed to explain the weak ferromagnetism observed in antiferromagnetic Mn compounds. The phenomenological Landau-Ginzburg model introduced by I. Dzyaloshinskii [55] was microscopically derived by T. Moriya [137]. This demonstration shows that the DM interaction comes from the second-order perturbation of the exchange interaction between two spins which is not zero only under some geometrical conditions of non-magnetic atoms found between them. The order of magnitude of DM interaction,  $D$ , is therefore, perturbation theory obliges, small. The explicit form of the DM interaction will be given in the next section. However, we can think that the demonstration of Moriya [137] is a special case and the general Hamiltonian may have the same form but with different microscopic origin.

The DM interaction has been shown to generate skyrmions in various kinds of crystals. For example, it can generate a crystal of skyrmions in which skyrmions arrange themselves in a periodic structure [161, 26, 105, 106]. Skyrmions have been shown to exist in crystal liquids [22, 111, 1] as well as quantum Hall systems. A single skyrmion has also been found. Effects of skyrmions have been investigated in thin films [59, 192]. Artificial skyrmion lattices have been devised for room temperatures [69]. Experimental observations of skyrmion lattices have been realized in MnSi in 2009 [139, 8] and in doped semiconductors in 2010 [194]. Needless to say, many potential applications using properties of skyrmions are expected in the years to come. At this stage, it should be noted that skyrmion crystals can also be created by competing exchange interactions without DM interactions [77, 147]. So, mechanisms for creating skyrmions are multiple.

We note that spin-wave excitations in systems with a DM interaction in the helical phase without skyrmions have been investigated by many authors [84, 154, 195, 174, 136].

In this chapter, we study :

- the magnon spectrum and the low-temperature behaviour of a thin film with a DM interaction in zero field. Surface effects as well as the film thickness effect are outlined. The method used is the self-consistent Green function technique.
- a skyrmion crystal created by the competition between the nearest-neighbour (NN) ferromagnetic interaction  $J$  and the DM interaction of magnitude  $D$  under an applied magnetic field  $H$ . We show by Monte Carlo (MC) simulation that the skyrmion crystal

is stable at finite temperatures up to a transition temperature  $T_c$  where the topological structure of each skyrmion and the periodic structure of skyrmions are destroyed.

The chapter is organized as follows. The first part is devoted to the study of magnons in thin films. In this part, we show several examples with a combination of frustration and surface effects where the spin configurations are non collinear. We will show in section [IV.2.2](#) how to calculate physical properties at temperature  $T = 0$  and at finite  $T$  using a Green function method in the case of DM interaction [[55](#), [137](#)] in thin films.

The second part is devoted to skyrmion crystals generated by an applied magnetic field. Section [IV.3.1](#) is devoted to the description of the model and the method to determine the ground state (GS). It is shown that our model generates a skyrmion crystal with a perfect periodicity at temperature  $T = 0$ . The GS phase diagram in the space  $(D, H)$  is presented. Results showing the stability of the skyrmion crystal at finite  $T$  obtained from MC simulations are shown in section [IV.3.2](#). We show in this section that the relaxation of the skyrmions is very slow and follows a stretched exponential law. The stability of the skyrmion phase is destroyed at a phase transition to the paramagnetic state. Concluding remarks are given in section [VI.4](#).

## IV.2 Magnons in thin films

### IV.2.1 Introduction

Surface effects in magnetic materials have been intensively investigated since the sixties due to an enormous number of industrial applications [[196](#), [18](#), [45](#), [117](#), [118](#), [11](#), [86](#), [49](#)].

Theoretically, magnetic systems with collinear spin configurations in the bulk state or in thin films have been well understood [[54](#), [46](#)]. Calculations of spin waves and their physical effects have been well carried out with no difficulty [[49](#)]. Phase transitions in those systems have been well analysed by renormalization group [[185](#)] and Monte Carlo (MC) simulations [[15](#)]. However, systems with non collinear spin configurations are more difficult to treat. The first of those systems is the helimagnetic magnets [[191](#), [182](#), [75](#), [156](#)] in which neighbouring spins make a turn angle due to competing interactions between spins. More generally, we have newly called "frustrated spin systems" systems in which competing interactions are at the origin of highly degenerate and/or non collinear ground state (GS) spin configurations, partial disorder at finite temperatures, re-entrant phenomena, multiple phase transitions, disorder lines, ... [[48](#)]. There are much difficulties to deal with these systems.

On the other hand, surface effects in materials have also induced additional difficulties in the study of materials at nanometric scale. The breaking of the translational invariance at the surface gives rise to modifications of surface interactions and surface geometry

[142, 141, 50]. Surface effects are strong when the the system becomes very small at the nanometric scale, they can modify completely the bulk properties of the materials.

## IV.2.2 Magnons with Dzyaloshinskii-Moriya interaction

### a) Theoretical formulation

The DM interaction has been initially introduced to explain the weak ferromagnetism observed in some antiferromagnetic Mn compounds. The phenomenological theory introduced by Dzyaloshinskii [55] has been microscopically demonstrated by Moriya [137] who has shown that the DM interaction results from a second-order perturbation of the spin-orbit coupling. The form of the Dzyaloshinskii-Moriya interaction between two spins  $\mathbf{S}_i$  and  $\mathbf{S}_j$  is

$$\mathcal{H}_{DM}^{ij} = \mathbf{D}_{ij} \cdot (\mathbf{S}_i \times \mathbf{S}_j) \quad (\text{IV.1})$$

where the operators  $\cdot$  and  $\times$  denote respectively the scalar and the cross product.  $\mathbf{D}_{ij}$  and  $\mathbf{S}_\ell$  (with  $\ell = i, j$ ) are then vectors such as

$$\mathbf{S}_\ell = S_\ell^x \hat{\mathbf{e}}_x + S_\ell^y \hat{\mathbf{e}}_y + S_\ell^z \hat{\mathbf{e}}_z, \quad (\text{IV.2})$$

$$\mathbf{D}_{ij} = D_{ij}^x \hat{\mathbf{e}}_x + D_{ij}^y \hat{\mathbf{e}}_y + D_{ij}^z \hat{\mathbf{e}}_z, \quad (\text{IV.3})$$

with  $\hat{\mathbf{e}}_\mu$  ( $\mu = x, y, z$ ) unit vectors in the direction of the  $\mu$ -axis.  $\mathbf{D}_{ij}$  is a vector which results from the displacement of non magnetic ions located between  $\mathbf{S}_i$  and  $\mathbf{S}_j$ , for example in Mn-O-Mn bonds in the historical papers [55, 137]. The direction of  $\mathbf{D}_{ij}$  depends on the symmetry of the displacement [137].

The DM interaction given by equation (IV.1) is antisymmetric with respect to the permutation of  $\mathbf{S}_i$  and  $\mathbf{S}_j$ . From this expression, we write a full Hamiltonian for a crystal with the sum performed on all spin pairs  $\langle i, j \rangle$  as follows

$$\mathcal{H}_{DM} = \sum_{\langle i, j \rangle} \mathbf{D}_{ij} \cdot (\mathbf{S}_i \times \mathbf{S}_j). \quad (\text{IV.4})$$

We see that if  $\mathbf{D}_{ij} = \mathbf{D}_{ji}$  then whatever the angle between  $\mathbf{S}_i$  and  $\mathbf{S}_j$  is, the sum is zero. The non-zero contribution of the DM interaction is possible only if  $\mathbf{D}_{ij} \neq \mathbf{D}_{ji}$ . One of the choices of  $\mathbf{D}_{ij}$  is the following

$$\mathbf{D}_{ij} = D (\mathbf{r}_i \times \mathbf{r}_j), \quad (\text{IV.5})$$

where  $D$  is a constant. The vectors  $\mathbf{r}_i$  and  $\mathbf{r}_j$  connect the spins  $\mathbf{S}_i$  and  $\mathbf{S}_j$  to the non-magnetic ion as shown in Figure IV.1. We see that with this choice  $\mathbf{D}_{ij} = -\mathbf{D}_{ji}$ . Note that changing the orientation of one of the vector, for example  $\mathbf{r}_j$ , will not change this results.

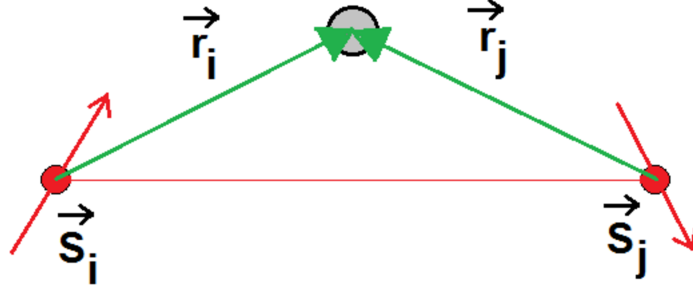


**Figure IV.1** – Example of a geometry to define  $D_{ij}$ : large gray circle is the non-magnetic ion, red small circles are spins, vectors  $\mathbf{r}_i$  and  $\mathbf{r}_j$  are defined as indicated. See text for comments.

To show a simple case of effects caused by the DM interaction, we consider a thin film of simple cubic (SC) lattice of  $N$  layers of lateral dimension  $L \times L$  stacked in the  $y$  direction perpendicular to the film surface.

We will see below that the GS configuration is planar in the  $xz$  film planes with the following Hamiltonian

$$\mathcal{H} = \mathcal{H}_e + \mathcal{H}_{DM}, \quad (\text{IV.6})$$

with  $\mathcal{H}_{DM}$  given by the equation (IV.4) and  $\mathcal{H}_e$  by

$$\mathcal{H}_e = - \sum_{\langle i,j \rangle} J_{ij} \mathbf{S}_i \cdot \mathbf{S}_j, \quad (\text{IV.7})$$

where  $J_{ij}$  and  $D_{ij}$  (cf. equation (IV.4)) are the exchange and DM interactions, respectively, between two Heisenberg spins  $\mathbf{S}_i$  and  $\mathbf{S}_j$  of magnitude  $S = 1/2$  occupying the lattice sites  $i$  and  $j$ .

We consider the case where the in-plane and inter-plane exchange interactions between NN are both ferromagnetic and denoted by  $J_{\parallel}$  and  $J_{\perp}$ , respectively. The DM interaction is supposed to be between NN in the plane with a constant  $D$ .

Due to the competition between the exchange  $J$  term which favours the collinear configuration, and the DM term which favours the perpendicular one, we expect that the spin  $\mathbf{S}_i$  makes an angle  $\theta_{ij}$  with its neighbour  $\mathbf{S}_j$ . Therefore, the quantization axis of  $\mathbf{S}_i$  is not the same as that of  $\mathbf{S}_j$ . Let us call  $\hat{\zeta}_i$  the quantization axis of  $\mathbf{S}_i$  and  $\hat{\xi}_i$  its perpendicular axis in the  $xz$  plane. The third axis  $\hat{\eta}_i$ , perpendicular to the film surface, is chosen in such a way to make  $(\hat{\xi}_i, \hat{\eta}_i, \hat{\zeta}_i)$  an orthogonal direct frame.

Note that it is very important to call the quantization axis  $z$  because the standard commutation relations we shall use below are defined with the  $z$  as the quantization axis. This quantization axis lies on  $\hat{\zeta}_i$ .

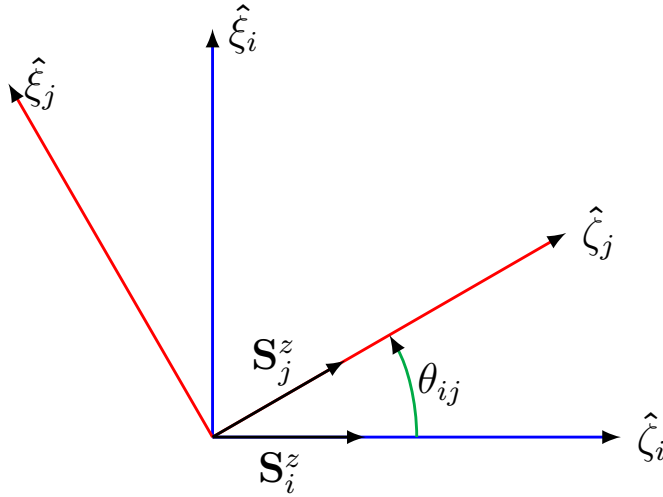


**Figure IV.2** – Local coordinates in the  $xz$ -plane. The spin quantization of  $\mathbf{S}_i$  and  $\mathbf{S}_j$  are  $\hat{\xi}_i$  and  $\hat{\xi}_j$ , respectively.

Writing  $\mathbf{S}_i$  and  $\mathbf{S}_j$  in their respective local coordinates, one has

$$\mathbf{S}_i = S_i^x \hat{\xi}_i + S_i^y \hat{\eta}_i + S_i^z \hat{\xi}_i, \quad (\text{IV.8})$$

$$\mathbf{S}_j = S_j^x \hat{\xi}_j + S_j^y \hat{\eta}_j + S_j^z \hat{\xi}_j, \quad (\text{IV.9})$$

where we have

$$\begin{cases} \hat{\xi}_j = \cos \theta_{ij} \hat{\xi}_i - \sin \theta_{ij} \hat{\xi}_i, \\ \hat{\xi}_j = \sin \theta_{ij} \hat{\xi}_i + \cos \theta_{ij} \hat{\xi}_i, \\ \hat{\eta}_j = \hat{\eta}_i. \end{cases} \quad (\text{IV.10})$$

We choose the vector  $\mathbf{D}_{ij}$  perpendicular to the  $xz$  plane, namely

$$\mathbf{D}_{ij} = D e_{ij} \hat{\eta}_i \quad (\text{IV.11})$$

where  $e_{ij} = +1$  ( $-1$ ) if  $j > i$  ( $j < i$ ) for NN on the  $\hat{\xi}_i$  or  $\hat{\xi}_i$  axis, according to the choice  $\mathbf{D}_{ij} = -\mathbf{D}_{ji}$ . Note that  $e_{ji} = -e_{ij}$ .

Using the local-energy minimization [50, 142], we can determine the GS of the Hamiltonian (IV.6). Starting from the energy  $E_i$  of a spin  $\mathbf{S}_i$  at lattice site  $i$  with its NN (in the same layer), with

$$E_i = -J_{\parallel} \mathbf{S}_i \cdot \mathbf{S}_j + D (\mathbf{r}_i \times \mathbf{r}_j) \cdot (\mathbf{S}_i \times \mathbf{S}_j), \quad (\text{IV.12})$$

$$\stackrel{\text{(1)}}{=} -J_{\parallel} \cos \theta + D \sin \theta, \quad (\text{IV.13})$$

and by minimizing this energy such as

$$\frac{dE_i}{d\theta} = J_{\parallel} \cos \theta + D \sin \theta = 0, \quad (\text{IV.14})$$

<sup>(1)</sup>Note that, we have used here the fact spins are normalized:  $\|\mathbf{S}_\ell\| = 1$  ( $\ell = i, j$ ). Remark also that, in the equation (IV.13),  $D$  has *absorbed* the norm of  $\mathbf{r}_i$  and  $\mathbf{r}_j$ .

it comes that the minimum angle between two NN is given by

$$\theta = \arctan\left(-\frac{D}{J_{\parallel}}\right). \quad (\text{IV.15})$$

We can also calculate the GS by the numerical steepest-descent method [142] if the Hamiltonian is more complicated. The GS is shown in Figure IV.3. Before showing the results, let

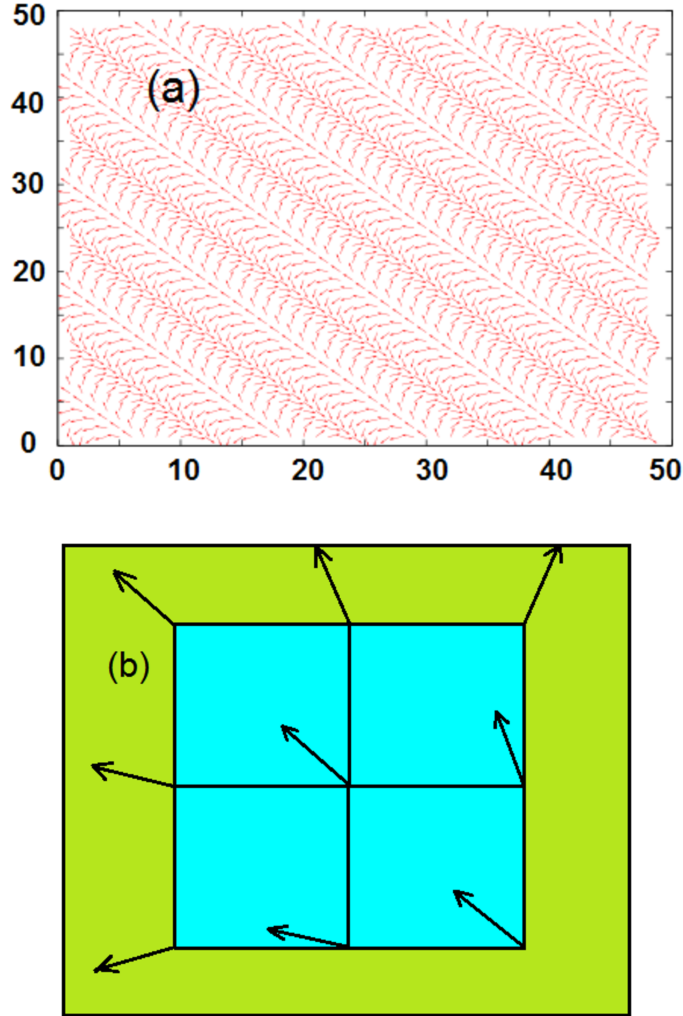


**Figure IV.3** - (a) The ground state is a planar configuration on the  $xz$  plane. The figure shows the case where  $\theta = \pi/6$  ( $D = -0.577$ ),  $J_{\parallel} = J_{\perp} = J = 1$ ; (b) a zoom is shown around a spin with its nearest neighbors.

us introduce the following anisotropy between  $\mathbf{S}_i$  and  $\mathbf{S}_j$  to stabilize the angle determined above between their local quantization axes  $S_i^z$  and  $S_j^z$ :

$$\mathcal{H}_a = - \sum_{\langle i,j \rangle} I_{ij} S_i^z S_j^z \cos \theta_{ij}, \quad (\text{IV.16})$$

where  $I_{ij}$  is taken to be positive, small compared to  $J_{\parallel}$ , and limited to NN. For simplicity, we take  $I_{ij} = I_1$  for all NN pairs in the  $xz$  plane. As will be seen below, this anisotropy

helps stabilize the SW spectrum of thin films  $T = 0$ . The total Hamiltonian is thus

$$\mathcal{H} = \mathcal{H}_e + \mathcal{H}_{DM} + \mathcal{H}_a. \quad (\text{IV.17})$$

By expanding  $\mathcal{H}$  in local coordinates thanks to the equations (IV.10) and by using the relations

$$\mathbf{S}^x = \frac{1}{2} (\mathbf{S}^+ + \mathbf{S}^-), \quad (\text{IV.18})$$

$$\mathbf{S}^y = \frac{1}{2i} (\mathbf{S}^+ - \mathbf{S}^-), \quad (\text{IV.19})$$

where  $\mathbf{S}^+$  and  $\mathbf{S}^-$  are the quantum spin operators<sup>(2)</sup> defined by

$$\mathbf{S}^\pm |S, m\rangle = \hbar \sqrt{S(S+1) - m(m \pm 1)} |S, m \pm 1\rangle, \quad (\text{IV.20})$$

with  $S$  the spin amplitude and  $m$  its component along the  $z$ -axis, being an eigenvalue of the operator  $\mathbf{S}^z$ , such as

$$\mathbf{S}^z |S, m\rangle = \hbar m |S, m\rangle \quad (\text{with } -S < m < S), \quad (\text{IV.21})$$

we reach

$$\begin{aligned} \mathcal{H} = & - \sum_{\langle i,j \rangle} J_{ij} \left\{ \frac{1}{4} (\cos \theta_{ij} - 1) (\mathbf{S}_i^+ \mathbf{S}_j^+ + \mathbf{S}_i^- \mathbf{S}_j^-) + \frac{1}{4} (\cos \theta_{ij} + 1) (\mathbf{S}_i^+ \mathbf{S}_j^- + \mathbf{S}_i^- \mathbf{S}_j^+) \right. \\ & + \frac{1}{2} \sin \theta_{ij} (\mathbf{S}_i^+ + \mathbf{S}_i^-) \mathbf{S}_i^z - \frac{1}{2} \sin \theta_{ij} \mathbf{S}_i^z (\mathbf{S}_i^+ + \mathbf{S}_i^-) + \cos \theta_{ij} \mathbf{S}_i^z \mathbf{S}_j^z \left. \right\} \\ & - \sum_{\langle i,j \rangle} \frac{D}{4} \left\{ (\mathbf{S}_i^+ + \mathbf{S}_i^-) (\mathbf{S}_j^+ + \mathbf{S}_j^-) + 4 \mathbf{S}_i^z \mathbf{S}_j^z \right\} e_{ij} \sin \theta_{ij} \\ & - \sum_{\langle i,j \rangle} I_{ij} \mathbf{S}_i^z \mathbf{S}_j^z \cos \theta_{ij}. \end{aligned} \quad (\text{IV.22})$$

## b) Spin waves and layer magnetisation

We calculate now some properties of the present model such as spin-wave spectrum and layer magnetisations. We use the general Green's function formulation for non-collinear magnets given above to obtain calculate thermodynamic properties. It is very important to emphasize that the local coordinates are necessary in this part because they allow one to use the commutation relations between spin operators of a spin which are valid only when the  $z$  spin component is defined on its quantification axis. This method has been applied for bulk helimagnets [75, 156]. A short introduction about the Green functions and their utilisation in condensed matter can be found in appendix D.

<sup>(2)</sup>Notice here that the operators  $\mathbf{S}^x$ ,  $\mathbf{S}^y$  and  $\mathbf{S}^z$  are in bold unlike in the expression (IV.8) for example. This is because we deal, for the following, with the *quantum definition* of these operators and not *simply* with the classical coordinates of the spin vector  $\mathbf{S}$ . It will make sense in the following subsection about the Green functions.



with  $E = \hbar\omega$ ,  $g$  and  $f$  the Fourier transforms of  $G^R$  and  $F^R$  respectively and

$$A_n = -4J_{\parallel} \left[ 2 \langle S_n^z \rangle (1 + d_n) \cos \theta - \gamma \langle S_n^z \rangle (\cos \theta + 1) \right] - 2J_{\perp} \left[ \langle S_{n-1}^z \rangle + \langle S_{n+1}^z \rangle \right] + 4D (2 - \gamma) \langle S_n^z \rangle \sin \theta, \quad (\text{IV.31})$$

$$B_n = 4J_{\parallel} \gamma \langle S_n^z \rangle (\cos \theta - 1) - 4D \gamma \langle S_n^z \rangle \sin \theta, \quad (\text{IV.32})$$

$$C_n = 2J_{\perp} \langle S_n^z \rangle, \quad (\text{IV.33})$$

and where  $n \in \llbracket 1, N \rrbracket$ ,  $d_n = I_1/J_{\parallel}$  and

$$\gamma = \frac{\cos(k_x a) + \cos(k_z a)}{2},$$

$k_x$  and  $k_z$  the components in the  $xz$  planes of the wave vector  $\mathbf{k}_{\parallel}$  and  $a$  the lattice constant. Let us have a brief remark about the *extrem* layers :

- if  $n = 1$  (surface layer), then there are no  $n - 1$  terms in the matrix coefficients,
- if  $n = N$ , then there are no  $n + 1$  terms.

Besides, we have distinguished the in-plane NN interaction  $J_{\parallel}$  from the inter-plane NN one  $J_{\perp}$ .

The calculation of the Green functions allow us to determine the spin-wave spectrum and to evaluate the layer magnetisation and other properties [113]. The spectrum is obtained by solving  $\det(M) = 0$ , *i.e.* by looking for the eigenvalues of  $M$ . The thermal average of the magnetisation of the  $n$ -th layers for a system where  $S = 1/2$ , is given by<sup>(5)</sup>

$$\langle S_n^z \rangle = \frac{1}{2} - \langle S_n^- S_n^+ \rangle, \quad (\text{IV.34})$$

where  $\langle S_n^- S_n^+ \rangle$  is given by the following spectral theorem [49]

$$\langle S_i^- S_j^+ \rangle = \lim_{\varepsilon \rightarrow 0} \frac{1}{\pi^2} \int_0^{\pi} \int_{\mathbb{R}} \frac{i g_{n,n'}(\omega + i\varepsilon) - g_{n,n'}(\omega - i\varepsilon)}{e^{\beta\hbar\omega} - 1} e^{i\mathbf{k}_{\parallel} \cdot (\mathbf{r}_i - \mathbf{r}_j)} d\omega d^2\mathbf{k}_{\parallel}, \quad (\text{IV.35})$$

$\varepsilon$  being an infinitesimal positive constant. By expressing the  $g_{n,n'}$  by applying the Cramer's rule on the matrix equation (IV.30) and with some calculations detailed in the Appendix D, we can show that the layer magnetisation can be reduced to

$$\langle S_n^z \rangle = \frac{1}{2} - \frac{1}{\pi^2} \int_0^{\pi} \sum_{i=1}^N \frac{\det(M_n(E_i))}{(e^{\beta E_i} - 1) \prod_{i \neq j} (E_i - E_j)} d^2\mathbf{k}_{\parallel}, \quad (\text{IV.36})$$

<sup>(5)</sup>Let us remark that the operators are not written in bold anymore. Indeed, we deal here with the vector spins components as we do numerically. The scale operators  $S^-$  and  $S^+$  are tied to the spin components  $S^x$  and  $S^y$  by the relations (IV.18) and (IV.19).

## IV.2. Magnons in thin films

where  $E_i = \hbar\omega_i$  are the pole of the Green functions and  $M_n$  denotes the matrix formed by replacing the  $n$ -th column of  $M$  by the vector  $\mathbf{u}$ .

For simplicity we take  $d_n = d$  for all layers. Due to the presence of the surface, the spin-wave spectrum at  $T = 0$  is stabilized (no imaginary frequency) only with an amount of anisotropy larger than a *critical value*  $d_c$ . This value of  $d_c$  depends on the value of  $D$ , namely the angle  $\theta$ . Figure IV.4 shows  $d_c$  as a function of  $\theta$ .

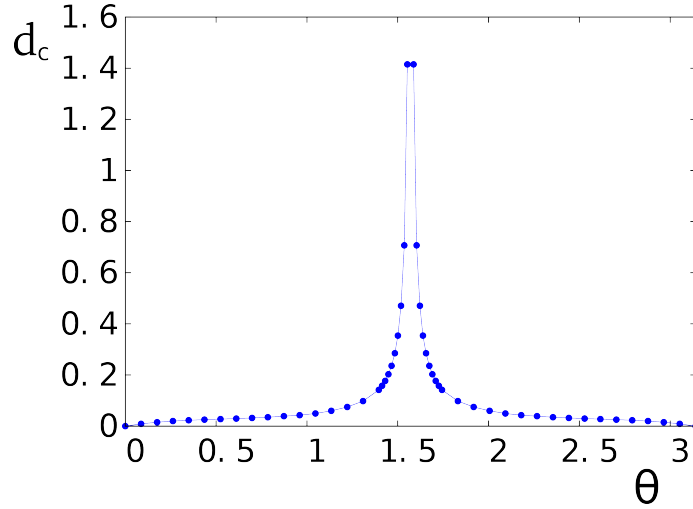


**Figure IV.4** - Value  $d_c$  above which the SW energy  $E(\mathbf{k} = \mathbf{0})$  is real as a function of  $\theta$  (in radian), for a 4-layer film. Note that no spin-wave excitations are possible near the perpendicular configuration  $\theta = \pi/2$ . See text for comments.

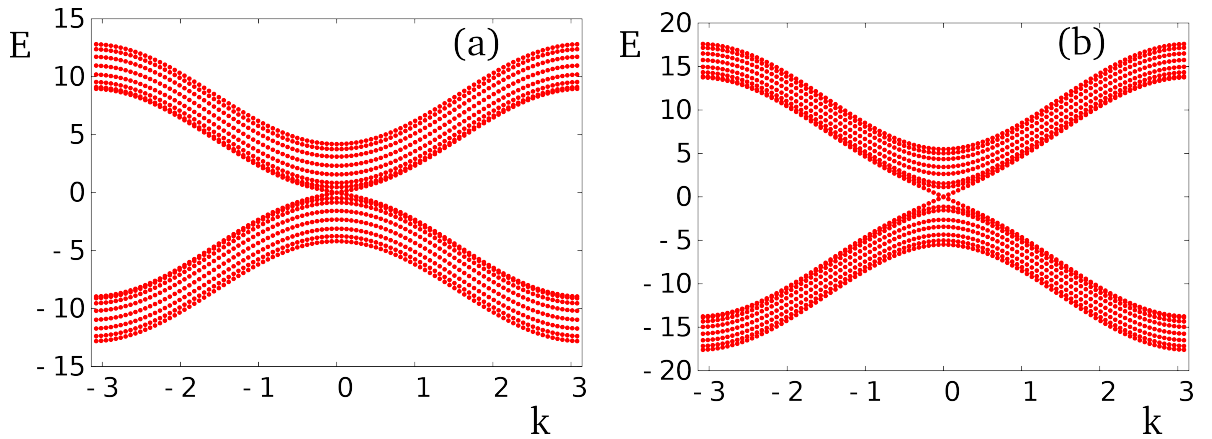


**Figure IV.5** - Spin-wave spectrum  $E(k)$  versus  $k \equiv k_x = k_z$  for a thin film of 8 layers: (a)  $\theta = \pi/6$  (in radian) (b)  $\theta = \pi/3$ , using  $d = d_c$  for each case ( $d_c = 0.012$  and  $0.021$ , respectively). Positive and negative branches correspond to right and left precessions. Note the linear- $k$  behaviour at low  $k$  for the large  $\theta$  case.

In Figure IV.5 the spin-wave spectrum for a 8-layer film  $\theta = \pi/6$  and  $\theta = \pi/3$  using  $d = d_c$  for each case. As seen, for the small angle case,  $E(k) \propto k^2$  as  $k \rightarrow 0$  just as in ferromagnets. However for large angle, the lowest branch of the spin-wave spectrum behaves as

$E(k) \propto k$  as in antiferromagnets. Note that there are no surface modes detached from the spectrum. Using the spectrum we calculate thermodynamic properties. We see that (not shown) the layer magnetisations for two values of  $\theta$  for comparison. We see that larger angles increase the transition temperature. The layer magnetisation is smallest at the surface and increases toward inside.

It is interesting to examine the spin length at  $T = 0$ . We know that for non-collinear magnets, there is a correction to the classical GS configuration due to quantum fluctuations. These quantum fluctuations reduce the spin length. Figure IV.6 shows the reduced spin length  $S_0$  layer by layer as a function of  $\theta$ . As seen, the larger  $\theta$  the smaller  $S_0$ . The

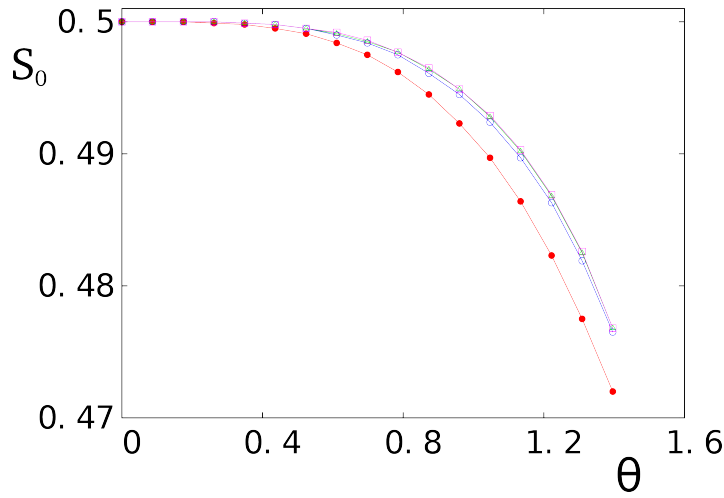


**Figure IV.6** - Spin length  $S_0$  at  $T = 0$  of the first 4 layers as a function of  $\theta$ , for  $N = 8$ ,  $d = 0.1$ . **Red** circles, **blue** void circles, **green** void triangles and **magenta** squares correspond respectively to the first, second, third and fourth layer.

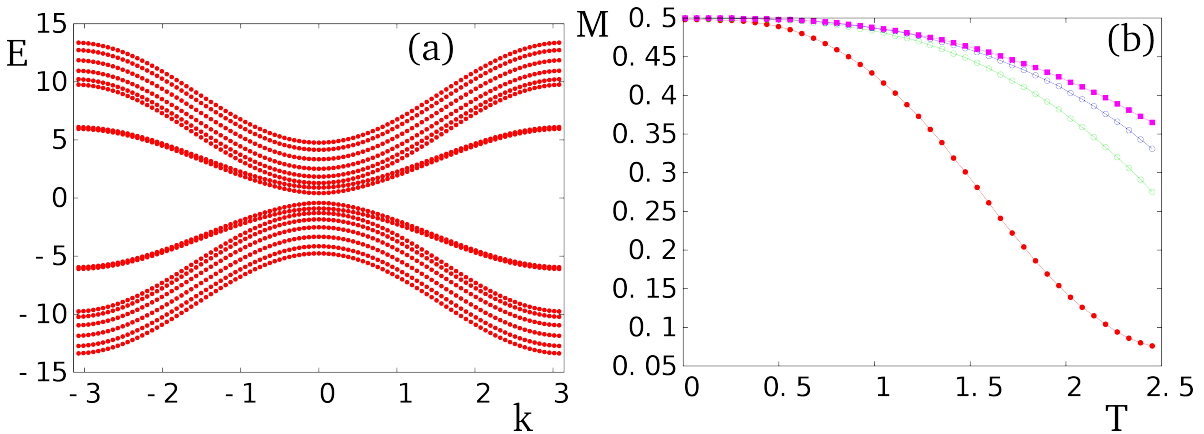


**Figure IV.7** - Surface effect: (a) spin-wave spectrum  $E(k)$  versus  $k = k_x = k_z$  for a thin film of 8 layers:  $\theta = \pi/6$ ,  $d = 0.2$ ,  $J_{\parallel}^s = 0.5$ ,  $J_{\perp}^s = 0.5$ , the gap at  $k = 0$  is due to  $d$ . The surface-mode branches are detached from the bulk spectrum. (b) Layer magnetisations versus  $T$  for the first, second, third and fourth layer (**red** circles, **green** void circles, **blue** void circles and **magenta** filled squares, respectively).

present model does not show localized surface modes unless the surface exchange interaction differs from the bulk one. We show an example in Figure IV.7a where the spectrum has two surface branches originating from the two surfaces of the film. These low-energy modes strongly reduce the surface magnetisation as seen in Figure IV.7b.

The critical temperature  $T_c$  is shown in Figure IV.8 as a function of the film thickness  $N$ . The 3D value is approached for films of 20 layers.

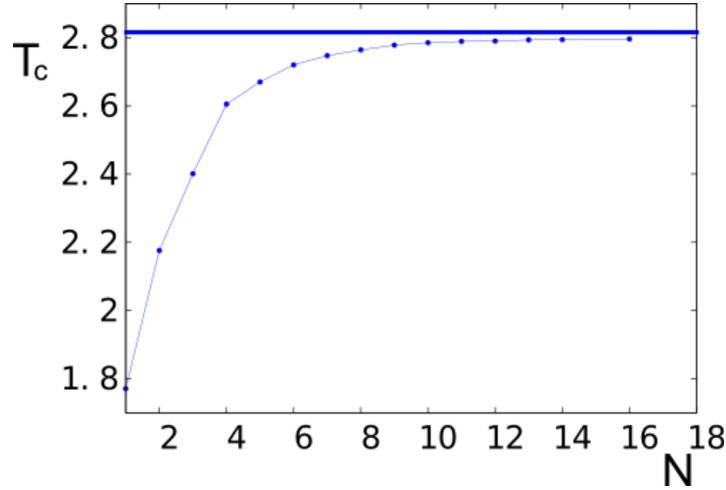


**Figure IV.8** - Critical temperature  $T_c$  versus the film thickness  $N$  calculated with  $\theta = \pi/6$  and  $d = 0.1$ . For the infinite thickness (namely 3D),  $T_c \simeq 2.8$  which is displayed by the horizontal blue line.

## IV.3 Skyrmion Crystal

### IV.3.1 Model and Ground State

Theoretical and experimental investigations on the effect of the DM interaction in various materials have been extensively carried out in the context of weak ferromagnetism observed in perovskite compounds (see references cited in references [167, 56]). As said in the Introduction, the interest in the DM interaction goes beyond the weak ferromagnetism. It has been shown that the DM interaction is at the origin of topological skyrmions [139, 192, 194, 122, 115, 163] and new kinds of magnetic domain walls [78, 160]. The increasing interest in skyrmions results from the fact that skyrmions may play an important role in the electronic transport which is at the heart of technological application devices [63].

In this chapter, we consider for simplicity the two-dimensional case where the spins are on a square lattice in the  $xy$  plane. We are interested in the stability of the skyrmion crystal generated in a system of spins interacting with each other via a DM interaction and a symmetric isotropic Heisenberg exchange interaction in an applied field perpendicular to the  $xy$  plane. All interactions are limited to NN. The full Hamiltonian is given by

$$\mathcal{H} = -J \sum_{\langle i,j \rangle} \mathbf{S}_i \cdot \mathbf{S}_j + \sum_i \sum_{\mu=x,y} D \hat{\mathbf{e}}_\mu \cdot \left[ \mathbf{S}_i \times (\mathbf{S}_{i+\mu} - \mathbf{S}_{i-\mu}) \right] - H \sum_i S_i^z, \quad (\text{IV.37})$$

where the DM interaction and the exchange interaction are taken between NN on both  $x$  and  $y$  directions. Rewriting it in a more convenient form, we have

$$\begin{aligned} \mathcal{H} = -J \sum_{\langle ij \rangle} \mathbf{S}_i \cdot \mathbf{S}_j + D \sum_i \left[ S_i^y (S_{i+x}^z - S_{i-x}^z) - S_i^z (S_{i+x}^y - S_{i-x}^y) \right. \\ \left. - S_i^x (S_{i+y}^z - S_{i-y}^z) + S_i^z (S_{i+y}^x - S_{i-y}^x) \right] - H \sum_i S_i^z. \end{aligned} \quad (\text{IV.38})$$

For the  $i$ -th spin, one has

$$\mathcal{H}_i = -\mathbf{S}_i \cdot \mathbf{H}_i = -\left( S_i^x H_i^x + S_i^y H_i^y + S_i^z H_i^z \right), \quad (\text{IV.39})$$

where the local-field components are given by

$$H_i^x = J \sum_{NN} S_j^x + D(S_{i+y}^z - S_{i-y}^z), \quad (\text{IV.40})$$

$$H_i^y = J \sum_{NN} S_j^y - D(S_{i+x}^z - S_{i-x}^z), \quad (\text{IV.41})$$

$$H_i^z = J \sum_{NN} S_j^z + D(S_{i+x}^y - S_{i-x}^y) - D(S_{i+y}^x - S_{i-y}^x) + H. \quad (\text{IV.42})$$

To determine the ground state (GS), we minimize the energy of each spin, one after another. This can be numerically achieved as the following. At each spin, we calculate its local-field components acting on it from its NN using the above equations. Next we align the spin in its local field, *i.e.* taking

$$\mathbf{S}_i = \frac{1}{\sqrt{(H_i^x)^2 + (H_i^y)^2 + (H_i^z)^2}} (H_i^x \hat{\mathbf{e}}_x + H_i^y \hat{\mathbf{e}}_y + H_i^z \hat{\mathbf{e}}_z). \quad (\text{IV.43})$$

The denominator is the modulus of the local field. In doing so, the spin modulus is normalized to be 1. As seen from equation (IV.39), the energy of the spin  $\mathbf{S}_i$  is minimum. We take another spin and repeat the same procedure until all spins are visited. This achieves one iteration. This algorithm is known as the *steepest descent* algorithm. We have to do a sufficient number of iterations until the system energy converges. For the skyrmion case, it takes about one thousand iterations to have the fifth-digit convergence.

An example of GS are shown in Figure IV.9: a crystal of skyrmions is seen using  $D = 1$  and  $H = 0.5$  (in unit of  $J = 1$ ). Note that we use here an example of large  $D$  for clarity, but we will show later that the skyrmion crystal exists for very small  $D$ .

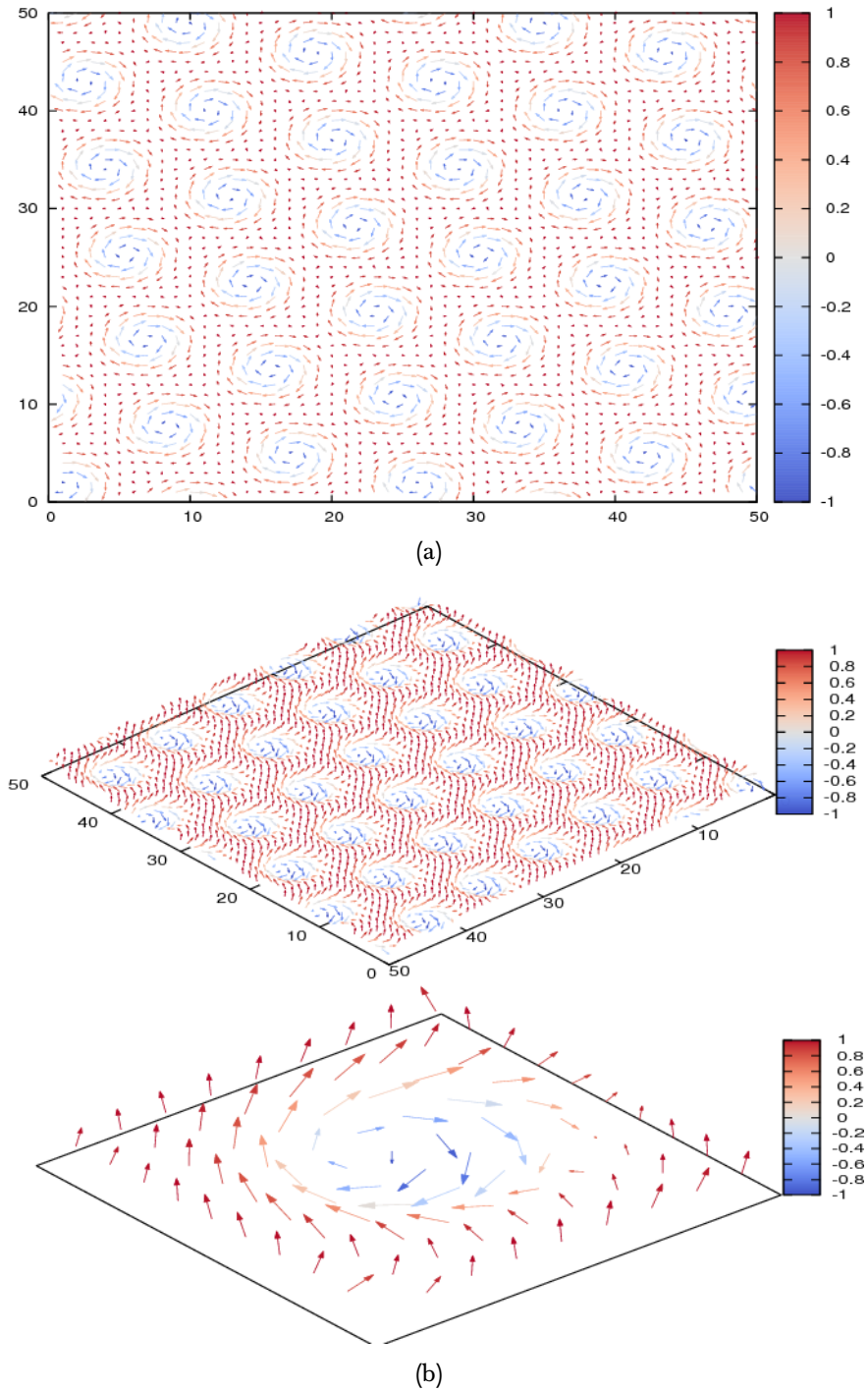


**Figure IV.9** - Ground state for  $D/J = 1$  and  $H/J = 0.5$  (in unit of  $J = 1$ ). We can observe a crystal of skyrmions. (a): Skyrmion crystal viewed in the  $xy$  plane. (b) *top*: a 3D view. (b) *bottom*: Zoom of the structure of a single vortex. The value of  $S_z$  is indicated on the color scale.

In Figure IV.10(a) on the following page we show a GS at  $H = 0$  where domains of long and round islands of up spins separated by labyrinths of down spins are mixed. When  $H$  is increased, vortices begin to appear. The GS is a mixing of long islands of up spins and vortices as seen in Figure IV.10(b) obtained with  $D = 1$  and  $H = 0.25$ . This phase can be

called *labyrinth phase* or *stripe phase*.

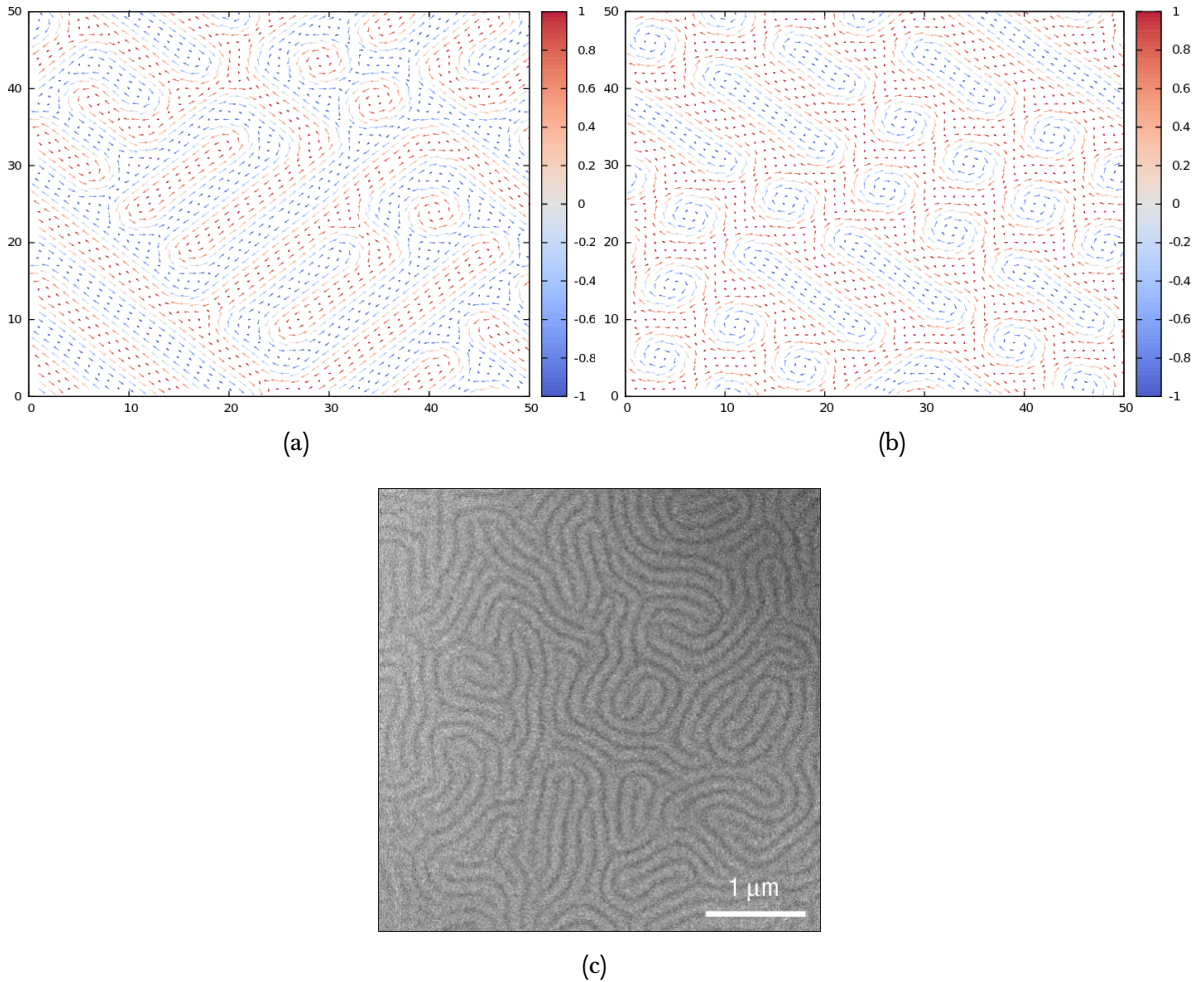


**Figure IV.10** - (a): Ground state for  $D/J = 1$  and  $H/J = 0$  (in unit of  $J = 1$ ), a mixing of domains of long and round islands. (b): Ground state for  $D/J = 1$  and  $H/J = 0.25$  (in unit of  $J = 1$ ), a mixing of domains of long islands and vortices. The latter are due to the increase of  $H$ . These structures can be termed *labyrinth phase*. (c): Experimental observation (with a transmission electron microscope) of a cholesteric liquid crystal (LC). The *fingerprints* structure is similar to the figure above. The dark and bright lines correspond to the region where molecules of LC are parallel and perpendicular, respectively, to the image plane (cf. article of Mitov *and al.* [134]).

It is interesting to note that skyrmion crystals with texture similar to those shown in Figures IV.9 and IV.10 have been experimentally observed in various materials [192, 69, 139, 193], but the most similar skyrmion crystal was observed in two-dimensional  $\text{Fe}(0.5)\text{Co}(0.5)\text{Si}$  by Yu *and al.* [194] and also in liquid crystals [134] (cf. Figure IV.10(c)) using both transmission electron microscopy (TEM).

We have performed the GS calculation taking many values in the plane  $(D, H)$ . The phase diagram is established in Figure IV.11. Above the blue line is the field-induced ferromagnetic

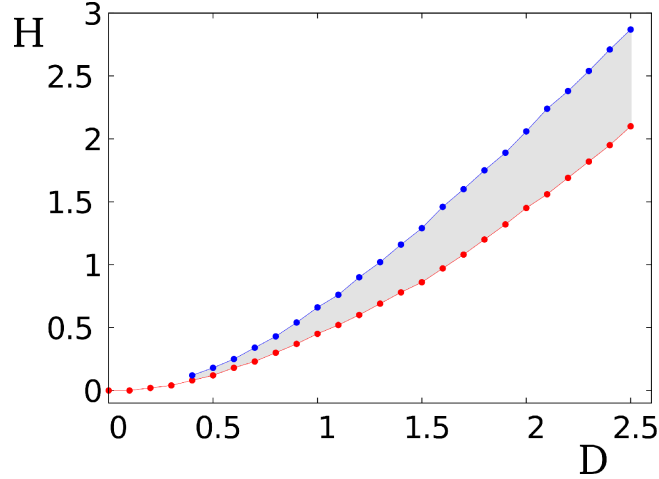


**Figure IV.11** – Phase diagram in the  $(D, H)$  plane for a lattice size  $100 \times 100$ . The region above the **blue** line corresponds to the field-induced ferromagnetic phase, while below the **red** line it corresponds to *labyrinth phase*, *i.e.* a phase with rectangular domains and skyrmions. The narrow **grey** band is the region of the skyrmion crystal phase.

phase. Below the red line is the labyrinth phase with a mixing of skyrmions and rectangular domains. The skyrmion crystal phase is found in a narrow region between these two lines, down to infinitesimal  $D$ .

In the following section, we are interested in the stability of the skyrmion crystal phase as the temperature ( $T$ ) is increased from zero.

### IV.3.2 Stability at finite temperatures

In this section, we show results obtained from MC simulations on a sheet of square lattice of size  $N \times N$  with periodic boundary conditions. The first step is to determine the GS spin configuration by minimizing the spin energy by iteration as described above. Using this GS configuration, we heat the system from  $T = 0$  to a temperature  $T$  during an equilibrating time  $t_0$  before averaging physical quantities over the next  $10^6$  MC steps per spin. The time  $t_0$  is the *waiting time* during which the system relaxes before we perform averaging during the next  $t_f$ .

The definition of an order parameter for a skyrmion crystal is not obvious. Taking advantage of the fact that we know the GS, we define the order parameter as the projection of an actual spin configuration at a given  $T$  on its GS and we take the time average. This order parameter is thus defined as

$$M(T) = \frac{1}{N^2(t_f - t_0)} \sum_i \left| \sum_{t=t_0}^{t_f} \mathbf{S}_i(T, t) \cdot \mathbf{S}_i^0(T=0) \right| \quad (\text{IV.44})$$

where  $\mathbf{S}_i(T, t)$  is the  $i$ -th spin at the time  $t$ , at temperature  $T$ , and  $\mathbf{S}_i^0(T=0)$  is its state in the GS. The order parameter  $M(T)$  is close to 1 at very low  $T$  where each spin is only

weakly deviated from its state in the GS.  $M(T)$  is zero when every spin strongly fluctuates in the paramagnetic state. The above definition of  $M(T)$  is similar to the Edward-Anderson order parameter used to measure the degree of freezing in spin glasses [131]: we follow each spin with time evolving and take the spatial average at the end.

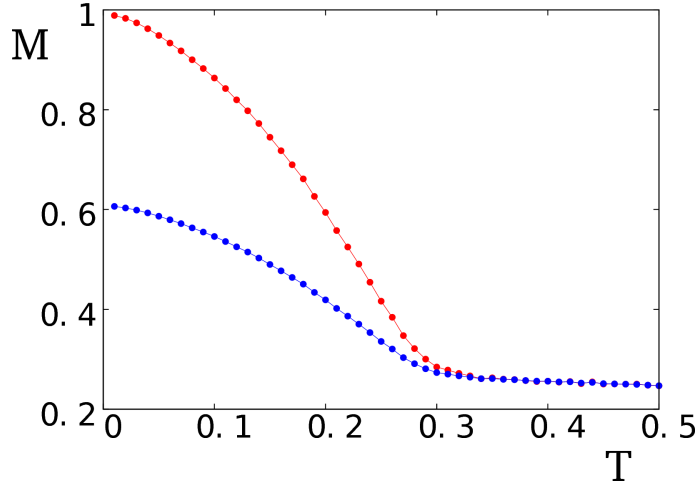


**Figure IV.12** - **Red** circles: order parameter defined in equation (IV.44) versus  $T$ , for  $H = 0.5$  and  $N = 1800$ , averaged during  $t_f = 10^5$  MC steps per spin after an equilibrating time  $t_0 = 10^5$  MC steps. **Blue** crosses: the projection of the  $S_z$  on  $S_z^0$  of the ground state as defined in equation (IV.44) but for the  $z$  components only. The magnetisation  $M$  does not vanish totally because of the applied field.

We show in Figure IV.12 the order parameter  $M$  versus  $T$  (**red** data points) as well as the average  $z$  spin component (**blue** data points) calculated by the projection procedure for the total time  $t = 10^5 + 10^6$  MC steps per spin. As seen, both two curves indicate a phase transition at  $T_c \simeq 0.26 J/k_B$ . The fact that  $M$  does not vanish above  $T_c$  is due to the effect of the applied field. It should be said that each skyrmion has a center with spins of negative  $z$  components (the most negative at the center), the spins turn progressively to positive  $z$  components while going away from the center.

We can also define another order parameter: since the field acts on the  $z$  direction, in the GS and in the skyrmion crystalline phase we have both positive and negative  $S_z$ . In the paramagnetic state, the negative  $S_z$  will turn to the field direction. We define thus the following parameters using the  $z$  spin-components

$$Q_+(T) = \frac{1}{N^2(t_f - t_0)} \sum_{S_i^z > 0} \sum_{t=t_0}^{t_f} S_i^z(T, t) \quad (\text{IV.45})$$

$$Q_-(T) = \frac{1}{N^2(t_f - t_0)} \sum_{S_i^z < 0} \sum_{t=t_0}^{t_f} S_i^z(T, t) \quad (\text{IV.46})$$

Figure IV.13 on the next page shows  $Q_+$  and  $Q_-$  versus  $T$ . As seen, at the transition  $Q_+$  undergoes a change of curvature and  $Q_-$  becomes zero. All spins have positive  $S_z$  after the

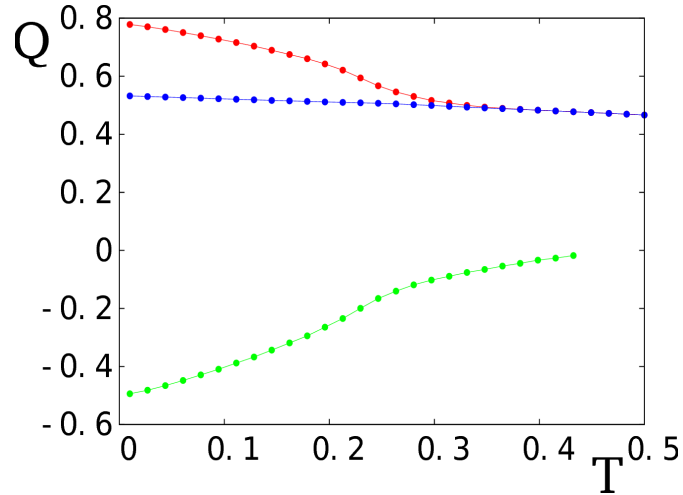


**Figure IV.13** – Order parameters defined in Eqs. (IV.45)-(IV.46) versus  $T$ , for  $H = 0.5$  and  $N = 800$ ,  $t_0 = 10^5$ ,  $t_f = 10^6$ . **Red** circles: total positive  $z$  component ( $Q_+(T)$ ). **Green** circles: total negative  $z$  component ( $Q_-(T)$ ). **Blue** circles: total  $z$  component. After the transition, all spin have positive  $z$  component.

transition due to spin reversal by the field.

The results obtained at the end of the simulation may depend on the overall time  $t = t_0 + t_f$ . In simple systems, the choices of  $t_0$  and  $t_f$  can be guided by testing the time-dependence of physical quantities, and the values of  $t_0$  and  $t_f$  are chosen when physical quantities do not depend on these run times. However, in disordered systems such as spin glasses and in complicated systems such as frustrated systems, the relaxation time is very long and out of the reach of simulation time. In such cases, we have to recourse to some scaling relations in order to deduce the values of physical quantities at equilibrium [153, 146]. We show below how to obtain the value of an order parameter at the infinite time.

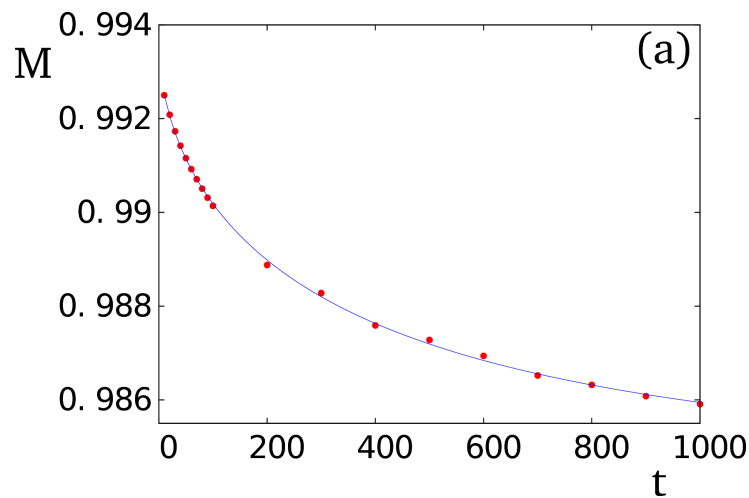


**Figure IV.14** – Cf. page 78 for the legend.

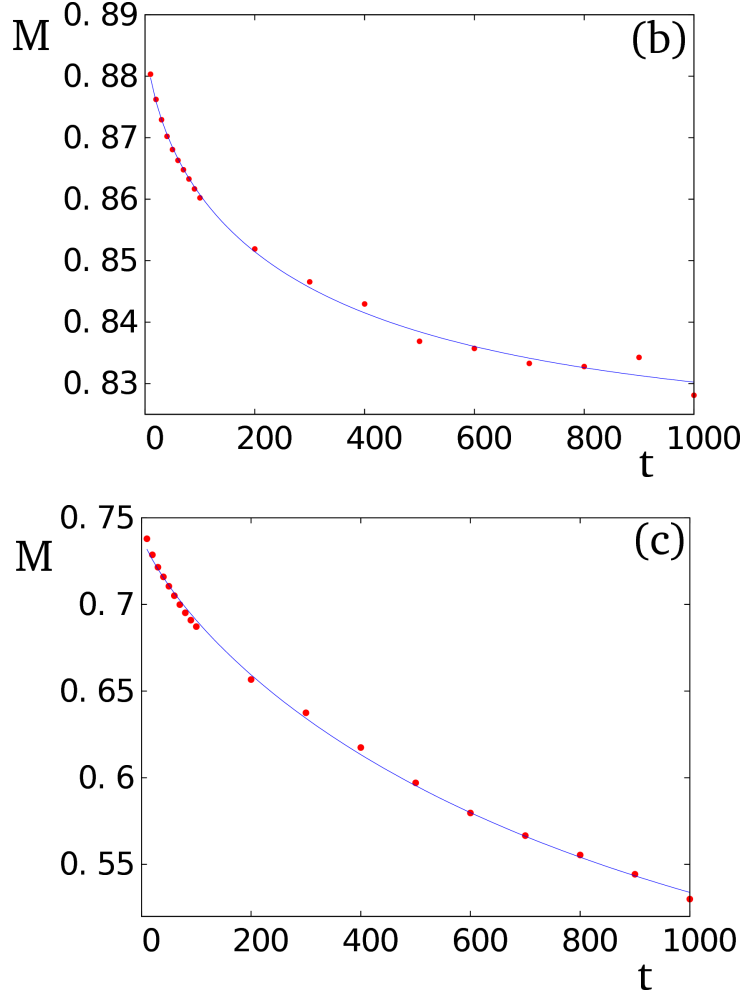


**Figure IV.14** - The order parameter  $M$  defined by equation (IV.44) versus MC time  $t$  in unit of 1000 MC steps per spin, for  $H = 0.5$  and  $N = 800$  (a)  $T = 0.01$ , values of fitting parameters  $\alpha = 0.6$ ,  $A = 0.008 \pm 0.00001$ ,  $\tau = (364 \pm 19) \times 10^3$ ,  $c = 0.984505 \pm 0.00012$ ; (b)  $T = 0.094$ ,  $\alpha = 0.6$ ,  $A = (0.0653 \pm 0.0013)$ ,  $\tau = (277 \pm 36) \times 10^3$ ,  $c = (0.822 \pm 0.018)$ ; (c)  $T = 0.17$ ,  $\alpha = 0.8$ ,  $A = 0.31 \pm 0.01$ ,  $\tau = (891 \pm 100) \times 10^3$ ,  $c = 0.43 \pm 0.017$ .

In order to detect the dependence of  $M(T)$  on the total MC time  $t = t_0 + t_f$ , we calculate the average of  $M(T)$  over  $10^6$  MC steps per spin, after a waiting time  $t_0$  as said above. We record the values of  $M(T)$  in different runs with  $t_0$  varying from  $10^4$  to  $10^6$  MC steps per spin. We plot these results as a function of different total time  $t$  in Figure IV.14 for three temperatures.

As said above, to find the value extrapolated at the infinite time, we use the stretched exponential relaxation defined by

$$M(T, t) = A e^{-(t/\tau)^\alpha} + c \quad (\text{IV.47})$$

where  $t$  is the total simulation time,  $\alpha$  is the stretched exponent,  $A$  a temperature-dependent constant, and  $\tau$  the relaxation time. Note that this definition, without the constant  $c$ , has been used by many previous authors in the context of spin glasses [37, 2, 13, 175, 123]. We

have introduced  $c$  which is the infinite-time limit of  $M(T)$ . We have taken  $t$  from  $10^4$  to  $10^6$  MC steps per spin in the simulation. At the infinite-time limit,  $c$  is zero for  $T \gg T_c$ , and  $c \neq 0$  for  $T < T_c$ . Figure IV.14 shows  $M(T, t)$  as a function of time  $t$  in unit of  $10^3$  MC steps per spin, for three temperatures  $T = 0.01, 0.094$  and  $0.17$ . As seen, the fit with equation (IV.47) presented by the continuous line is very good for the whole range of  $t$ .

Several remarks can be done about the results :

- The precision of all parameters are between 1% to 5% depending on the parameter.
- The value of  $\alpha$  can vary a little bit according to the choice and the precision of the other parameters in the fitting but this variation is within a very small window of values around the value given above. For example, at  $T = 0.17$ ,  $\alpha$  can only be in the interval  $[0.8 \pm 0.02]$ . The value of  $\alpha$  can vary with temperature as seen here: at low  $T$ ,  $\alpha = 0.6$ , and at a higher  $T$ , we have  $\alpha = 0.8$ . This variation has been seen in other systems, in particular in spin glasses [143].
- The relaxation time, within statistical errors, is approximatively constant at low  $T$ , but it increases rapidly when  $T$  tends to  $T_c$  as seen in the value of  $\tau$  at  $T = 0.17$ . This increase is a consequence of the so-called *critical slowing-down* when the system enters the critical region.

Let us show  $M(T)$  as a function of  $T$  in Figure IV.15 using the results of different run times from  $t = 10^4 + 10^6$  MC steps per spin to  $t = 10^6 + 10^6$ . The values of at infinite time for each  $T$  deduced from equation (IV.47) is also shown. We see that while the total time  $10^5 + 10^6$  MC steps per spin is sufficient at low  $T$ , it is not enough at higher  $T$ . That was the reason why we should use equation (IV.47) to find the value of  $M(T)$  at infinite time to be sure that the skyrmion crystal is stable at finite temperatures.

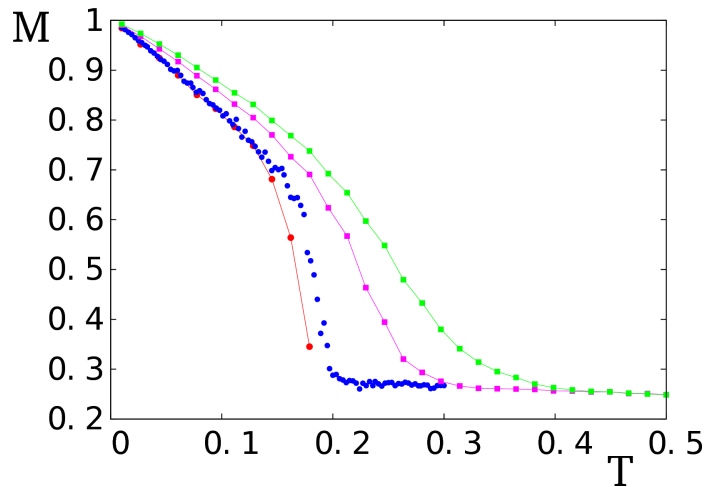


**Figure IV.15** - The order parameter  $M(T)$  versus  $T$  for several waiting times  $t$ , for  $H = 0.5$  and  $N = 800$ : from above  $t = 10^3, 2 \times 10^5, 10^6, \infty$  (by fitting with equation (IV.47)).

We have studied finite-size effects on the phase transition at  $T_c$  and we have seen that from  $N = 800$ , all curves coincide: there is no observable finite size effects for  $N \geq 800$ . The present 2D skyrmion lattice phase therefore remains stable for the infinite dimension, unlike the ferromagnetic Heisenberg model in 2D [129]. Note that the nature of the ordering at low  $T$  and the phase transition observed here, in spite of the vortex nature of skyrmions, are not those of the Kosterlitz-Thouless vortex mechanism observed in ferromagnetic XY spin systems [100, 101] since our *vortices* are stable without changing their position up to the transition temperature.

## IV.4 Conclusion

In the first part of this chapter, we have studied the magnon spectrum and low-temperature behaviour of a thin film with a DM interaction. We would emphasize the importance of the use of local coordinates because the commutation relations between spin operators are expressed for a spin lying on its quantization axis. The results show that the DM interaction affects strongly the low-energy spin-wave frequencies: it has the  $k^2$  behaviour for a weak interaction, but the  $k$  behaviour for a strong interaction. Note that the spin-wave spectrum is symmetric, in spite of the fact that the DM interaction is antisymmetric with respect to the permutation of two spins. Indeed, due to the antisymmetry of the vector  $\mathbf{D}_{ij}$ , the energy of a spin pair  $E(i, j) = \mathbf{D}_{ij} \cdot \mathbf{S}_i \times \mathbf{S}_j$  is invariant with respect to the permutation  $i \rightleftharpoons j$ .

In the second part of this chapter, we have shown that the competition between a ferromagnetic interaction  $J$  and a Dzyaloshinskii-Moriya interaction  $D$  under an applied magnetic field  $H$  in two dimensions generate a skyrmion crystal in a region of the phase space  $(D, H)$ . The spin model is the classical Heisenberg model. We have numerically determined the ground state by minimizing the local energy, spin by spin, using an iteration procedure. The skyrmion lattice is then heated to a finite temperature by the use of Monte Carlo simulations. We have shown that the skyrmion lattice is stable up to a finite temperature  $T_c$  beyond which the system becomes disordered. We have also shown that the relaxation follows a stretched exponential law. We believe that such a stability can be experimentally observed in real systems.

Perhaps, our model is the simplest model able to generate a skyrmion crystal without the need to include more complicated interactions such as long-range dipolar interactions, easy and uniaxial anisotropies [106, 115, 193]. Note that other authors have shown that skyrmion crystals can also be generated only with frustrated short-range interactions without even the DM interaction [77, 147]. So, we have to keep in mind that there are many interaction mechanisms of different nature which can generate skyrmion crystals. The origin of a skyrmion crystal determines its structure, its stability, its dynamics and in short its properties (see a discussion on this point in [193]). Experiments can be used therefore to determine the

#### IV.4. Conclusion

---

interaction mechanism which is at the origin of the formation of a skyrmion crystal.



# Chapter V

## Potts model to study the dynamics of nematic and smectic liquid crystals

### Contents

---

V.1	Introduction . . . . .	84
V.2	Method of simulation . . . . .	84
V.3	The smectic phase . . . . .	85
V.3.1	Model . . . . .	85
V.3.2	Results . . . . .	86
V.4	The nematic phase . . . . .	88
V.4.1	Model . . . . .	88
V.4.2	Results . . . . .	89
V.5	Conclusion . . . . .	91

---

In this chapter, we are interested in the dynamics leading to the formation of two mesophases (nematic and smectic) of liquid crystals upon cooling from an isotropic phase. For this study, we used the mobile Potts model described in a previous chapter.

## V.1 Introduction



nematic and smectic ordering has been subject of intensive investigations since the discovery of liquid crystals (LC) [41]. Most of theoretical studies have used Frank's free energy [67, 31, 32] which cannot show the formation of the smectic and nematic ordering when the temperature varies. There is no statistical study of systems of molecules constituting liquid crystals.

Consider a system of  $N$  molecules interacting with each others. Experimentally, we know that temperature variation can create different kind of ordering in LC such as nematic, smectic, etc... But there is absence of theoretical study starting with such an assembly of molecules with a macroscopic Hamiltonian. In particular, there is no investigation on the dynamics of how nematic and smectic ordering are reached from isotropic phase when the temperature decreases.

This motivates the study presented in this chapter. Here, we use the mobile Potts model with appropriate interactions allowing to generate the nematic and smectic ordering.

As we know that the nematic phase is the closest phase to the liquid phase and the most common. It has no long-range positional order but a global orientational order. As for the smectic phase, it is the contrary. Indeed, it is the phase that looks like the most to a crystalline solid and for which molecules are ordered in equidistant layers. It shows a long-range positional order (at least in one direction) and also an orientational order.

We will first describe the model in the following section and then we show the results obtained by Monte Carlo (MC) simulations.

As we will be seen, we succeed in obtaining nematic and smectic ordering, by following the motion of molecules.

## V.2 Method of simulation

The model used in this chapter is similar to the one used in the chapter III, *i.e.* it is based on a mobile Potts model but with different kinds of interactions. Indeed, we still consider a system of  $N_s$  Potts spins on a simple cubic lattice with  $N_L$  sites. Each site  $i$  can thus be vacant or occupied at most by a spin  $\sigma_i$  having  $q$  states ( $\sigma_i = 1, 2, \dots, q$ ). A spin can thus move from one site to a neighbouring empty site thanks to the effects of the interactions and/or the temperature  $T$ . Obviously, the concentration of spins  $c = N_s/N_L$  must be lower than one to permit their motion.

We fix a concentration  $c$  low enough to allow the motion of spin inside the recipient.

The use of periodic boundary conditions in three directions reduces the size effect. We use several recipient volumes to test the validity of our results and we see that results do not qualitatively change.

The simulation is carried out as follows: we generate the positions and the orientations of the spin randomly in the recipient, we update each spin position and orientation at the same time by using the Metropolis algorithm (as explained in chapter II) applying to its old and trial energies. The position update is done by moving the spin to a nearby vacant site with a probability for the simple cubic lattice. The motion of each spin is therefore driven by just the interaction with its neighbours at a given temperature  $T$ . We start thus from a random configuration, *from the disordered phase*, and we slowly cool the system with an extremely small interval of  $T$ .

As usual, we discard a large number of MC steps per spin to equilibrate the system before averaging physical quantities over a large number of MC steps. We calculate in general the energy, the specific heat, an appropriate order parameter and its fluctuations (namely, susceptibility), the average coordination number, and the diffusion coefficient. For the smectic phase, the order parameter is the layer magnetisation, while for the nematic phase it is just the total magnetisation without long-range position ordering (no lines, no planes).

We record all physical quantities and the motion of molecules as the time evolves.

In the following, we consider that a spin can reach  $q = 6$  different states, *i.e.* two states per spatial direction.

## V.3 The smectic phase

### V.3.1 Model

The Hamiltonian used to model the smectic LC is given by

$$\mathcal{H} = - \sum_{\langle i,j \rangle} J_{ij} \delta_{\sigma_i, \sigma_j} \quad (\text{V.1})$$

where  $\langle i, j \rangle$  denotes the NN.  $J_{ij}$  is the spin-spin exchange interaction such as

$$J_{ij} = \begin{cases} J_{\parallel} > 0, & \text{in-plane interactions between NN,} \\ J_{\perp} < 0, & \text{inter-plane interactions between NN.} \end{cases}$$

The in-plane and inter-plane exchange interactions are then ferromagnetic and anti-ferromagnetic, respectively. The use of an antiferromagnetic between planes is to avoid a correlation between adjacent planes: the antiferromagnetic interaction favours different spin orientations between NN planes.

### V.3.2 Results

Let us show in Figure V.1 snapshots taken in the isotropic phase and in the final phase at  $T = 0.1$  with  $J_{\parallel} = 3.0$ ,  $J_{\perp} = -1.0$ . As seen, the low- $T$  phase is smectic with ordered planes but no correlation in the perpendicular direction. A video showing the cooling of the system is available [here](#). Another video showing the evolution of the system during a cycle in temperature, *i.e.* after heating and then cooling down the temperature, can be viewed at [here](#). The video shows the dynamics leading to the formation of the smectic phase.

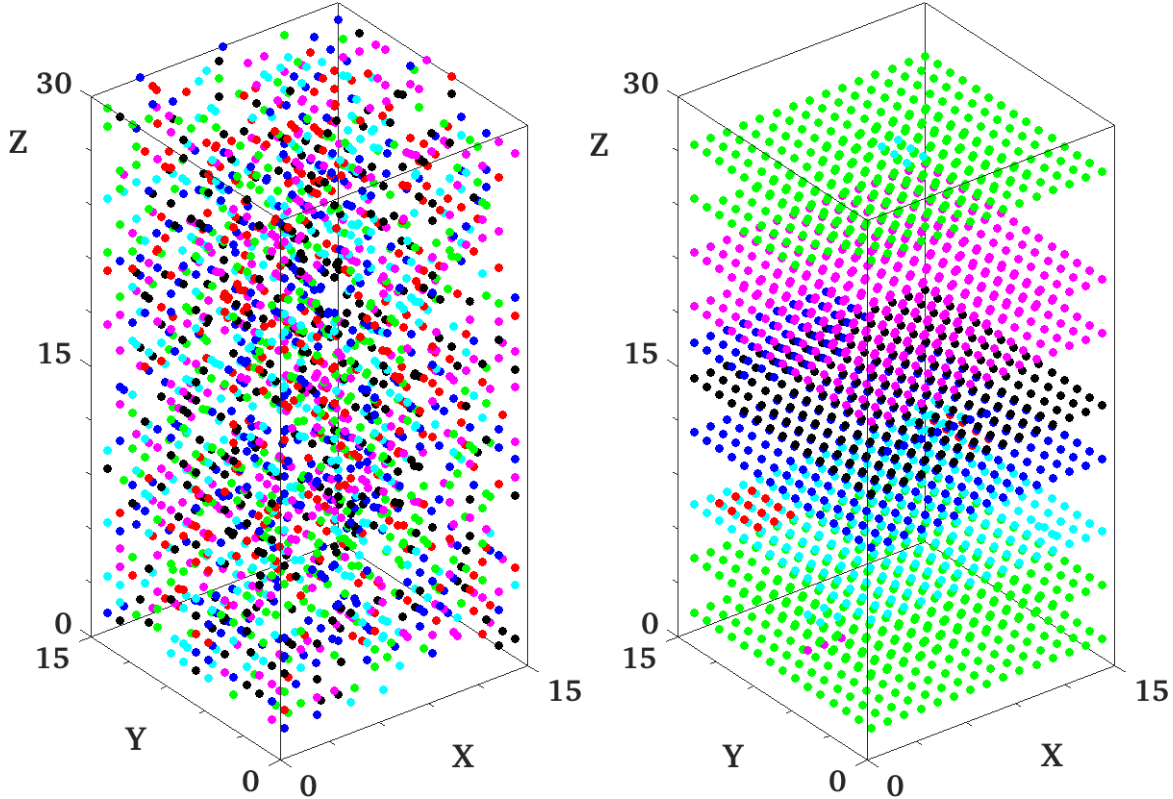


**Figure V.1** – Snapshot of the system at two different temperatures. Spins are contained in a *box* with periodic boundary conditions. There is  $N_L = 15 \times 15 \times 30 = 6750$  sites and 2025 spins, *i.e.* a spin concentration equal to  $c = 30\%$ . Each colored point corresponds to a spin state. *Left:* Initial configuration of the system at a high temperature  $T = 5$ . The system is completely disordered. *Right:* Final configuration at low temperature  $T = 0.1$ . The system was cooled down from the disordered phase. Spins are staged in independent layers and within a layer all the spins have the same orientation (color). It corresponds to a smectic phase.

The energy per molecule  $U$  and the diffusion coefficient  $D$  are shown in Figure V.2 versus  $T$ . We see clearly that there is a transition from the isotropic state to the smectic ordering at  $T_c \simeq 1.40$  where  $U$  and  $D$  change the curvature.

It should be noted that for other ferromagnetic values of  $J_{\parallel}$ , we obtain the same results with a shift in the value of  $T_c$ . Let us show in Figure V.3 the histogram of the coordination

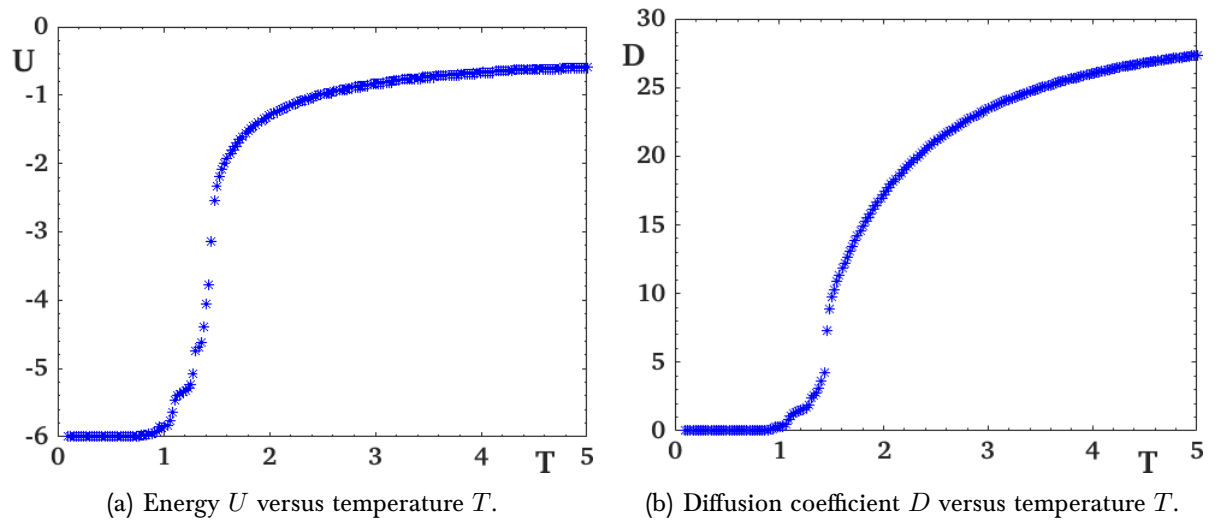


**Figure V.2** - Evolution of energy and diffusion coefficient as functions of temperature. The spin concentration  $c$  is  $c = N_s/N_L = 30\%$ , with  $N_L = 15 \times 15 \times 30$ . The exchange interactions are  $J_{\parallel} = 3.0$ ,  $J_{\perp} = -1.0$ .

number of the lattice sites in the smectic phase. As seen all of them has 4 neighbours, indicating a planar or smectic phase phase. The antiferromagnetic interaction in the  $z$  direction prevents two adjacent planes from having the same orientation.

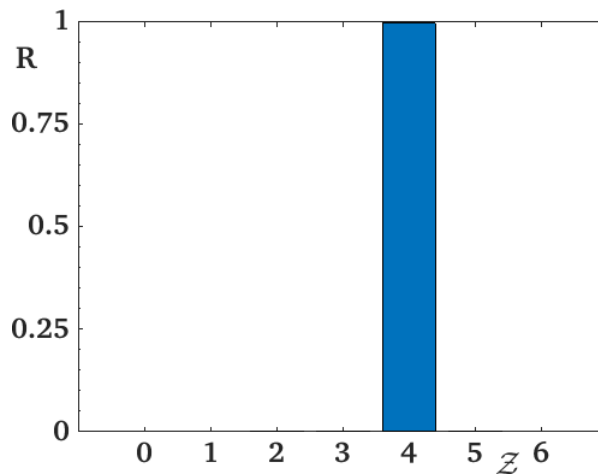


**Figure V.3** - Histogram showing the percentage  $R$  of sites having  $Z$  nearest neighbors at  $T = 0.1$ , *i.e.* corresponding to the snapshot at the bottom in the Figure V.1. Spins are distributed such as they have only 4 neighbors, meaning they are staged in layers.

The order parameter of the smectic phase is the layer magnetisations. Different layers have slightly different magnetisations, with more or less order but they all show the transition at  $T_c$ . Two typical layer magnetisations are shown in Figure V.4 on the next page together with their susceptibilities.

Other recipient sizes and values of interactions give the same qualitative results. The only constraint of the model is the in-plane interaction is ferromagnetic and the inter-plane one

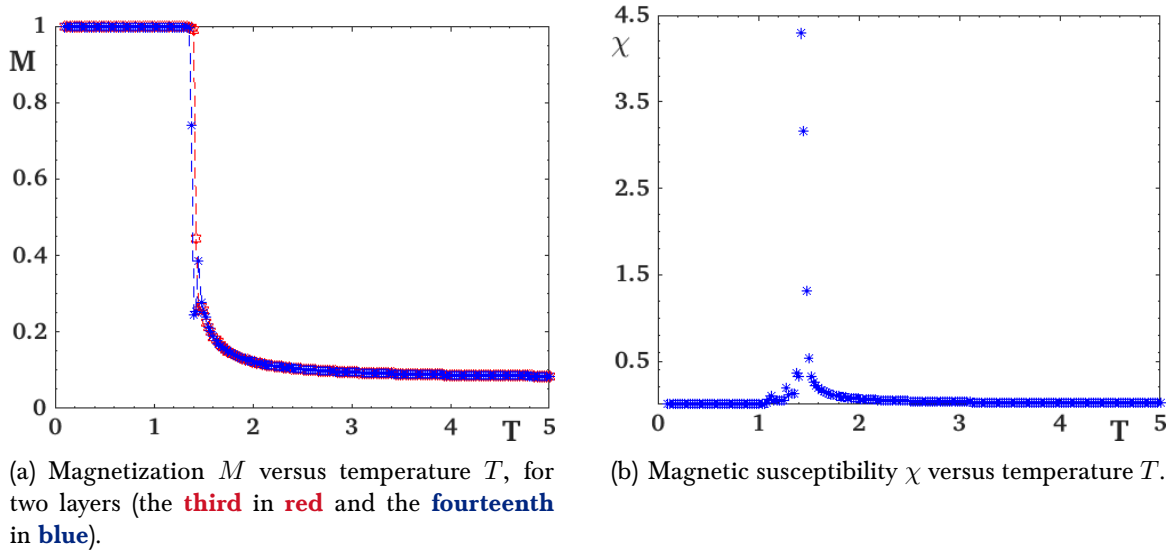


**Figure V.4** - Evolution of magnetisation and susceptibility as functions of temperature. The spin concentration  $c$  is  $c = N_s/N_L = 30\%$ , with  $N_L = 15 \times 15 \times 30$ . The exchange interactions are  $J_{\parallel} = 3.0$ ,  $J_{\perp} = -1.0$ .

is antiferromagnetic.

## V.4 The nematic phase

### V.4.1 Model

To model the nematic phase, we use also the mobile Potts model as above and in chapter III, except that the interactions are given by the following Hamiltonian

$$\mathcal{H} = -J_1 \sum_{\langle i,j \rangle} \delta_{\sigma_i, \sigma_j} - J_2 \sum_{\langle\langle i,j \rangle\rangle} \delta_{\sigma_i, \sigma_j} - A_z \sum_i S_{\sigma_i}^z, \quad (\text{V.2})$$

where the two first sums are performed over the nearest neighbours (NN) and the next-nearest neighbours (NNN), respectively.  $\delta$  is the Kronecker delta and  $J_1$  and  $J_2$  denote the exchange interactions between spins and are chosen such as the interactions between NN are antiferromagnetic ( $J_1 < 0$ ), and ferromagnetic for the NNN ( $J_2 > 0$ ). The last sum is performed over all the sites and corresponds to a slight anisotropy along the  $z$ -direction. To each state  $\sigma_i$  is associated a 3-components normalized vector  $\mathbf{S}_{\sigma_i}$ .  $S_{\sigma_i}^z$  is then the  $z$ -component of the spin  $\sigma_i$ .

We explain the choice of the above Hamiltonian which is guided by the following nematic phase:

- there should not be molecules sticking to each other by mutual NN interaction, the NN antiferromagnetic interaction is to thus avoid the formation of ordered aggregates at low  $T$ ;

- the NNN ferromagnetic interaction between further neighbours allows for a directional ordering observed in nematic phase;
- the small single-ion anisotropy is introduced to break the degeneracy of the three direction.

The method of simulation is shown above, and physical quantities are recorded with time evolution.

### V.4.2 Results

We show in Figure V.5 snapshots taken in the isotropic phase and in the final phase at  $T = 0.1$  with  $J_1 = -1$ ,  $J_2 = 2.0$ . At low- $T$  the nematic phase is found molecules oriented in the  $z$  direction without positional ordering. A video showing the cooling of the system and the dynamics leading to the formation of the nematic phase is available [here](#).

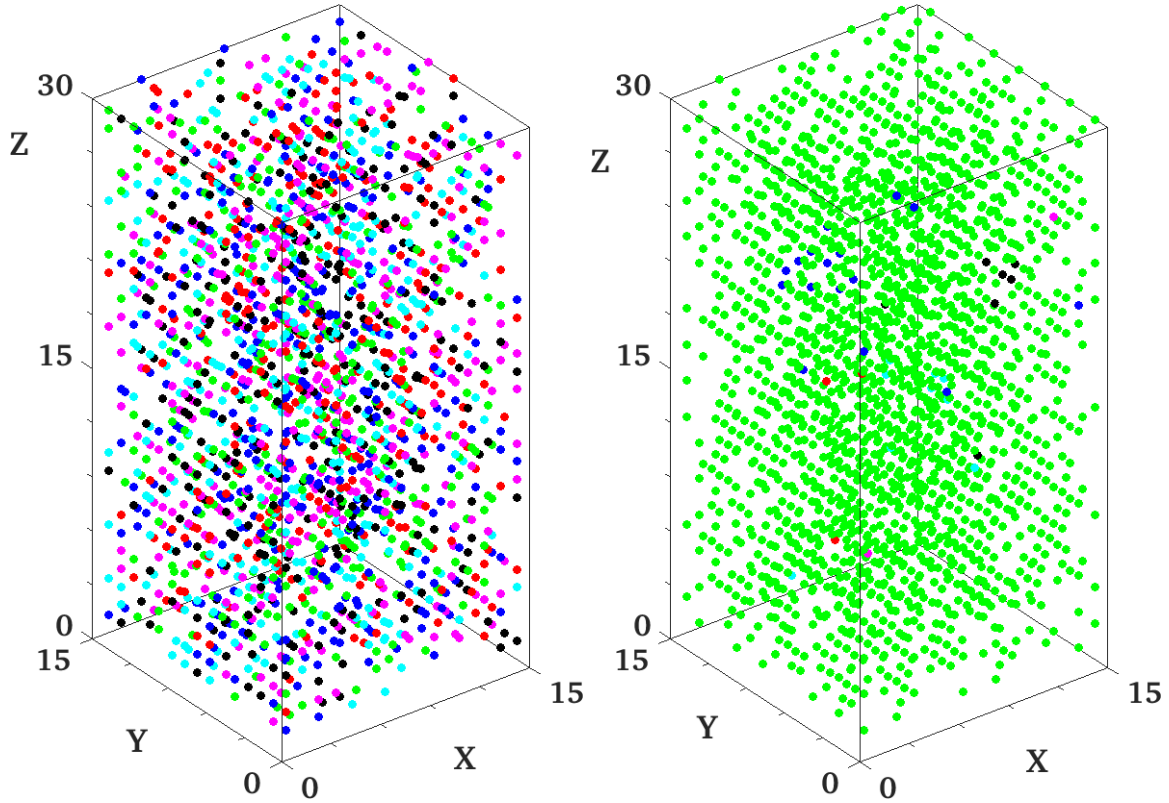


**Figure V.5** - Snapshot of the system at two different temperature. Spins are contained in a *box*. There is  $N_L = 15 \times 15 \times 30 = 6750$  sites and 2025 spins, *i.e.* a spin concentration equal to  $c = 30\%$ . Each colored point corresponds to a spin state. *Left*: Initial configuration of the system at high temperature  $T = 3$ . The system is completely disordered. *Right*: Final configuration at low temperature  $T = 0.1$  obtained by a slow cooling. Note that there is no positional order like for liquids. It corresponds to a nematic phase. A video showing the cooling of the system is available [here](#).

The internal energy per molecule and the diffusion coefficient  $D$  are shown in Figure V.6.

One observes that there is a transition from the isotropic phase to the nematic phase at  $T_c \simeq 2.20$ , with the change of curvature of  $U$  and  $D$ .

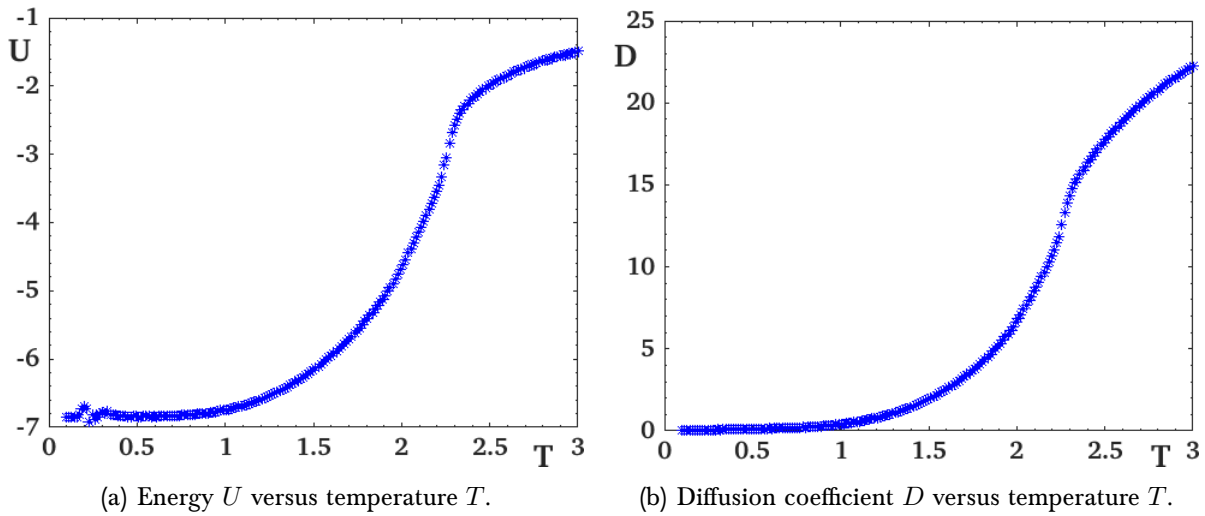


**Figure V.6** - Evolution of energy  $U$  and diffusion coefficient  $D$  versus  $T$ . The spin concentration  $c$  is  $c = N_s/N_L = 30\%$ , with  $N_L = 15 \times 15 \times 30$ . The exchange interactions are  $J_1 = -1.0$ ,  $J_2 = 2.0$  and the anisotropy is equal to  $A_z = 0.5$ .

We show in Figure V.7 the orientational order parameter which is in fact a sum of all spins averaged with time evolution. The susceptibility is also show. these quantities confirm the sharp transition mentioned above.

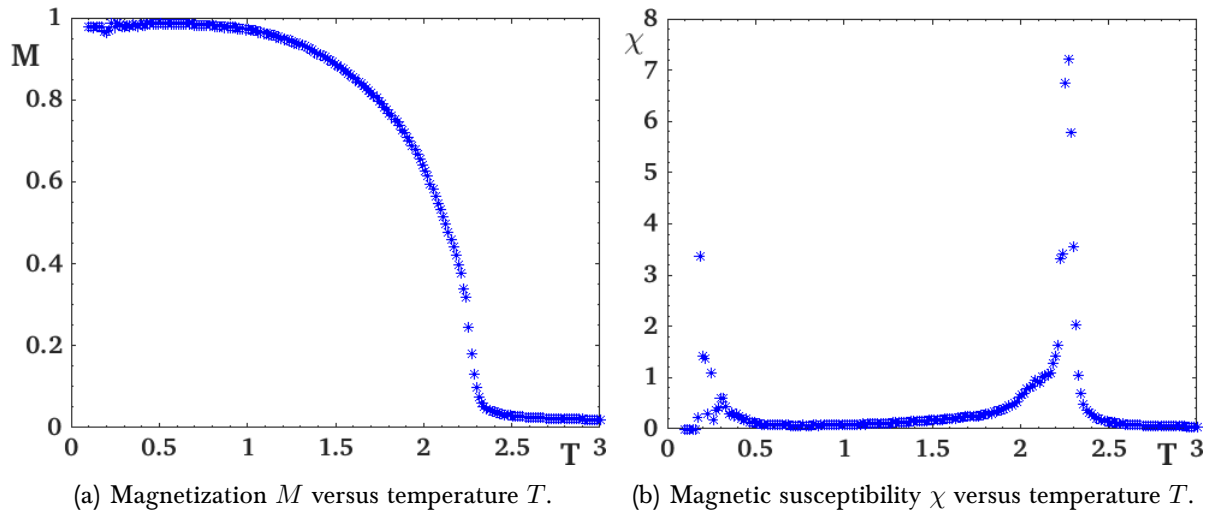


**Figure V.7** - Evolution of the orientational order parameter and its susceptibility as functions of  $T$ . The spin concentration  $c$  is  $c = N_s/N_L = 30\%$ , with  $N_L = 15 \times 15 \times 30$ . The exchange interactions are  $J_1 = -1.0$ ,  $J_2 = 2.0$  and the anisotropy is equal to  $A_z = 0.5$ .

Note that the irregularities observed in the energy (cf. Figure V.6), in the magnetization and then obviously magnetic susceptibility (cf. Figure V.7) at low temperature are due to the algorithm and are not physical. In the current MC algorithm used here, the state and the position of the spin are updated at the same time. But, the correlation times are not the same. By proceeding in two steps, *i.e.* by updating first the state and then position, there are no longer irregularities at low temperature.

The histogram of the coordination number is shown in Figure V.8 where one sees that molecules have no NN as it should be in a nematic phase.

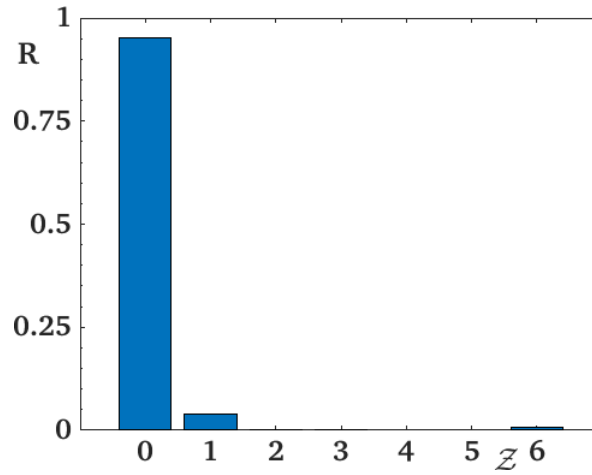


**Figure V.8** - Histogram showing the percentage  $R$  of sites having  $Z$  nearest neighbors at  $T = 0.1$ , *i.e.* corresponding to the snapshot on the right in the Figure V.5. Spins have distributed such as they have no neighbors.

## V.5 Conclusion

In this chapter, we have shown that by choosing the appropriate interactions for the Potts Hamiltonian we can get the nematic and smectic ordering from the isotropic phase by decreasing the temperature.

For both systems, we have considered Potts spins moving in three dimensional *recipients* with periodic boundary conditions in all directions. Various physical quantities, such as energy, order parameters and diffusion coefficient, as functions of temperature have been calculated

For the smectic phase, it suffices to take a strong in-plane ferromagnetic interaction and an antiferromagnetic interaction in  $z$  direction. Upon cooling the system from the isotropic phase, the molecules gathered in independent planes constituting thus a smectic structure.

To simulate nematic phase, we obviously had to take other kinds of interactions into account.

Indeed, we have chosen antiferromagnetic interactions between the NN and a stronger ferromagnetic interaction between NNN. We also have added a slight anisotropy following the  $z$  component of each spin. When cooling the system from the liquid phase, *i.e.* isotropic phase, molecules have all the same direction but no long-range positional ordering of any kind, namely no chains or planes.

# Chapter VI

## Nanodots: dipolar interaction

### Contents

---

VI.1 Introduction . . . . .	94
VI.2 Ground state . . . . .	95
VI.2.1 Model and method of ground-state determination . . . . .	95
VI.3 Melting: Mobile Spin Model . . . . .	97
VI.3.1 Model and method . . . . .	97
VI.3.2 Comparison with a localized-spin system . . . . .	99
VI.3.3 Effect on the number of layers that can melt . . . . .	100
VI.4 Conclusion . . . . .	102

---

We study in this chapter properties of a nanodot embedded in a support by Monte Carlo simulation. The nanodot is a piece of simple cubic lattice where each site is occupied by a Heisenberg spin. We take into account the short-range exchange interaction between spins, a long-range dipolar interaction, an uniaxial anisotropy. We show that the ground-state configuration is a vortex. Finite-temperature properties are studied. We show the surface melting and determine thermodynamic behaviour such as layer magnetizations as functions of temperature. The liquid phase is also studied and discussed in relation of nematic and smectic phases.

## VI.1 Introduction

 In finite systems such as magnetic thin films and nanodots, spin configurations are often non uniform near the surface. The ground-state (GS) structure results from the competition between interactions in the system. The combination of the frustration [48] resulting from competing interactions and the boundary effects in finite systems gives rise to unexpected phenomena [49]. Among the competing forces, let us focus on the dipolar interaction which favors an in-plane spin configuration in flat samples, and the perpendicular anisotropy which tends to align spins in the perpendicular axis. The perpendicular anisotropy is known to arise with a large magnitude in ultrathin films [196, 18]. Note that, in thin films with Heisenberg and Potts models, the competing dipolar interaction and perpendicular anisotropy causes a spin re-orientation transition at a finite temperature [165, 81]. There has been a great number of other works treating the dipolar interaction in the presence of a perpendicular anisotropy in 2D monolayers and thin films. All of them found various ground states (GS) such as in-plane, out-of-plane and non-uniform strip-domain configurations. Let us mention a few of them: in reference [190] an analytical calculation has been performed at zero temperature ( $T$ ) to find GS by varying the uniaxial surface anisotropy in a monolayer and in thin films (*i.e.* infinite lateral dimension). In references [138, 119, 180], Monte Carlo (MC) simulations have been carried out for monolayers and thin films at finite  $T$  where reorientation phase transitions have been found. Except in reference [180] where all transitions are of second order, the two other works found first- and second-order transitions depending of the ratio of perpendicular anisotropy to dipolar strength. In reference [128], the authors used micro-magnetic simulations to calculate the  $T = 0$  configurations for wires and disks. They did not consider finite- $T$  behaviours. The absence of works dealing with ultrathin dots at finite  $T$  has motivated the present work.

In this chapter, we focus on the case of a small magnetic nanodot with Heisenberg spins. Various GS configurations have been observed in such nanosystems [159], depending on the size of the sample, the ratio between the exchange and dipolar interactions, and the type of the lattice. Systems in which the core vortex structure occurs hold much promise from the commercial point of view; the occurrence of this structure has already been demonstrated experimentally [168, 157, 183] by different imaging techniques. A major advantage of core vortex structures is the central region (core) of nonzero perpendicular magnetization, the polarization of which is stable at room temperature (as shown by Shinjo *and al.* [168]). Interestingly, core magnetization reversal [96, 189] can be realized in two ways, by applying a strong magnetic field *perpendicular* to the surface of the sample, or a short pulse of magnetic field *parallel* to it. This property of magnetic nanodots opens the door to their application in magnetoresistive random access memory (MRAM).

The current development of a technology that allows to obtain nanosamples with a very

strong perpendicular anisotropy [44, 104, 82] has inspired us to investigate, with the use of MC simulations [108, 24], the behaviour of the core vortex structure, so interesting from the point of view of applications, under the impact of *giant* perpendicular anisotropy.

The GS structure found for a nanodot can be considered as a single skyrmion [170]. There are several mechanisms and interactions leading to the appearance of skyrmions in various kinds of matter. The most popular one is certainly the Dzyaloshinskii-Moriya (DM) interaction which was initially proposed to explain the weak ferromagnetism observed in antiferromagnetic Mn compounds. The phenomenological Landau-Ginzburg model introduced by I. Dzyaloshinskii [55] was microscopically derived by T. Moriya [137]. The DM interaction has been shown to generate skyrmions in various kinds of crystals [83, 51, 52].

In this chapter, we study a nanodot embedded in an undeformable, non magnetic crystal. The dot can be heated to high temperatures to melt. Experimentally, one can imagine periodic arrays of such a dot embedded on a crystal plane and transport properties of itinerant spins across such a plane can be studied in the presence of dots. Itinerant spins are scattered by magnetic dots and desired transport properties can be obtained by modifying dot structures.

In this chapter, thanks to MC simulations, our purpose is

- to investigate the GS configuration in magnetic nanodots taking into account the short-range exchange interaction, the long-range dipolar interaction and the perpendicular anisotropy,
- to study the nature of the ordering and the phase transition at finite temperatures in such nanodots,
- and to study melting behaviour.

The chapter is organized as follows. Section VI.2 is devoted to the determination of the GS, while section VI.3 shows MC results of finite-temperature behaviours. Concluding remarks are given in section VI.4.

## VI.2 Ground state

### VI.2.1 Model and method of ground-state determination

Let us consider a dot of size  $N \times N \times N_z$  with the cubic lattice where  $N$  is the  $x$  and  $y$  linear dimension, and  $N_z$  the height ( $z$  direction). Each lattice site is occupied by a Heisenberg spin. The Hamiltonian of the system is assumed to have the standard form:

$$\mathcal{H} = - \sum_{\langle i,j \rangle} J_{ij} \mathbf{S}_i \cdot \mathbf{S}_j - \sum_{i \neq k} \frac{D}{\|\mathbf{r}_{ik}\|^3} \left[ (\mathbf{S}_i \cdot \hat{\mathbf{e}}_{ik})(\mathbf{S}_k \cdot \hat{\mathbf{e}}_{ik}) - \mathbf{S}_i \cdot \mathbf{S}_k \right], \quad (\text{VI.1})$$

where  $J_{ij}$  denotes the exchange integral between two nearest neighbours (NN) sites  $i$  and  $j$ ,  $D$  is the dipolar coupling parameter,  $\mathbf{S}_\ell$  ( $|\mathbf{S}_\ell| = 1, \forall \ell = i, j$  or  $k$ ) is the spin at  $\ell$ -site and  $\mathbf{r}_{ik}$  is the position vector connecting the spins at the  $i$ -th and  $k$ -th sites and  $\hat{\mathbf{e}}_{ik} = \mathbf{r}_{ik}/\|\mathbf{r}_{ik}\|$  is a unit vector. The first sum is performed over all the NN spin pairs and the second over all the spin pairs.

The dipolar energy is calculated from the expression included in the Hamiltonian (VI.1) without any numerical approximations; in particular we do not introduce the cut-off radius, since this has been shown [159, 181] to affect quantitatively the calculation results in a sensible manner.

The ground state (GS) is calculated using the steepest method algorithm. As explained in the subsection IV.3.1 on page 71, for a spin on site  $i$  we calculate its local field  $\mathbf{H}_i$ , such as

$$\mathbf{H}_i = \sum_{\langle i,j \rangle} J_{ij} \mathbf{S}_j + \sum_{k \neq i} \frac{D}{\|\mathbf{r}_{ik}\|^3} \left[ (\mathbf{S}_k \cdot \hat{\mathbf{e}}_{ik}) \hat{\mathbf{e}}_{ik} - \mathbf{S}_j \right] \quad (\text{VI.2})$$

and then we align the spin in its local field, *i.e.* taking  $\mathbf{S}_i = \mathbf{H}_i/\|\mathbf{H}_i\|$ . This operation is repeated until all spins have been visited achieving thus one iteration. We performed 2000 iterations until for getting the system energy converged. Moreover, we start from different configurations to ensure it does not converge to a local minima.

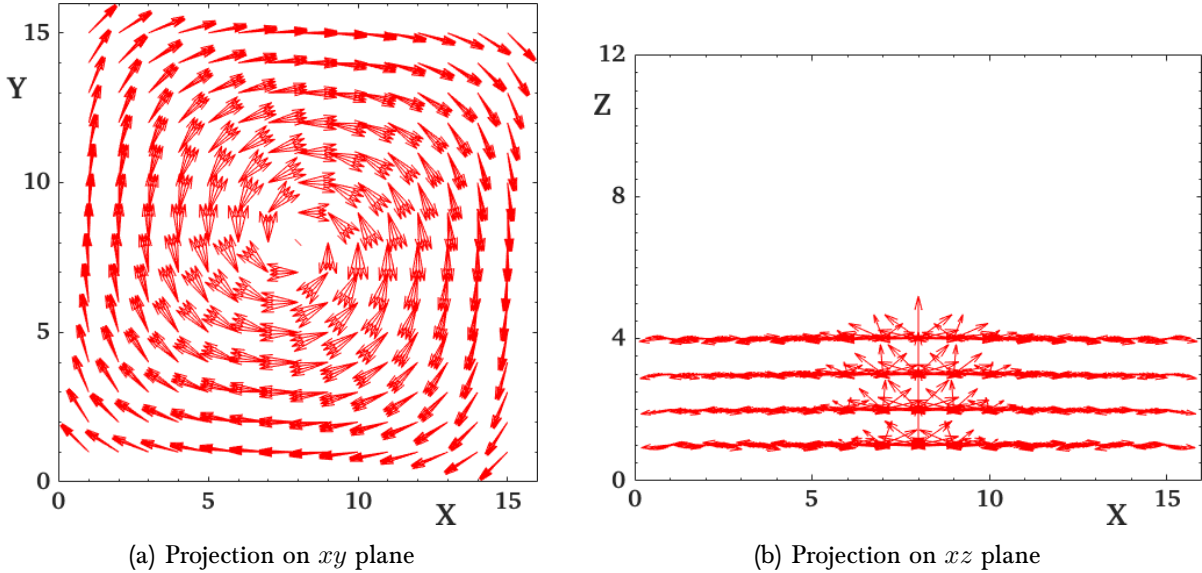


**Figure VI.1** – Ground state (GS) of the nanodot. The lattice size is  $15 \times 15 \times 12$  with a spin concentration equal to  $c = 30\%$  and with a dipolar interaction  $D = 0.7$ . The GS exhibits a vortex around the center of the dot. The spins lie in the  $xy$  plane at the border except around the vicinity of the center where they have a non-zero  $z$  component.

In the following,  $J_{ij} = J_{\perp} = 1$  between NN in the  $z$  direction and  $J_{ij} = J_{\parallel} = 4$  between in-plane NN. As will be seen below, another choice will not change physically our results but the value range of  $D$  to have vortex changes.

The GS exhibits a vortex around the dot center as shown by the Figure VI.1. The spins lie in the  $xy$  plane at the border of the dot but go out of the  $xy$  plane at the dot center to give rise to a non-zero  $z$  component. The vortex occurs only when  $D$  is larger a certain value. For instance, for four layers and  $J_{\perp} = 1$  and  $J_{\parallel} = 4$ ,  $D$  should be larger than 0.20.

## VI.3 Melting: Mobile Spin Model

### VI.3.1 Model and method

In this section, we embed the dot in a recipient of the same lateral size  $N$  but the height is much larger than the thickness  $L$  of the dot, namely the recipient of size  $N \times N \times N_z$ . The recipient is not deformable with temperature. The empty space in the  $z$  direction, namely  $N_z - L$  allows the dot to melt to become a liquid at high temperature ( $T$ ).

Let us define the concentration  $c$  by  $c = L/N_z$ . The mobile spin model consists in assuming that a spin can move from one lattice site to a nearest site. MC simulation is used to update the spin position and the spin orientation. The spin position is updated whenever there are vacant sites next to it, at the same time with the orientation update, using the Metropolis algorithm.

We start the simulation using the GS state configuration and we heat the system to a temperature  $T$ . As usual, we discard a large number of MC steps to equilibrate the system before averaging physical quantities over a large number of MC steps. Physical quantities which are calculated include the energy, the magnetization, the heat capacity and the magnetic susceptibility as functions of  $T$  for different  $c$ , different sizes of the recipient. We have also calculated the diffusion coefficient, which is the sum of the mean square of the distance made by each spin at each  $T$ . We have also computed the mean value of the number of nearest neighbours as a function of  $T$ . We recall some definitions, like The total energy

$$E = \langle \mathcal{H} \rangle \quad (\text{VI.3})$$

and the Edwards-Anderson order parameter  $Q_{EA}$  defined by

$$Q_{EA} = \frac{1}{N_T(t_f - t_0)} \sum_i \left\| \sum_{t=t_0}^{t_f} \mathbf{S}_i(t) \right\|, \quad (\text{VI.4})$$

where  $\langle \cdot \rangle$  indicates the thermal average with  $N_T$  being the total number of spins. Note that the  $Q_{EA}$  is calculated by taking the time average of each spin before averaging over all

spins of the system. This order parameter is very useful in the case of disordered systems such as spin glasses [131] or doped compounds: it expresses the degree of freezing of spins independent of whether the system has a long-range order or not [49].

To study the change of behaviour, we adopt the following method by supposing that

- all spins are localized on their site and study this case as the behaviour of the solid model;
- spins on one, two, three, ... layers (starting from the top) are mobile and study the partial; melting process
- all spins are mobile. This case corresponds to the full melting when going to high enough  $T$ .

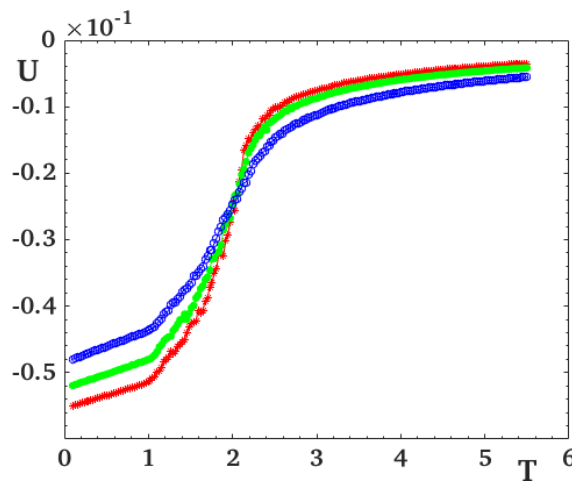


**Figure VI.2** - Effect of the concentration. The lattice size of the system is:  $15 \times 15 \times 12$  with an interaction exchange in-plane and between layers equal to  $J_{\parallel} = 4$  and  $J_{\perp} = 1$ , respectively. The **blue curve** corresponds to a spin concentration equal to  $c = 50\%$  with a magnetic dipole-dipole interaction equal to  $D = 0.3$ . The **green curve** corresponds to  $c = 0.3\%$  and  $D = 0.7$ . The **red curve** corresponds to  $c = 25\%$  and  $D = 1$ .

In Figure VI.2 are shown the results of the energy as a function of  $T$  for various  $L$ , namely various liquid concentration  $c$  with a choice of  $J_{\parallel} = 4$  and  $J_{\perp} = 1$ . All spins are mobile. It is interesting to note that the three energy curves have the same transition temperature  $T_c$ , a kind of fixed point independent of  $L$ .

The Edwards-Anderson order parameter shown in Figure VI.3(a) confirms that the transition is at the same temperature within statistical errors. We show in Figure VI.3(b) the diffusion coefficient. We see here that the spins start to move after the transition at  $T_c$  from the vortex configuration to disordered phase.

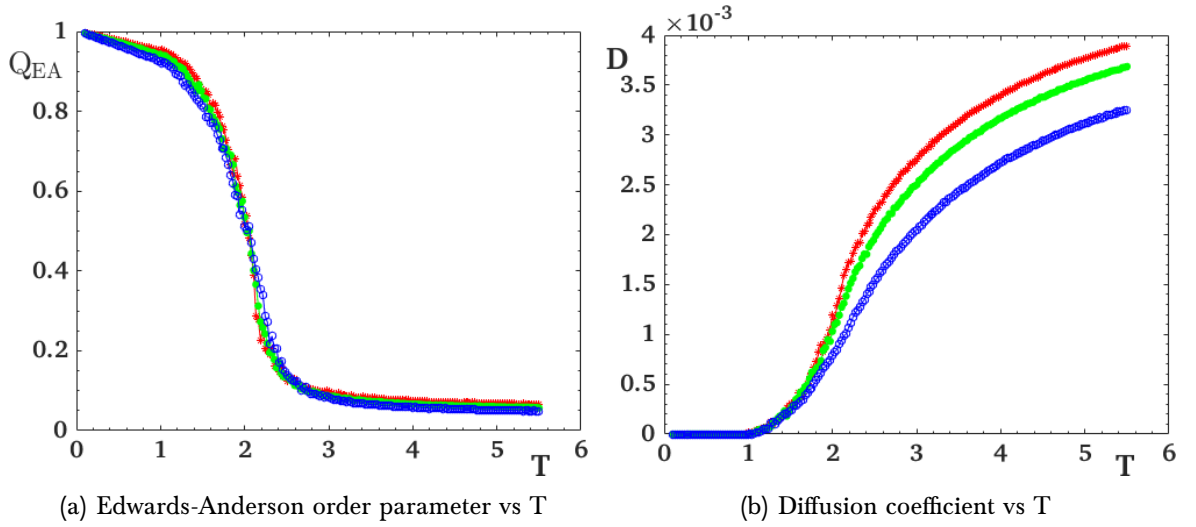


**Figure VI.3** - Effect of the concentration. The lattice size of the system is:  $15 \times 15 \times 12$  with an interaction exchange in-plane and between layers equal to  $J_{\parallel} = 4$  and  $J_{\perp} = 1$ , respectively. The **blue curve** corresponds to a spin concentration equal to  $c = 50\%$  with a magnetic dipole-dipole interaction equal to  $D = 0.3$ . The **green curve** corresponds to  $c = 0.3\%$  and  $D = 0.7$ . The **red curve** corresponds to  $c = 25\%$  and  $D = 1$ .

### VI.3.2 Comparison with a localized-spin system

We show here the case of a system of localized spins to compare with the mobile spins shown above. Figure VI.4 shows the energy for three thicknesses of the dot. Unlike the full melting case shown above, the transition occurs at a different temperature for a different thickness. This is well-known in magnetism of thin film: the transition temperature increases with increasing thickness [49].

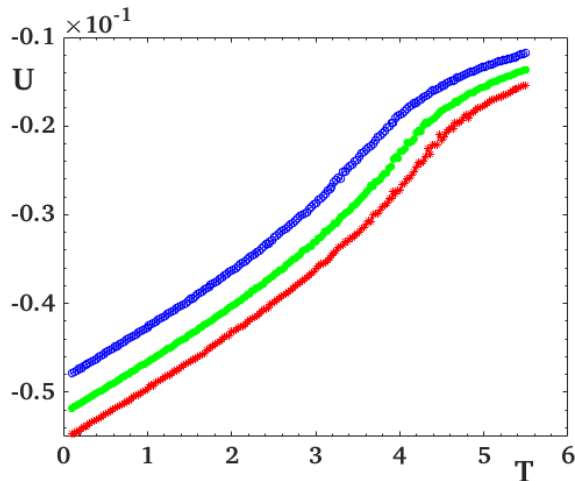


**Figure VI.4** - No mobile spin. The lattice size of the system is:  $15 \times 15 \times 12$  with an interaction exchange in-plane and between layers equal to  $J_{\parallel} = 4$  and  $J_{\perp} = 1$ , respectively. The **blue curve** corresponds to a spin concentration equal to  $c = 50\%$ , *i.e.* 6 layers, with a magnetic dipole-dipole interaction equal to  $D = 0.3$ . The **green curve** corresponds to  $c = 30\%$  (4 layers) and  $D = 0.7$ . The **red curve** corresponds to  $c = 25\%$  (3 layers) and  $D = 1$ .

In addition to the Edwards-Anderson order parameter, we can define an order parameter in the case of no long-range GS ordering: if the GS is well defined by a numerical method, then we can project the actual spin configuration of at a given  $T$  at a given time on the GS. Needless to say, if the spin configuration is not strongly deviated from the GS, the order parameter is close to 1. This has already been used in chapter IV and is defined as:

$$Q_P(T) = \frac{1}{N_T(t_f - t_0)} \sum_i \left| \sum_{t=t_0}^{t_f} \mathbf{S}_i(T, t) \cdot \mathbf{S}_i^0(T=0) \right| \quad (\text{VI.5})$$

where  $\mathbf{S}_i(T, t)$  is the  $i$ -th spin at the time  $t$ , at temperature  $T$ , and  $\mathbf{S}_i^0(T=0)$  is its state in the GS. The order parameter  $Q_P(T)$  is close to 1 at very low  $T$  where each spin is only weakly deviated from its state in the GS.  $Q_P(T)$  is zero when every spin strongly fluctuates in the paramagnetic state. The above definition of  $Q_P(T)$  is similar to the Edward-Anderson order parameter used to measure the degree of freezing in spin glasses [131]: we follow each spin with time evolving and take the spatial average at the end.

We show in Figure VI.5 the Edwards-Anderson order parameter  $Q_{EA}$  and the projection order parameter  $Q_P$  as functions of  $T$ . These confirm the difference of  $T_c$  for different  $L$ .

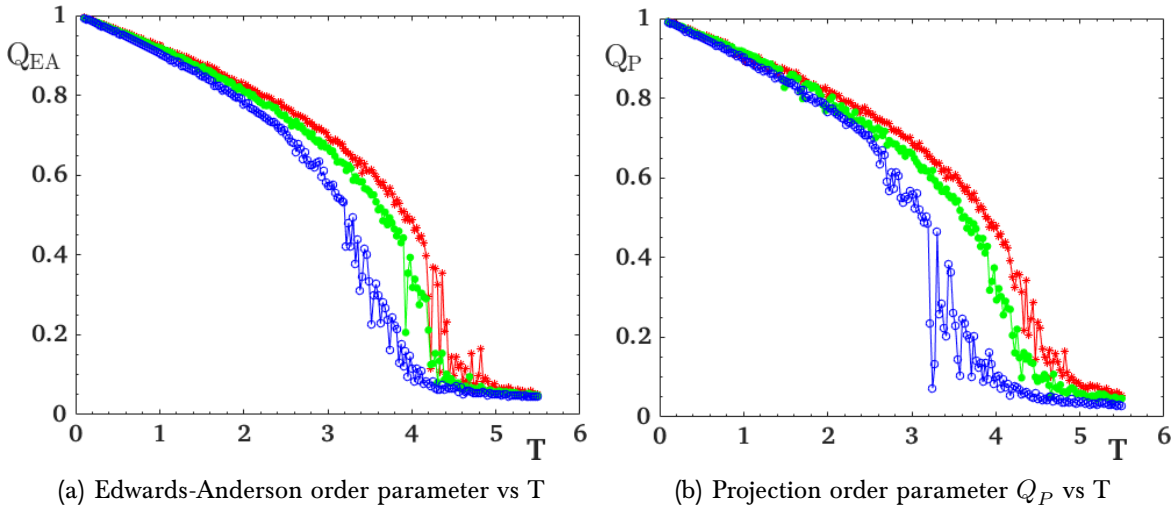


**Figure VI.5** - No mobile spin. The lattice size of the system is:  $15 \times 15 \times 12$  with an interaction exchange in-plane and between layers equal to  $J_{\parallel} = 4$  and  $J_{\perp} = 1$ , respectively. The **blue curve** corresponds to a spin concentration equal to  $c = 50\%$ , *i.e.* 6 layers, with a magnetic dipole-dipole interaction equal to  $D = 0.3$ . The **green curve** corresponds to  $c = 0.3\%$  (4 layers) and  $D = 0.7$ . The **red curve** corresponds to  $c = 25\%$  (3 layers) and  $D = 1$ .

### VI.3.3 Effect on the number of layers that can melt

Let us show now the case where spins in one, two or more layers are mobile. This allows us to follow the melting progressively. Though artificial, this procedure corresponds to a

reality when the surface layer melts first, then the second layer, ... with increasing  $T$  [21].

Figure VI.6 shows the energy and the diffusion coefficient. The case of localized spins is also shown for comparison. One sees that the transition temperature decreases as the

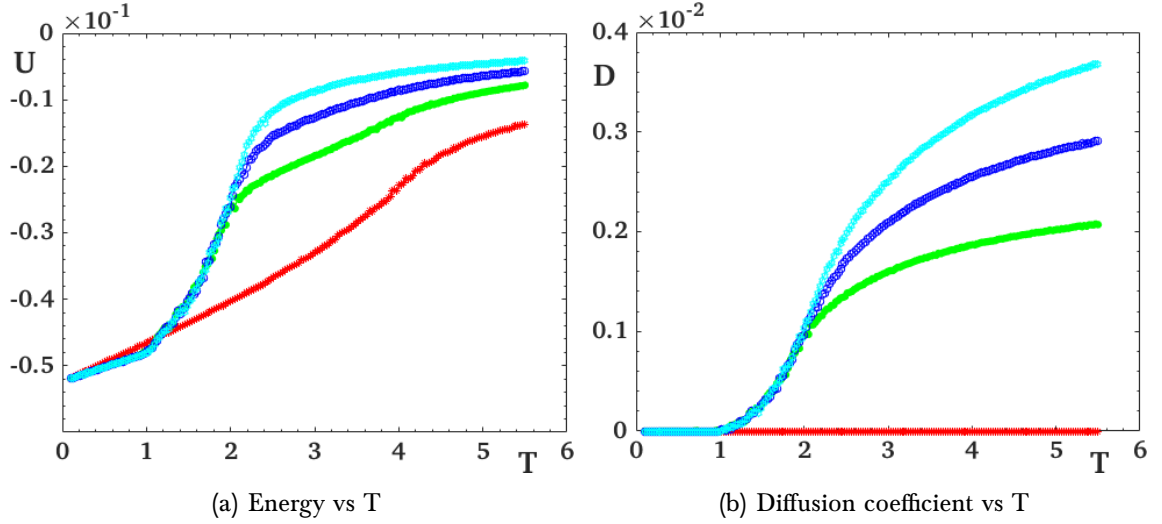


**Figure VI.6** - Effect of the number of layers that can melt. The lattice size of the system is:  $15 \times 15 \times 12$  with an interaction exchange in-plane and between layers equal to  $J_{\parallel} = 4$  and  $J_{\perp} = 1$ , respectively and  $D = 0.7$ . The concentration is fixed to  $c = 30\%$ , *i.e.* 4 filled layers. The **red curve** corresponds to a localized-spin system. The **green curve** corresponds to the two first layers (starting from the top) can melt; the **blue curve** to three mobile layers and the **cyan curve** to four mobile layers.

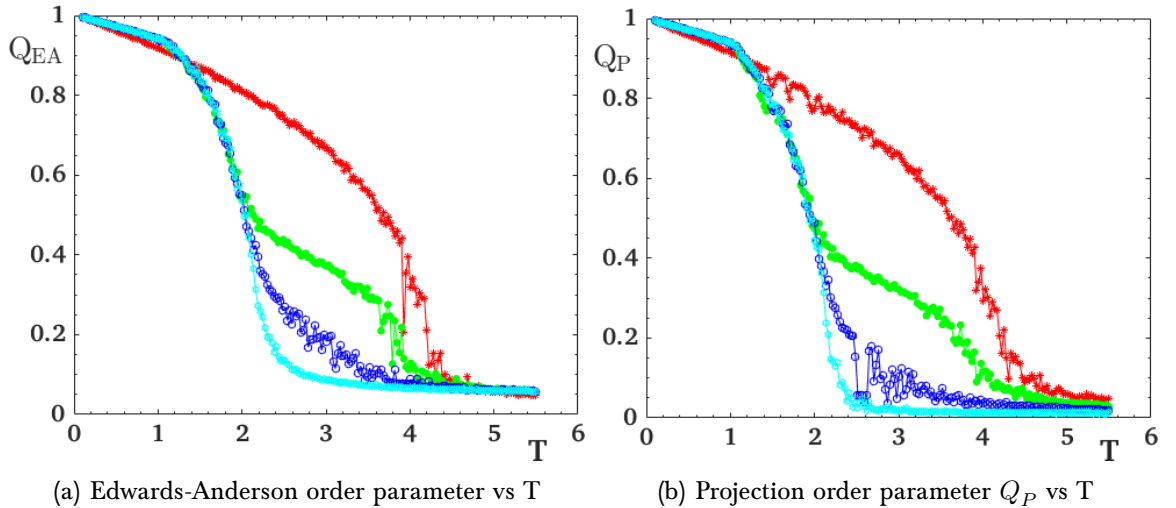


**Figure VI.7** - Effect of the number of layers that can melt. The lattice size of the system is:  $15 \times 15 \times 12$  with an interaction exchange in-plane and between layers equal to  $J_{\parallel} = 4$  and  $J_{\perp} = 1$ , respectively and  $D = 0.7$ . The concentration is fixed to  $c = 30\%$ , *i.e.* 4 filled layers. The **red curve** corresponds to a freezed system. The **green curve** corresponds to the two first layers (starting from the top) can melt; the **blue curve** to three mobile layers and the **cyan curve** to four mobile layers.

number of mobile layers increases. Note that the case of a system of completely localized spins has a very high  $T_c$ .

Figure VI.7 on the preceding page shows the Edwards-Anderson order parameter and the order parameter  $Q_P$ . Several remarks are in order

- for a system of completely localized spins or a system of completely mobile spins, there is only one transition,
- when a number of layers are mobile, the system has a partially ordered system: the localized layers are still ordered but the mobile layers are already disordered. This causes a step in the order parameters observed in Figure VI.7.

Finally, we show in Figure VI.8 the occupation rate of each layer in the system in the case  $c = 30\%$  (4 fully occupied layers). As seen, at low  $T$  only the first four layers are occupied, but after the melting, all layers have the same occupation rate as expected in the liquid phase.

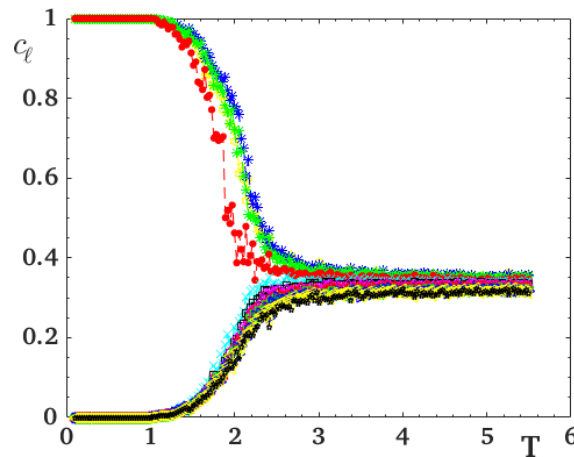


**Figure VI.8** – Occupation rate per layer  $c_\ell$  versus temperature. The lattice size of the system is:  $15 \times 15 \times 12$  with an interaction exchange in-plane and between layers equal to  $J_{\parallel} = 4$  and  $J_{\perp} = 1$ , respectively and  $D = 0.7$ . The concentration is fixed to  $c = 30\%$ , *i.e.* 4 filled layers.

## VI.4 Conclusion

In this chapter, we have studied a dot where the lattice sites are occupied by Heisenberg spins. The dot is embedded in a close recipient which allows to conserve the number of spins. We have taken into account the in-plane and perpendicular exchange interactions and the long-range dipolar interaction without cut-off. The confined geometry of the dot and the competition between exchange interactions and the dipolar interaction gives rise to a ground state which is a vortex around the dot center with the spins at the center go out of the  $xy$  plane. We have studied the melting of such a dot with increasing temperature

#### VI.4. Conclusion

---

and found that, among other results, the melting to the liquid phase takes place at the same temperature regardless of the system size. This is not the case of order-disorder phase transition in a solid film.



# Chapter VII

## Conclusion

### Contents

---

General overview . . . . .	106
----------------------------	-----

---

## General overview



In this thesis an ensemble of works has been studied with the aim to have a better understanding of properties of liquid crystals (LC). Some works deal directly with LC models and other works deal with problems related in one way or in another to properties of LC. In order to carry out this work, various and sophisticated methods have been employed: mean-field theory, spin-wave theory, Green's functions (GF) techniques and Monte Carlo (MC) simulations.

After a global Introduction (chapter I), we introduced MC methods for mobile spin systems (chapter II). The standard MC for localised spin systems cannot be applied to systems of mobile spins.

As an application of the mobile spin algorithm, we have studied a model of liquid crystals using the Potts spin model. At low temperatures ( $T$ ) the model exhibits a solid phase and at high enough temperatures the crystal melts into a liquid phase. The results of the simulations show a first-order phase transition in the bulk and a surface sublimation at the same time. These results have been confirmed by a mean-field theory. We have studied in details the surface sublimation.

The fourth chapter is devoted to spins systems with a Dzyaloshinskii-Moriya (DM) perpendicular interaction in competition with a ferromagnetic exchange interaction. It is known that these interactions give rise to topological excitations like skyrmions and stripes structures observed in LC. We studied in this chapter the spin-wave excitation in thin films. Using the spin-wave spectrum, we have calculated properties at  $T = 0$  (quantum fluctuations) and at finite temperatures. Surface effects on layer magnetisations have been shown at finite  $T$ . With an applied magnetic field perpendicular to the film surface, we have observed a crystal of skyrmions. We have shown that it is stable up to high temperatures. We have also shown that the relaxation follows a stretched exponential law which has been found in disordered systems such as spin glasses.

In chapter V, we studied the dynamics of a mobile Potts model to find how the LC orderings such as nematic and smectic phases are dynamically formed by the motion of molecules. It is very important to note the choice of appropriate interactions is crucial to realize each kind of LC phases. We have recorded video to show how such structures are formed upon cooling from the isotropic phase. We have calculated various physical quantities which confirm a transition from a liquid phase to a LC phase. This is the first time such a direct observation has been realized.

The chapter VI is devoted to a study of the effect of dipolar interaction in nanodots with the Heisenberg spin model. A ground state (GS) is determined by the minimization of the

---

energy, indicating a vortex around a dot center. The spins at the dot border lie in the plane, but they go out of the plane at the center of the dot, giving rise to a non-zero  $z$  spin component. This may have interesting applications in magnetic recording. We have studied the effect of temperature on the vortex and shown that the dot melts sharply at a temperature  $T_c$ . The melting temperature  $T_c$  surprisingly does not depend on the system size. This is very different with the case of localized spins, where the transition temperature increases with increasing film thickness. This work is the first step in direction to a complete model of helicoidal LC.

Numerous interesting results of this thesis have been published. Recent results on nanodots and on the dynamic formation of nematic and smectic phases are subject of publications (preprints).

The works of this thesis pave the way for future investigations with models closer to reality.



# Appendix A

## Markov chains

### Contents

---

A.1	Introduction . . . . .	110
A.2	Discrete-time Markov Chains . . . . .	110
A.2.1	Definitions . . . . .	110
A.2.2	Chapman-Kolmogorov equation . . . . .	112
A.2.3	Irreducibility (ergodicity) . . . . .	114
A.2.4	Stationary distribution and reversibility . . . . .	116
A.2.5	Asymptotic theorem . . . . .	118
A.2.6	Generalisation to continuous space state . . . . .	120
A.3	Continuous-time Markov chain . . . . .	120

---

We introduce here the basic knowledges about the Markov chains required to understand the mechanisms hidden behind the Markov Chain Monte Carlo (MCMC) methods, such as the Metropolis algorithm. We only deal with *homogeneous* and *discrete*-time Markov chains. For more details, one can refer to the Ross' book [162].

## A.1 Introduction



et us consider a discrete sequence of a random variables  $(X_n)_{n \in \mathbb{N}}$ , where  $X_n$  represents the state of a system at time  $n$ . This sequence constitutes a Markov chain if the evolution of the system at time  $n + 1$  depends only on the present state  $n$  and not on the previous states, *i.e.* the past. This is known as the Markov property. In the next sections,  $X$  denotes a Markov chain, which means the sequence  $X = (X_n)_{n \in \mathbb{N}}$  satisfies this property.

In the following, we consider  $\mathcal{S}$  as a discrete space in which the random variables  $X_n$  can take  $k$  discrete values :

$$X_n \in \{x_0, x_1, x_2, \dots, x_k\}. \quad (\text{A.1})$$

We also consider only the *time-homogeneous* Markov chains for which the evolution of  $X_{n+1}$  given  $X_n$  does not depend on the time  $n$ . The Markov chain is then governed by the *transition matrix* and by the initial transition probability law of the random variable  $X_0$ . The probability law of the random variable  $X_n$  at time  $n$  is defined by a row vector  $\pi_n$  such as

$$\pi_n = (\mathbb{P}(X_n = x_0), \mathbb{P}(X_n = x_1), \dots, \mathbb{P}(X_n = x_k)) \text{ and } \sum_{x_i \in \mathcal{S}} \pi_n(x_i) = 1, \quad (\text{A.2})$$

where  $\pi_n(x_i) = \mathbb{P}(X_n = x_i)$  denotes an element of  $\pi$ .

**Remark A.1 (Notations).** We use here the traditional notation  $P$  for the transition matrix and  $\pi$  for the probability distribution. It corresponds respectively to the matrix  $W$  and the probability distribution  $P$  in the sub-subsection [II.1.3.a](#).

## A.2 Discrete-time Markov Chains

### A.2.1 Definitions

We give here basic definitions about Markov chains for a better understanding.

**Definition A.1.** A matrix  $P = (P(x_i, x_j), (x_i, x_j) \in \mathcal{S}^2)$  is called stochastic if all entries are positive and their sum on each line is equal to 1, *i.e.*,

$$P(x_i, x_j) \geq 0 \text{ and } \sum_{x_j \in \mathcal{S}} P(x_i, x_j) = 1, \forall (x_i, x_j) \in \mathcal{S}^2. \quad (\text{A.3})$$

$P$  is also termed *transition matrix* or *Markov matrix*.

**Remark A.2.** Equation (A.3) can be written as the product of the transition matrix by a column vector  $\mathbf{1}$  having all its entries equal to 1, such as

$$P \cdot \mathbf{1} = \mathbf{1}. \quad (\text{A.4})$$

This relation means  $\lambda = 1$  is an eigenvalue of  $P$  and  $\mathbf{1}$  its eigenvector.

**Remark A.3 (Notations).**  $P(x_i, x_j)$  denotes the probability transition from a realisation  $x_i$  to  $x_j$ . It corresponds to an  $i^{\text{th}}$  row and  $j^{\text{th}}$  column element  $P_{ij}$  of the matrix, such as  $P(x_i, x_j) = P_{ij} = P_{i \rightarrow j}$  (according to the notations used in II.1.3.a).

**Definition A.2 (Markov chain).** Let  $P$  be a stochastic matrix. A sequence of random variable  $(X_n)_{n \in \mathbb{N}}$  with values in  $\mathcal{S}$  is termed Markov chain characterized by a transition matrix  $P$ , if for all  $n \in \mathbb{N}$  and  $x \in \mathcal{S}$ , we have

$$\mathbb{P}(X_{n+1} = x | X_n, \dots, X_0) = \mathbb{P}(X_{n+1} = x | X_n) = P(X_n, x). \quad (\text{A.5})$$

The expression (A.5) means that the element  $P(x_n, x)$  is a conditional probability of  $x$  given  $x_n$  and its totally equivalent to

$$\mathbb{P}(X_{n+1} = x | X_n = x_n, \dots, X_0 = x_0) = \mathbb{P}(X_{n+1} = x | X_n = x_n) = P(x_n, x), \quad (\text{A.6})$$

for all realisations  $x_0, \dots, x_n \in \mathcal{S}$  such as  $\mathbb{P}(X_n = x_n, \dots, X_0 = x_0) > 0$ .

**Example A.1.** Example of a basic Markov chain with two accessible states such as  $\mathcal{S} = \{x_0, x_1\}$ .

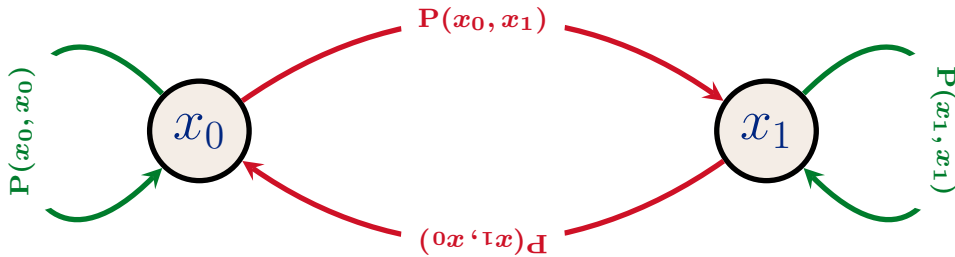


**Figure A.1** - Example of directed graph of a transition matrix  $P$ , where the nodes are elements belonging to  $\mathcal{S}$  and each directed arc is labelled by a probability transition.

**Proposition A.1.** The probability law of a Markov chain is entirely characterised by its transition matrix  $P$  and the probability law of  $X_0$ ,  $\pi_0$ . Moreover, for all  $n \in \mathbb{N}^*$  and  $x_0, \dots, x_n \in \mathcal{S}$ , we have

$$\mathbb{P}(X_0 = x_0, \dots, X_n = x_n) = \pi_0(x_0) \prod_{\ell=1}^n P(x_{\ell-1}, x_\ell), \quad (\text{A.7})$$

where  $\pi_0(x_0)$  is the first element of the vector  $\pi_0$ , such as  $\pi_0(x_0) = \mathbb{P}(X_0 = x_0)$ .

**Proof A.1.** Let  $n \in \mathbb{N}^*$  and  $x_0, \dots, x_n \in \mathcal{S}$ . If  $\mathbb{P}(X_0 = x_0, \dots, X_n = x_n) > 0$ , then by using the formula of the conditional probabilities, we have :

$$\begin{aligned} \mathbb{P}(X_n = x_n | X_0 = x_0, \dots, X_{n-1} = x_{n-1}) &= \frac{\mathbb{P}(X_0 = x_0, \dots, X_n = x_n)}{\mathbb{P}(X_0 = x_0, \dots, X_{n-1} = x_{n-1})}, \\ \mathbb{P}(X_{n-1} = x_{n-1} | X_0 = x_0, \dots, X_{n-2} = x_{n-2}) &= \frac{\mathbb{P}(X_0 = x_0, \dots, X_{n-1} = x_{n-1})}{\mathbb{P}(X_0 = x_0, \dots, X_{n-2} = x_{n-2})}, \\ &\vdots \\ \mathbb{P}(X_1 = x_1 | X_0 = x_0) &= \frac{\mathbb{P}(X_0 = x_0, X_1 = x_1)}{\mathbb{P}(X_0 = x_0)}. \end{aligned}$$

By multiplying all these equalities between them and using the equation (A.6), we reach

$$\frac{\mathbb{P}(X_0 = x_0, \dots, X_n = x_n)}{\mathbb{P}(X_0 = x_0)} = \prod_{i=1}^n P(x_{i-1}, x_i) \Leftrightarrow \mathbb{P}(X_0 = x_0, \dots, X_n = x_n) = \pi_0(x_0) \prod_{i=1}^n P(x_{i-1}, x_i).$$

□

## A.2.2 Chapman-Kolmogorov equation

In the first section, we gave an idea of what is a time-homogeneous Markov chain. We now give here a mathematical definition:

**Definition A.3.** A time-homogeneous Markov chain is one that does not depend on time and its transition probabilities are independent of time  $n$ , such as  $\forall n \in \mathbb{N}$  and  $(x_i, x_j) \in \mathcal{S}^2$ ,

$$\mathbb{P}(X_{n+1} = x_j | X_n = x_i) = \mathbb{P}(X_n = x_j | X_{n-1} = x_i) = P(x_i, x_j), \quad (\text{A.8})$$

that yields to the  $m$ -step transition probabilities

$$P^{(m)}(x_i, x_j) = \mathbb{P}(X_{n+m} = x_j | X_n = x_i), \quad (\text{A.9})$$

with  $m \in \mathbb{N}$  and  $P^{(0)}(x_i, x_j) = \delta_{i,j}$ .

From equation (A.9), we can deduce the Chapman-Kolmogorov :

$$P^{(m)}(x_i, x_j) = \sum_{x_k \in \mathcal{S}} P^{(n)}(x_i, x_k) P^{(m-n)}(x_k, x_j). \quad (\text{A.10})$$

**Proof A.2.** Let us start from equation (A.9)

$$\begin{aligned} P^{(m)}(x_i, x_j) &= \mathbb{P}(X_{n+m} = x_j | X_n = x_i) \stackrel{\langle 1 \rangle}{=} \mathbb{P}\left(X_{n+m} = x_j, \bigcup_{x_k \in \mathcal{S}} X_\ell = x_k | X_n = x_i\right), \\ &= \mathbb{P}\left(\bigcup_{x_k \in \mathcal{S}} (X_{n+m} = x_j, X_\ell = x_k) | X_n = x_i\right). \end{aligned}$$

Two different realisations of  $X_\ell$  can not occur in the *same time* (they are incompatible), their intersection two by two is then equal to the empty set. It yields

$$\begin{aligned} P^{(m)}(x_i, x_j) &= \sum_{x_k \in \mathcal{S}} \mathbb{P}(X_{n+m} = x_j, X_\ell = x_k | X_n = x_i), \\ &= \sum_{x_k \in \mathcal{S}} \frac{\mathbb{P}(X_{n+m} = x_j, X_\ell = x_k, X_n = x_i)}{\mathbb{P}(X_n = x_i)}. \end{aligned}$$

Using the equation (A.6), it comes

$$\begin{aligned} P^{(m)}(x_i, x_j) &= \sum_{x_k \in \mathcal{S}} \frac{\mathbb{P}(X_n = x_i) \mathbb{P}(X_{n+m} = x_j | X_\ell = x_k) \mathbb{P}(X_\ell = x_k | X_n = x_i)}{\mathbb{P}(X_n = x_i)}, \\ &= \sum_{x_k \in \mathcal{S}} P^{(\ell-n)}(x_i, x_k) P^{(m+n-\ell)}(x_k, x_m). \end{aligned}$$

If  $\ell = m$ , we find the expression (A.10).

□

For convenience, we can write the Chapman-Kolmogorov equation as a matrix product :

$$P^m = P^{m-n} P^n, \tag{A.11}$$

where we assume the corollary  $P^{(m)} = P^m$ , that can be easily proved by induction<sup>[⟨2⟩](#)</sup>. We can then determine the probability law  $\pi_{n+m}$  at time  $n + m$  of  $X_{n+m}$  from  $\pi_n$

$$\pi_{n+m} = \pi_n P^m. \tag{A.12}$$

This equation yields to an important consequence. Indeed, knowing the initial distribution  $\pi_0$ , we get

$$\pi_n = \pi_0 P^n, \forall n \geq 0, \tag{A.13}$$

or in an equivalent manner,

$$\mathbb{P}(X_n = x_j) = \sum_{x_i \in \mathcal{S}} \mathbb{P}(X_0 = x_i) P^n(x_i, x_j), \forall (x_i, x_j) \in \mathcal{S}^2. \tag{A.14}$$

---

<sup>[⟨1⟩](#)</sup> This equation means there is a probability to pass from a *position*  $x_i$  at time  $n$  to  $x_j$  at  $m + n$ . For that *one must be somewhere* at time  $n < \ell < m + n$ . There are different possible *paths* leading to (or leaving) a position  $X_\ell$ . One must then sum over all the paths to calculate the probability to transit from  $x_i$  to  $x_j$  passing by  $X_\ell$ .

<sup>[⟨2⟩](#)</sup>  $P^{(2)} = P \times P = P^2, P^{(3)} = P \times P^{(2)} = P^3, \dots, P^{(m+1)} = P \times P^{(m)} = P^{m+1}.$

### A.2.3 Irreducibility (ergodicity)

We now want to study all the possible paths of a Markov chain. For that, we are going to classify the different states of the chain in different *classes*. We introduce here the notions of *irreducibility* or *ergodicity* that are important for Monte Carlo simulations.

We will say two states belong to the same class if they *communicate*. We give here a definition of this notion.

**Definition A.4.** Let  $x_i$  and  $x_j$  be two states of the finite space  $\mathcal{S}$ .

A state  $x_j$  is said *accessible* from  $x_i$ , noted  $x_i \rightsquigarrow x_j$  if it exists  $n \in \mathbb{N}$  such as  $P^{(n)}(x_i, x_j) > 0$ , *i.e.* we can reach the *position*  $x_j$  starting from  $x_i$  with a positive probability in a finite time  $n$ . We will say  $x_i$  and  $x_j$  communicate, noted  $x_i \longleftrightarrow x_j$ , if we have  $x_i \rightsquigarrow x_j$  and  $x_j \rightsquigarrow x_i$ .

We are now able to define the ergodicity of a Markov chain.

**Definition A.5 (Ergodicity or irreducibility).** A Markov chain, or its transition matrix, is said *ergodic* or *irreducible* if there is only one class, *i.e.* if all the states communicate with each others. In other words, if we have  $x_i \longleftrightarrow x_j$  for all  $(x_i, x_j) \in \mathcal{S}$ . If it exists a power  $P^n$  of  $P$  such as

$$P^n(x_i, x_j) > 0, \forall (x_i, x_j) \in \mathcal{S}^2, \quad (\text{A.15})$$

*i.e.* if all the entries of  $P$  are strictly positive, the chain is said *regular*.

Obviously a regular Markov chain is irreducible, but the reverse is not true (see the example A.3). In terms of physics, a system is ergodic if all the states of the space phase can be visited over time, that is why this notion is primordial in Monte Carlo simulations.

**Remark A.4 (Mixing time).** One could naively think that more a system is ergodic faster the chain will converge on a stationary distribution. But this is not that simple. Indeed the mixing time, *i.e.* the time needed for a chain to reach the equilibrium, is actually a vast research domain in mathematics [12, 112].

**Remark A.5 (Ergodicity and aperiodicity).** In the literature, one can find another (historical) definition of the ergodicity: a *positive recurrent* (see definition A.9) and *aperiodic*<sup>(3)</sup> chain is often called an ergodic chain [169]. Actually the concept of ergodicity has nothing to do with periodicity and any positive recurrent chains is ergodic (as defined in definition A.5).

**Example A.2.** Let us consider two finite states Markov chains characterised by their transition matrix  $P_1$  and  $P_2$ . The set of accessible states, for each of them, is  $\mathcal{S} = \{x_0, x_1, x_2, x_3\}$ .  $P_1$  and

<sup>(3)</sup>The period  $d_{x_i}$  of a state  $x_i \in \mathcal{S}$  is defined as  $d_{x_i} = \text{gcd}\{n \geq 0 | P(x_i, x_i) > 0\}$ , where gcd denotes the greatest common divisor. It means  $x_i$  is periodic with period  $d$ , if  $d$  is the smallest integer such as  $P^{(n)}(x_i, x_i) > 0$  for all  $n$  non-multiple of  $d$ . If  $d = 1$ , the state is said aperiodic. If for all the states of  $\mathcal{S}$ ,  $d$  is equal to one, the chain is said aperiodic.

$P_2$  are defined by

$$P_1 = \begin{pmatrix} 0 & 1 & 0 & 0 \\ 1/2 & 1/4 & 1/4 & 0 \\ 0 & 1/8 & 3/4 & 1/8 \\ 2/3 & 0 & 0 & 1/3 \end{pmatrix}, P_2 = \begin{pmatrix} 0 & 1 & 0 & 0 \\ 3/4 & 1/4 & 0 & 0 \\ 1/8 & 0 & 7/8 & 0 \\ 0 & 0 & 1/9 & 8/9 \end{pmatrix}$$

and their directed graphs are showed on the figure A.2. The matrix  $P_1$  is irreducible as we can see on the graph on the left of the figure. Indeed, there is only one class; it is possible to get to any state from any state. It exists a time  $n = 3$  such as all the entries of  $P_1^3$  are strictly positive, i.e. regular. But this is not the case for  $P_2$ . The states  $x_2$  and  $x_3$  are not accessible from  $x_0$  and  $x_1$ ; and  $x_3$  is not accessible from the other states (see the graph on the right of the figure). The chain is not irreducible; there are three classes:  $\{x_3\} \rightsquigarrow \{x_2\} \rightsquigarrow \{x_0, x_1\}$ .

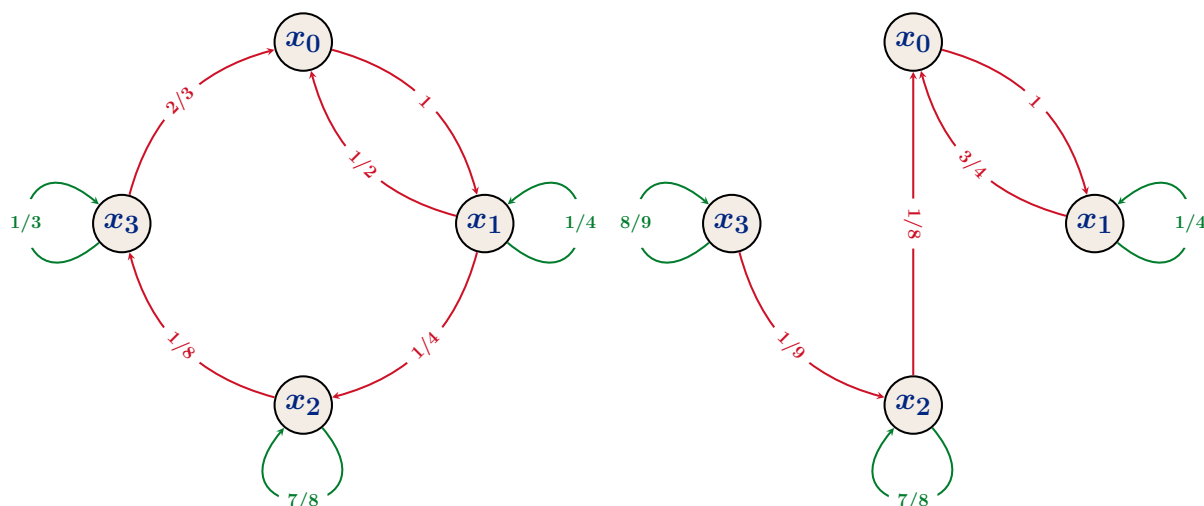


**Figure A.2** - Directed graphs of two Markov chains. *Left*: All the states communicate; the Markov chain is then irreducible. *Right*: The states  $x_2$  and  $x_3$  are not accessible form  $x_0$  and  $x_1$ . Moreover  $x_3$  is inaccessible from  $x_2$ . The chain is then not irreducible.

**Example A.3 (Ehrenfest model).** *This simple system is motivated by the thermodynamic and the statistical physics in order to model the repartition of gas molecules between two containers. The model can be expressed in this way : there are  $N$  discernible balls, numbered from 1 to  $N$ , shared among two urns. We draw randomly a number, equally distributed, between 1 and  $N$  and we move the corresponding ball into the other urn. To study its evolution over time, this system can be described by a Markov chain with the state space  $\mathcal{S} = \{0, 1, 2, \dots, N\}$ , where the state number correspond, for instance, to the number of the balls contained in the **red** urn, i.e. the right one on the Figure A.3.*

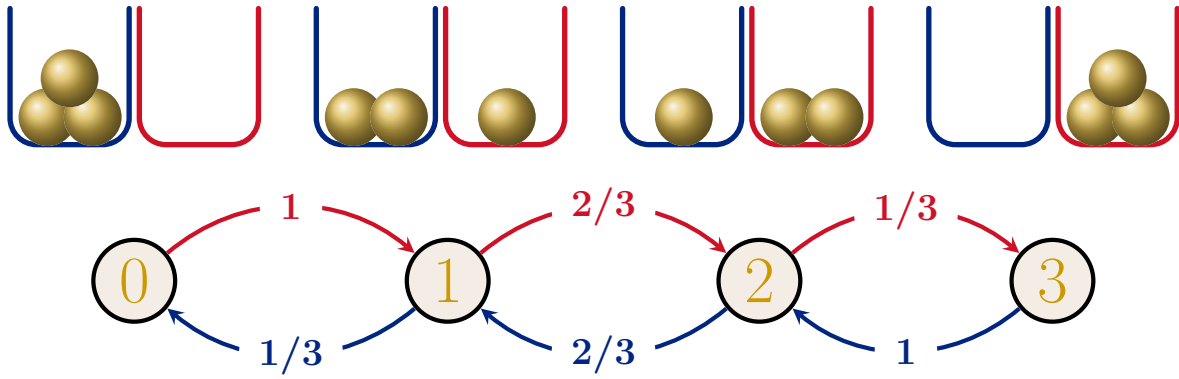


**Figure A.3** – Ehrenfest model with three balls. Let  $\mathcal{S} = \{0, 1, 2, 3\}$  be the state space of system. Each state of  $\mathcal{S}$  correspond to zero, one, two or three balls contained in the red urn, respectively. *Top*: Representation of the Ehrenfest’s urns for each state. *Down*: The oriented graph of the Markov chain associated to the model. The **red** arrows correspond to a move from the **blue** urn to the **red** one. The **blue** arrows are for the opposite moves.

As we can see on the graph, all the sates are accessible from the others in a finite time. The transition matrix is ergodic but not regular. The number of balls in the **red** urn is alternatively odd and even. Each alternate elements of the matrix are then always equal to zero for all time  $n$ . For example with  $n = 1$  and  $n = 2$ , we have:

$$P^{(1)} = \begin{pmatrix} 0 & 1 & 0 & 0 \\ 1/3 & 0 & 2/3 & 0 \\ 0 & 2/3 & 0 & 1/3 \\ 0 & 0 & 1 & 0 \end{pmatrix}, P^{(2)} = \begin{pmatrix} 1/3 & 0 & 2/3 & 0 \\ 0 & 7/9 & 0 & 2/9 \\ 2/9 & 0 & 7/9 & 0 \\ 0 & 2/3 & 0 & 1/3 \end{pmatrix}.$$

### A.2.4 Stationary distribution and reversibility

When we do Monte Carlo simulations, we need to *thermalize* the system to reach the equilibrium, *i.e.*, the stationary distribution before to calculate the averages (cf. the subsubsection II.1.3.d). In other words, we perform the procedure during a time *long enough* so that the probability law  $\pi_n$  of the Markov chain converges on an invariant distribution  $\pi$ .

**Definition A.6.** A probability distribution  $\pi$  is said to be *stationary* (or *invariant*) for the Markov chain of transition matrix  $P$  if

$$\pi = \pi P, \tag{A.16}$$

*i.e.*, if  $\pi$  is a *left*-eigenvector of  $P$  associated to the *left*-eigenvalue  $\lambda = 1$ .

The meaning of stationary distribution is explicit here. Indeed, we have

$$\pi P^n = (\pi P) P^{n-1} = \dots = \pi P = \pi, \quad (\text{A.17})$$

*i.e.* at any time the distribution is constant. Thus to determine the stationary distribution, one just need to solve a linear system.

**Remark A.6.** It can be easily proved that the module of the eigenvalue  $\lambda = 1$  is the spectral radius of the transition matrix  $P$  and its associated eigenvector is strictly positive. Under certain conditions on  $P$ , the stationary distribution is moreover unique.

**Remark A.7.** The equation (A.16) is sometimes termed *global balance* equation.

**Definition A.7.** A Markov chain with a stationary distribution  $\pi$  is *time-reversible* if and only if

$$\pi(x_i)P(x_i, x_j) = \pi(x_j)P(x_j, x_i), \forall (x_i, x_j) \in \mathcal{S}^2. \quad (\text{A.18})$$

The equation (A.18) is known as the *detailed balance*. It means the rate at which the process moves from a state  $x_i$  to a state  $x_j$  is equal to the rate at which it goes from  $x_j$  to  $x_i$ . If we assume  $X_n = x_i$  and  $X_{n-1} = x_j$ , the transition from  $x_j$  to  $x_i$  going forward in time is equivalent to the opposite transition ( $x_i \rightarrow x_j$ ) going backward in time. In one way ( $x_j \rightarrow x_i$ ), it is like we are looking forward in time and in the other way it is like to look backward in time.

**Lemma A.1.** If a distribution probability  $\pi$  satisfies the time-reversibility condition, then  $\pi$  is invariant.

**Proof A.3.** Starting from equation (A.18), let us sum over all the realisations  $x_i \in \mathcal{S}$  :

$$\begin{aligned} \sum_{x_i \in \mathcal{S}} \pi(x_i)P(x_i, x_j) &= \sum_{x_i \in \mathcal{S}} \pi(x_j)P(x_j, x_i), \forall x_j \in \mathcal{S}, \\ &= \pi(x_j) \sum_{x_i \in \mathcal{S}} P(x_j, x_i), \\ &= \pi(x_j) \text{ (cf. equation (A.3))}. \end{aligned}$$

The last equation can be written in matrix form:  $\pi = \pi P$ . According to the definition A.6,  $\pi$  is an invariant probability distribution.

□

The time-reversibility condition is an essential condition of the Metropolis algorithm; it ensures us that a stationary distribution  $\pi$  is reached.

**Example A.4 (Ehrenfest model (part 2)).** Let us find the stationary distribution  $\pi$  of the Ehrenfest model characterised by the transition matrix  $P^{(1)}$  introduced in the example A.3. The

equation (A.16) gives us a set of four linear equations. By posing  $\pi = (\alpha_0 \alpha_1 \alpha_2 \alpha_3)$ , with  $\alpha_k \in \mathbb{R}$  being the probability to have  $k = 0, 1, 2$  or  $3$  ball(s) in the **red** urn (cf. Figure A.3), it yields

$$\begin{cases} \pi = \pi P^{(1)} \\ \sum_{k=0}^3 \alpha_k = 1 \end{cases} \Rightarrow \pi = \left( \frac{1}{8} \frac{3}{8} \frac{3}{8} \frac{1}{8} \right).$$

The stationary distribution can then readily be calculated with little calculations. A smarter analysis shows it follows a binomial distribution  $\mathcal{B}(3, \frac{1}{2})$ <sup>(4)</sup>, i.e.  $\alpha_k = \binom{3}{k} (\frac{1}{2})^3$ . One can easily check the chain satisfies the equation (A.18); it is then reversible. One could have guessed it in view of the oriented graph A.3.

### A.2.5 Asymptotic theorem

In this section, we show two important results of the Markov chain. The first one concerns the uniqueness of the stationary distribution and the second one is about the convergence on the ensemble average of the time averages. But we first briefly introduce some definitions and properties that lead us to these results.

**Definition A.8 (Hitting time).** The *first hitting* time of a Markov chain  $X$  is the random variable  $T_{x_i}$  given by

$$T_{x_i} = \inf\{n \geq 1 | X_n = x_i\}, \quad (\text{A.19})$$

i.e. the time (number of transitions) needed for chain to return to the state  $x_i$ .

Let  $f_{x_i} = \mathbb{P}(T_{x_i} < +\infty | X_0 = x_i)$  be the probability that the process returns in the state  $x_i$  starting from  $x_i$ . Another way to define  $f_{x_i}$  is

$$f_{x_i} = \mathbb{P}(\exists n \geq 1, X_n = x_i | X_0 = x_i). \quad (\text{A.20})$$

**Definition A.9 (Recurrent, transient and absorbing states).**

1. If  $f_{x_i} = 1$ , the state  $x_i$  is said *recurrent* or *persistent*: starting from the *position*  $x_i$ , we are sure to go back to  $x_i$ ;
2. If  $f_{x_i} < 1$ , the state  $x_i$  is said *transient*: starting from the *position*  $x_i$ , there is a non zero probability to return to  $x_i$ ;
3. If  $P(x_i, x_i) = 1$ , the state  $x_i$  is said *absorbing*: once we are at the *position*  $x_i$ , we cannot leave it.

**Remark A.8.** If all the states of a Markov chain are recurrent (transient, respectively) the chain is then qualified of recurrent (transient, respectively).

<sup>(4)</sup>For the general case with  $N$  balls, the probability law is  $\mathcal{B}(N, \frac{1}{2})$ , i.e.  $\alpha_k = \binom{N}{k} (\frac{1}{2})^N$ , with  $k \in \llbracket 0, N \rrbracket$ .

Before to define the *positive* and *null recurrent* states, we need to introduce the notion of *mean recurrence time* defined as the expected value  $\mu_{x_i}$  of the return time  $T_{x_i}$  such as

$$\mu_{x_i} = \mathbb{E} [T_{x_i} | X_0 = x_i]. \quad (\text{A.21})$$

It is not because the first hitting time is finite that it has a finite expectation.

**Definition A.10 (Positive and null recurrent states).** Let  $x_i$  be a recurrent state. If the mean recurrence time is finite, *i.e.* if  $\mu_{x_i} < +\infty$ , the state  $x_i$  is said *positive recurrent*. Otherwise  $\mu_{x_i} = +\infty$ , the state  $x_i$  is said *null recurrent*.

**Remark A.9.** A chain is said positive recurrent (null recurrent) if all the states are positive recurrent (null recurrent).

**Theorem A.1.** If a Markov chain  $X$  with a finite space is irreducible,  $X$  is necessary positive recurrent.

To simulate a system with Monte Carlo procedures, we only consider irreducible (ergodic) Markov chain with a finite space. According to the last theorem, it means we work only with positive recurrent Markov chain and leads us naturally to the two important following theorems.

**Theorem A.2.** A positive recurrent and irreducible Markov chain has an **unique** probability distribution  $\pi$  given by

$$\pi(x_i) = \frac{1}{\mu_{x_i}}, \forall x_i \in \mathcal{S}. \quad (\text{A.22})$$

**Remark A.10.** A positive recurrent chain has then a probability distribution  $\pi$  strictly positive.

**Theorem A.3 (Ergodic theorem).** Let  $X = (X_n)_{n \in \mathbb{N}}$  be a irreducible and positive recurrent Markov chain with state space  $\mathcal{S}$ . For any functions  $h : \mathcal{S} \rightarrow \mathbb{R}$ , such as  $(\pi, |h|) < \infty$ <sup>(5)</sup>, we have:

$$\frac{1}{n+1} \sum_{\ell=0}^n h(X_\ell) \xrightarrow[n \rightarrow +\infty]{\text{a.s.}} \mathbb{E} [h(X_0)] = \sum_{x_i \in \mathcal{S}} h(x_i) \pi(x_i). \quad (\text{A.23})$$

This theorem is essential in Monte Carlo simulations. Indeed, it allows to estimate the expected value of a random variable  $h(X_0)$  thanks to the time average  $h(X_\ell)$  with  $\ell \in \mathbb{N}$ . The time averages and the ensemble averages become *equivalent*. It is similar to the law of large numbers for the Markov chains. The proof of the theorem and further information can be found here [16, 17, 93].

---

<sup>(5)</sup> $(\pi, |h|)$  denotes the scalar product, such as  $(\pi, |h|) = \sum_{x_i \in \mathcal{S}} |h(x_i)| \pi(x_i)$ . In a continuous state space  $\mathcal{S}$ ,

we would have  $(\pi, |h|) = \int_{\mathcal{S}} |h| d\pi$ , *i.e.*  $h \in L^1(\pi)$ .

**Remark A.11.** Thus the term ergodic has two definitions in appearance (at least for the physicists): it denotes the fact all the states of a system are visited over time and the equivalence of the two types of averages as described just above. That is because this theorem concerns only irreducible Markov chain (cf. definition A.5).

### A.2.6 Generalisation to continuous space state

The previous results can be generalised to a continuous space state  $\mathcal{S}$ . But instead of a two-dimension transition matrix  $P$ , we consider a function  $\wp$  of two continuous variables which is the density probability of the transition law and obviously, the discrete sums become integrals.

For instance, if  $\pi_n(x) = \mathbb{P}(X_n = x)$  represents, at time  $n$ , the density probability associated to the random variable  $X_n$ , then at time  $n + 1$ , the density probability associated to the law of  $X_{n+1}$  is given by

$$\pi_{n+1}(y) = \int \pi_n(x) \wp(x, y) dx, \quad (\text{A.24})$$

where  $(x, y) \in \mathcal{S}^2$ . This is the analogue of the equation (A.12).

## A.3 Continuous-time Markov chain

In the previous section, we only studied discrete-time Markov chain. They can be extended to the *continuous-time* Markov chain. As their discrete-time analogues, they are also characterised by the Markov property. The equivalent of the definition A.5 in the case of continuous-time Markov chains is

$$\mathbb{P}(X(t+s) = x_j | X(s) = x_i, X(u)) = \mathbb{P}(X(t+s) = x_j | X(s) = x_i), \quad (\text{A.25})$$

where  $(s, t, u) \in \mathbb{R}^3$  such as  $0 \leq t, 0 \leq u \leq s$  and  $(x_i, x_j) \in \mathcal{S}^2$ . The probability distribution  $\pi$  becomes also a continuous function of time, such as

$$\pi(t) = (\mathbb{P}(X(t) = x_0), \mathbb{P}(X(t) = x_1), \dots, \mathbb{P}(X(t) = x_k)), \quad (\text{A.26})$$

with  $x_0, x_1, \dots, x_k \in \mathcal{S}$ .

The purpose of this appendix being not to study the time-continuous Markov chains, we do not deal with this topic in details here (cf. [162] for further information).

# Appendix **B**

## Monte Carlo error analysis

### Contents

---

B.1	Statistical error and correlation time . . . . .	122
B.2	Numerical error analysis methods . . . . .	124

---

We introduce here the statistical errors occurring and we show the importance of the correlation time during a Monte Carlo simulation.

## B.1 Statistical error and correlation time



We are interested, in this appendix, in the statistical error  $\varepsilon_{\bar{\mathcal{O}}}$  on the estimator  $\bar{\mathcal{O}}$  of the theoretical average of a quantity (observable)  $\mathcal{O}$ , noted  $\langle \mathcal{O} \rangle$ . During a Monte Carlo simulation, the estimator chosen is an arithmetical mean. In other words, it is defined from a set  $\mathcal{E}$  of  $\mathcal{N}$  different measurements  $\mathcal{O}_i$  of the observable such as  $\mathcal{E} = \{\mathcal{O}_i\}_{i \in [1, \mathcal{N}]}$  and

$$\bar{\mathcal{O}} = \frac{1}{\mathcal{N}} \sum_{i=1}^{\mathcal{N}} \mathcal{O}_i. \quad (\text{B.1})$$

By performing  $\Omega$  simulation runs, in order to get  $\Omega$  different sets of measurements  $\mathcal{E}_{\Omega}$ , one can have an estimation of the mean squared error  $\varepsilon_{\bar{\mathcal{O}}}$  through

$$\varepsilon_{\bar{\mathcal{O}}} = \left\langle (\bar{\mathcal{O}} - \langle \mathcal{O} \rangle)^2 \right\rangle_{\Omega} = \left\langle (\bar{\mathcal{O}} - \langle \bar{\mathcal{O}} \rangle_{\Omega})^2 \right\rangle_{\Omega} = \langle \bar{\mathcal{O}}^2 \rangle_{\Omega} - \langle \bar{\mathcal{O}} \rangle_{\Omega}^2, \quad (\text{B.2})$$

where  $\langle \cdot \rangle_{\Omega}$  denotes an average taken over  $\Omega$  runs and  $\langle \bar{\mathcal{O}} \rangle_{\Omega}$  is the estimator of  $\langle \mathcal{O} \rangle$  and where the last term is obtained by applying the König-Huygens theorem<sup>(1)</sup>.

Then by inserting the equation (B.1) into the equation (B.2), it yields

$$\begin{aligned} \varepsilon_{\bar{\mathcal{O}}} &= \frac{1}{\mathcal{N}^2} \sum_{i=1}^{\mathcal{N}} \sum_{j=1}^{\mathcal{N}} \langle \mathcal{O}_i \mathcal{O}_j \rangle_{\Omega} - \frac{1}{\mathcal{N}^2} \sum_{i=1}^{\mathcal{N}} \langle \mathcal{O}_i \rangle_{\Omega} \sum_{j=1}^{\mathcal{N}} \langle \mathcal{O}_j \rangle_{\Omega} \\ &= \frac{1}{\mathcal{N}^2} \left\{ \sum_{i=1}^{\mathcal{N}} \left( \langle \mathcal{O}_i^2 \rangle_{\Omega} - \langle \mathcal{O}_i \rangle_{\Omega}^2 \right) - 2 \sum_{i=1}^{\mathcal{N}-1} \sum_{j=i+1}^{\mathcal{N}} \left( \langle \mathcal{O}_i \mathcal{O}_j \rangle_{\Omega} - \langle \mathcal{O}_i \rangle_{\Omega} \langle \mathcal{O}_j \rangle_{\Omega} \right) \right\}, \quad (\text{B.3}) \end{aligned}$$

where we have separated the *diagonal* and *off-diagonal* terms to pass from the first to the second line.

Let us assume the system has reached the equilibrium and therefore all the measurements, made during the MC runs, follow the Boltzmann equilibrium distribution. Then any time  $t$  can be considered as a *time zero* for the calculation of averages leading thus to a translational time invariance

$$\langle \mathcal{O}_i \mathcal{O}_j \rangle_{\Omega} = \langle \mathcal{O}_0 \mathcal{O}_t \rangle_{\Omega} = \langle \mathcal{O}_n \mathcal{O}_{n+t} \rangle_{\Omega}, \forall n \in \mathbb{N} \text{ and } t = j - i. \quad (\text{B.4})$$

<sup>(1)</sup>Let  $X$  be a random variable and  $\mathbb{E}[X]$  its expected value. The variance of  $X$ , noted  $\text{Var}(X)$ , is given by

$$\begin{aligned} \text{Var}(X) &= \mathbb{E} \left[ (X - \mathbb{E}[X])^2 \right] \\ &= \mathbb{E} \left[ X^2 - 2X\mathbb{E}[X] + \mathbb{E}[X]^2 \right] \\ &= \mathbb{E}[X^2] - 2\mathbb{E}[X]\mathbb{E}[X] + \mathbb{E}[X]^2 \\ &= \mathbb{E}[X^2] - \mathbb{E}[X]^2. \end{aligned}$$

Note that we have considered in the text the equivalence:  $\mathbb{E}[\cdot] = \langle \cdot \rangle$ .

## B.1. Statistical error and correlation time

Moreover, at the equilibrium, the individual variances  $\sigma_{\mathcal{O}_i}^2 = \langle \mathcal{O}_i^2 \rangle_\Omega - \langle \mathcal{O}_i \rangle_\Omega^2$  do not depend on time [91], having thus

$$\frac{1}{\mathcal{N}^2} \sum_{i=1}^{\mathcal{N}} \sigma_{\mathcal{O}_i}^2 = \frac{\sigma_{\mathcal{O}_i}^2}{\mathcal{N}} \quad (\text{B.5})$$

With the help of the above equations (B.4), it comes

$$\begin{aligned} \varepsilon_{\bar{\mathcal{O}}} &= \frac{1}{\mathcal{N}} \left\{ \langle \mathcal{O}_i^2 \rangle_\Omega - \langle \mathcal{O}_i \rangle_\Omega^2 + \frac{2}{\mathcal{N}} \sum_{t=1}^{\mathcal{N}-1} (\mathcal{N} - t) \left( \langle \mathcal{O}_0 \mathcal{O}_t \rangle_\Omega - \langle \mathcal{O}_0 \rangle_\Omega \langle \mathcal{O}_t \rangle_\Omega \right) \right\}, \\ &= \frac{1}{\mathcal{N}} \left\{ \sigma_{\mathcal{O}_i}^2 + 2 \sum_{t=1}^{\mathcal{N}-1} \left( 1 - \frac{t}{\mathcal{N}} \right) \left( \langle \mathcal{O}_0 \mathcal{O}_t \rangle_\Omega - \langle \mathcal{O}_0 \rangle_\Omega \langle \mathcal{O}_t \rangle_\Omega \right) \right\}, \end{aligned} \quad (\text{B.6})$$

where the factor  $(\mathcal{N} - 1)$  is the number of terms of the sum over  $j$ , in the equation (B.3), for each fixed value of the index  $i$ , which is equivalent to the number of times we have the equality  $j - i = t$ <sup>(2)</sup>.

The equation (B.6) can be expressed thanks to the normalised autocorrelation function,

$$R_{\mathcal{O}\mathcal{O}}(t) = \frac{\langle \mathcal{O}_n \mathcal{O}_{n+t} \rangle_\Omega - \langle \mathcal{O}_n \rangle_\Omega \langle \mathcal{O}_{n+t} \rangle_\Omega}{\langle \mathcal{O}_n^2 \rangle_\Omega - \langle \mathcal{O}_n \rangle_\Omega^2}, \quad (\text{B.7})$$

allowing to determine the amount of correlation between configurations. By definition this function decreases over time such as  $R_{\mathcal{O}\mathcal{O}}(0) = 1$ , meaning configurations are entirely correlated, and  $\lim_{t \rightarrow +\infty} R_{\mathcal{O}\mathcal{O}}(t) = 0$ , *i.e.* they are no longer correlated<sup>(3)</sup>. Thus, considering the translational invariance and inserting the equation (B.7) into (B.6), it comes that

$$\varepsilon_{\bar{\mathcal{O}}} = \frac{\sigma_{\mathcal{O}_i}^2}{\mathcal{N}} \left[ 1 + 2 \sum_{t=1}^{\mathcal{N}-1} \left( 1 - \frac{t}{\mathcal{N}} \right) R_{\mathcal{O}\mathcal{O}}(t) \right]. \quad (\text{B.8})$$

Let us now introduce the *proper* integrated correlation time defined by

$$\tau_{\mathcal{O}}^i = \frac{1}{2} + \sum_{t=1}^{\mathcal{N}} \left( 1 - \frac{t}{\mathcal{N}} \right) R_{\mathcal{O}\mathcal{O}}(t), \quad (\text{B.9})$$

for which the correction  $t/\mathcal{N}$  is often omitted when  $\mathcal{N} \rightarrow +\infty$ , giving thus

$$\tau_{\mathcal{O}}^i \simeq \frac{1}{2} + \sum_{t=1}^{+\infty} R_{\mathcal{O}\mathcal{O}}(t). \quad (\text{B.10})$$

<sup>(2)</sup> For instance, if  $\mathcal{N} = 4$ , there are two terms such as  $t = j - i = 2$ :  $\langle \mathcal{O}_1 \mathcal{O}_3 \rangle_\Omega = \langle \mathcal{O}_2 \mathcal{O}_4 \rangle_\Omega = \langle \mathcal{O}_0 \mathcal{O}_2 \rangle_\Omega$ .

<sup>(3)</sup> Because having configurations statistically independent, it implies:  $\langle \mathcal{O}_n \mathcal{O}_{n+t} \rangle_\Omega = \langle \mathcal{O}_n \rangle_\Omega \langle \mathcal{O}_{n+t} \rangle_\Omega = \langle \mathcal{O}_n \rangle_\Omega^2$ .

Finally, the mean squared error can be expressed as

$$\varepsilon_{\bar{\mathcal{O}}} = 2\tau_{\mathcal{O}}^i \frac{\langle \mathcal{O}_i^2 \rangle_{\Omega} - \langle \mathcal{O}_i \rangle_{\Omega}^2}{\mathcal{N}}, \quad (\text{B.11})$$

$$= 2\tau_{\mathcal{O}}^i \frac{\sigma_{\mathcal{O}_i}^2}{\mathcal{N}}. \quad (\text{B.12})$$

We see clearly the error due to temporal correlations through the correlation time and that for totally uncorrelated measurements, *i.e.*  $R_{\mathcal{O}\mathcal{O}}(t) = 0$ , the error is reduced to the classical formula of statistics. It can also be expressed in function of the number of independent measures  $\mathcal{N}_{eff} = \mathcal{N}/2\tau_{\mathcal{O}}^i$ , by

$$\varepsilon_{\bar{\mathcal{O}}} = \frac{\sigma_{\mathcal{O}_i}^2}{\mathcal{N}_{eff}}. \quad (\text{B.13})$$

$\mathcal{N}_{eff}$  describes the statistical efficiency and shows that every  $2\tau_{\mathcal{O}}^i$  iterations the measurements can be considered as uncorrelated.

## B.2 Numerical error analysis methods

The purpose of this appendix being to give the mathematical justification of the equation (II.37) and to highlight the relation between the statistical error and the correlation time, we just cite here the name of several methods dedicated to the error analysis.

As we have seen in the previous section, to calculate the statistical error on the estimator  $\bar{\mathcal{O}}$  of the quantity  $\langle \mathcal{O} \rangle$  we need to perform several sets of measurements. There are different methods allowing to get the error of these sets such as the jackknife, the bootstrap or the blocking analysis method [133, 57].

# Appendix C

## Metropolis criterion: a non normalised transition probability matrix?

### Contents

---

C.1 A brief reminder of the theoretical framework . . . . .	126
C.2 Metropolis criterion and transition matrix . . . . .	126

---

The Metropolis *strategy*, to make the Markov chain converge on an equilibrium probability distribution, has been discussed at length in chapter II. But by looking closer, it seems that the Metropolis criterion do not verify the elementary rule of probabilities, namely probabilities are normalised.

## C.1 A brief reminder of the theoretical framework



et us remind quickly several equations of the chapter about the Monte Carlo method. We have seen that Metropolis Monte Carlo relies on discrete-time Markov chains, *i.e.* the state of the chain at a given time depends only on the previous state. The evolution of these chains over time are governed by the following master equation

$$\frac{dP_f}{dt}(t) = \sum_{i \neq f} \left[ W_{i \rightarrow f} P_i(t) - W_{f \rightarrow i} P_f(t) \right], \quad (\text{C.1})$$

where  $P_i$  denotes the probability for a system to be in a state  $i$  and  $W_{i \rightarrow f}$  is the transition probability to move from a state  $i$  to  $f$ . To be more specific,  $W_{i \rightarrow f}$  is an element of the transition matrix  $W$ . The purpose of the algorithm being to find a way to reach an equilibrium probability distribution, such as  $P_i(t) \xrightarrow{t \gg 1} P_i^{eq}$ , it comes naturally

$$\frac{dP_f^{eq}}{dt} = \sum_{i \neq f} \left[ W_{i \rightarrow f} P_i^{eq} - W_{f \rightarrow i} P_f^{eq} \right] = 0, \quad (\text{C.2})$$

known as the *global balance* equation. A trivial solution of the equation (C.2) leads to the *detailed balance* condition

$$W_{i \rightarrow f} P_i^{eq} = W_{f \rightarrow i} P_f^{eq}, \quad \forall (i, f). \quad (\text{C.3})$$

One of the possible *strategies* for constructing the transition matrix so that it satisfies the above condition (C.3) is

$$W_{i \rightarrow f} = \min \left\{ 1, \frac{P_f^{eq}}{P_i^{eq}} \right\}, \quad \forall (i, f). \quad (\text{C.4})$$

This is known as the Metropolis criterion and means that if a system has a higher probability to be in a configuration  $f$  than a configuration  $i$ , then the transition from  $i$  to  $f$  occurs with a probability equal to 1. Otherwise the transition takes place with a probability equal to the ratio of  $P_f^{eq}$  to  $P_i^{eq}$ .

## C.2 Metropolis criterion and transition matrix

All the entries of the transition matrix represent a probability transition and then, by definition, the sum over all elements on each line is equal to one, *i.e.*,

$$\sum_f W_{i \rightarrow f} = 1, \quad \forall f. \quad (\text{C.5})$$

The Metropolis criterion (C.4) should also satisfy this equation, but as we will see below, this is not always true.

Let us assume we are in a *canonical description* and that the probabilities follow a Boltzmann distribution, such as

$$W_{i \rightarrow f} = \min \{1, e^{-\beta(E_f - E_i)}\}, \forall (i, f), \quad (\text{C.6})$$

and that we want to perform a simulation, based on a Metropolis algorithm, on a system with a set  $\mathcal{E}$  of possible moves from configuration  $i$  to  $f$  divided into two subsets such as

$$\mathcal{E} = \mathcal{A} \cup \mathcal{B}, \quad (\text{C.7})$$

where :

- $\mathcal{A}$  is the set of *energetically favorable* transitions, i.e.  $E_f \leq E_i$  and then  $W_{i \rightarrow f} = 1$ , according to (C.6),
- and  $\mathcal{B}$  the set of transitions such as  $E_i < E_f$  hence  $W_{i \rightarrow f} = e^{-\beta(E_f - E_i)}$ , according to (C.6).

Thus, the sum in the equation (C.5) can be split into two sums, such as

$$\sum_{i \in \mathcal{E}} W_{i \rightarrow f} = \sum_{i \in \mathcal{A}} W_{i \rightarrow f} + \sum_{i \in \mathcal{B}} W_{i \rightarrow f} \quad (\text{C.8})$$

$$= \sum_{i \in \mathcal{A}} 1 + \sum_{i \in \mathcal{B}} e^{-\beta(E_f - E_i)} \quad (\text{C.9})$$

$$= \lambda_f. \quad (\text{C.10})$$

It is obvious that  $\lambda_f$  is a constant greater or equal to one and that the relation (C.5) is not satisfied. To get normalised probabilities, we have to redefine then the elements of the transition matrix, such as

$$\widetilde{W}_{i \rightarrow f} = \frac{W_{i \rightarrow f}}{\lambda_f}. \quad (\text{C.11})$$

During a simulation, it is (almost) impossible to determine the  $\lambda_f$ ; it could be a problem. But the matrix  $\widetilde{W}$  satisfies the master equation (C.1) and given the expression of the entries of the *normalised* transition matrix, namely

$$\widetilde{W}_{i \rightarrow f} = \frac{1}{\lambda_f} \min(1, e^{-\beta(E_f - E_i)}), \quad (\text{C.12})$$

we are sure that the probabilities will reach the same equilibrium distribution as with (C.6) through the detailed balance equation, which is linear.

Let us go back to the master equation with :

$$\frac{dP_f}{dt}(t) = \sum_{i \neq f} \left[ \widetilde{W}_{i \rightarrow f} P_i(t) - \widetilde{W}_{f \rightarrow i} P_f(t) \right], \quad (\text{C.13})$$

$$= \frac{1}{\lambda_f} \sum_{i \neq f} \left[ W_{i \rightarrow f} P_i(t) - W_{f \rightarrow i} P_f(t) \right], \quad (\text{C.14})$$

where to pass from the first to the second line, we have used the equation (C.11). We now introduce a *dilated* time  $\tau = t/\lambda_f$  such as the equation (C.14) can be written as

$$\frac{dP_f}{d\tau}(\tau) = \sum_{i \neq f} \left[ W_{i \rightarrow f} P_i(\tau) - W_{f \rightarrow i} P_f(\tau) \right]. \quad (\text{C.15})$$

Thus, starting from (C.13), we finally get a master equation with non normalised probabilities  $W_{i \rightarrow f}$ , *affecting* then the repartition of the probabilities in the non stationary regime. However, when  $\dot{P}_f = 0$  is satisfied, the same probability distribution is reached independently of the kind of matrix used, *i.e.*  $W$  or  $\widetilde{W}$ . Then there is no specific problem as for the *non normalisation* of the transition matrix. Note that an analogous analysis can be done for the Metropolis-Hastings criterion leading to a similar conclusion.

# Appendix D

## Green's functions

### Contents

---

D.1	Classical Green's functions . . . . .	130
D.2	Quantum Green's functions . . . . .	131
D.2.1	Schrödinger equation and propagators . . . . .	131
D.2.2	Single-particle quantum Green's function . . . . .	132
D.3	Some calculations . . . . .	133
D.3.1	Equation of motion . . . . .	134
D.3.2	Layer magnetisation . . . . .	136

---

This appendix deals with the Green functions. A first part is dedicated to their use to solve linear differential problems. Then it is shown how they can be applied on a simple quantum mechanic case to lead us to their necessary adaptation for the quantum field theory.

## D.1 Classical Green's functions



he Green functions (GF) have been introduced by the physicist Georges Green in the first half of the nineteenth century. His works permit to create the first mathematical theory of electricity and magnetism. The GF are now commonly used in other fields like in stochastic processes theory, quantum mechanic and quantum field theory, where they are termed *propagators*. They were initially used for solving linear differential equations of the type

$$\mathfrak{D} f(t) = h(t), \quad (\text{D.1})$$

where  $\mathfrak{D}$  is a continuous linear differential operator<sup>(1)</sup>,  $f$  an unknown function we are looking for and  $h$  a given function. By analogy with signal processing,  $h$  and  $f$  can be seen as a source and an output signal<sup>(2)</sup>, respectively. To find  $f$  is then equivalent to find how to *invert* the action of  $\mathfrak{D}$ . Obviously, in some cases, one can solve this kind of equations in a *classical way*, but in some tricky cases it can be convenient (or even mandatory) to use Green's functions and therefore to treat this problem in terms of *distributions*<sup>(3)</sup>.

Let us suppose that  $\mathfrak{D}$ , in addition to be continuous and linear, is shift invariant<sup>(4)</sup>. Then it can be expressed as a convolution product<sup>(5)</sup> and it exists thus a distribution  $D$  such as [4]

$$h = \mathfrak{D} f = D * f, \quad (\text{D.2})$$

where  $*$  denotes the convolution operator. We define the Green function as every distribution  $G$  satisfying

$$\mathfrak{D} G = D * G = \delta, \quad (\text{D.3})$$

with  $\delta$  the Dirac distribution<sup>(6)</sup>. From this equation, it comes that

- $\delta$  being the neutral element of the convolution product, then  $G$  is the inverse distribution of  $D$  and then can also be seen as the inverse operator of  $\mathfrak{D}$ .

<sup>(1)</sup>  $\mathfrak{D} = \sum_{n=0}^m a_n \frac{\partial^n}{\partial t^n}$ ,  $(n, m) \in \mathbb{N}^2$ .

<sup>(2)</sup> The equations of motion are a good illustration. In this case,  $\mathfrak{D}$  corresponds to a second order time derivative operator,  $h$  to the set of forces applied on the system and  $f$  to the position of the studied object over time.

<sup>(3)</sup> Also called *generalised functions* in mathematical analysis. Distributions allow to find solutions of partial differential equations that do not admit classical solutions in terms of functions or whose initial conditions are distributions (for instance in electrostatic, a charge density locally dropped off on single point, *i.e.* a Dirac distribution).

<sup>(4)</sup> It means that  $\mathcal{T}$ , a translation operator, and  $\mathfrak{D}$  commute, such as:  $\mathcal{T}[\mathfrak{D}f] = \mathfrak{D}[\mathcal{T}f] = \mathcal{T}h$ .

<sup>(5)</sup> Indeed we have:  $\mathfrak{D}f = \mathfrak{D}[\delta * f] = \mathfrak{D}\delta * f = \delta * \mathfrak{D}f = D * f$ .

<sup>(6)</sup> Abusively defined by physicists as:  $\int_{\mathbb{R}} \delta(t - t') f(t') dt' = f(t)$ . This notation is abusive because the notion of integral concerns only functions and because the integral here lets assume that  $\delta$  is defined continuously over an interval, which is absolutely not true by definition. A rigorous definition must be done with the distribution theory:  $\langle \delta_a, \varphi \rangle = \varphi(a)$ , with  $a \in \mathbb{R}$ ,  $\phi \in \mathcal{D}$  and where  $\mathcal{D}$  is the set of *test functions*, *i.e.* the set of smooth functions of  $\mathbb{R}$  with values in  $\mathbb{C}$  with compact support.

- the Green function is the response of a system to a Dirac impulse. One speaks then of *impulse response*.

Thanks to the equation (D.3) and by *convolving* (D.2) with  $G$ , the solution of the differential equation (D.1) reads

$$f = G * h. \quad (\text{D.4})$$

The difficulty of this method lies in the determination of the Green function  $G$ . An usual method is to take the Fourier transform (FT) of the equation (D.3) to reach the algebraic form

$$\mathcal{F}[D * G] = \widehat{D} \cdot \widehat{G} = 1, \quad (\text{D.5})$$

in order to get  $\widehat{G}$  and then to take the invert FT such as we get<sup>(7)</sup>

$$G = \mathcal{F}^{-1} \left[ \frac{1}{\widehat{D}} \right]. \quad (\text{D.6})$$

Note that the circumflex denotes the FT of  $D$  and  $G$ , and that  $\mathcal{F}$  is the FT operator.

## D.2 Quantum Green's functions

### D.2.1 Schrödinger equation and propagators

The Green functions are then really adapted to solve the time-dependent Schrödinger equation, defined by

$$i\hbar \frac{\partial \psi}{\partial t}(\mathbf{r}, t) = \mathcal{H} \psi(\mathbf{r}, t), \quad (\text{D.7})$$

where  $\mathcal{H}$  is a time-independent Hamiltonian and  $\psi$  a wave function. Indeed, in order to solve the above equation, it comes that we can define a Green function  $G$  such as

$$\left[ i\hbar \frac{\partial}{\partial t} - \mathcal{H} \right] G(\mathbf{r}, t; \mathbf{r}', t') = \delta(t - t') \delta(\mathbf{r} - \mathbf{r}'), \quad (\text{D.8})$$

yielding to the self-consistent solution [25, 107]

$$\psi(\mathbf{r}, t) = \int d\mathbf{r}' \int dt' G(\mathbf{r}, t; \mathbf{r}', t') \psi(\mathbf{r}', t'), \quad (\text{D.9})$$

for  $t' < t$ . This can be easily checked by applying the operator  $[i\hbar \frac{\partial}{\partial t} - \mathcal{H}]$  on the wave function (D.9). We can also note that  $G$  plays the role of a *propagator* because it makes evolve

---

<sup>(7)</sup> As shown in the footnote <sup>(5)</sup>,  $D = \mathfrak{D}\delta$ , which implies that we are able (in most of the cases) to calculate its Fourier transform. Because of the properties of  $\delta$  and those of the FT on the derivatives, it comes that  $\widehat{D}$  is a polynomial of the same order as  $\mathfrak{D}$ .

$\psi$  from a position and time  $(\mathbf{r}', t')$  to  $(\mathbf{r}, t)$ . Actually, by expressing the wave function in the Schrödinger picture<sup>(8)</sup>, *i.e.* thanks to the time operator evolution  $U$  such as

$$\psi(\mathbf{r}, t) = U(t - t') \psi(\mathbf{r}, t') = e^{-\frac{i}{\hbar}(t-t')\mathcal{H}} \psi(\mathbf{r}, t'), \quad (\text{D.10})$$

and by using the completeness relation<sup>(9)</sup> and by expressing  $\psi(\mathbf{r}, t)$  with *bra-ket* notations as

$$\psi(\mathbf{r}, t) = \langle \mathbf{r} | \psi(t) \rangle, \quad (\text{D.11})$$

it comes naturally

$$\psi(\mathbf{r}, t) = \int \langle \mathbf{r} | e^{-\frac{i}{\hbar}(t-t')\mathcal{H}} | \mathbf{r}' \rangle \langle \mathbf{r}' | \psi(t') \rangle d\mathbf{r}'. \quad (\text{D.12})$$

Thus, by identification, the Green function  $G$  reads

$$G(\mathbf{r}, t; \mathbf{r}', t') = \theta(t - t') \langle \mathbf{r} | e^{-\frac{i}{\hbar}(t-t')\mathcal{H}} | \mathbf{r}' \rangle, \quad (\text{D.13})$$

where  $\theta$  denotes the Heaviside function<sup>(10)</sup> ensuring thus the propagation from time  $t' < t$ . Note that  $G$  is indeed a solution<sup>(11)</sup> (up to a factor  $i$ ) of the equation (D.8) [107].

## D.2.2 Single-particle quantum Green's function

After to have been introduced in quantum mechanics, Green's functions and their applications have been extended as propagators in quantum field theory notably by Richard Feynman and *its path integrals* formalism leading the equation (D.9) to another interpretation, *i.e.* being the sum over the probability amplitudes for a particle to take a specific path to *transit* from  $(\mathbf{r}, t)$  to  $(\mathbf{r}', t')$ . Later, because the second quantisation is more adapted (implicitly than the first quantisation) for the study of quantum many-body systems, he re-defined the quantum propagator that yields to the so-called single-particle retarded Green's function such as [25, 107]

$$G^R(\mathbf{r}, t; \mathbf{r}', t') = -i \theta(t - t') \left\langle \left[ \Psi(\mathbf{r}, t), \Psi^\dagger(\mathbf{r}', t') \right]_{B, F} \right\rangle, \quad (\text{D.14})$$

<sup>(8)</sup>For a time-independent Hamiltonian, the equation (D.8) yields to the solution (D.10).

<sup>(9)</sup> $\int |\mathbf{r}'\rangle \langle \mathbf{r}'| d\mathbf{r}' = \mathbb{1}$ .

<sup>(10)</sup>The Heaviside step function  $\theta$  is defined as

$$\theta(t - t') = \begin{cases} 1, & \text{for } t' < t, \\ 0, & \text{otherwise.} \end{cases}$$

<sup>(11)</sup>It can be easily checked by reminding that  $\frac{\partial \theta}{\partial t}(t - t') = \delta(t - t')$  and by rewriting  $G$  in function of eigenstates  $|n\rangle$  on which  $H$  acts ( $H|n\rangle = E_n|n\rangle$ ) such as

$$G(\mathbf{r}, t; \mathbf{r}', t') = \theta(t - t') \sum_n \langle \mathbf{r} | e^{-\frac{i}{\hbar}(t-t')E_n} | n \rangle \langle n | \mathbf{r}' \rangle = \theta(t - t') \sum_n e^{-\frac{i}{\hbar}(t-t')E_n} \varphi_n(\mathbf{r}) \varphi_n^*(\mathbf{r}'),$$

where the completeness relation had been used and where the  $\varphi_n(\mathbf{r}) = \langle \mathbf{r} | n \rangle$  are the eigenfunctions of the Hamiltonian.

### D.3. Some calculations

where  $\langle \cdot \rangle$  denotes the thermal average,  $[\cdot]_{B,F}$  a commutator or anti-commutator<sup>(12)</sup> depending on the nature of the field operator  $\Psi$  (bosonic or fermionic). It is obviously termed *retarded* because of the  $\theta(t-t')$  factor. In equivalent way, we can define the advanced Green function<sup>(13)</sup>

$$G^A(\mathbf{r}, t; \mathbf{r}', t') = i\theta(t' - t) \left\langle [\Psi(\mathbf{r}, t), \Psi^\dagger(\mathbf{r}', t')]_{B,F} \right\rangle. \quad (\text{D.15})$$

In the same manner that the Green function (D.13) is solution of the Schrödinger equation, the many-body Green function (D.14) (and then (D.15)) is solution of similar differential equation [25], the equation of motion such as

$$\begin{aligned} i\hbar \partial_t G^R(\mathbf{r}, t; \mathbf{r}', t') &= \hbar \partial_t \theta(t - t') \left\langle [\Psi(\mathbf{r}, t), \Psi^\dagger(\mathbf{r}', t')]_{B,F} \right\rangle \\ &+ \hbar \theta(t - t') \left\langle [\partial_t \Psi(\mathbf{r}, t), \Psi^\dagger(\mathbf{r}', t')]_{B,F} \right\rangle, \end{aligned} \quad (\text{D.16})$$

$$= \hbar \delta(t - t') \delta(\mathbf{r} - \mathbf{r}') + i\theta(t - t') \left\langle [[\mathcal{H}, \Psi(\mathbf{r}, t)], \Psi^\dagger(\mathbf{r}', t')]_{B,F} \right\rangle, \quad (\text{D.17})$$

where we have used the fact that the derivative of the step function is a Dirac distribution,  $[\Psi(\mathbf{r}, t), \Psi^\dagger(\mathbf{r}', t')]_{B,F} = \delta(\mathbf{r} - \mathbf{r}')$  and also that the time-derivative of an operator in Heisenberg picture<sup>(14)</sup> is reduced to  $[\mathcal{H}, \Psi(\mathbf{r}, t)]$ . This equation of motion allows us to calculate the evolution in time of the Green functions. As shown with the equation (D.17), the dynamics totally depends on the Hamiltonian and a way to determine it is to apply the Fourier transform (FT) on both side of the equality.

Note also that the Green functions can be evaluated by considering other operators than  $\Psi$ . Indeed in the chapter IV, we deal with the quantum spin operators  $S^+$  and  $S^-$ .

## D.3 Some calculations

In this subsection, we just give the results of certain calculations of the section IV.2.2.b on page 66.

<sup>(12)</sup>The bosonic commutator  $[A, B]_B = [A, B] = AB - BA$  and the fermionic anti-commutator  $[A, B]_F = \{A, B\} = AB + BA$ .

<sup>(13)</sup>Let us remark that  $G^A = (G^R)^\dagger$  for fermionic operators and  $G^A = -(G^R)^\dagger$  for bosonic operators.

<sup>(14)</sup>Note that the Schrödinger and Heisenberg representation are totally equivalent. Indeed, we have

$$\langle A \rangle(t) = \langle \psi | A_H(t) | \psi \rangle = \langle \psi(t) | A_S | \psi(t) \rangle,$$

where  $|\psi(t)\rangle = e^{-\frac{i}{\hbar}\mathcal{H}t} |\psi(0)\rangle = e^{-\frac{i}{\hbar}\mathcal{H}t} |\psi\rangle$ , while the subscripts  $H$  and  $S$  denote the Heisenberg and Schrödinger pictures, respectively. Consequently, we get  $A_H(t) = e^{\frac{i}{\hbar}\mathcal{H}t} A_S e^{-\frac{i}{\hbar}\mathcal{H}t}$ , yielding thus to

$$\frac{\partial A_H}{\partial t}(t) = \frac{i}{\hbar} \left\{ e^{\frac{i}{\hbar}\mathcal{H}t} \mathcal{H} A_S e^{-\frac{i}{\hbar}\mathcal{H}t} - e^{\frac{i}{\hbar}\mathcal{H}t} A_S \mathcal{H} e^{-\frac{i}{\hbar}\mathcal{H}t} \right\} = \frac{i}{\hbar} [\mathcal{H}, A_H(t)],$$

for a time-independent Hamiltonian and where we have used the fact that  $[e^{\pm \frac{i}{\hbar}\mathcal{H}t}, \mathcal{H}] = 0$ .

### D.3.1 Equation of motion

We want to calculate the equations of motion :

$$i\hbar \frac{\partial G_{k\ell}^R}{\partial t}(t, t') = 2 \langle \mathbf{S}_k^z \rangle \delta_{k,\ell} \delta(t - t') - \langle \langle [\mathcal{H}, \mathbf{S}_k^+(t)] ; \mathbf{S}_\ell^-(t') \rangle \rangle, \quad (\text{D.18})$$

$$i\hbar \frac{\partial F_{k\ell}^R}{\partial t}(t, t') = - \langle \langle [\mathcal{H}, \mathbf{S}_k^-(t)] ; \mathbf{S}_\ell^-(t') \rangle \rangle. \quad (\text{D.19})$$

Depending on the Hamiltonian, the calculations of the commutators can be *laborious*. We only deal here with the expansion of  $[\mathcal{H}, \mathbf{S}_k^+(t)]$ <sup>(15)</sup>, where  $\mathcal{H} = \mathcal{H}_e + \mathcal{H}_{DM} + \mathcal{H}_a$ . The expanded expression of the Hamiltonian is given by the equation (IV.22). By using the relations

$$[\mathbf{S}_k^+, \mathbf{S}_\ell^-] = 2 \mathbf{S}_k^z \delta_{k,\ell} \quad (\text{D.20})$$

$$[\mathbf{S}_k^z, \mathbf{S}_\ell^\pm] = \pm \mathbf{S}_\ell^\pm \delta_{k,\ell}, \quad (\text{D.21})$$

$$[AB, C] = [A, C]B + A[B, C], \quad (\text{D.22})$$

let us calculate the following commutators:

$$\begin{aligned} [\mathcal{H}_a, \mathbf{S}_k^+] &= \left[ - \sum_{\langle i,j \rangle} I_{ij} \mathbf{S}_i^z \mathbf{S}_j^z \cos \theta_{ij}, \mathbf{S}_k^+ \right], \\ &= - \sum_{\langle i,j \rangle} I_{ij} \left\{ [\mathbf{S}_i^z, \mathbf{S}_k^+] \mathbf{S}_j^z + \mathbf{S}_i^z [\mathbf{S}_j^z, \mathbf{S}_k^+] \right\} \cos \theta_{ij}, \\ &= - \sum_{\langle i,j \rangle} I_{ij} \left\{ \mathbf{S}_k^+ \mathbf{S}_j^z \delta_{ik} + \mathbf{S}_i^z \mathbf{S}_k^+ \delta_{jk} \right\} \cos \theta_{ij}, \\ &= -I_1 \left\{ \sum_j \mathbf{S}_k^+ \mathbf{S}_j^z \cos \theta_{kj} + \sum_i \mathbf{S}_i^z \mathbf{S}_k^+ \cos \theta_{ki} \right\}, \\ &= -I_1 \sum_i \left\{ \mathbf{S}_i^z \mathbf{S}_k^+ \cos \theta_{ki} + \mathbf{S}_i^z \mathbf{S}_k^+ \cos \theta_{ki} \right\}, \\ &= -2I_1 \sum_i \mathbf{S}_k^+ \mathbf{S}_i^z \cos \theta_{ki}, \end{aligned} \quad (\text{D.23})$$

where we have used the fact two operators acting on different sites commute and where we have *played* with the dummy variables to gather the sums in order to get the two last equations. We have also set  $I_{ij} = I_1$ .

For the other terms of  $[\mathcal{H}, \mathbf{S}_k^+(t)]$ , we proceed exactly in the same way and we reach

$$[\mathcal{H}_{DM}, \mathbf{S}_k^+] = D \sum_i \left\{ - \mathbf{S}_k^z (\mathbf{S}_i^+ + \mathbf{S}_i^-) + 2\mathbf{S}_i^+ \mathbf{S}_k^z \right\} e_{ki} \sin \theta_{ki}, \quad (\text{D.24})$$

<sup>(15)</sup>The method being exactly the same with  $\mathbf{S}_k^-(t)$ .

### D.3. Some calculations

$$\begin{aligned}
[\mathcal{H}_e, \mathbf{S}_k^+] &= - \sum_i J_{ik} \left\{ (1 - \cos \theta_{ki}) \mathbf{S}_i^- \mathbf{S}_k^z - (1 + \cos \theta_{ki}) \mathbf{S}_i^+ \mathbf{S}_k^z \right. \\
&\quad - \sin \theta_{ki} \mathbf{S}_k^z - \frac{1}{2} \sin \theta_{ki} (\mathbf{S}_k^+ \mathbf{S}_i^+ + \mathbf{S}_k^+ \mathbf{S}_i^- - 2\mathbf{S}_k^+ \mathbf{S}_i^+) \\
&\quad \left. + 2 \cos \theta_{ki} \mathbf{S}_k^+ \mathbf{S}_i^z \right\}. \tag{D.25}
\end{aligned}$$

The commutators  $[\mathcal{H}_a, \mathbf{S}_k^\pm]$  and  $[\mathcal{H}_e, \mathbf{S}_k^\pm]$  make appear, in the equations (D.18) and (D.19), terms such as  $\langle\langle \mathbf{S}_i^z \mathbf{S}_k^+; \mathbf{S}_\ell^- \rangle\rangle$  and  $\langle\langle \mathbf{S}_i^\pm \mathbf{S}_k^\pm; \mathbf{S}_\ell^- \rangle\rangle$ . We use a Tyablikov decoupling, to simplify the expressions of the above equations of motion, such as:

$$\langle\langle \mathbf{S}_i^z \mathbf{S}_k^+; \mathbf{S}_\ell^- \rangle\rangle \simeq \langle \mathbf{S}_i^z \rangle \langle\langle \mathbf{S}_k^+; \mathbf{S}_\ell^- \rangle\rangle, \tag{D.26}$$

$$\langle\langle \mathbf{S}_i^\pm \mathbf{S}_k^\pm; \mathbf{S}_\ell^- \rangle\rangle \simeq \langle \mathbf{S}_i^\pm \rangle \langle\langle \mathbf{S}_k^\pm; \mathbf{S}_\ell^- \rangle\rangle \simeq 0. \tag{D.27}$$

$\mathbf{S}_i^z$  is the constant of motion whereas the average value of the operator  $\mathbf{S}_i^\pm$  is zero with time. Indeed spins rotate around a  $z$ -axis by keep their  $z$  component constant; the transverse spin wave motions (relative to  $\mathbf{S}_i^x$ ,  $\mathbf{S}_i^y$  and then  $\mathbf{S}_i^\pm$ ) are then null in average.

In the same way, the  $[\mathcal{H}_{DM}, \mathbf{S}_k^\pm]$  leads to following Green's functions terms

$$\langle\langle \mathbf{S}_k^z \mathbf{S}_i^\pm; \mathbf{S}_\ell^- \rangle\rangle \simeq \langle \mathbf{S}_k^z \rangle \langle\langle \mathbf{S}_i^\pm; \mathbf{S}_\ell^- \rangle\rangle. \tag{D.28}$$

By using the above equations, the equation of motion (D.18) becomes

$$\begin{aligned}
i\hbar \frac{\partial G_{k\ell}^R}{\partial t}(t, t') &= - \sum_i \left\{ - 2 \langle \mathbf{S}_i^z \rangle [I_1 + J_{ki}] \cos \theta_{ki} G_{k\ell}^R \right. \\
&\quad + \langle \mathbf{S}_k^z \rangle [D \sin \theta_{ki} + J_{ki} (1 + \cos \theta_{ki})] G_{ki}^R \\
&\quad \left. + \langle \mathbf{S}_k^z \rangle [D \sin \theta_{ki} - J_{ki} (1 - \cos \theta_{ki})] F_{ki}^R \right\} \\
&\quad + 2 \langle \mathbf{S}_{k'}^z \rangle \delta_{k,\ell} \delta(t - t'). \tag{D.29}
\end{aligned}$$

In order to overcome the difficulties relative to the derivative term, we introduce the inverse time and two-dimensional Fourier transforms as follows:

$$G_{k\ell}^R(t, t') = \frac{1}{\pi^2} \int_0^\pi d^2 \mathbf{k}_\parallel \frac{1}{2\pi} \int_{-\infty}^{+\infty} d\omega e^{i\omega(t-t')} \widehat{G}_{mn}^R(\omega, \mathbf{k}_\parallel) e^{i\mathbf{k}_\parallel \cdot (\mathbf{r}_i - \mathbf{r}_j)}, \tag{D.30}$$

where  $\widehat{G}^R$  denotes the FT of the Green's function  $G^R$ ,  $\mathbf{k}_\parallel$  is a wave vector in the  $xz$  plane and  $n, m = 1, \dots, N$  are the layer ordering numbers (1 being the first layer and  $N$  the last one)<sup>(16)</sup> Note that the first integral is performed in the first zone of Brillouin.

Inserting the equation (D.30) into (D.29) and by putting  $g_{mn} = \widehat{G}_{mn}^R(\omega, \mathbf{k}_\parallel)$  and by processing exactly in the same manner for the second equation of motion (D.19), we get the set of equations defined by the linear system (IV.30).

<sup>(16)</sup>It is important to note that the  $k$  and  $\ell$  subscripts of  $G_{k\ell}^R$  denote the sites on which the GF is applied and not the layer ordering.

### D.3.2 Layer magnetisation

We show in this subsection the different step to calculate the layer magnetisation given by the equation (IV.36)

The layer magnetisation for spins system such as  $S = 1/2$  is given by

$$\langle S_n^z \rangle = \frac{1}{2} - \langle S_n^- S_n^+ \rangle, \quad (\text{D.31})$$

where  $n \in \llbracket 1, N \rrbracket$  denote the layer's numbering and  $\langle S_n^- S_n^+ \rangle$  is given by the following spectral theorem

$$\langle S_i^- S_j^+ \rangle = \lim_{\varepsilon \rightarrow 0} \frac{1}{\pi^2} \int_0^\pi \int_{\mathbb{R}} \frac{i}{2\pi} \frac{g_{n,n'}(\omega + i\varepsilon) - g_{n,n'}(\omega - i\varepsilon)}{e^{\beta\hbar\omega} - 1} e^{i\mathbf{k}_{\parallel} \cdot (\mathbf{r}_i - \mathbf{r}_j)} d\omega d^2\mathbf{k}_{\parallel}, \quad (\text{D.32})$$

$\varepsilon$  being an infinitesimal positive constant. Inserting equation (D.32) into (D.31), it comes that

$$\langle S_n^z \rangle = \frac{1}{2} - \lim_{\varepsilon \rightarrow 0} \frac{1}{\pi^2} \int_0^\pi d^2\mathbf{k}_{\parallel} \int_{\mathbb{R}} \frac{i}{2\pi} \frac{g_{n,n}(\omega + i\varepsilon) - g_{n,n}(\omega - i\varepsilon)}{e^{\beta\hbar\omega} - 1} d\omega \quad (\text{D.33})$$

where the  $g_{n,n}$  can be expressed, according to the Cramer's rule, as

$$g_{n,n} = \frac{\det(M_n)}{\det(M)}. \quad (\text{D.34})$$

$M_n$  denotes the matrix formed by replacing the  $n$ -th column of  $M$  by the vector  $\mathbf{u}$  ( $M$  and  $\mathbf{u}$  being given by the equation (IV.30)). By expressing  $M$  in a basis such as it becomes a diagonal matrix, we have then

$$M = \prod_{i=1}^N (E - E_i), \quad (\text{D.35})$$

meaning that  $E_i$  are the poles of the GF. By performing a partial fraction expansion, it comes thus

$$g_{n,n} = \frac{\det(M_n)}{\prod_i (E - E_i)} = \sum_{i=1}^N \frac{f_n(E_i)}{E - E_i} = \sum_{i=1}^N \left[ \frac{f_n(E_i)}{\prod_j (E - E_\ell)_{\ell \neq i}} \prod_{\ell \neq i} (E - E_j) \right], \quad (\text{D.36})$$

where the subscript  $j$  and  $\ell$  are such  $(j, \ell) \in \llbracket i, N \rrbracket^2$ . From this equation, we get

$$\sum_{i=1}^N \left[ f_n(E_i) \prod_{\ell \neq i} (E - E_\ell) \right] = \det(M_n). \quad (\text{D.37})$$

Thus, by putting  $E = E_i$  and by identification we reach

$$f_n(E_i) = \frac{\det(M_n(E_i))}{\prod_{j \neq i} (E_i - E_j)} \quad (\text{D.38})$$

and the GF can finally be rewritten as

$$g_{n,n} = \sum_{i=1}^N \frac{\det(M_n(E_i))}{(E - E_i) \prod_{j \neq i} (E_i - E_j)}. \quad (\text{D.39})$$

We now insert the equation (D.39) in (D.33). By using the fact that

$$\lim_{\varepsilon \rightarrow 0} \left( \frac{1}{x - i\varepsilon} - \frac{1}{x + i\varepsilon} \right) = 2i\pi\delta(x), \quad (\text{D.40})$$

with  $x = (E - E_i)$  here, we get the expression (IV.36), *i.e.*

$$\langle S_n^z \rangle = \frac{1}{2} - \frac{1}{\pi^2} \int_0^\pi \sum_{i=1}^N \frac{\det(M_n(E_i))}{(e^{\beta E_i} - 1) \prod_{i \neq j} (E_i - E_j)} d^2 \mathbf{k}_\parallel. \quad (\text{D.41})$$



# List of Publications

- *Skyrmion crystals: Dynamics and phase transition*  
H. T. Diep, S. El Hog and A. Bailly-Reyre  
AIP Advances **8**, 055707 (2018)  
<https://doi.org/10.1063/1.5006269>
- *Stability and Phase Transition of Skyrmion Crystals Generated by Dzyaloshinskii-Moriya Interaction*  
S. El Hog, A. Bailly-Reyre and H. T. Diep  
Journal of Magnetism and Magnetic Materials **455**, 32 (2018)  
<https://doi.org/10.1016/j.jmmm.2017.10.031>
- *Phase transition and surface sublimation of a mobile Potts model*  
A. Bailly-Reyre, H. T. Diep and M. Kaufman  
Physical Review E **92**, 042160 (2015)  
<https://doi.org/10.1103/PhysRevE.92.042160>
- *Phase Transition of Mobile Potts Model for Liquid Crystals*  
A. Bailly-Reyre and H. T. Diep  
ICM 2015: 20th International Conference on Magnetism  
Physics Procedia **75**, 557 (2015)  
<https://doi.org/10.1016/j.phpro.2015.12.071>



# Bibliography

- [1] P. J. Ackerman, R. P. Trivedi, B. Senyuk, J. van de Lagemaat, and I. I. Smalyukh, “Two-dimensional skyrmions and other solitonic structures in confinement-frustrated chiral nematics,” *Physical Review E*, vol. 90, p. 012505, 2014.
- [2] R. d. Almeida, N. Lemke, and I. Campbell, “Stretched exponential relaxation and independent relaxation modes,” *Brazilian Journal of Physics*, vol. 30, p. 701, 2000.
- [3] D. Amit, *Field Theory, the Renormalization Group, and Critical Phenomena*. World Scientific, 1984.
- [4] W. Appel, *Mathématiques pour la physique et les physiciens*. H&K éditions, 2002.
- [5] W. Appel, *Probabilités pour les non-probabilistes*. H&K éditions, 2013.
- [6] J. R. Banavar and A. J. Bray, “Heisenberg and potts spin glasses: A renormalization-group study,” *Physical Review B*, vol. 38, p. 2564, Aug 1988.
- [7] M. N. Barber, “Finite-size scaling,” in *Phase Transitions and Critical Phenomena*, C. Domb and J. L. Lebowitz, Eds., vol. 8. Academic Press, 1983, p. 146.
- [8] A. Bauer and C. Pfleiderer, “Magnetic phase diagram of mnsi inferred from magnetization and ac susceptibility,” *Physical Review B*, vol. 85, p. 214418, 2012.
- [9] R. J. Baxter, *Exactly solved models in statistical mechanics*. London: Academic Press, 1982.
- [10] A. Bazavov, B. A. Berg, and S. Dubey, “Phase transition properties of 3d potts models,” *Nuclear Physics B*, vol. 802, no. 3, p. 421, 2008.
- [11] F. Bechstedt, *Principles of Surface Physics*. Springer, 2003.
- [12] N. Berestycki, “Lectures on mixing times : A crossroad between probability, analysis and geometry,” Cambridge University, March 2014.

- 
- [13] A. Billoire and I. A. Campbell, “Dynamics in the sherrington-kirkpatrick Ising spin glass at and above  $T_g$ ,” *Physical Review B*, vol. 84, p. 054442, 2011.
- [14] K. Binder, “Finite size scaling analysis of Ising model block distribution functions,” *Zeitschrift für Physik B Condensed Matter*, vol. 43, no. 2, p. 119, 1981.
- [15] K. Binder and D. W. Heermann, *Monte Carlo Simulation in Statistical Physics*, 5th ed. Springer Berlin Heidelberg, 2010.
- [16] G. Birkhoff, “Proof of the ergodic theorem,” *Proceedings of the National Academy of Science*, vol. 17, p. 656, 1931.
- [17] G. Birkhoff, “What is the ergodic theorem?” *The American Mathematical Monthly*, vol. 49, no. 4, p. 222, 1942.
- [18] J. Bland and B. Heinrich, Eds., *Ultrathin Magnetic Structures*. Springer Verlag, 1994, vol. I and II.
- [19] N. A. Bobrova, A. A. Esaulov, J.-I. Sakai, P. V. Sasorov, D. J. Spence, A. Butler, S. M. Hooker, and S. V. Bulanov, “Simulations of a hydrogen-filled capillary discharge waveguide,” *Physical Review E*, vol. 65, p. 016407, 2001.
- [20] V. Bocchetti and H. T. Diep, “Melting of rare-gas crystals: Monte Carlo simulation versus experiments,” *The Journal of Chemical Physics*, vol. 138, no. 10, p. 104122, 2013.
- [21] V. Bocchetti and H. T. Diep, “Monte Carlo simulation of melting and lattice relaxation of the (111) surface of silver,” *Surface Science*, vol. 614, p. 46, 2013.
- [22] A. N. Bogdanov, U. K. Röbner, and A. A. Shestakov, “Skyrmions in nematic liquid crystals,” *Physical Review E*, vol. 67, p. 016602, 2003.
- [23] W. H. Bragg and W. L. Bragg, “The reflection of x-rays by crystals,” vol. 88, no. 605, p. 428, 1913.
- [24] S. Brooks, A. Gelman, G. Jones, and X.-L. Meng, *Handbook of Markov Chain Monte Carlo*. CRC press, 2011.
- [25] H. Bruus and K. Flensberg, *Many-Body Quantum Theory in Condensed Matter Physics: An Introduction*, ser. Oxford Graduate Texts. Oxford University Press, 2004.
- [26] S. Buhrandt and L. Fritz, “Skyrmion lattice phase in three-dimensional chiral magnets from Monte Carlo simulations,” *Physical Review B*, vol. 88, p. 195137, 2013.
- [27] G. Canevari, “Singularités dans le modèle de Landau-de Gennes pour les cristaux liquides,” Ph.D. dissertation, Université Pierre et Marie Curie, 2015.

- [28] S. Caracciolo, A. Pelissetto, and A. D. Sokal, "A general limitation on Monte Carlo algorithms of the Metropolis type," *Physical Review Letters*, vol. 72, p. 179, 1994.
- [29] P. Chaikin and T. Lubensky, *Principles of Condensed Matter Physics*. Cambridge University Press, 2000.
- [30] S. Chandrasekhar, *Liquid Crystals*, 2nd ed. Cambridge University Press, 1992.
- [31] J.-h. Chen and T. C. Lubensky, "Landau-ginzburg mean-field theory for the nematic to smectic-*c* and nematic to smectic-*a* phase transitions," *Physical Review A*, vol. 14, p. 1202, 1976.
- [32] K. C. Chu and W. L. McMillan, "Unified landau theory for the nematic, smectic *a*, and smectic *c* phases of liquid crystals," *Physical Review A*, vol. 15, p. 1181, 1977.
- [33] P. D. Coddington, "Analysis of random number generators using monte Carlo simulation," *International Journal of Modern Physics C*, vol. 05, no. 03, p. 547, 1994.
- [34] P. D. Coddington, "Tests of random number generators using Ising model simulations," *International Journal of Modern Physics C*, vol. 07, no. 03, p. 295, 1996.
- [35] J. P. Colombier, P. Combis, F. Bonneau, R. Le Harzic, and E. Audouard, "Hydrodynamic simulations of metal ablation by femtosecond laser irradiation," *Physical Review B*, vol. 71, p. 165406, 2005.
- [36] P. Davidson, D. Petermann, and A. M. Levelut, "The measurement of the nematic order parameter by X-ray scattering reconsidered," *Journal de Physique II*, p. 131, 1995.
- [37] C. De Dominicis, H. Orland, and F. Lainée, "Stretched exponential relaxation in systems with random free energies," *Journal de Physique Lettres*, vol. 46, no. 11, p. 463, 1985.
- [38] P. G. de Gennes, "Short range order effects in the isotropic phase of nematics and cholesterics," *Molecular Crystals and Liquid Crystals*, vol. 12, no. 3, p. 193, 1971.
- [39] P. G. de Gennes, "Viscous flow in smectic A liquid crystals," *The Physics of Fluids*, vol. 17, no. 9, p. 1645, 1974.
- [40] P. G. de Gennes, "An analogy between superconductors and smectics A," *Solid State Communications*, vol. 88, no. 11, p. 1039, 1993.
- [41] P. G. de Gennes and J. Prost, *The Physics of Liquid Crystals*, 2nd ed. Oxford University Press, 1995.
- [42] H. de Vries, "Rotatory power and other optical properties of certain liquid crystals," *Acta Crystallographica*, vol. 4, no. 3, p. 219, 1951.

- 
- [43] D. Demus, “Plenary lecture. one hundred years of liquid-crystal chemistry: Thermotropic liquid crystals with conventional and unconventional molecular structure,” *Liquid Crystals*, vol. 5, no. 1, p. 75, 1989.
- [44] F.J. A. den Broeder, D. Kuiper, A. P. van de Mosselaer, and W. Hoving, “Perpendicular magnetic anisotropy of Co-Au multilayers induced by interface sharpening,” *Physical Review Letters*, vol. 60, p. 2769, 1988.
- [45] M. Desjonqueres and D. Spanjaard, *Concepts in Surface Physics*. Springer, 1996.
- [46] H. T. Diep, “Quantum effects in antiferromagnetic thin films,” *Physical Review B*, vol. 43, p. 8509, 1991.
- [47] H. T. Diep, *Frustrated Spin Systems*. World Scientific, 2004, ch. 1.
- [48] H. T. Diep, Ed., *Frustrated Spin Systems*, 2nd ed. World Scientific, 2013.
- [49] H. T. Diep, *Theory of Magnetism: Application to Surface Physics*. World Scientific, 2013.
- [50] H. T. Diep, *Statistical Physics: Fundamentals and Application to Condensed Matter*. World Scientific Publishing Company, 2015.
- [51] H. T. Diep, S. El Hog, and A. Bailly-Reyre, “Skyrmion crystals: Dynamics and phase transition,” *AIP Advances*, vol. 8, no. 5, p. 055707, 2018.
- [52] H. T. Diep, S. El Hog, and A. Bailly-Reyre, “Theory and simulation: Magnetic films with Dzyaloshinskii-Moriya interaction,” *To appear in IEEE Transactions on Magnetics*, 2018.
- [53] H. T. Diep and M. Kaufman, “Extended defects in the potts-percolation model of a solid: Renormalization group and Monte Carlo analysis,” *Physical Review E*, vol. 80, p. 031116, 2009.
- [54] H. T. Diep, J. C. S. Levy, and O. Nagai, “Effect of surface spin-waves and surface anisotropy in magnetic thin films at finite temperatures,” *Physica Status Solidi b*, vol. 93, p. 351, 1979.
- [55] I. E. Dzyaloshinskii, “Thermodynamical theory of weak ferromagnetism in antiferromagnetic substances,” *Soviet Physics JETP*, vol. 465, p. 1259, 1957.
- [56] C. Ederer and N. A. Spaldin, “Weak ferromagnetism and magnetoelectric coupling in bismuth ferrite,” *Physical Review B*, vol. 71, p. 060401, 2005.
- [57] B. Efron, “Computers and the theory of statistics: Thinking the unthinkable,” *SIAM Review*, vol. 21, no. 4, p. 460, 1979.

- [58] F. Elste and C. Timm, “Theory for transport through a single magnetic molecule: Endohedral  $N@C_{60}$ ,” *Physical Review B*, vol. 71, p. 155403, 2005.
- [59] M. Ezawa, “Giant skyrmions stabilized by dipole-dipole interactions in thin ferromagnetic films,” *Physical Review Letters*, vol. 105, p. 197202, 2010.
- [60] J. L. Fergason, “Liquid crystals in nondestructive testing,” *Applied Optics*, vol. 7, no. 9, p. 1729, Sep 1968.
- [61] A. M. Ferrenberg, D. P. Landau, and K. Binder, “Statistical and systematic errors in Monte Carlo sampling,” *Journal of Statistical Physics*, vol. 63, no. 5, p. 867, 1991.
- [62] A. M. Ferrenberg and R. H. Swendsen, “New Monte Carlo technique for studying phase transitions,” *Physical Review Letters*, vol. 61, p. 2635, 1988.
- [63] A. Fert, V. Cros, and J. Sampaio, “Skyrmions on the track,” *Nature nanotechnology*, vol. 8, no. 3, p. 152, 2013.
- [64] F. C. Frank, “I. liquid crystals. on the theory of liquid crystals,” *Discussion of the Faraday Society*, vol. 25, p. 19, 1958.
- [65] G. Friedel, “Les états mésomorphes de la matière,” *Annales de Physique*, vol. 18, p. 273, 1922.
- [66] A. Gaaff and J. Hijmans, “Symmetry relations in the sixteen-vertex model,” *Physica A: Statistical Mechanics and its Applications*, vol. 80, no. 2, p. 149, 1975.
- [67] I. C. Gârlea and B. M. Mulder, “The landau-de gennes approach revisited: A minimal self-consistent microscopic theory for spatially inhomogeneous nematic liquid crystals,” *The Journal of Chemical Physics*, vol. 147, no. 24, p. 244505, 2017.
- [68] H.-O. Georgii, S. Miracle-Sole, J. Ruiz, and V. A. Zagrebnov, “Mean-field theory of the potts gas,” *Journal of Physics A: Mathematical and General*, vol. 39, no. 29, p. 9045, 2006.
- [69] D. A. Gilbert, B. B. Maranville, A. L. Balk, B. J. Kirby, P. Fischer, D. T. Piercen, J. Unguris, J. A. Borchers, and K. Liu, “Realization of ground-state artificial skyrmion lattices at room temperature,” *Nature Communication*, vol. 6, p. 8462, 2015.
- [70] S. C. Glotzer, N. Jan, T. Lookman, A. B. MacIsaac, and P. H. Poole, “Dynamical heterogeneity in the Ising spin glass,” *Physical Review E*, vol. 57, p. 7350, 1998.
- [71] L. Gómez, A. Dobry, and H. T. Diep, “Monte Carlo simulation of the role of defects as a melting mechanism,” *Physical Review B*, vol. 63, p. 224103, 2001.

- [72] L. Gómez, A. Dobry, C. Geuting, H. T. Diep, and L. Burakovsky, “Dislocation lines as the precursor of the melting of crystalline solids observed in Monte Carlo simulations,” *Physical Review Letters*, vol. 90, p. 095701, 2003.
- [73] D. J. Gross, I. Kanter, and H. Sompolinsky, “Mean-field theory of the potts glass,” *Physical Review Lett.*, vol. 55, p. 304, 1985.
- [74] C. Güven, A. N. Berker, M. Hinczewski, and H. Nishimori, “Reentrant and forward phase diagrams of the anisotropic three-dimensional Ising spin glass,” *Physical Review E*, vol. 77, p. 061110.
- [75] I. Harada and K. Motizuki, “Effect of magnon-magnon interaction on spin wave dispersion and magnon sideband in mns,” *Journal of the Physical Society of Japan*, vol. 32, no. 4, p. 927, 1972.
- [76] W. K. Hastings, “Monte Carlo sampling methods using Markov chains and their applications,” *Biometrika*, vol. 57, no. 1, p. 97, 1970.
- [77] S. Hayami, S.-Z. Lin, and C. D. Batista, “Bubble and skyrmion crystals in frustrated magnets with easy-axis anisotropy,” *Physical Review B*, vol. 93, p. 184413, 2016.
- [78] M. Heide, G. Bihlmayer, and S. Blügel, “Dzyaloshinskii-Moriya interaction accounting for the orientation of magnetic domains in ultrathin films: Fe/W(110),” *Physical Review B*, vol. 78, p. 140403, 2008.
- [79] M. Herrero-Collantes and J. C. Garcia-Escartin, “Quantum random number generators,” *Reviews of Modern Physics*, vol. 89, p. 015004, 2017.
- [80] D.-T. Hoang and H. T. Diep, “Phase transition in dimer liquids,” *Journal of Physics: Condensed Matter*, vol. 26, no. 3, p. 035103, 2014.
- [81] D.-T. Hoang, M. Kasperski, H. Puzskarski, and H. T. Diep, “Re-orientation transition in molecular thin films: Potts model with dipolar interaction,” *Journal of Physics: Condensed Matter*, vol. 25, no. 5, p. 056006, 2013.
- [82] Y. Hodumi, J. Shi, and Y. Nakamura, “Controlling the magnetic anisotropy of CoPt / AlN multilayer films,” *Applied Physics Letters*, vol. 90, no. 21, p. 212506, 2007.
- [83] S. E. Hog, A. Bailly-Reyre, and H. Diep, “Stability and phase transition of skyrmion crystals generated by Dzyaloshinskii-Moriya interaction,” *Journal of Magnetism and Magnetic Materials*, vol. 455, p. 32, 2018.
- [84] S. E. Hog, H. T. Diep, and H. Puzskarski, “Theory of magnons in spin systems with Dzyaloshinskii-Moriya interaction,” *Journal of Physics: Condensed Matter*, vol. 29, no. 30, p. 305001, 2017.

- [85] P. C. Hohenberg and B. I. Halperin, "Theory of dynamic critical phenomena," *Review of Modern Physics*, vol. 49, p. 435, 1977.
- [86] H. Ibach, *Physics of Surfaces and Interfaces*. Springer, 2006.
- [87] E. Ilker and A. N. Berker, "Odd  $q$ -state clock spin-glass models in three dimensions, asymmetric phase diagrams, and multiple algebraically ordered phases," *Physical Review E*, vol. 90, p. 062112, 2014.
- [88] Intel, "Parking lot test," notes for the MKL Intel Vector Statistics Library (VSL). [Online]. Available: <https://software.intel.com/en-us/node/590396>
- [89] Intel, "Results of the tests performed on the mersenne twister prng," notes for the MKL Intel Vector Statistics Library (VSL). [Online]. Available: <https://software.intel.com/en-us/node/590405>
- [90] F. James, "A review of pseudorandom number generators," *Computer Physics Communications*, vol. 60, no. 3, p. 329, 1990.
- [91] W. Janke, "Monte Carlo methods in classical statistical physics," in *Computational Many-Particle Physics*, H. Fehske, R. Schneider, and A. Weiße, Eds. Springer Berlin Heidelberg, 2008, ch. 4, p. 79.
- [92] D. L. Johnson, C. F. Hayes, R. J. deHoff, and C. A. Schantz, "Specific heat near the nematic-smectic-A transition of octyloxycyanobiphenyl," *Physical Review B*, vol. 18, p. 4902, 1978.
- [93] G. L. Jones, "On the markov chain central limit theorem," *Probability Surveys*, vol. 1, p. 299, 2004.
- [94] M. Kaufman, "Square-lattice Ising model in a weak uniform magnetic field: Renormalization-group analysis," *Physical Review B*, vol. 36, p. 3697, 1987.
- [95] M. Kaufman and M. Kardar, "Short-range and infinite-range bond percolation," *Physical Review B*, vol. 29, p. 5053, 1984.
- [96] N. Kikuchi, S. Okamoto, O. Kitakami, Y. Shimada, S. G. Kim, Y. Otani, and K. Fukamichi, "Vertical bistable switching of spin vortex in a circular magnetic dot," *Journal of Applied Physics*, vol. 90, no. 12, p. 6548, 2001.
- [97] S. Kirkpatrick and E. P. Stoll, "A very fast shift-register sequence random number generator," *Journal of Computational Physics*, vol. 40, no. 2, p. 517, 1981.
- [98] P. Knoll and H. Kelker, *Otto Lehmann*. Books on Demand, 2010.
- [99] D. E. Knuth, *The Art of Computer Programming, Volume 2 (3rd Ed.): Seminumerical Algorithms*. Boston, MA, USA: Addison-Wesley Longman Publishing Co., Inc., 1997.

- [100] J. M. Kosterlitz and D. J. Thouless, “Long range order and metastability in two dimensional solids and superfluids. (Application of dislocation theory),” *Journal of Physics C : Solid State Physics*, vol. 5, p. L124, 1972.
- [101] J. M. Kosterlitz and D. J. Thouless, “Ordering, metastability and phase transitions in two-dimensional systems,” *Journal of Physics C: Solid State Physics*, vol. 6, no. 7, p. 1181, 1973.
- [102] W. Krauth, “Cluster Monte Carlo algorithms,” in *New Optimization Algorithms in Physics*, A. K. Hartmann and H. Rieger, Eds. Wiley-VCH, 2005, ch. 2.
- [103] W. Krauth, *Statistical Mechanics: Algorithms and Computations*. Oxford University Press, 2006.
- [104] H. Kurt, M. Venkatesan, and J. M. D. Coey, “Enhanced perpendicular magnetic anisotropy in Co/Ni multilayers with a thin seed layer,” *Journal of Applied Physics*, vol. 108, no. 7, p. 073916, 2010.
- [105] H. Y. Kwon, S. P. Kang, Y. Z. Wu, and C. Won, “Magnetic vortex generated by Dzyaloshinskii-Moriya interaction,” *Journal of Applied Physics*, vol. 113, no. 13, p. 133911, 2013.
- [106] H. Kwon, K. Bu, Y. Wu, and C. Won, “Effect of anisotropy and dipole interaction on long-range order magnetic structures generated by Dzyaloshinskii-Moriya interaction,” *Journal of Magnetism and Magnetic Materials*, vol. 324, no. 13, p. 2171, 2012.
- [107] T. Lancaster and S. J. Blundell, *Quantum field theory for the gifted amateur*. Oxford University Press, 2014.
- [108] D. Landau and K. Binder, *A Guide to Monte Carlo Simulations in Statistical Physics*. New York, NY, USA: Cambridge University Press, 2005.
- [109] P. Lecuyer, D. Munger, B. Oreshkin, and R. Simard, “Random numbers for parallel computers: Requirements and methods, with emphasis on GPUs,” *Mathematics and Computers in Simulation*, vol. 135, p. 3, 2017, special Issue: 9th IMACS Seminar on Monte Carlo Methods.
- [110] O. Lehmann, “Über fließende krystalle,” *Zeitschrift für Physikalische Chemie*, vol. 4, p. 462, 1889.
- [111] A. O. Leonov, I. E. Dragunov, U. K. Röbller, and A. N. Bogdanov, “Theory of skyrmion states in liquid crystals,” *Physical Review E*, vol. 90, p. 042502, 2014.
- [112] D. A. Levin, Y. Peres, and E. L. Wilmer, *Markov chains and mixing times*. American Mathematical Society, 2006.

- [113] J. C. S. Levy, T. H. Diep, and O. Nagai, "Effects of surface spin waves and surface anisotropy in magnetic thin films at finite temperatures," *physica status solidi (b)*, vol. 93, no. 1, p. 351, 1979.
- [114] T. G. Lewis and W. H. Payne, "Generalized feedback shift register pseudorandom number algorithm," *Journal of ACM*, vol. 20, no. 3, p. 456, 1973.
- [115] S.-Z. Lin, A. Saxena, and C. D. Batista, "Skyrmion fractionalization and merons in chiral magnets with easy-plane anisotropy," *Physical Review B*, vol. 91, p. 224407, 2015.
- [116] T. C. Lubensky, "Hydrodynamics of cholesteric liquid crystals," *Physical Review A*, vol. 6, p. 452, 1972.
- [117] H. Lüth, *Surfaces and Interfaces of Solids*. Springer, 1993.
- [118] H. Lüth, *Solid Surfaces, Interfaces and Thin Films*. Springer, 2001.
- [119] A. B. MacIsaac, K. De'Bell, and J. P. Whitehead, "Simulation of the reorientation transition in ultrathin magnetic films with striped and tetragonal phases," *Physical Review Letters*, vol. 80, p. 616, 1998.
- [120] M. D. MacLaren and G. Marsaglia, "Uniform random number generators," *Journal of ACM*, vol. 12, no. 1, p. 83, 1965.
- [121] A. Majumdar, "Equilibrium order parameters of liquid crystals in the landau-de gennes theory," *arXiv:0808.1870*, 2009.
- [122] S. V. Maleyev, "Cubic magnets with Dzyaloshinskii-Moriya interaction at low temperature," *Physical Review B*, vol. 73, p. 174402, 2006.
- [123] A. Malinowski, V. L. Bezusyy, R. Minikayev, P. Dziawa, Y. Syryanyy, and M. Sawicki, "Spin-glass behavior in Ni-doped  $\text{La}_{1.85}\text{Sr}_{0.15}\text{CuO}_4$ ," *Physical Review B*, vol. 84, p. 024409, 2011.
- [124] G. Marsaglia, "Random numbers fall mainly in the planes," *Proceedings of the National Academy of Sciences of the United States of America*, vol. 61, no. 1, p. 25, 1968.
- [125] G. Marsaglia, "A current view of random number generators," *Proceedings, Computer Science and Statistics: 16th Symposium on the Interface*, p. 3, 1985.
- [126] G. Marsaglia, B. Narasimhan, and A. Zaman, "A random number generator for pc's," *Computer Physics Communications*, vol. 60, no. 3, p. 345, 1990.
- [127] M. Matsumoto and T. Nishimura, "Mersenne twister: A 623-dimensionally equidistributed uniform pseudo-random number generator," *ACM Transactions on Modeling and Computer Simulation*, vol. 8, no. 1, p. 3, 1998.

- [128] A. Maziewski, V. Zablotkii, and M. Kisielewski, "Geometry-driven out-of-plane magnetization states in nanostructures," *Physical Review B*, vol. 73, p. 134415, 2006.
- [129] N. D. Mermin and H. Wagner, "Absence of ferromagnetism or antiferromagnetism in one- or two-dimensional isotropic Heisenberg models," *Physical Review Letters*, vol. 17, p. 1133, 1966.
- [130] N. Metropolis, A. W. Rosenbluth, M. N. Rosenbluth, A. H. Teller, and E. Teller, "Equation of state calculations by fast computing machines," *The journal of chemical physics*, vol. 21, no. 6, p. 1087, 1953.
- [131] M. Mezard, G. Parisi, and M. A. Virasoro, *Spin Glass Theory and Beyond An Introduction to the Replica Method and Its Applications*. World Scientific, 1986.
- [132] M. Michel, S. C. Kapfer, and W. Krauth, "Generalized event-chain Monte Carlo: Constructing rejection-free global-balance algorithms from infinitesimal steps," *The Journal of Chemical Physics*, vol. 140, p. 54116, 2014.
- [133] R. G. Miller, "The jackknife - a review," *Biometrika*, vol. 61, no. 1, p. 1, 1974.
- [134] M. Mitov, C. Portet, C. Bourgerette, E. Snoeck, and M. Verelst, "Long-range structuring of nanoparticles by mimicry of a cholesteric liquid crystal," *Nature Materials*, vol. 1, p. 229, 2002.
- [135] S. Miyashita and H. Takano, "Dynamical nature of the phase transition of the two-dimensional kinetic Ising model," *Progress of Theoretical Physics*, vol. 73, no. 5, p. 1122, 1985.
- [136] J.-H. Moon, S.-M. Seo, K.-J. Lee, K.-W. Kim, J. Ryu, H.-W. Lee, R. D. McMichael, and M. D. Stiles, "Spin-wave propagation in the presence of interfacial Dzyaloshinskii-Moriya interaction," *Physical Review B*, vol. 88, p. 184404, 2013.
- [137] T. Moriya, "Anisotropic superexchange interaction and weak ferromagnetism," *Physical Review*, vol. 120, p. 91, 1960.
- [138] A. Moschel and K. D. Usadel, "Reorientation transitions of first and second order in thin ferromagnetic films," *Physical Review B*, vol. 51, p. 16111, 1995.
- [139] S. Mühlbauer, B. Binz, F. Jonietz, C. Pfleiderer, A. Rosch, A. Neubauer, R. Georgii, and P. Böni, "Skyrmion lattice in a chiral magnet," *Science*, vol. 323, no. 5916, p. 915, 2009.
- [140] A. K. Murtazaev, A. Babaev, and G. Aznaurova, "Investigation of the critical properties in the 3Ds site-diluted potts model," in *Magnetism and Magnetic Materials*, ser. Solid State Phenomena, vol. 152. Trans Tech Publications, 10 2009, p. 571.

- [141] V. T. Ngo and H. T. Diep, “Frustration effects in antiferromagnetic face-centered cubic Heisenberg films,” *Journal of Physics: Condensed Matter*, vol. 19, p. 386202, 2007.
- [142] V. T. Ngo and H. Diep, “Effects of frustrated surface in Heisenberg thin films,” *Physical Review B*, vol. 75, p. 035412, 2007.
- [143] V. T. Ngo, D. T. Hoang, H. T. Diep, and I. A. Campbell, “Effect of disorder in the frustrated Ising fcc antiferromagnet: phase diagram and stretched exponential relaxation,” *Modern Physics Letters B*, vol. 28, no. 09, p. 1450067, 2014.
- [144] B. Nienhuis, A. N. Berker, E. K. Riedel, and M. Schick, “First- and second-order phase transitions in potts models: Renormalization-group solution,” *Physical Review Letters*, vol. 43, p. 737, 1979.
- [145] M. P. Nightingale and H. W. J. Blöte, “Dynamic exponent of the two-dimensional Ising model and Monte Carlo computation of the subdominant eigenvalue of the stochastic matrix,” *Physical Review Letters*, vol. 76, p. 4548, 1996.
- [146] A. T. Ogielski, “Dynamics of three-dimensional Ising spin glasses in thermal equilibrium,” *Physical Review B*, vol. 32, p. 7384, 1985.
- [147] T. Okubo, S. Chung, and H. Kawamura, “Multiple- $q$  states and the skyrmion lattice of the triangular-lattice Heisenberg antiferromagnet under magnetic fields,” *Physical Review Letters*, vol. 108, p. 017206, 2012.
- [148] L. Onsager, “Crystal statistics. I. A two-dimensional model with an order-disorder transition,” *Physical Review*, vol. 65, p. 117, 1944.
- [149] C. W. Oseen, “The theory of liquid crystals,” *Trans. Faraday Soc.*, vol. 29, p. 883, 1933.
- [150] G. Parisi and F. Rapuano, “Effects of the random number generator on computer simulations,” *Physics Letters B*, vol. 157, no. 4, p. 301, 1985.
- [151] C. S. Petrie and J. A. Connelly, “A noise-based ic random number generator for applications in cryptography,” *IEEE Transactions on Circuits and Systems I: Fundamental Theory and Applications*, vol. 47, no. 5, p. 615, 2000.
- [152] C.-E. Pfister, “Interface free energy or surface tension: definition and basic properties,” *ArXiv:0911.5232*, 2009.
- [153] J. C. Phillips, “Stretched exponential relaxation in molecular and electronic glasses,” *Reports on Progress in Physics*, vol. 59, no. 9, p. 1133, 1996.
- [154] H. Puzkarski and P. E. Wigen, “Effect of dzialoshinsky-Moriya interactions on propagation of spin waves in ferromagnets: Dynamical canting,” *Physical Review Letters*, vol. 35, p. 1017, 1975.

- [155] S. Putterman, “Superfluid hydrodynamics,” in *Low Temperature Physics*, N.-H. Series, Ed., vol. 3, 1974.
- [156] R. Quartu and H. T. Diep, “Phase diagram of body-centered tetragonal helimagnets,” *Journal of Magnetism and Magnetic Materials*, vol. 182, no. 1, p. 38, 1998.
- [157] J. Raabe, R. Pulwey, R. Sattler, T. Schweinböck, J. Zweck, and D. Weiss, “Magnetization pattern of ferromagnetic nanodisks,” *Journal of Applied Physics*, vol. 88, no. 7, p. 4437, 2000.
- [158] M. Ribière, R. Maisonnay, and T. d’Almeida, “Numerical and experimental characterization of a plasma induced on a solid target by an intense pulsed multi-MeV e-beam,” *Physics of Plasmas*, vol. 24, no. 6, p. 063105, 2017.
- [159] J. C. S. Rocha, P. Z. Coura, S. A. Leonel, R. A. Dias, and B. V. Costa, “Diagram for vortex formation in quasi-two-dimensional magnetic dots,” *Journal of Applied Physics*, vol. 107, no. 5, p. 053903, 2010.
- [160] S. Rohart and A. Thiaville, “Skyrmion confinement in ultrathin film nanostructures in the presence of Dzyaloshinskii-Moriya interaction,” *Physical Review B*, vol. 88, p. 184422, 2013.
- [161] H. D. Rosales, D. C. Cabra, and P. Pujol, “Three-sublattice skyrmions crystal in the antiferromagnetic triangular lattice,” *arXiv:1507.05109v1*, 2015.
- [162] S. Ross, *Stochastic processes*, 2nd ed., ser. Wiley series in probability and statistics: Probability and statistics. Wiley, 1996.
- [163] U. Röbber, A. N. Bogdanov, and C. Pfleiderer, “Spontaneous skyrmion ground states in magnetic metals,” *Nature*, vol. 442, p. 797, 2006.
- [164] V. Rusakov and M. I. Shliomis, “Landau-de Gennes free energy expansion for nematic polymers,” *Journal de Physique Lettre*, vol. 46, p. 935, 1985.
- [165] C. Santamaria and H. T. Diep, “Dipolar interactions in magnetic thin films: perpendicular to in-plane ordering transition,” *Journal of Magnetism and Magnetic Materials*, vol. 212, no. 1, p. 23, 2000.
- [166] A. Saupe, “Kernresonanzen in kristallinen Flüssigkeiten und in kristallinflüssigen Lösungen.” *Zeitschrift für Naturforschung*, p. 161, 1964.
- [167] I. A. Sergienko and E. Dagotto, “Role of the Dzyaloshinskii-Moriya interaction in multiferroic perovskites,” *Physical Review B*, vol. 73, p. 094434, 2006.
- [168] T. Shinjo, T. Okuno, R. Hassdorf, K. Shigeto, and T. Ono, “Magnetic vortex core observation in circular dots of permalloy,” *Science*, vol. 289, no. 5481, p. 930, 2000.

- [169] K. Sigman, “Lecture notes on stochastic modeling I,” Master’s thesis, Columbia University NYC.
- [170] T. H. R. Skyrme, “A non-linear field theory,” *Proceedings of the Royal Society of London A: Mathematical, Physical and Engineering Sciences*, vol. 260, no. 1300, p. 127, 1961.
- [171] T. H. R. Skyrme, “A unified field theory of mesons and baryons,” *Nuclear Physics*, vol. 31, p. 556, 1962.
- [172] A. D. Sokal, *Monte Carlo Methods in Statistical Mechanics: Foundations and New Algorithms*. Springer US, 1997, p. 131.
- [173] A. D. Sokal and L. E. Thomas, “Exponential convergence to equilibrium for a class of random-walk models,” *Journal of Statistical Physics*, vol. 54, no. 3, p. 797, 1989.
- [174] A. A. Stashkevich, M. Belmeguenai, Y. Roussigné, S. M. Cherif, M. Kostylev, M. Gabor, D. Lacour, C. Tiusan, and M. Hehn, “Experimental study of spin-wave dispersion in Py/Pt film structures in the presence of an interface Dzyaloshinskii-Moriya interaction,” *Physical Review B*, vol. 91, p. 214409, 2015.
- [175] I. S. Suzuki and M. Suzuki, “Stretched-exponential relaxation in the three-dimensional short-range Ising spin-glass  $\text{Cu}_{0.5}\text{Co}_{0.5}\text{Cl}_2\text{-FeCl}_3$  graphite bi-intercalation compound,” *Physical Review B*, vol. 78, p. 214404, 2008.
- [176] R. H. Swendsen and J.-S. Wang, “Nonuniversal critical dynamics in Monte Carlo simulations,” *Physical Review Letters*, vol. 58, p. 86, 1987.
- [177] P. Tamayo, R. C. Brower, and W. Klein, “Single-cluster Monte Carlo dynamics for the Ising model,” *Journal of Statistical Physics*, vol. 58, p. 1083, 1990.
- [178] D. F. B. ten Haaf and J. M. J. van Leeuwen, “High-temperature series expansions for the hubbard model,” *Physical Review B*, vol. 46, p. 6313, 1992.
- [179] K. Ugajin, Y. Terashima, K. Iwakawa, A. Uchida, T. Harayama, K. Yoshimura, and M. Inubushi, “Real-time fast physical random number generator with a photonic integrated circuit,” *Optics Express*, vol. 25, no. 6, p. 6511, 2017.
- [180] E. Y. Vedmedenko, H. P. Oepen, A. Ghazali, J.-C. S. Lévy, and J. Kirschner, “Magnetic microstructure of the spin reorientation transition: A computer experiment,” *Physical Review Letters*, vol. 84, p. 5884, 2000.
- [181] E. Y. Vedmedenko, A. Ghazali, and J.-C. S. Lévy, “Magnetic vortices in ultrathin films,” *Physical Review B*, vol. 59, p. 3329, Feb 1999.
- [182] J. Villain, “La structure des substances magnetiques,” *Journal of Physics and Chemistry of Solids*, vol. 11, no. 3, p. 303, 1959.

- [183] A. Wachowiak, J. Wiebe, M. Bode, O. Pietzsch, M. Morgenstern, and R. Wiesendanger, "Direct observation of internal spin structure of magnetic vortex cores," *Science*, vol. 298, no. 5593, p. 577, 2002.
- [184] J.-S. Wang and R. H. Swendsen, "Transition matrix Monte Carlo method," *Journal of Statistical Physics*, vol. 106, no. 1, p. 245, 2002.
- [185] K. G. Wilson, "Renormalization group and critical phenomena. I. renormalization group and the Kadanoff scaling picture," *Physical Review B*, vol. 4, p. 3174, 1971.
- [186] U. Wolff, "Collective Monte Carlo updating for spin systems," *Physical Review Letters*, vol. 62, p. 361, 1989.
- [187] U. Wolff, "Comparison between cluster Monte Carlo algorithms in the Ising model," *Physics Letters B*, vol. 228, p. 379, 1989.
- [188] F. Y. Wu, "The potts model," *Reviews of Modern Physics*, vol. 54, p. 235, 1982.
- [189] Q. F. Xiao, J. Rudge, E. Girgis, J. Kolthammer, B. C. Choi, Y. K. Hong, and G. W. Donohoe, "Dynamics of magnetic vortex core switching in Fe nanodisks by applying in-plane magnetic field pulse," *Journal of Applied Physics*, vol. 102, no. 10, p. 103904, 2007.
- [190] Y. Yafet and E. M. Gyorgy, "Ferromagnetic strip domains in an atomic monolayer," *Physical Review B*, vol. 38, p. 9145, 1988.
- [191] A. Yoshimori, "A new type of antiferromagnetic structure in the rutile type crystal," *Journal of the Physical Society of Japan*, vol. 14, no. 6, p. 807, 1959.
- [192] X. Z. Yu, N. Kanazawa, Y. Onose, K. Kimoto, W. Z. Zhang, S. Ishiwata, Y. Matsui, and Y. Tokura, "Near room-temperature formation of a skyrmion crystal in thin-films of the helimagnet FeGe," *Nature materials*, vol. 10, no. 2, p. 106, 2011.
- [193] X. Z. Yu, M. Mostovoy, Y. Tokunaga, W. Z. Zhang, K. Kimoto, Y. Matsui, Y. Kaneko, N. Nagaosa, and Y. Tokura, "Magnetic stripes and skyrmions with helicity reversals," *Proceedings of the National Academy of Sciences of the United States of America*, vol. 109, p. 8856, 2012.
- [194] X. Z. Yu, Y. Onose, N. Kanazawa, J. H. Park, J. H. Han, Y. Matsui, N. Nagaosa, and Y. Tokura, "Real-space observation of a two-dimensional skyrmion crystal," *Nature*, vol. 465, no. 7300, p. 901, 2010.
- [195] K. Zakeri, Y. Zhang, J. Prokop, T.-H. Chuang, N. Sakr, W. X. Tang, and J. Kirschner, "Asymmetric spin-wave dispersion on Fe(110): Direct evidence of the Dzyaloshinskii-Moriya interaction," *Physical Review Letters*, vol. 104, p. 137203, 2010.

- [196] A. Zangwill, *Physics at Surfaces*. Cambridge University Press, 1988.
- [197] J. Zinn-Justin, *Quantum Field Theory and Critical Phenomena*. Oxford University Press, 2002.
- [198] V. Zwetkoff, “Über die Molekülordnung in der anisotrop-flüssigen Phase,” *Acta Physicochimica USSR*, p. 132, 1942.



